Department of Mathematics and Physics
University of Freiburg

Masterthesis

Investigation of the Higgs-gluon Coupling Tensor Structure in the Decay Channel $H \to \gamma\gamma$ with the ATLAS Experiment

Marco Zimmermann

January 8, 2015

under the supervision of
Professor Dr. Markus Schumacher

Abstract

The production of the Higgs boson detected in 2012 is dominated by the loop-induced gluon-fusion process. A direct, model-independent evidence for the coupling of this particle to the top quark, as predicted in the Standard Model of particle physics (SM), has not been provided yet. In this thesis, the Higgs-gluon coupling tensor structure is analysed based on an effective field theory. The presence of point-like coupling vertices in addition to the SM predicted gluon fusion coupling structure is discussed. The contribution of the coupling operators describing these point-like vertices is determined by Wilson coefficients. The analysis is based on data taken with the ATLAS detector in 2012 in proton-proton collisions at a center of mass energy of $8\,\mathrm{TeV}$ and investigates events in the $H \to \gamma\gamma$ decay channel. The observable used to test different theoretical predictions is the Higgs boson transverse momentum spectrum, in events with at least one reconstructed jet. As a result of this analysis, confidence intervals at 90% C.L. are determined for the Wilson coefficients considered. No deviations from the SM predictions for the transverse Higgs boson momentum were found in these investigations.

Zusammenfassung

Die Produktion des im Juli 2012 entdeckten Higgs-Bosons wird durch den schleifeninduzierten Prozess der Gluon-Gluon-Fusion dominiert. Ein direkter, modellunabhängiger Nachweis der Kopplung dieses Teilchens an das Top-Quark, wie sie im Standardmodell der Teilchenphysik (SM) vorhergesagt wird, steht noch aus. In der vorgestellten Arbeit wird die Tensorstruktur der Higgs-Gluon-Kopplung anhand einer effektiven Feldtheorie untersucht. Das Vorhandensein von punktförmigen Kopplungsvertices zusätzlich zur im SM vorhergesagten Kopplungsstruktur wird diskutiert. Diese punktförmigen Kopplungsvertices werden durch verschiedene Kopplungsoperatoren beschrieben, deren Beitrag durch Wilson-Koeffizienten festgelegt wird. Die vorgestelle Analyse verwendet Daten, die 2012 mit dem ATLAS-Detektor in Proton-Proton-Kollisionen bei einer Schwerpunktsenergie von $8\,\mathrm{TeV}$ aufgezeichnet wurden und untersucht Ereignisse im Zerfallskanal $H \to \gamma\gamma$. Das Transversalimpulsspektrum des Higgs-Bosons in Ereignissen mit mindestens einem rekonstruiertem Jet wird als sensitive Observable verwendet und mit verschiedenen Theorievorhersagen verglichen. Als Ergebnis dieser Analyse werden Vertrauensintervalle für die betrachteten Wilson-Koeffizienten mit einem Konfidenzniveau von 90% angegeben. In diesen Untersuchungen konnten keine Abweichungen in der Transversalimpulsverteilung des Higgs-Bosons von der Vorhersage des Standard-Modells gefunden werden.

Contents

List of Figures

List of Tables

1. Introduction

At the end of the 19th century, many physicists shared the belief that the field of theoretical physics was nearly completely investigated. A famous remark representing this notion was quoted by Max Planck in 1924. He mentioned that his tutor Philipp v. Jolly approximately 50 years earlier had told to him that physics was "a highly developed, almost fully mature science that [..] would probably have soon adopted its final stable form" [1, tr.]. This thinking has been proven wrong not only by the contributions of Planck himself to the establishment of quantum mechanics, but also in particular by the development of elementary particle physics over the past century.

Elementary particle physics questions the composition and interaction of matter observed in the universe. In the second half of the 20th century, the Standard Model of elementary particle physics was established. Most observations of elementary particles and their interactions have been found to be described well by this relativistic quantum field theory. It is based on the principle of local gauge invariance and considers particles as excitations of quantum fields. However, the quantum fields introduced in the Standard Model do intrinsically not contain any mass terms since these terms would violate the requirement of local gauge invariance. Nevertheless, a theory of elementary particle physics must account for the experimental observations of massive fermions and massive gauge bosons.

This problem can be solved by introducing the Higgs mechanism which was derived in the 1960's by several physicists. By utilizing the mechanism of electroweak symmetry breaking, it allows massive elementary particles and at the same time ensures local gauge invariance. The incorporation of this mechanism comes with an additional field, the so-called Higgs field, coupling to all massive particles. The realisation of this new field results in a new boson, the Higgs boson. The observation of this proposed new boson has therefore been one of the main goals of experiments performed in the field of elementary particle physics over the last decades.

In 2012, the collaborations of the ATLAS[1] and CMS[2] experiments, both placed at the Large Hadron Collider built at CERN[3], announced the observation of a new boson with a mass around $125\,\mathrm{GeV}$[4] [2, 3]. The observation of this new boson was followed in 2013 by the awarding of Peter Higgs and Francois Englert with the Nobel prize "for the theoretical discovery of a mechanism that contributes to our understanding of the origin of mass of subatomic particles" [4].

[1] ***A** **T**oroidal **L**HC **A**pparatu**S***
[2] **C**ompact **M**uon **S**olenoid
[3] European Organisation for Nuclear Research, fr. *Conseil **E**uropéen pour la **R**echerche **N**ucléaire*
[4] using natural units with $\hbar = c = 1$.

First property measurements indicate the observed boson to be consistent with Standard model predictions. Analyses performed within the ATLAS collaboration have shown that a spin parity configuration of $J^P = 0^+$ is statistically preferred. Furthermore, the measured signal strengths for different decay channels and production processes of the Higgs boson are so far compatible with the SM prediction. However, the compatibility of the gluon fusion signal strength with the SM prediction does not imply any statement on the coupling structure. Extensive studies on the coupling properties therefore still need to be accomplished. In particular, it has to be investigated if the Higgs-gluon coupling vertex is described by a top-quark loop, as it is predicted in the SM.

In this thesis, the tensor structure of the Higgs-gluon coupling is investigated with an effective theory approach using point-like coupling operators up to mass dimension seven [5]. The analysis considers a possible presence of the point-like vertices described by these operators in addition to the gluon-fusion coupling structure described in the SM. The contribution of these coupling operators is determined by the Wilson coefficients. Each Wilson coefficient is investigated individually while the other coefficients are set to zero. The additional contributions can manifest themselves in the p_T spectrum of observed Higgs bosons. This p_T spectrum was investigated with data of proton-proton collisions at $\sqrt{s} = 8\,\mathrm{TeV}$ that was recorded with the ATLAS detector in 2012. As a result of the analysis presented in this thesis, the best fit values and confidence intervals for the Wilson coefficients are given based on the observations in data.

This thesis is structured as follows: At the beginning, the Standard Model theory and the incorporation of the Higgs mechanism are discussed and possible problems of this description are briefly addressed. Moreover, the effective theory describing the Higgs-gluon coupling with point-like coupling operators is summarised. The description of the ATLAS detector at the LHC in chapter 3 is followed by a discussion of the signal and background processes which are relevant for this analysis. Their simulation according to predictions in the Standard Model or to different parameter realisations in the effective theory are also treated in chapter 4. The object reconstruction and event selection used for this analysis are discussed in chapter 5. In chapter 6, the estimation of the background is addressed. The systematic uncertainties which are considered in this analysis are explained in chapter 7. In chapter 8, studies with simulated events are described which are used to interpret the observations in data. The results based on the Higgs p_T distribution extracted from data are then given in chapter 9 and include the influence of systematic uncertainties. Finally, the thesis concludes in chapter 10 with a summary and interpretation of the obtained results.

2. Theory Basics

This chapter aims to give a short overview of the theoretical background on which the analysis described in this thesis is based. First, an introduction to the Standard Model of particle physics (SM), that is currently the best description of the known elementary (in the sense of *"point-like"*, without substructure) particles and their interactions, is given. Afterwards, the phenomenology of the Higgs boson in proton-proton collisions at the LHC is summarized. Furthermore, a short report on its detection and the current status of property measurements at the ATLAS and CMS experiments is given. Finally, possible problems of the SM are addressed followed by an alternative description of the Higgs-gluon coupling.

A more detailed description of the concepts outlined in the following two sections can be found in [6–10] and other references given in the text.

2.1. The Standard Model of Particle Physics

The SM is a relativistic quantum field theory describing the known elementary particles and their interactions. It combines theories that describe electromagnetic, weak and strong force. The gravitational force is the only known fundamental interaction which is not included in the SM. However, at energy scales of elementary particle interactions accessible in current collider experiments, gravitation does not influence the behaviour of the particles. Several predictions of the SM have been confirmed experimentally during the last decades, establishing the SM as the best currently known description of fundamental particle physics.

2.1.1. Elementary Particles

Particles in the SM can be categorized by their quantum numbers, one of them is their spin. Fermions are particles with half-integer spin, they obey the Pauli exclusion principle and Fermi-Dirac statistics. The SM contains twelve elementary fermions and their respective antiparticles with opposite charges. They have spin $\frac{1}{2}$ and are currently considered as the fundamental constituents of matter. These fermions can be further classified by their masses, electric charge and colour charge. Particles carrying electric charge interact electromagnetically, colour-charged particles take part in the strong interaction.

Quarks are colour-charged fermions and can be further sub-categorised by their masses into three mass generations. Each generation contains one up-type quark with electric charge[1]

[1] in units of the elementary charge e

	Quarks					Leptons				
mass generation		flavour	electric charge [e]	colour	mass [MeV]		flavour	electric charge [e]	colour	mass [MeV]
I	u	up	+2/3	✓	$2.3^{+0.7}_{-0.5}$	e	electron	−1	✗	0.511
	d	down	−1/3	✓	$4.8^{+0.5}_{-0.3}$	ν_e	el. neutrino	0	✗	$<2\times10^{-6}$
II	c	charm	+2/3	✓	1275(25)	μ	muon	−1	✗	105.66
	s	strange	−1/3	✓	95(5)	ν_μ	μ-neutrino	0	✗	<0.19
III	t	top	+2/3	✓	$173.07^{\pm0.52(\text{stat})}_{\pm0.72(\text{sys})}$	τ	τ-lepton	−1	✗	1776.82(16)
	b	bottom	−1/3	✓	4.18(3)	ν_τ	τ-neutrino	0	✗	<18.2

Table 2.1.: *Quarks and leptons in the SM [8].*

$+\frac{2}{3}$ and one down-type quark with $-\frac{1}{3}$, giving six different quark flavours (up, down, charm, strange, top, bottom) characterized by their mass and electric charge.

Leptons are colourless fermions and therefore do not interact strongly. Similar to quarks, they come in three mass generations (lepton flavour): the electron e, the muon μ and the τ-lepton, each with electric charge -1, together with the corresponding uncharged massless[2] neutrinos ν_e, ν_μ, ν_τ. The properties and categorisation of elementary fermions are summarized in table 2.1.

Next to spin, electric charge, colour charge and particle flavour, the weak isospin, or more precisely, its third component I_3 relating to the weak interaction, is another quantum number of particles in the SM. Left-handed fermions (stating negative chirality) have $I_3 = \pm\frac{1}{2}$ and can therefore be written in doublets χ_L as shown in table 2.2. For quark states, it has to be considered that the isospin eigenstates with $I_3 = -\frac{1}{2}$, denoted by d', s', and b', are not the corresponding observed mass eigenstates (d, s, b), but related to them by the Cabibbo-Kobayashi-Maskawa matrix V_{CKM}:

$$\begin{pmatrix} d' \\ s' \\ b' \end{pmatrix} = \begin{pmatrix} V_{ud} & V_{us} & V_{ub} \\ V_{cd} & V_{cs} & V_{cb} \\ V_{td} & V_{ts} & V_{tb} \end{pmatrix} \begin{pmatrix} d \\ s \\ b \end{pmatrix} \tag{2.1}$$

where V_{ud}, for example, specifies the coupling of u to d ($d \to u + W^-$)[6]. In contrast to the lepton flavour[2], the quark flavour is therefore not necessarily conserved in weak processes. Right-handed fermions form singlets χ_R with $I_3 = 0$. They are therefore not affected by weak interaction. Consequently, right-handed neutrinos would not interact at all and are not existent in the SM. Instead of quoting the weak isospin I_3, it is also possible to characterize a particle by specifying the weak hypercharge Y. It is related to the weak Isospin I_3 and the

[2] In the original formulation of the SM, neutrinos are massless. However, observations of neutrino mixing indicate small finite neutrino masses [11–13] and violate lepton flavour conservation.

	Fermion multiplets			I	I_3	Q	Y
Leptons	$\begin{pmatrix} \nu_e \\ e \end{pmatrix}_L$	$\begin{pmatrix} \nu_\mu \\ \mu \end{pmatrix}_L$	$\begin{pmatrix} \nu_\tau \\ \tau \end{pmatrix}_L$	$1/2$	$+1/2$ $-1/2$	0 -1	-1 -1
	e_R	μ_R	τ_R	0	0	-1	-2
Quarks	$\begin{pmatrix} u \\ d' \end{pmatrix}_L$	$\begin{pmatrix} c \\ s' \end{pmatrix}_L$	$\begin{pmatrix} t \\ b' \end{pmatrix}_L$	$1/2$	$+1/2$ $-1/2$	$2/3$ $-1/3$	$+1/3$ $+1/3$
	u_R	c_R	t_R	0	0	$+2/3$	$+4/3$
	d_R	s_R	b_R	0	0	$-1/3$	$-2/3$

Table 2.2.: *Summary of fermion multiplets of the electroweak interaction. [7]*

electric charge Q of a particle by the Gell-Mann–Nishijima formula [7]

$$Q = \frac{Y}{2} + I_3 \ . \tag{2.2}$$

Bosons are particles with integer spin, they obey Bose-Einstein statistics. In the SM, gauge bosons with spin 1 mediate the fundamental interactions. The uncharged and massless photon (γ) mediates the electromagnetic interaction. The strong force is mediated by the exchange of gluons (g), which are massless and colour-charged. They come in eight different colour states. In contrast to gluons and photons, the mediators of the weak interaction, the uncharged Z-boson and the electrically charged $W^\pm$-bosons, have masses of $91.1876(21)\,\mathrm{GeV}$ and $80.385(15)\,\mathrm{GeV}$ [8], respectively. The additional Higgs particle is a scalar boson. Its existence has been an open question for the last 40 years. The Higgs boson was detected in 2012 at ATLAS [2] and CMS [3]. According to recent analyses, it has a mass around $125\,\mathrm{GeV}$ ($m_H = 125.36 \pm 0.37(\mathrm{stat.}) \pm 0.18(\mathrm{sys.})\,\mathrm{GeV}$ (ATLAS [14]) and $m_H = 124.70 \pm 0.31(\mathrm{stat.}) \pm 0.15(\mathrm{sys.})\,\mathrm{GeV}$ (CMS [15])). The particles in the SM and their categorisation are illustrated in figure 2.1.

2.1.2. Interactions and Gauge Theories

A theory of particle physics has to describe all known particles, their properties and the fundamental interactions. In the SM, the fundamental interactions are mediated by bosons as exchange particles. Since the SM is a relativistic quantum field theory, each particle is the excitation of the corresponding quantum field. Any quantum field theory can be described in the Lagrange formalism. For example, the free Dirac Lagrangian $\mathcal{L}$ of a fermion field ψ reads[3]

$$\mathcal{L} = i\,\overline{\psi}\gamma^\mu\partial_\mu\psi - m\overline{\psi}\psi \tag{2.3}$$

[3] a precise definition of all objects, especially the gamma matrices γ^μ, can be found e.g. in ref. [6].

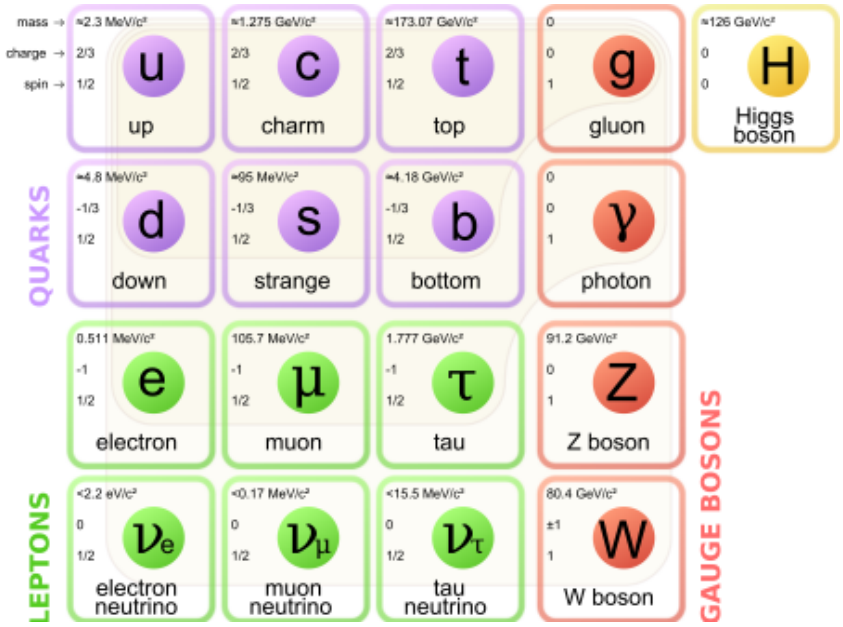

Figure 2.1.: *Elementary particles in the Standard Model*[a] *with their masses [8] and their quantum numbers of spin and electric charge.*

[a] illustration: *Standard Model of Elementary Particles*, Licensed under Creative Commons Attribution 3.0 via Wikimedia Commons - `http://commons.wikimedia.org/wiki/File:Standard_Model_of_Elementary_Particles.svg`

with the adjoint spinor $\overline{\psi} \equiv \psi^\dagger \gamma^0$ and the fermion mass m[4]. By applying the Euler-Lagrange equation to $\overline{\psi}$, the relativistic Dirac equation describing massive spin-$\frac{1}{2}$-fermions is derived:

$$i\gamma^\mu \partial_\mu \psi - m\psi = 0. \tag{2.4}$$

A gauge theory demands the Lagrange density $\mathcal{L}$ to be locally invariant under all symmetry transformations in the symmetry group describing the theory. The electromagnetic interaction does not modify the quantum numbers of interacting particles and therefore can be described by the group $U(1)$ [7]. However, the free Dirac Lagrangian is not invariant under the local $U(1)$ gauge transformation

$$\psi \rightarrow e^{-iq\lambda(x)}\,\psi\,, \tag{2.5}$$

with q denoting the electric charge, but transforms according to [6]

$$\mathcal{L} \rightarrow \mathcal{L} + (q\,\overline{\psi}\gamma^\mu\psi)\partial_\mu\lambda\,. \tag{2.6}$$

To obtain an invariant Lagrangian of quantum electrodynamics (QED), which is the relativistic quantum field theory describing electromagnetic interactions, a new vector field A_μ

[4] To be precise, one would need to distinguish between a mass operator $\mathcal{M}$ and its eigenvalues m: $\mathcal{M}\Psi = m\Psi$. In the following, mass operator and eigenvalues are both denoted by m and the distinction has to be done from the context. The same shortened notation is in the following used for several other quantum numbers.

transforming according to

$$A_\mu \rightarrow A_\mu + \partial_\mu \lambda \tag{2.7}$$

has to be introduced. Defining the covariant derivative

$$\mathcal{D}_\mu \equiv \partial_\mu + iq A_\mu \,, \tag{2.8}$$

the QED Lagrangian for one particle species satisfying local gauge invariance reads [9]

$$\mathcal{L}^{\mathrm{QED}} = \overline{\psi}(i\gamma^\mu \mathcal{D}_\mu - m)\psi - \frac{1}{4}F_{\mu\nu}F^{\mu\nu} \tag{2.9}$$

with $F_{\mu\nu} \equiv \partial_\mu A_\nu - \partial_\nu A_\mu$. The vector field A_μ can be identified as the photon field. It is forced to be massless since any QED Lagrangian including a mass term for the introduced vector field is not invariant.

In the Standard Model, electromagnetic and weak interaction are described in a unified theory by the electroweak interaction formulated by Glashow, Salam and Weinberg [16–18]. This theory is based on the symmetry group $SU(2)_L \times U(1)_Y$. The weak interaction of fermions depends on their chiral states, every Dirac spinor ψ can be divided into a left-handed chiral state ψ_L and a right handed one ψ_R by

$$\psi = \psi_L + \psi_R = \frac{1}{2}\left(1 - \gamma^5\right)\psi + \frac{1}{2}\left(1 + \gamma^5\right)\psi \,. \tag{2.10}$$

The Dirac spinor includes information on space-time-dependence, spin and charge of a particle. Moreover, the particle wave function includes information of the isospinor state and the weak hypercharge of the particle. In isospinor space, left handed particles form isospinor doublets and right handed fermions form isospinor singlets, as summarized in table 2.2. Rotations of the wave function can be performed in each independent subspace and leave the particle state in other independent spaces unchanged.

Left handed isospinor doublets are transformed in the $SU(2)_L$ group by

$$\psi_L \rightarrow \exp\left(i\,\tfrac{g}{2}\vec{\tau}\cdot\vec{\alpha}(x)\right)\psi_L \tag{2.11}$$

in which $\vec{\tau}$ is the vector of the 2×2 Pauli matrices and g is a coupling constant, the vector function $\vec{\alpha}(x)$ depends on three transformation angles in the isospinor space. This transformation leaves the space-time, spin and hypercharge of the wave function unchanged. The transformations under $U(1)_Y$ are

$$\psi_L \rightarrow \exp\left(i\left(\tfrac{g'}{2}Y\right)\beta(x)\right)\psi_L \tag{2.12}$$

$$\psi_R \rightarrow \exp\left(i\left(\tfrac{g'}{2}Y\right)\beta(x)\right)\psi_R \tag{2.13}$$

with a different coupling constant g'. The demand of local gauge invariance this time requires the introduction of three vector fields $\vec{W}_\mu$ for the $SU(2)$ symmetry group and one single vector field B_μ for $U(1)$. With these new gauge fields, the covariant derivative can be deduced and

reads [10]

$$\partial_\mu \rightarrow \mathcal{D}_\mu^L = \partial_\mu + i\,\frac{g}{2}\,\vec{\tau}\cdot\vec{W}_\mu + i\,\frac{g'}{2}Y\,B_\mu \tag{2.14}$$

for left-handed fermion fields and

$$\partial_\mu \rightarrow \mathcal{D}_\mu^R = \partial_\mu + i\,\frac{g'}{2}Y\,B_\mu \tag{2.15}$$

for right-handed charged fermion fields. Finally, inserting these covariant derivatives into equation 2.4 and adding kinematic terms for the new fields gives the electroweak Lagrangian for one fermion generation

$$\mathcal{L}^{\mathrm{EW}} = \overline{\psi}_L\left(i\,\gamma^\mu\mathcal{D}_\mu^L - m\right)\psi_L + \overline{\psi}_R\left(i\,\gamma^\mu\mathcal{D}_\mu^R - m\right)\psi_R - \frac{1}{4}\,\vec{W}_{\mu\nu}\cdot\vec{W}^{\mu\nu} - \frac{1}{4}\,B_{\mu\nu}B^{\mu\nu} \tag{2.16}$$

with

$$W_{\mu\nu}^a = \partial_\mu W_\nu^a - \partial_\nu W_\mu^a - 2g\,\epsilon_{abc}W_\mu^b W_\nu^c \text{ and} \tag{2.17}$$

$$B_{\mu\nu} = \partial_\mu B_\nu - \partial_\nu B_\mu\ . \tag{2.18}$$

However, this Lagrangian is only invariant under local gauge transformations in the group $SU(2)_L \times U(1)_Y$ for the case that $m = 0$ holds for all fermions. The demand of local invariance also forbids mass terms of the gauge fields, which is in contrast to the experimentally observed massive gauge bosons Z and $W^\pm$ of the weak interaction.

To account for those deviations from experimental observations, the Higgs mechanism with an additional Higgs field is incorporated and allows massive gauge bosons and massive fermions without destroying local gauge invariance. The Higgs mechanism and the Higgs boson in the Standard Model are described in the following sections.

The photon field A^μ can be identified with none of the fields $\vec{W}_\mu$ or B_μ since each of them couples to neutrinos. The observable fields must therefore be linear combinations of the gauge fields $\vec{W}_\mu$ and B_μ. The photon field must not couple to neutrinos and couples to left and right chiral fields with the same strength. It has to be orthogonal to the field Z^μ of the neutral Z-boson, so that one obtains [10]

$$A^\mu = B^\mu\cos\theta_W + W_3^\mu\sin\theta_W \tag{2.19}$$

$$Z^\mu = -B^\mu\sin\theta_W + W_3^\mu\cos\theta_W \tag{2.20}$$

with the weak mixing angle θ_W defined by

$$\cos\theta_W = \frac{g}{\sqrt{g^2+g'^2}} \tag{2.21}$$

$$\sin\theta_W = \frac{g'}{\sqrt{g^2+g'^2}}\ . \tag{2.22}$$

Considering the processes $\nu_e \rightarrow e^- + W^+$ with $\Delta I_3 = -1$ and $e^- \rightarrow \nu_e + W^-$ with $\Delta I_3 = 1$ and the generation of their isospinor transformations by the matrices $\tau^- = \frac{1}{2}(\tau_1 - i\,\tau_2)$ and

$\tau^+ = \frac{1}{2}(\tau_1 + i\,\tau_2)$, one finds that the W-boson fields are given by

$$W^{\pm} = \frac{1}{\sqrt{2}}\left(W_1^{\mu} \mp i\,W_2^{\mu}\right) \ . \tag{2.23}$$

Quantum chromodynamics (QCD) is the quantum field theory describing strong interactions. The evidence for a further quantum number, named colour charge, can be found e.g. in the quark wave function of the observed Δ^{++} state. Without an additional quantum number, the total wave function $\psi_{\Delta^{++}}$ would be symmetric. Experimental evidence for three different colour charges is particularly found in the observed cross sections for hadron production in e^+e^- collisions [19]. The particle wave function hence has to be extended by a tensor product with a colour function χ_{colour} in a three-dimensional space.

Three colour charges point that the principle of local gauge invariance in QCD must apply to transformations in the SU(3) symmetry group. They can be written as

$$\psi \rightarrow \exp\left(i\,\frac{g_s}{2}\sum_{i=1}^{8}\lambda_j\beta_j(x)\right)\psi \tag{2.24}$$

with eight 3×3 Gell-Mann matrices λ_j and an eight-component transformation function $\vec{\beta}(x)$ depending on eight phases. Again, only the colour-dependent part of the wave function is transformed. Introducing eight vector fields G_j^{μ} that transform like [10]

$$G_j^{\mu} \rightarrow G'^{\mu}_j = G_j^{\mu} - \partial^{\mu}\beta_j - g_s\,f_{jkl}\beta_k G_l^{\mu} \tag{2.25}$$

for infinitesimal transformations β_j and the totally antisymmetric structure functions f_{jkl}, local gauge invariance is ensured with the covariant derivative

$$\mathcal{D}^{\mu} = \partial^{\mu} + i\,\frac{g_s}{2}\,\lambda_j\,G_j^{\mu} \ . \tag{2.26}$$

The QCD Lagrangian then reads

$$\mathcal{L} = \overline{\psi}\left(i\,\gamma_{\mu}\mathcal{D}^{\mu} - m\right)\psi - \tfrac{1}{4}G_{j,\,\mu\nu}G_j^{\mu\nu} \tag{2.27}$$

with the field tensor $G_j^{\mu\nu} = \partial^{\mu}G_j^{\nu} - \partial^{\nu}G_j^{\mu} - g_s f_{jkl}G_k^{\mu}G_l^{\nu}$. There are eight massless gluon fields G_j^{μ}, which is in agreement with experimental observations.

2.1.3. The Higgs Mechanism

The previous section introduced the principle of local gauge invariance in the SM, which lead to the introduction of several gauge fields and ensures renormalisability [20]. As a result of this principle, the gauge fields in all cases need to be massless. There is no problem with that fact for the electromagnetic and the strong interaction, but the observed masses of $W^{\pm}$ and Z-boson cannot be explained in that way. In the Standard model, these gauge bosons and fermions get their masses (see fig. 2.1) by the so-called Higgs mechanism [21–26].

For this purpose, a new scalar field represented by an isospinor doublet of two complex fields Φ^+ and Φ^- is introduced [10]

$$\Phi = \begin{pmatrix} \Phi^+ \\ \Phi^0 \end{pmatrix} \equiv \begin{pmatrix} \Phi_3 + i\,\Phi_4 \\ \Phi_1 + i\,\Phi_2 \end{pmatrix} \;,\; \Phi_1 \ldots \Phi_4 \in \mathbb{R}, \tag{2.28}$$

with quantum numbers $Y = 1$ and $I = 1/2$. The corresponding Higgs potential considered is given by

$$V_H = -\mu^2 \Phi^\dagger \Phi + \lambda \left(\Phi^\dagger \Phi\right)^2 \,,\, \lambda > 0 \,, \tag{2.29}$$

and leads to the Lagrange densitiy of the Higgs field:

$$\mathcal{L} = (\partial^\mu \Phi)^\dagger (\partial_\mu \Phi) + \mu^2 \Phi^\dagger \Phi - \lambda \left(\Phi^\dagger \Phi\right)^2 \,. \tag{2.30}$$

The Lagrangian must be gauge invariant under local transformations of Φ in the SU(2) and U(1) symmetry groups analogous to (2.11) and (2.12), respectively. This is achieved replacing ∂^μ of Φ by the covariant derivative $\mathcal{D}^\mu$ as written in (2.14) and by adding the kinematic terms for the gauge fields. Consequently, one gets

$$\mathcal{L} = \underbrace{(\mathcal{D}^\mu \Phi^\dagger)(\mathcal{D}_\mu \Phi) + \mu^2 (\Phi^\dagger \Phi) - \lambda^2 (\Phi^\dagger \Phi)}_{\mathcal{L}^{\text{Higgs}}} - \frac{1}{4}\, \vec{W}_{\mu\nu} \cdot \vec{W}^{\mu\nu} - \frac{1}{4}\, B_{\mu\nu} B^{\mu\nu} \tag{2.31}$$

with the field tensors defined according to (2.17) and (2.18). This Lagrangian is invariant under local $SU(2) \times U(1)$ gauge transformations. However, considering the Higgs potential V_H in (2.29), it can be seen that $\Phi = 0$ is obviously not the ground state of the physical system described by this Lagrangian. Since calculations in the Standard Model are performed with a perturbative approach starting from the ground state of the fields involved, this formulation is not suited to read off physical quantities. For the case of $\mu > 0$, the ground state for the Higgs potential in (2.29) is found at

$$\left(\Phi^\dagger \Phi\right)_{\text{min}} = |\Phi|^2_{\text{min}} = \frac{\mu^2}{2\lambda} = \frac{v^2}{2} \tag{2.32}$$

with the vacuum expectation value v. This ground state is continuously degenerated since it is occupied by different configurations of the real fields $\Phi_1 \ldots \Phi_4$. Figure 2.2 illustrates this degeneration in two dimensions. The choice of the particular vacuum state

$$\Phi_0 = \frac{1}{\sqrt{2}} \begin{pmatrix} 0 \\ v \end{pmatrix} \tag{2.33}$$

with quantum numbers $I_3 = -1/2$ and $Y = 1$ breaks the $SU(2)_L \times U(1)_Y$ symmetry of the Lagrangian in (2.31) spontaneously. According to (2.2), this ground state has $Q = 0$, therefore $U(1)_Q$ symmetry remains unbroken. The choice of a vacuum state with $\Phi^+ \neq 0$ would lead to a massive photon, a possible contribution of Φ_2 can be eliminated by applying a gauge transformation [10]. Using this unitary gauge, the scalar field $\Phi(x)$ can be parametrised

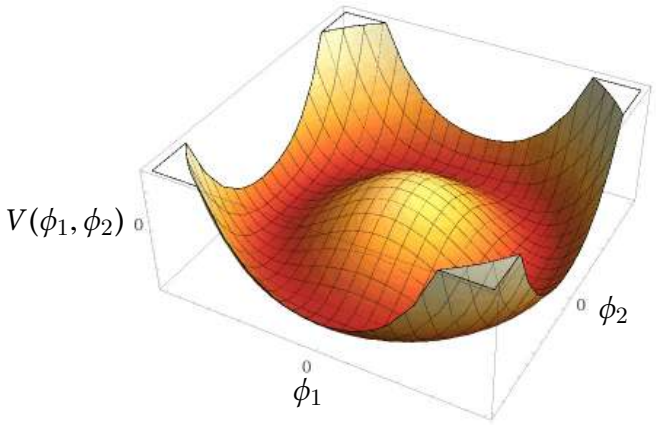

Figure 2.2.: *Higgs potential $V(\phi_1, \phi_2)$ in two dimensions for the case of spontaneous symmetry breaking $\mu > 0$ [27].*

around the chosen vacuum state writing

$$\Phi(x) = \frac{1}{\sqrt{2}} \begin{pmatrix} 0 \\ v + h(x) \end{pmatrix} . \tag{2.34}$$

By rewriting the Lagrangian (2.31) with this parametrisation, gauge boson mass terms occur. They come from the first term in (2.31) evaluated at the vacuum state Φ_0. The corresponding component $\Delta\mathcal{L}$ of the full Lagrangian is therefore obtained to be [9]

$$\Delta\mathcal{L} = \frac{1}{2}\frac{v^2}{4}\left[g^2(W_\mu^1)^2 + g^2(W_\mu^2)^2 + (-gW_\mu^3 + g'B_\mu)^2\right] . \tag{2.35}$$

Consequently, the masses of the photon (γ), Z-boson and the $W^\pm$-bosons with their fields according to (2.19), (2.20) and (2.23) can be read off with the following values:

$$m_\gamma = 0 \tag{2.36}$$

$$m_Z = \frac{v}{2}\sqrt{g^2 + g'^2} \tag{2.37}$$

$$m_{W^\pm} = \frac{v}{2}g . \tag{2.38}$$

Considering the excitation $h(x)$ from the ground state, the Lagrangian $\mathcal{L}^{\text{Higgs}}$ as defined in (2.31) becomes

$$\mathcal{L}^{\text{Higgs}} = \underbrace{-\lambda v^2 h^2 - \lambda v h^3 - \frac{1}{4}\lambda h^4}_{\text{potential terms}} + \underbrace{\frac{1}{2}(\partial_\mu h)^2 + \left[m_W^2 W^{\mu+} W_\mu^- + \frac{1}{2}m_Z^2 Z^\mu Z_\mu\right] \cdot \left(1 + \frac{h}{v}\right)^2}_{\text{kinematic terms}} . \tag{2.39}$$

The field $h(x)$ therefore results in a scalar particle H with mass

$$m_H = \sqrt{2\lambda}\, v \tag{2.40}$$

that couples to the massive gauge bosons and to itself. This particle is known as the Higgs boson. Fermion masses are implemented in a similar way, again exploiting the principle of spontaneous symmetry breaking. A Higgs-fermion coupling has to be introduced that leaves the neutrinos massless in the ground state (2.33). For the electron as an example, the added Yukawa-coupling term becomes

$$\mathcal{L}_e^{\text{Yukawa}} = -\lambda_e \left(\overline{\nu}_e, \overline{e}\right)_L \cdot \Phi \, e_R + \text{h.c.} \, . \tag{2.41}$$

Thus, the electron acquires a mass of

$$m_e = \frac{1}{\sqrt{2}} \lambda_e v \, . \tag{2.42}$$

Similar terms are added for all charged fermions in the Standard Model. Evaluating these coupling terms in unitary gauge, one finds that the coupling of the Higgs boson to any fermion f is proportional to the fermion mass [9]

$$\mathcal{L}_f^{\text{Yukawa}} = -m_f \overline{f} f \left(1 + \frac{h}{v}\right) \, . \tag{2.43}$$

The vacuum expectation value v can be determined by measuring the $W^{\pm}$-boson mass and the electroweak couplings, as it can be seen from (2.38). Couplings of the weak interaction are commonly expressed in terms of the Fermi coupling constant [8]

$$G_F = \frac{\sqrt{2}}{8} \left(\frac{g}{m_W}\right)^2 = 1.166\,378\,7(6) \times 10^{-5}\,\text{GeV}^{-2} \, . \tag{2.44}$$

The vacuum expectation value is then given by

$$v = \left(\sqrt{2} G_F\right)^{-1/2} \approx 246\,\text{GeV} \, . \tag{2.45}$$

Regarding the Lagrangian given in (2.39), λ is therefore the only remaining unknown coupling parameter. Consequently, when m_H is measured experimentally, all coupling parameter included in the SM are determined.

The full Standard Model Lagrangian finally reads

$$\mathcal{L}^{\text{SM}} = \mathcal{L}^{\text{Higgs}} + \mathcal{L}^{\text{EW}} + \mathcal{L}^{\text{QCD}} + \mathcal{L}^{\text{Yukawa}} \, . \tag{2.46}$$

2.2. The Higgs Boson

The incorporation of the Higgs mechanism into the Standard Model, as described in the previous section, predicts the existence of a new boson with particular properties. The SM Higgs Boson is predicted to have no electrical charge, no colour charge and a spin-parity configuration of 0^+. The coupling of the Higgs boson to fermions and the weak gauge bosons is proportional to their masses. These properties of the SM Higgs Boson need to be measured

to confirm its existence and to rule out other extended and more complicated theories. After the detection of a Higgs-candidate in 2012 at ATLAS [2] and CMS [3], this is one of the main goals of ongoing analyses.

The search for the Higgs boson gives rise to several experimental challenges explaining the fact that the existence of the Higgs Boson has been an unanswered question for more than 40 years. First of all, the SM Higgs boson is predicted to have a very short lifetime (about 10^{-22}s for an assumed Higgs boson mass of $125\,\mathrm{GeV}$, calculated from [28]) allowing only its decay particles to be detected. Very small production cross sections and signal-to-background-ratios require particle accelerators with high centre of mass energies and luminosities as well as the development of sophisticated data selection strategies.

In the first part of this section, constraints on the Higgs Boson mass based on the Standard Model prediction and their compatibility to the measured mass of the new boson detected at ATLAS and CMS are discussed. Afterwards, the phenomenology of the Higgs production at proton-proton collisions and the decay of the Higgs boson to detectable particles are summarized. Finally, a short review on the Higgs observation at the LHC and the current status of property measurements is given.

2.2.1. Constraints on the Higgs Boson Mass in the Standard Model

According to (2.40), the Higgs boson mass depends on the vacuum expectation value v and on the scale parameter λ which is a free parameter in the Standard Model. However, there are some theoretical constraints on the SM Higgs boson mass. For the process $e^-e^+ \to W^+W^-$, divergencies occur in amplitudes with longitudinally polarized W-bosons at high energies and violate unitarity if $m_H \lesssim 1\,\mathrm{TeV}$ [29] does not hold. Furthermore, several couplings involving the Higgs boson enter a non-pertubative domain for very high Higgs boson masses [30] resulting in another upper bound (triviality or perturbativity bound). The demand of a (meta)stable vaccuum additionally leads to a lower bound on the Higgs boson mass. Since these problems with very low or high Higgs boson masses could be solved by physics beyond the Standard Model, these bounds depend on the scale at which so-called new physics becomes relevant, as shown in figure 2.3a.

On the experimental side, indirect constraints on the Higgs boson mass can be derived from electroweak precision measurements. These indirect measurements exploit that couplings and therefore particle masses in the SM depend on the Higgs boson mass m_H. As shown in figure 2.3b, the best fit value is $m_H = 93^{+25}_{-21}\mathrm{GeV}$ [33]. Assuming the new particle detected at the LHC to be the SM Higgs boson, this value is compatible to the average ATLAS and CMS mass measurements [14, 15] within 1.3σ. These predictions are only valid for a SM Higgs boson. The search for possible Higgs bosons is performed over a wider mass range of about $(110 - 1000)\,\mathrm{GeV}$ to be sensitive to extended theoretical models.

2.2.2. Higgs Boson Production in Proton-Proton Collisions

At the LHC, the Higgs Boson is produced in proton-proton collisions. The interactions of interest can be considered as hard scattering processes of gluons and (anti)quarks. In previous

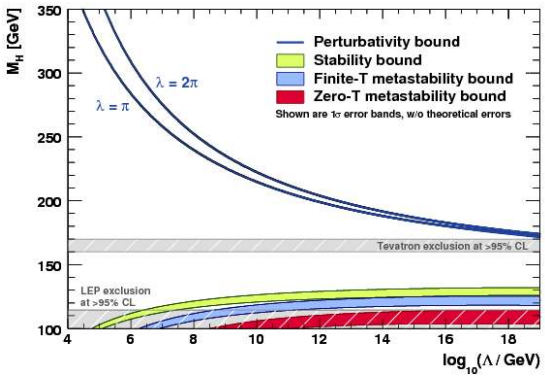

(a) *Theoretic bounds on m_H depending on the scale Λ on which new physics has to appear in order to avoid the bounds. The different bands account for theoretic uncertainties. The grey bands represent 95% C.L. exclusion limits determined in experiments before the LHC. [31]*

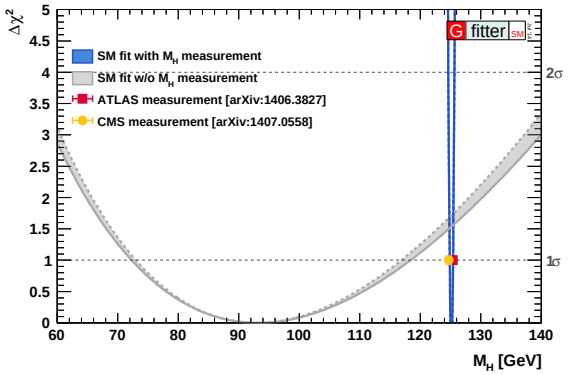

(b) *$\Delta\chi^2$ profile for a fit of electroweak precision measurements as a function of the Higgs boson mass m_H and data points from ATLAS [14] and CMS [15]. The grey (blue) band shows the results when excluding (including) the new direct m_H measurements from (in) the fits. The solid (dotted) lines illustrate the fit results including (ignoring) theoretical uncertainties in the fit [32, 33].*

Figure 2.3.: *Theoretical (a) and experimental (b) constraints on the Higgs boson mass. The results including direct mass measurements at the LHC assume the detected particle to be the SM Higgs Boson.*

experiments, parton density functions (PDF) $f(x_i, Q)$ for protons were determined. They predict the probability to find a particular parton i (in this case a gluon or a(n) (anti)quark) with momentum fraction x_i in the proton at a given energy scale Q. In proton-proton collisions, the presence of several partons cause so-called underlying events of partons interacting with small momentum transfer. They occur in addition to the actual hard scattering process. Considering this hard scattering process of two particular partons i and j with cross section σ_{ij}, the cross section of this process in the collision of two protons A and B is, according to the factorisation theorem, given by [34, 35]

$$\sigma_{AB} = \iint \mathrm{d}x_i \, \mathrm{d}x_j \, f_A(x_i, \mu_F) \, f_B(x_j, \mu_F) \, \sigma_{ij}(\mu_R) \; . \tag{2.47}$$

Here, μ_F is the factorisation scale, which can be thought of as the scale that separates the long- and short-distance physics, and μ_R is the renormalisation scale for the QCD running coupling. The numerical result will depend on the choice of these scales, it is sensible to choose $\mu_F = \mu_R$ values of the order of the typical momentum scales of the hard scattering process [35]. The choice of a particular μ_R can equivalently be expressed by the corresponding strong coupling constant $\alpha_s(\mu_R)$.

The four different Higgs boson production modes with largest cross sections in hadron colliders are represented by their Feynman graphs in figure 2.4. The production cross sections for a Higgs boson mass of $m_H = 125\,\mathrm{GeV}$ are given in table 4.1.

The most important production mechanism is gluon fusion. The contribution to the total Higgs boson production is about 86.5% at $m_H = 125\,\mathrm{GeV}$ [28]. The coupling of the Higgs

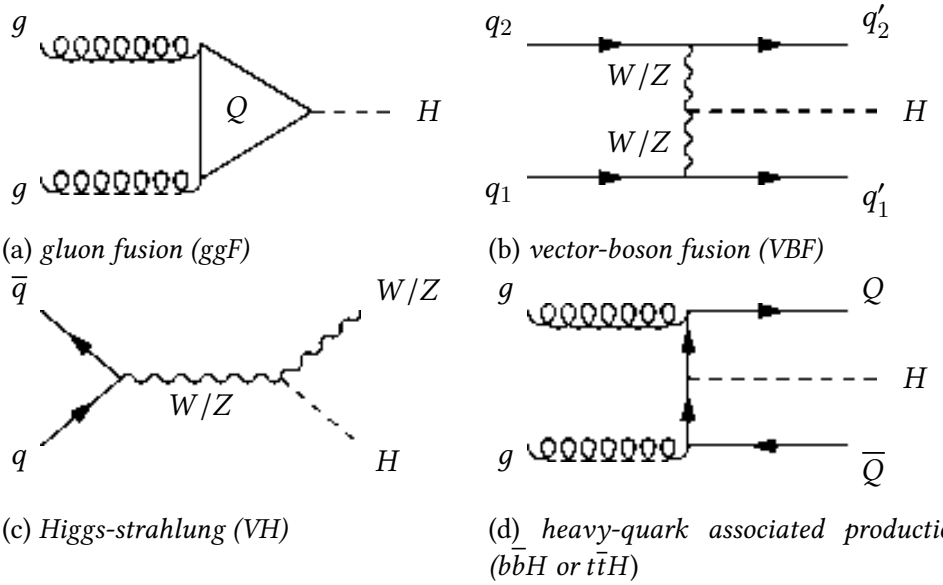

(a) *gluon fusion (ggF)*

(b) *vector-boson fusion (VBF)*

(c) *Higgs-strahlung (VH)*

(d) *heavy-quark associated production ($b\bar{b}H$ or $t\bar{t}H$)*

Figure 2.4.: *Leading order Feynman graphs for the main Higgs boson production modes at hadron colliders. Heavy quarks (top or bottom) are denoted by Q, light quarks by q. Time axis in horizontal direction.*

boson to the gluons in the initial state is mediated by a heavy quark loop. Top quarks are preferred because of their high mass. At leading order, the Higgs boson is the only particle in the final state and thus has no transverse[5] momentum p_T. Considering next-to-leading-order (NLO) processes, initial states with one or even two quarks are possible. Figure 2.5 shows for each possible initial state one exemplary NLO Feynman graph with a gluon-gluon-Higgs-vertex as predicted in the SM . In these next-to-leading-order processes, the Higgs boson acquires a non-zero transverse momentum.

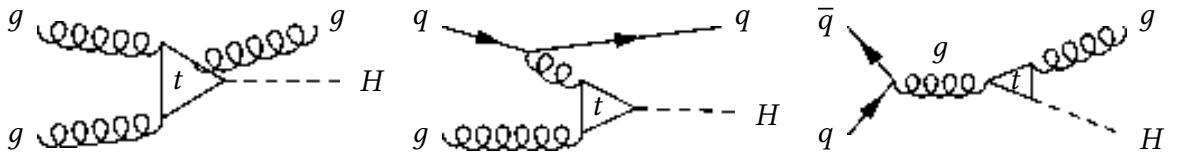

(a) *gluon - gluon initial state*

(b) *(anti-)quark - gluon initial state*

(c) *quark - anti-quark initial state*

Figure 2.5.: *Exemplary NLO Feynman graphs for Higgs production in gluon fusion with different initial states . The process in (b) is also possible with an anti-quark in the initial state.*

In vector boson fusion (VBF), the Higgs Boson is produced by fusion of two vector bosons ($W^{\pm}$- or Z-bosons), each emitted by a quark of the colliding protons. The contribution to the total Higgs boson production is about 7%. The additional jets in the final state prefer a forward-backward configuration which means a large seperation in pseudorapidity (for definition see section 3.2.1). Tagging these two high-p_T jets allows to define event categories enriched with VBF production. Associated production with vector bosons (VH), which is also called Higgsstrahlung, is the third important production process. The Higgs boson is

[5]The coordinate system in which transverse observables are defined is described in the next chapter

radiated from a weak gauge boson which is produced in $q\bar{q}$ annihilation. This production process contributes to the total Higgs boson production cross section by about 5%. Heavy-quark associated production does not play an important role in the Higgs production because of its small relative cross section of less than 1%. One main reason for this small production cross section is the high invariant mass that is required to produce the heavy quark pair in the final state.

The cross sections of the different Higgs boson production modes depend on the collision energy $\sqrt{s}$. The analysis presented in this thesis is based on data taken in the ATLAS experiment in 2012 with $\sqrt{s} = 8\,\mathrm{TeV}$. The corresponding cross sections for the different production modes are shown depending on different Higgs boson mass hypotheses in figure 2.6. The theoretical uncertainties mainly originate from limited order calculations and uncertainties on the proton parton density functions. The peak at around $350\,\mathrm{GeV}$ in the gluon fusion curve is explained by the fact that for $m_H \approx 2m_t$, the top quark is on its mass shell.

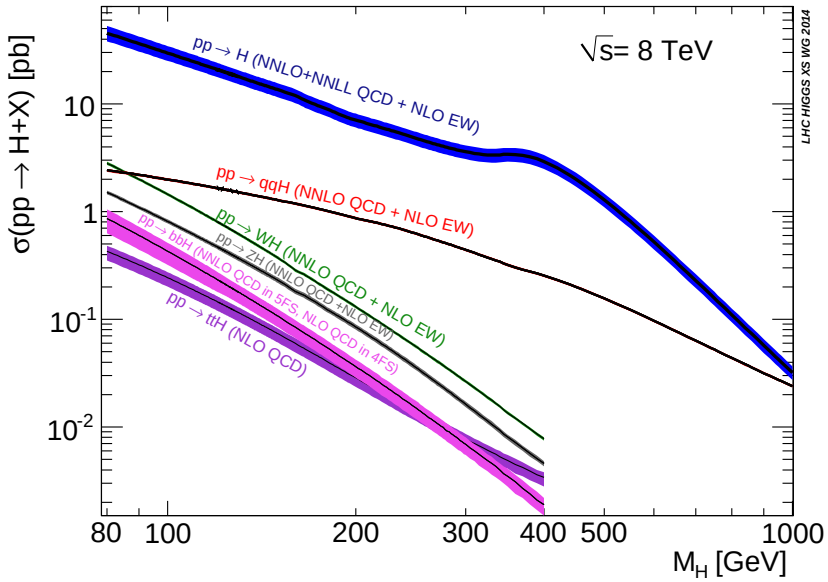

Figure 2.6.: *Standard Model Higgs boson production cross sections at* $\sqrt{s} = 8\,\mathrm{TeV}$ *[28]*

2.2.3. Higgs Boson Decay Processes

The Higgs boson is unstable and can therefore only be reconstructed by the detection of its decay particles. The branching ratio *BR* of a possible decay channel is defined as the decay width of the Higgs Boson in this particular decay channel divided by the total Higgs boson decay width,

$$BR(H \to X) \equiv \frac{\Gamma_{H\to X}}{\Gamma_{\mathrm{tot}}}\,, \tag{2.48}$$

and corresponds to the decay probability.

The Higgs Boson can decay to either bosonic or fermionic particle states. Possible fermionic decay products are quark-anti-quark pairs as well as lepton-anti-lepton pairs. The fermion coupling to the Higgs boson is proportional to the fermion mass, but top quark pairs are too heavy to be produced in a Higgs boson decay if $m_H \lesssim 2m_t$. Only branching ratios for $b\bar{b}$, $c\bar{c}$, $\tau^+\tau^-$ and $\mu^+\mu^-$ as fermionic decay products are shown in figure 2.7a because other fermions are too light to contribute significantly.

Possible bosonic decay states are ZZ, W^+W^-, gg, $Z\gamma$ and the decay considered in this analysis into two photons $\gamma\gamma$. The Higgs decay into massless photons is similar to the gluon fusion production process mediated by a particle loop, predominantly of top quarks and $W^\pm$ bosons. For a Higgs boson mass of $125\,\mathrm{GeV}$, the largest branching ratio can be observed for the $b\bar{b}$ decay state with $BR > 0.5$. However, this Higgs boson decay is hardly accessible experimentally in gluon fusion and VBF Higgs boson production because of the high hadronic background rates at LHC. Consequently, at least one photon, lepton or a tau decay is required for a final particle state to be reliably reconstructed as a Higgs boson decay product.

The high reconstruction efficiency for photons is the main reason why the two photon decay $H \to \gamma\gamma$ with a branching ratio of only $BR = 2.28 \times 10^{-3}$ nevertheless has a high sensitivity for the detection and property measurements of the Higgs boson. Furthermore, it has a high mass resolution and a lower background rate compared to other final states with higher branching ratios.

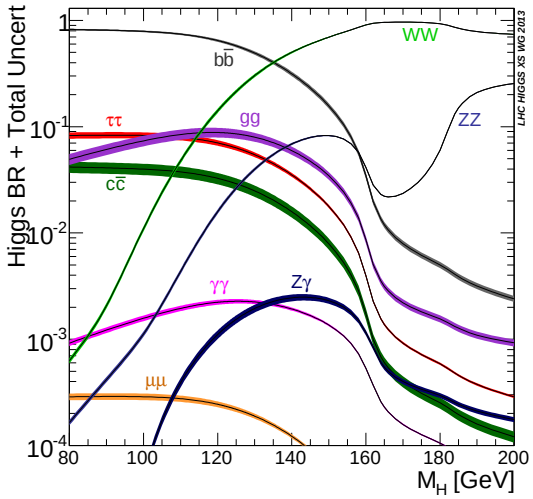

(a) *Standard Model Higgs boson decay branching ratios with theoretical uncertainties*

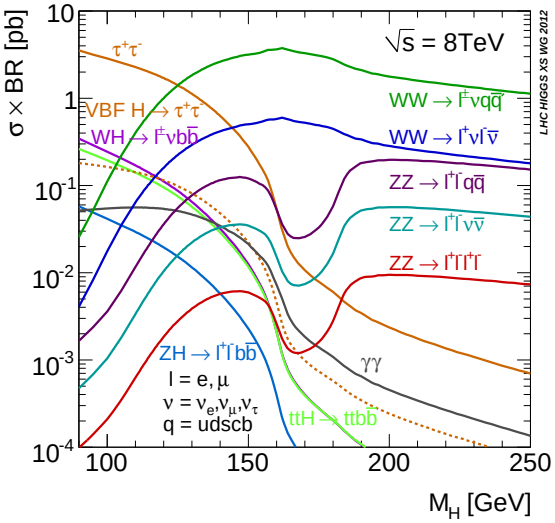

(b) *Standard Model Higgs boson production cross section times branching ratio at $\sqrt{s} = 8\,\mathrm{TeV}$. For $H \to \tau\tau$ both inclusive (solid line) and VBF (dashed line) mode are plotted.*

Figure 2.7.: *Predicted branching ratios and cross sections of different SM Higgs boson decay channels [28]*

The massive gauge boson pairs produced by a decaying Higgs boson decay themselves to leptonic or hadronic final states (or mixtures of both). Figure 2.7b shows the Higgs boson production cross section times branching ratio at $\sqrt{s} = 8\,\mathrm{TeV}$ for different hypothetical Higgs

boson masses for final particles that are actually detected directly in the detector (apart from the tau leptons). The highest cross sections are obtained for final states containing neutrinos (decaying tau leptons also produce at least one neutrino). Since neutrinos cannot be detected directly and only appear as missing transverse energy E_T^{miss} (for definition, see sec. 3.2.1), these final states have only low mass resolutions. This underlines the importance of the two photon final state for mass measurements.

2.2.4. Observation of a new Boson at the Large Hadron Collider

In 2012, ATLAS and CMS announced the observation of a new boson with a mass of around $125.5\,\text{GeV}$ and a significance of 5.9σ and 5.0σ, respectively [2, 3]. This corresponds to a maximum local p_0-value (background fluctuation probability) of 1.7×10^{-9} for the ATLAS analysis, as shown in figure 2.8. A p_0-value corresponding to 5σ is required to consider a

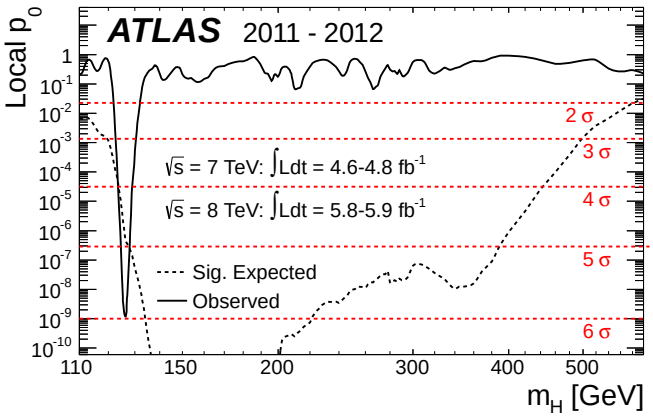

Figure 2.8.: *Combined search results in the ATLAS experiment: The observed (solid) local p_0 as a function of m_H and the expectation (dashed) for a SM Higgs boson signal hypothesis ($\mu = 1$) at the given mass [2].*

particle as observed.

The observation of the Higgs boson is essential to confirming the mechanism of electroweak symmetry breaking, but the properties of the detected Higgs boson must be carefully analysed to verify the predictions of the Standard Model. The detection of the new particle decaying into two photons implies that it is an uncharged boson. The Landau-Yang theorem forbids the decay of a spin-1 particle into two photons [36, 37], while further analyses at the ATLAS experiment exclude spin parity configurations for the Higgs boson of $J^P = 0^-, 1^+, 1^-, 2^+$ [38]. Figure 2.6 shows the perturbatively calculated SM prediction for the Higgs boson production cross sections.

These theoretical predictions can be compared to measurements from data to determine the signal strength

$$\mu = \frac{\sigma_{\text{obs}}}{\sigma_{\text{SM}}} \,. \tag{2.49}$$

This analysis can be performed separately for different production modes exploiting particular event topologies of the different production processes. Furthermore, the signal strengths μ are determined for each decay channel separately and for their combination. Figure 2.9a shows the corresponding results for the simultaneous determination of μ_{ggF} and μ_{VBF} in the $H \to \gamma\gamma$ decay. The best fit value for the gluon fusion signal strength μ_{ggF} determined in the diphoton Higgs boson decay at a Higgs boson mass of $m_H = 125.4\,\mathrm{GeV}$ is 1.32 ± 0.38 [39]. In figure 2.9b, the corresponding signal strength measurements in the different decay channels and their combination is shown. The results of these coupling strength measurements are so far compliant to the SM prediction $\mu = 1$. However, the compatibility of μ_{ggF} with the SM does not imply any statement on the coupling structure itself. Moreover, despite observed evidence for gluon fusion in cross-channel analyses, no model-independent evidence that the gluon-Higgs-coupling is mediated by a top quark and not by other heavy particles has been found, yet. Further analyses of Higgs properties therefore investigate possible anomalous contributions to coupling structures and (differential) cross section measurements.

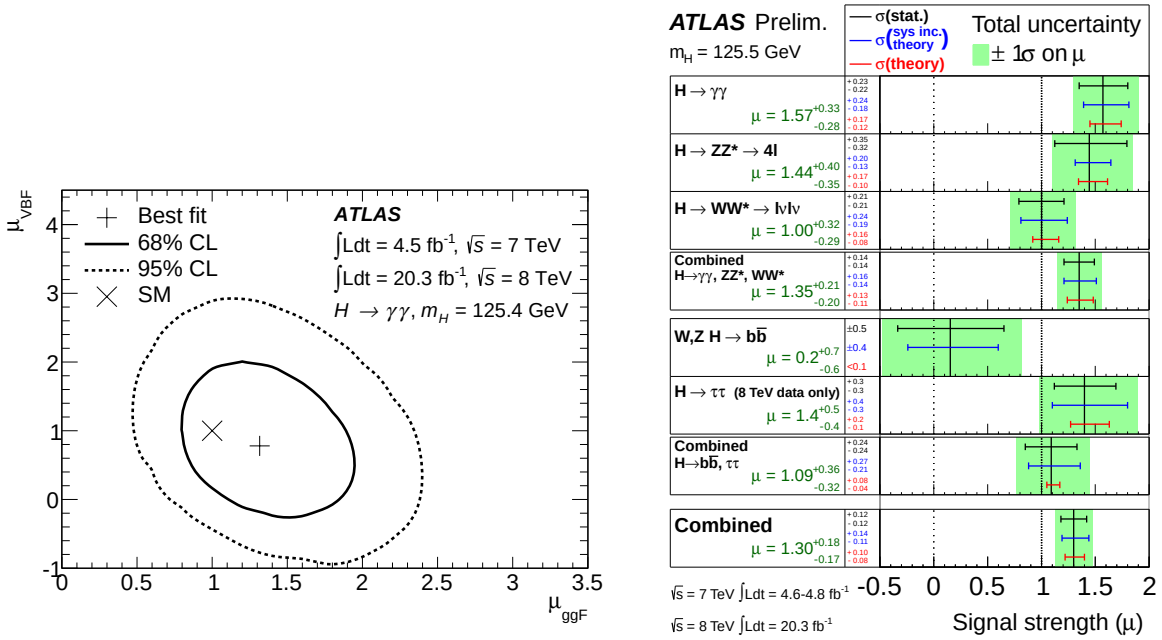

(a) *The two-dimensional best-fit value of (μ_{VBF}, μ_{ggF}) for a Higgs boson of mass $m_H = 125.4\,\mathrm{GeV}$ decaying via $H \to \gamma\gamma$ when fixing $\mu_{t\bar{t}H}$ and $\mu_{b\bar{b}H}$ to 1 and profiling the other signal strength parameters [39].*

(b) *The measured signal strengths for a Higgs boson of mass $m_H = 125.5\,\mathrm{GeV}$, for the individual final states and combinations. [40].*

Figure 2.9.: *Coupling strength measurements of the detected Higgs Boson at the ATLAS detector. The Standard Model prediction corresponds to $\mu = 1$ in all cases.*

2.3. Physics Beyond the Standard Model

With the recent discovery of the Higgs Boson at the LHC, all elementary particles predicted in the Standard Model are confirmed to exist. The identification of electroweak symmetry

breaking realized in the Higgs mechanism further validates the SM to be an accurate description of elementary particles at currently accessible energy scales. Nevertheless, there are still some open questions for which the Standard Model does not give a satisfactory answer. This relates to the problem of the large mass hierarchy and small neutrino masses[6], the missing unification with gravity and the existence of dark matter [42]. Different implementations of a Grand Unified Theory (GUT) are proposed in which strong, electromagnetic and weak force are unified and characterized by one larger gauge symmetry.

Signatures of such new physics might arise at energy scales accessible at the LHC and be identified in the form of new particles or processes. Next to these direct searches, the precise measurement of the Higgs boson properties and possible deviations from the SM expectations provide another probe for new physics. In addition to searches for new physics at high energy scales at the LHC, other precision experiments intend to find signatures of new physics even at lower energy scales e.g. by providing very high intensities and branching ratio sensitivities [43].

2.4. Probing the Nature of the Higgs-Gluon Coupling

In this section, an effective theory for a general description of a point-like gluon-Higgs coupling, that is compatible with the gauge symmetries of the SM, is introduced. This concept is described in detail in [5] so that only the parts relevant for the analysis presented in this thesis are summarized in the following.

In elementary particle physics, effective theories are often used to give predictions that are in agreement to observations at a limited energy scale. This means that an effective theory ignores substructures and further degrees of freedom at shorter distances (corresponding to higher energies). Above a particular energy scale Λ, these additional degrees of freedom become relevant and manifest themselves in observable phenomena that are not predicted in the effective theory. At lower energies, the dynamics can be predicted at sufficient accuracy without the knowledge of the high energy Lagrangian. Generally, an effective Lagrangian

$$\mathcal{L} = \sum_i c_i O_i \tag{2.50}$$

is a sum of local, gauge and Lorentz invariant operators O_i [44]. The contribution of the individual operators is determined by a set of coefficients c_i.

A commonly cited example of an effective theory in elementary particle physics is the Fermi Theory of Beta Decay [45, 46] that can also be used to approximate other weak processes such as the muon decay. According to this theory proposed in 1933, the muon decays in one single vertex at which muon, muon neutrino, electron and electron neutrino interact. The four fermion operator describing this point-like coupling vertex is of dimension six. The coupling strength of this four fermion interaction is described by the Fermi coupling constant G_F which was given in (2.44) and has dimensions GeV^{-2}. However, cross sections calculated

[6] An extension of the SM accounts for this finding and introduces the Pontecorvo-Maki-Nakagawa-Sakata matrix (PMNS) [41] that relates the neutrino eigenstates of the weak interaction with their mass eigenstates.

in the Fermi theory grow with the square of the energy, $\sigma \sim G_F^2 E^2$ and are therefore not in agreement to observations at energy scales above $100\,\mathrm{GeV}$. The reason for this observation are the additional degrees of freedom of the massive W-boson that cannot be neglected at energies comparable to the W-boson mass. The point-like vertex described in the Fermi Theory is the low energy limit of the weak interaction as described in the SM in which the $\mu^{\pm}$-decay is accomplished by the exchange of a $W^{\pm}$-boson. Figure 2.10 shows the Feynman graph of a muon decay according to the point-like Fermi interaction and according to the Standard Model.

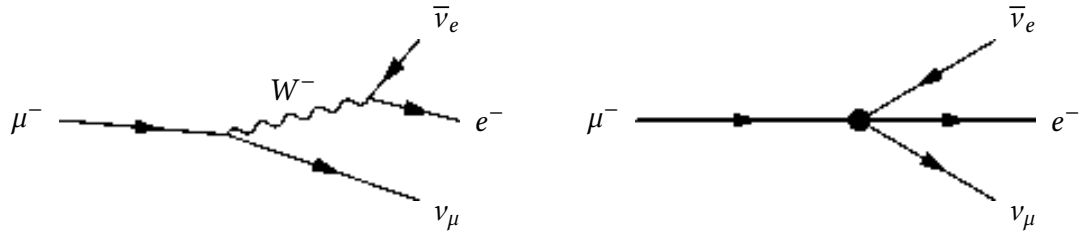

(a) *Standard Model μ^--decay* (b) *μ^--decay in Fermi's interaction*

Figure 2.10.: *Feynman graphs of a μ^--decay in the SM with the exchange of a W^--boson and in the limit $m_W \to \infty$ representing a point-like coupling proposed in the Fermi Theory.*

Even the Standard Model of Particle Physics can be considered as an effective theory that is only valid at energies below a particular energy scale. Moreover, the SM prediction of the Higgs-gluon coupling mediated by a top quark (see section 2.2.2) is often approximated in an effective approach by a point-like coupling derived in the limit $m_t \to \infty$. This point-like coupling can then be described by a coupling operator of mass dimension five which given by

$$O_1 = H G_{j,\mu\nu} G_j^{\mu\nu} \tag{2.51}$$

with the Higgs boson H and the gluon field tensor $G_j^{\mu\nu}$. In this analysis, the transverse momentum distribution of the Higgs boson measured with the ATLAS experiment is tested for an observable effect of higher dimensional operators. The difference between a loop-induced coupling and a point-like coupling is expected to be particularly strong in events in which a jet with high transverse momentum is observed in addition to the Higgs boson [5]. Possible Feynman graphs representing SM Higgs boson production processes with a Higgs-gluon vertex and with one additional jet are shown in figure 2.5 for different initial particle states. Considering point-like vertices in an effective theory instead of a coupling induced by a top quark, the Lagrangian taking into account operators up to mass dimension seven for a CP even Higgs boson can be written as [5]

$$\mathcal{L} = \frac{C_1}{\Lambda} O_1 + \sum_{n=2}^{5} \frac{C_n}{\Lambda^3} O_n\,, \tag{2.52}$$

$$O_1 = H G_{j,\mu\nu} G_j^{\mu\nu}, \qquad O_2 = H D_\alpha G_{j,\mu\nu} D^\alpha G_j^{\mu\nu}, \qquad O_3 = H G^{\mu}_{j,\nu} G^{\nu}_{k,\sigma} G^{\sigma}_{l,\mu} f_{jkl}, \tag{2.53}$$

$$O_4 = H D^\alpha G_{j,\alpha\nu} D_\beta G_j^{\beta\nu}, \qquad O_5 = H G_{j,\alpha\nu} D^\nu D^\beta G^{\alpha}_{j,\beta}$$

where

$$G_j^{\mu\nu} = \partial^\mu G_j^\nu - \partial^\nu G_j^\mu - g_s f_{jkl} G_k^\mu G_l^\nu \,, \qquad D^\mu G_j^\nu = \partial^\mu G_j^\nu - g_s f_{jkl} G_k^\mu G_l^\nu \quad (2.54)$$

with the gluon field G_j^μ and the Higgs boson H. The strong coupling is denoted by g_s and f_{jkl} are the SU(3) structure constants. This Lagrangian describes the coupling of a scalar Higgs boson to gluons. An effective Lagrangian with pseudo-scalar operators is also given in [5], but not considered in this analysis. The operator O_1 is of mass dimension five and describes the SM Higgs-gluon coupling in the $m_t \to \infty$ limit (neglecting lighter quark loops). The operators O_2, O_3, O_4 and O_5 are of mass dimension seven. The operators defined in 2.53 are not linearly independent, but are related by $m_H^2 O_1 = 4O_5 - 2O_2 + 4g_s O_3$ [5]. The mass parameter Λ is undetermined a priori and represents the energy scale of some new physics generating the point-like vertices. The coefficients C_i are free parameters called Wilson coefficients and must be determined experimentally. Differential cross sections calculated in this effective theory then take the (symbolic) form

$$\mathrm{d}\sigma = \sum_{i,j=1}^{5} \mathrm{d}\sigma_{ij} = \frac{C_1^2}{\Lambda^2}\,\mathrm{d}\widetilde{\sigma}(O_1 O_1^\dagger) + \sum_{j=2}^{5} \frac{C_1 C_j}{\Lambda^4}\,\mathrm{d}\widetilde{\sigma}(O_1 O_j^\dagger) + O\left(\frac{1}{\Lambda^6}\right) \quad (2.55)$$

The mixed terms $O_1 O_j^\dagger$ are therefore a priori suppressed by $1/\Lambda^2$ with respect to the leading term $O_1 O_1^\dagger$.

Considering the influence of the top quark on the kinematics of the Higgs boson produced in gluon fusion as physics emerging at an energy scale around $\Lambda = m_t$, this effective theory approach can be used to approximate the SM description of the Higgs-gluon vertex induced by a top quark loop. This procedure allows to calculate pertubative expressions C_i^{SM} for the Wilson coefficients matching the SM prediction [5]:

$$\begin{aligned}
C_1^{\mathrm{SM}} &= \frac{g_s^2 \lambda_t}{48\pi^2} + O(g_s^4) \approx 2.2 \times 10^{-3} \,, \\
C_2^{\mathrm{SM}} &= \frac{-7 g_s^2 \lambda_t}{2880\pi^2} + O(g_s^4) \approx -2.6 \times 10^{-4} \,, \\
C_3^{\mathrm{SM}} &= \frac{-g_s^3 \lambda_t}{240\pi^2} + O(g_s^5) \approx -5.3 \times 10^{-4} \,, \\
C_4^{\mathrm{SM}} &= \frac{g_s^2 \lambda_t}{1440\pi^2} + O(g_s^4) \approx 7.3 \times 10^{-5} \,, \\
C_5^{\mathrm{SM}} &= \frac{g_s^2 \lambda_t}{80\pi^2} + O(g_s^4) \approx 1.3 \times 10^{-3} \,,
\end{aligned} \quad (2.56)$$

with $\lambda_t = m_t/v$ and $g_s = \sqrt{4\pi\alpha_s}$. The coefficients are therefore not constant, the numerical values are given for illustration by inserting $m_t = 172\,\mathrm{GeV}$, $v = 246\,\mathrm{GeV}$ and $\alpha_s = 0.118$ [5]. Since the coefficients are proportional to the top quark mass, the suppression of the $O_1 O_j^\dagger$ terms is partly canceled. The predictions of the effective theory concerning gluon fusion events with one additional radiated jet with SM matching coefficients work well to describe the transverse momentum of the Higgs boson produced in a top-quark loop, in particular if two gluons are in the initial particle state and $p_T \lesssim m_t$ [5]. For higher energies, the effective

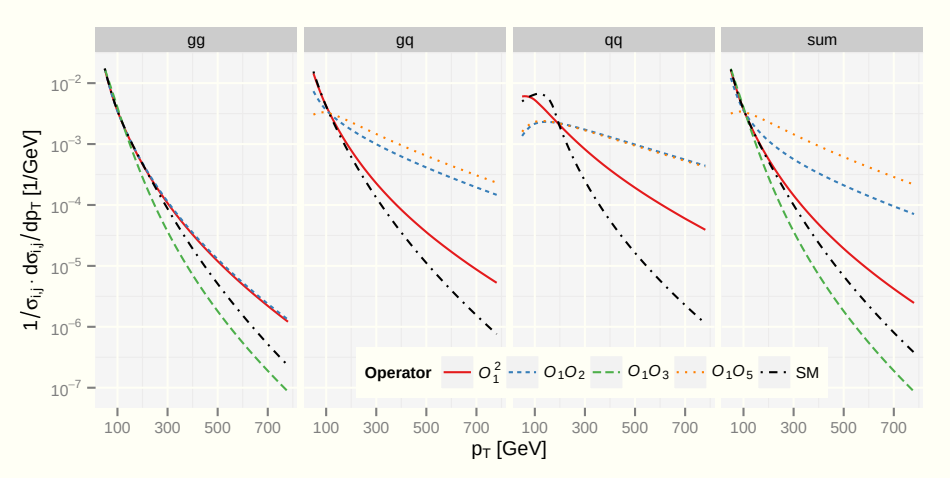

Figure 2.11.: *Normalized Higgs boson transverse momentum distributions in one-jet-events in proton-proton collisions with* $\sqrt{s} = 13\,\mathrm{TeV}$ *for different point-like coupling operator terms up to* $1/\Lambda^4$*-suppression [5].*

theory predictions differ from the predictions in the SM.

In a similar way as for the top-quark loop, possible new physics concerning the Higgs-gluon coupling structure that emerge at a higher energy scale Λ can be investigated in the given effective theory approach. For energies $E < \Lambda$, differential cross sections are dominated by the contribution attributed to the $O_1 O_1^\dagger$ operator term, but contributions of the operators O_j, which are suppressed by $1/\Lambda^2$ with respect to the leading term, might nevertheless be observable at energy scales accessible at the LHC. Moreover, it is possible that the suppression of the higher order operator terms is, analogously to the observation for the SM matching of the effective theory, partly cancelled by the Wilson coefficients.

In this analysis, the Higgs boson transverse momentum distribution in $H + 1$ jet-events is considered to search for possible contributions of the operators O_i. The operator O_4 only contributes in couplings involving two quarks and does therefore not contribute to processes considered in this analysis. The operator O_5 requires at least one quark to participate in the interaction and does therefore not contribute to events with two gluons in the initial state [5]. Figure 2.11 shows the normalised Higgs boson p_T-distributions of the different operator terms in (2.55) up to $1/\Lambda^4$-suppression in one-jet-events separately for the different initial states and for the sum of them compared to the SM top-quark loop prediction. The notation q in this case includes anti-quarks $\overline{q}$. It can be seen that the form of the distributions looks similar in the dominant gg initial state, but deviations from the SM p_T-distribution, calculated for a top-loop induced coupling, are observed especially for the O_1O_2- and O_1O_5-terms in the gq- and qq-sub-channels.

In the presented analysis, it is assumed that only one of the operators O_i contributes at the same time in addition to the SM coupling structure. Consequently, one C_i is fitted to the data while the other coefficients C_j are set to zero. This procedure is chosen because of the limited statistics of signal events in the currently available data set that was recorded with the ATLAS detector. With the number of observed signal events, a fit of more than one parameter at the same time is not expected to give meaningful results in terms of deriving

confidence intervals for the Wilson coefficients. The differential cross sections considered in this ansatz then for each operator O_i take the (symbolic) form of

$$\frac{\mathrm{d}\sigma}{\mathrm{d}p_T} = \frac{\mathrm{d}\sigma_{\mathrm{SM}}}{\mathrm{d}p_T} + \frac{\mathrm{d}}{\mathrm{d}p_T}\left[\left(\frac{C_i}{\Lambda^n}\right)\widetilde{\sigma}(O_{\mathrm{SM}}O_i^\dagger) + \left(\frac{C_i}{\Lambda^n}\right)^2\widetilde{\sigma}(O_iO_i^\dagger)\right], \begin{cases} n=1 & \text{if } i=1 \\ n=3 & \text{if } i=2,3,5 \end{cases} \tag{2.57}$$

with the SM prediction of the gluon fusion process described by the operator O_{SM}. The contribution of the interference term can be negative. Without taking into account the contribution of the $O_iO_i^\dagger$ operator terms, the cross section term would not be restricted to positive values for all possible kinematics. Consequently, the squared operator terms are considered. The analysis is hence not at a fixed order in $\frac{1}{\Lambda}$, but assumes that gluon fusion Higgs boson production is realised by the SM processes and a possible additional contribution of one of the operators O_i.

3. The ATLAS Detector at the Large Hadron Collider

This chapter gives a short overview on the conceptual design of the ATLAS detector and the Large Hadron Collider (LHC) at which it is placed. Detailed descriptions on the collider and the detector can be found in [47, 48].

3.1. The Large Hadron Collider

The Large Hadron Collider (LHC) at CERN near Geneva is a two-ring-superconducting-hadron accelerator and collider. It is installed in the tunnel that was built for the Large Electron-Positron Collider (LEP) that ran from 1989 to 2000. With a circumference of about $27\,\mathrm{km}$, it is the world's largest circular hadron collider. The LHC is built as a particle-particle collider with counter-rotating beams of protons or heavy ions (Pb). The LHC magnets are constructed such that opposite magnetic fields are provided for the two separated rings that are placed inside one module. Figure 3.1 shows a schematic view of the LHC ring and the four main particle detector experiments: ATLAS, CMS, ALICE[1] and LHCb[2]. Protons are pre-accelerated in one linear and three circular accelerators before entering the LHC with an energy of $450\,\mathrm{GeV}$. The Super Proton Synchrotron (SPS) as the final link in the pre-acceleration chain is also shown in figure 3.1.

The performance of a particle collider is mainly determined by the centre of mass energy $\sqrt{s}$ and the instantaneous luminosity $\mathcal{L}$ provided. The LHC is designed to collide proton beams with a centre of mass energy of $\sqrt{s} = 14\,\mathrm{TeV}$. The maximum beam energy is determined by the peak dipole field of the 1232 superconducting dipole magnets accommodated in the storage ring. The maximum value is $8.33\,\mathrm{T}$. Additional quadrupole magnets are installed in order to focus the proton beams. The luminosity is the proportionality factor between the event rate for a given process and the production cross section. For two colliding bunches of Gaussian and equal shape, the instantaneous luminosity is given by [49]

$$\mathcal{L} = n_b \frac{N^2 f \gamma}{4\pi\beta^* \epsilon_n} S \tag{3.1}$$

where N is the number of particles per bunch, n_b the number of bunches per beam, f is the revolution frequency, γ the relativistic factor, β^* the value of the beta function at the interaction point, ϵ_n the normalised transverse beam emittance and S is the geometric reduction

[1] A Large Ion Collider Experiment
[2] Large Hadron Collider beauty

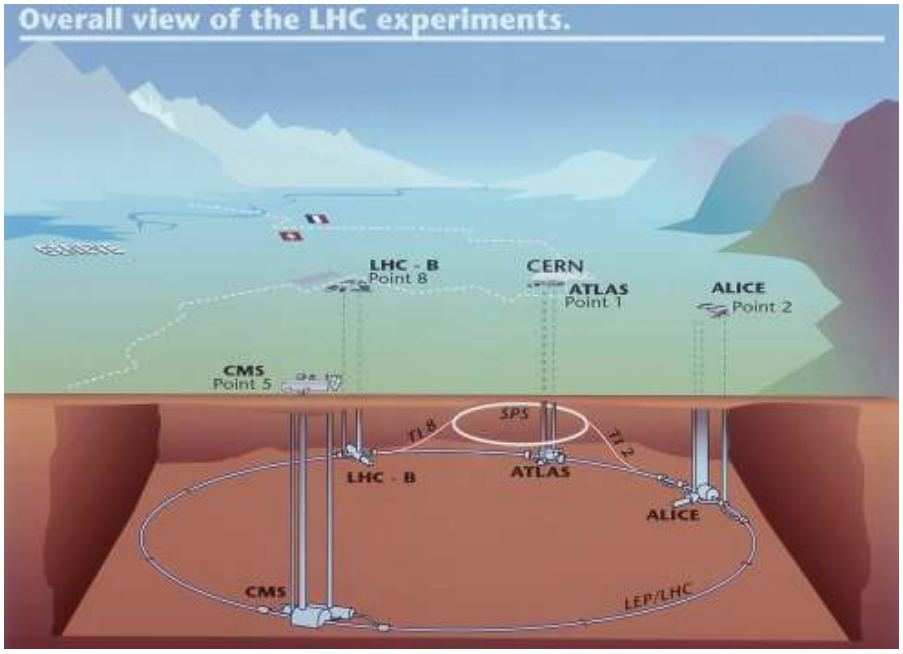

Figure 3.1.: *Locations of the four main experiments (ALICE, ATLAS, CMS and LHCb) taking place at the LHC. Located between* $50\,\mathrm{m}$ *and* $150\,\mathrm{m}$ *underground, huge caverns have been excavated to house the giant detectors. The SPS, the final link in the pre-acceleration chain, and its connection tunnels to the LHC are also shown [51].*

factor due to the crossing angle. The LHC is designed for an instantaneous luminosity of[3] $1 \times 10^4\,\mu\mathrm{b}^{-1}\,\mathrm{s}^{-1}$ in proton-proton collisions. At this designed maximum performance level, there are 2808 bunches with each 1.15×10^{11} protons and a bunch spacing of $25\,\mathrm{ns}$ [50]. In 2012, the LHC was operated at a centre of mass energy of $\sqrt{s} = 8\,\mathrm{TeV}$ reaching a peak instantaneous luminosity of $0.77 \times 10^4\,\mu\mathrm{b}^{-1}\,\mathrm{s}^{-1}$ and an integrated luminosity of up to $23.2\,\mathrm{fb}^{-1}$ [50]. In this operation period, the LHC was mostly filled with around 1380 bunches which were $50\,\mathrm{ns}$-spaced. The beam intensity of 1.65×10^{11} protons per bunch exceeded the LHC design value [50].

3.2. The ATLAS Detector

The ATLAS detector is designed as a multipurpose detector aiming to investigate a variety of particle physics phenomena that are presumable observable at the high energy and luminosity provided by the LHC. The requirements for the ability to detect the SM Higgs boson up to masses of $m_H = 1\,\mathrm{TeV}$ in proton-proton collisions were set as a benchmark of the ATLAS experiment. Further goals include e.g. precision measurements to perform stringent tests of the SM but also the search for new particles predicted in Grand Unified Theories (see section 2.3). Very small signal cross sections but an overwhelming hadronic background require good particle identification and momentum resolution abilities as well as fast and radiation-hard electronics.

[3] $1\,\mathrm{b}$ (barn) $= 1 \times 10^{-24}\,\mathrm{cm}^2$

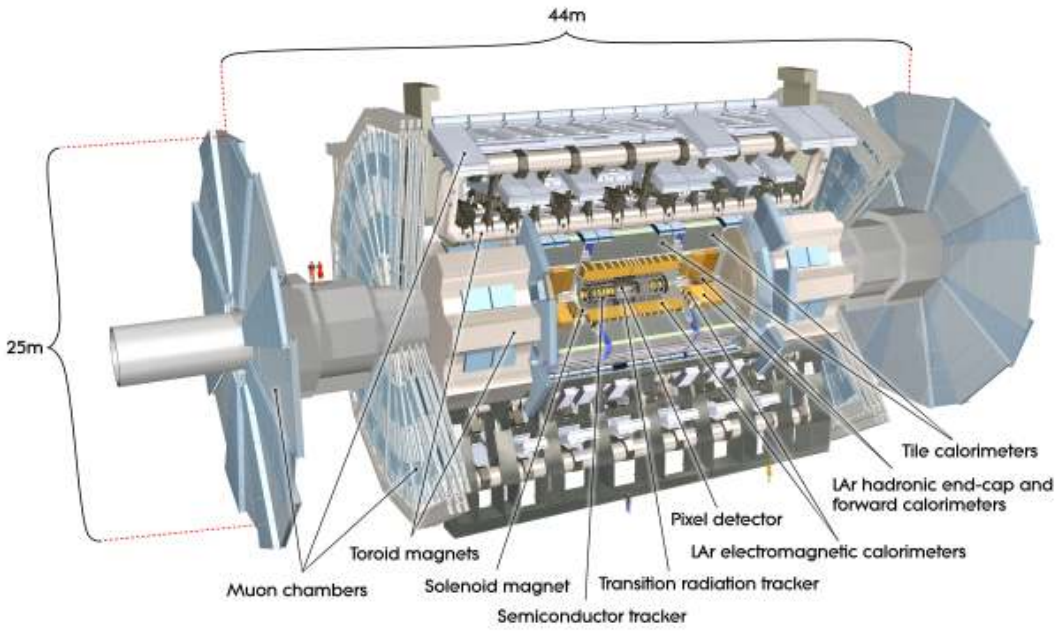

Figure 3.2.: *Cut-away view of the ATLAS detector [48].*

The construction of the ATLAS detector was finished in 2008 and long-term operation started with the first proton-proton collisions at the LHC in 2009. During the LHC shut-down phase in 2013 and 2014, the detector is upgraded to account for the increased detection and readout challenges imposed on the operation at $\sqrt{s} = 14\,\mathrm{TeV}$. This concerns particularly the number of interactions per crossing (called pile-up) reflecting that each signal event candidate might come with several additional events of other (inelastic) scattering processes.

The detector has a forward backward symmetric cylindrical geometry with respect to the interaction point. It has a diameter of about $25\,\mathrm{m}$ and a length of about $44\,\mathrm{m}$. The overall weight of the detector is approximately $7000\,\mathrm{t}$. The detector can be subdivided into three parts: the inner tracking detector (ID), the calorimeter system and the muon spectrometer. A sketch of the ATLAS detector is shown in figure 3.2.

After describing the coordinate system used in the ATLAS experiment, the subsequent sections describe the main components of the ATLAS detector while concentrating on the parts which are of particular importance for the reconstruction of photons. The descriptions refer to [48] where more details about the detector hardware can be found.

3.2.1. Coordinate System

The origin of the coordinate system in the ATLAS experiment is defined at the nominal interaction point of the proton-proton collision. The z-axis points in (anti-clockwise) beam-direction, whereas the x-axis points to the centre of the LHC ring and the y-axis upwards to form a right-handed coordinate system. The azimuthal angle Φ is then measured around the beam axis and the polar angle θ from the beam axis. Transverse observables such as the transverse momentum p_T of a particle are defined as the projection of the corresponding

observable to the $(x-y)$-plane,

$$p_T = \sqrt{p_x^2 + p_y^2}\,. \tag{3.2}$$

The vector sum of transverse observables such as for example the transverse energy E_T of all detected particles in one collision event is expected to be nearly zero for a negligible crossing angle. If the transverse energy that is measured for a particular event differs from this expectation, it is considered as missing transverse energy E_T^{miss} and might be attributed to non-detectable neutrinos involved in the event kinematics. The pseudorapidity η and the rapidity y of a particle are defined as[4]

$$\eta = \frac{1}{2}\log\left(\frac{|\vec{p}| + p_z}{|\vec{p}| - p_z}\right) = -\log\left(\tan\frac{\theta}{2}\right) \tag{3.3}$$

$$y = \frac{1}{2}\log\left(\frac{E + p_z}{E - p_z}\right)\,. \tag{3.4}$$

The relation $\eta = y$ holds for relativistic (massless) particles, while in other cases with $E \gg m$, the pseudorapidity is an approximation of the rapidity. The pseudorapidity is particularly useful since it only depends on the polar angle θ and is therefore often stated instead of this angle. Rapidity differences Δy are Lorentz invariant for transformations along the z-axis. This invariance also holds for the quantity ΔR which expresses the distance of two particles in the $(\eta - \Phi)$-plane, so that

$$\Delta R = \sqrt{(\Delta\eta)^2 + (\Delta\Phi)^2}\,. \tag{3.5}$$

3.2.2. Inner Detector

The inner detector (ID) is the innermost portion of the detector built cylindrically symmetrical around the beam pipe. Its dimensions are $6.2\,\mathrm{m}$ (length) $\times$ $2.1\,\mathrm{m}$(radius) and it covers a rapidity range of $|\eta| < 2.5$. The inner detector is surrounded by a solenoid generating a magnetic field in beam direction with field strength $B = 2\,\mathrm{T}$. The ID is mainly responsible for the detection of charged particle tracks. Precise momentum measurements and vertex reconstruction at high luminosities can be performed due to a high detector granularity. This is achieved with pixel sensors around the interaction point, strip detectors in the inner tracking volume and transition radiation trackers in the outer part. The layout of the inner detector is illustrated in figure 3.3.

In the barrel region, the pixel sensors are arranged on three layers of concentric hollow cylinders around the beam axis while in the two end-cap regions they are located on three layers of disks perpendicular to the beam axis. This positioning ensures that most of the particles traverse three pixel layers. Tracks of charged particles are curved because of the magnetic field. The pixel sensors are made of $250\,\mu\mathrm{m}$ thick silicon semiconductors. With 46080 readout channels for each of the 1744 pixel sensors (pixel size of $50 \times 400\,\mu\mathrm{m}^2$ to

[4] Here, log denotes the natural logarithm

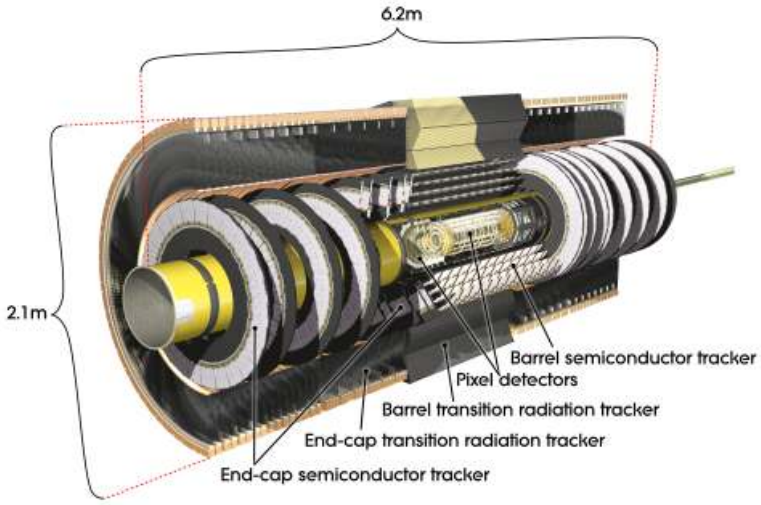

Figure 3.3.: *Cut-away view of the ATLAS inner detector [48].*

$50{\times}600\,\mu\mathrm{m}^2$), the pixel detector is the detector part with the highest granularity. The intrinsic point resolutions are $10\,\mu\mathrm{m}$ in the $(R-\Phi)$-plane and $115\,\mu\mathrm{m}$ in z-direction.

The silicon microstrip trackers (SCT) are positioned around the pixel sensors in a similar configuration, but this time four layers in the barrel region and 9 layers in the end-cap regions are assembled. Hence, at least four space points are obtained for every traversing charged particle. The SCT is built of 768 active strips of $12\,\mathrm{cm}$ length per sensor and a strip pitch of $80\,\mu\mathrm{m}$ was chosen. The sensors are $285\,\mu\mathrm{m}$ thick. Although using strips instead of pixels, both space coordinates are measured in the barrel region using stereo strips of which one layer is rotated by $40\,\mathrm{mrad}$. The nominal resolutions of the silicon microstrips are $17\,\mu\mathrm{m}$ in the $(R-\Phi)$-plane and $580\,\mu\mathrm{m}$ in z-direction. The total number of readout channels in the SCT is approximately 6.3 million. The semiconductor trackers also allow impact parameter measurements. The resolution of the transverse collision impact parameter $|d_0|$ measurement was found to be around $27\,\mu\mathrm{m}$ [52].

The transition radiation tracker (TRT) consists of polyimide straw tubes of $4\,\mathrm{mm}$ diameter. They are interleaved with material providing transition radiation for electron identification. The anodes consist of $31\,\mu\mathrm{m}$ diameter wire. Each tube is filled with a gas mixture allowing to distinguish between transition photons and minimum-ionising charged particles by applying thresholds on the signal amplitudes. In the barrel region, the straw tubes are $144\,\mathrm{cm}$ long and positioned in beam direction whereas in the end-cap regions, they are arranged radially in wheels and only $37\,\mathrm{cm}$ long. The TRT covers a pseudorapidity range of $|\eta| \leq 2.0$. Mechanically, the straws are stabilised using carbon fibres. The spatial resolution for the information provided in the $(R-\Phi)$-plane is $130\,\mu\mathrm{m}$ per straw while a total number of around $351\,000$ readout channels is implemented.

The resolution goals on p_T measurements in the inner detector and other detector parts are given in table 3.1.

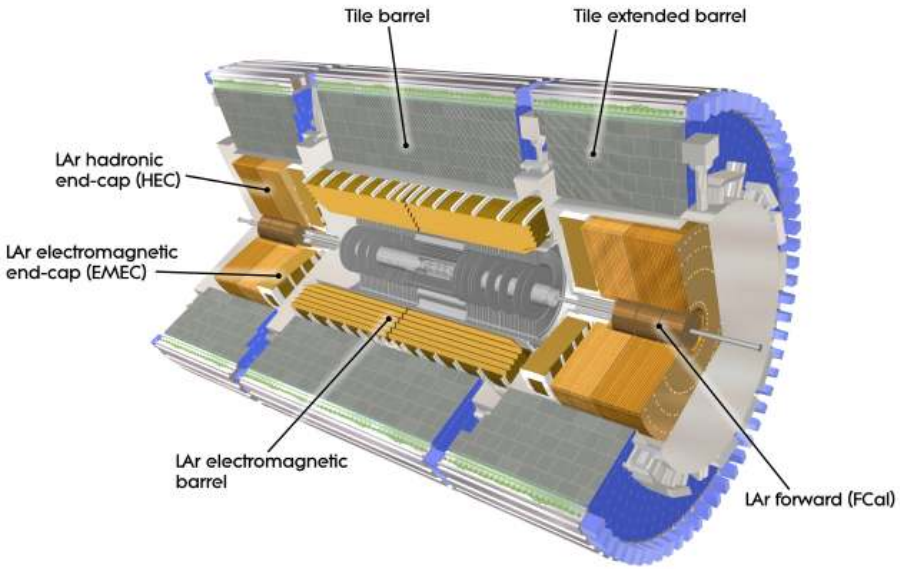

Figure 3.4.: *Cut-away view of the ATLAS calorimeter system [48].*

3.2.3. Calorimetry

The calorimeter system encloses the solenoid around the inner detector (see fig. 3.2) and covers a pseudorapidity range of $|\eta| \leq 4.9$. It is divided into electromagnetic calorimeters (ECAL), that are responsible for energy measurements of electrons and photons, and hadronic calorimeters (HCAL) which are particularly responsible for the determination of jet energies. The calorimeter system is very important for the photon reconstruction since photons typically leave the inner detector undetected. Figure 3.4 shows the geometry of the calorimeter system built around the inner detector and the beam pipe.

The electromagnetic calorimeters provide a fine granularity allowing for precise energy measurements and additional position information especially of photons and electrons. Muons as minimum ionizing particles traverse the calorimeter system leaving an ionising track. The ECALs are so-called sampling calorimeters meaning that they are constructed of alternating layers of active and absorbing material positioned in an accordion-shape. This geometry allows full coverage in the Φ-direction. The electromagnetic calorimeter is divided into a barrel section ($|\eta| < 1.475$) and two end-cap components (EMEC) covering $1.375 < |\eta| < 3.2$, both consisting of liquid argon (LAr) as the active medium and lead as the absorption material. In order to correct for the energy loss of electrons and photons moving forward in the calorimeter, an additional LAr layer is placed in the barrel region at $|\eta| < 1.8$ acting as a presampler. For charged particles with $|\eta| \leq 2.5$, the energy deposit and position measurement of the calorimeter can be matched to track information of the inner detector if existent. In this precision measurement region, an accurate position measurement is obtained by finely segmenting the first ECAL layer in η. The actual granularities of the calorimeter sections depend on $|\eta|$, the calorimeter layer and the detector region (barrel or end-cap). The highest granularity of 0.025×0.025 in $\Delta\eta \times \Delta\Phi$ is mainly accomplished in the first (second) barrel calorimeter layer at $|\eta| < 1.475(1.40)$ and in the second layer of the end-cap region at $1.425 < |\eta| < 2.5$.

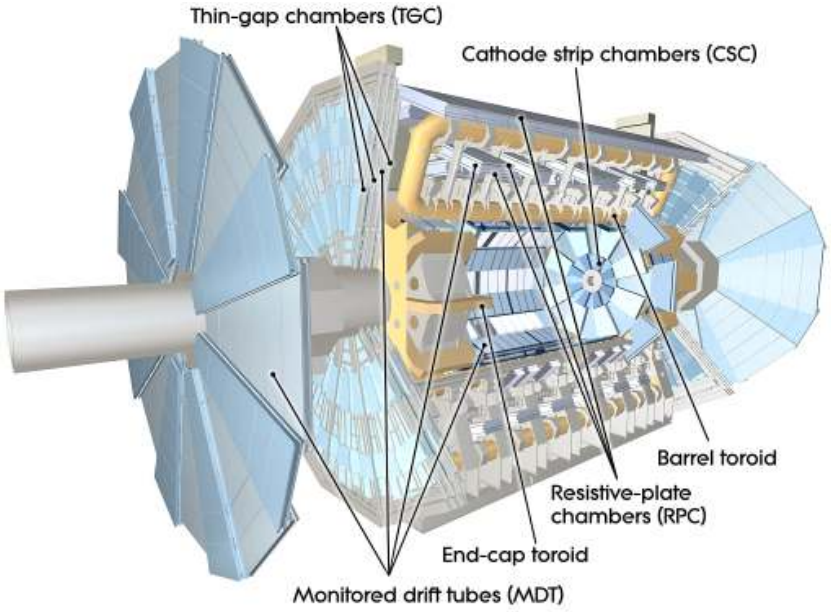

Figure 3.5.: *Cut-away view of the ATLAS muon system including barrel and end-cap toroid [48].*

The hadronic calorimeter is responsible to provide information for jet reconstruction and E_T^{miss} measurements. It is divided into the tile calorimeter, the hadronic end-cap calorimeter (HEC) and an additional LAr forward calorimeter (FCal). The tile barrel covers $|\eta| < 1.0$, two extended barrels cover $0.8 < |\eta| < 1.7$ (see figure 3.4). They are constructed as sampling calorimeters made of steel for the absorption of hadronic particles and scintillating tiles for the detection of evolving particle showers. The HEC is also designed as sampling calorimeter and uses copper plates as absorption material interleaved with $8.5\,\text{mm}$ LAr gaps as active medium. It covers the rapidity range $1.5 < |\eta| < 3.2$ slightly overlapping with the tiles and the forward calorimeter, which covers the high rapidity range of $3.1 < |\eta| < 4.9$. Hence, the FCal detects particles near the beam pipe. It is not only designed to detect hadronic particles, but also electrons and photons in this direction. For that purpose, it consists of three modules: The first one uses copper as absorber material and is optimised for electromagnetic measurements, the other two use tungsten as absorber. All modules of the forward calorimeter use LAr as active medium.

3.2.4. Muon System

Muons are ideally the only known and directly detectable particles traversing the calorimeter system. They are detected in the muon system, the outermost part of the ATLAS detector. In the muon spectrometer, a toroidal magnetic field is produced which is mostly orthogonal to the muon trajectories so that muons are deflected related to their momentum. This magnetic field is provided by the barrel toroid magnet for $|\eta| < 1.4$ and by two smaller end-cap toroid magnets in the range $1.6 < |\eta| < 2.7$. The $|\eta|$-range in between is known as transition region in which both superconducting air-core magnets contribute to the muon track deflection. The muon trajectory is detected by different muon chamber types of which Monitored Drift Tubes (MDT) are predominantly used and cover most of the $|\eta|$-range. However, for

Detector Part	Required Resolution
Inner Detector (Tracking)	$\sigma_{p_T}/p_T = 0.05\% \, p_T \oplus 1\%$
Electromagnetic Calorimetry (γ /$e^{\pm}$)	$\sigma_E/E = 10\%/\sqrt{E} \oplus 0.7\%$
Hadronic Calorimetry (jets)	
• barrel and end-cap	$\sigma_E/E = 50\%/\sqrt{E} \oplus 3\%$
• forward	$\sigma_E/E = 100\%/\sqrt{E} \oplus 10\%$
Muon Spectrometer	$\sigma_{p_T}/p_T = 10\%$ at $p_T = 1\,\mathrm{TeV}$

Table 3.1.: *General resolution goals of the ATLAS detector [48]. The relative and the absolute contribution must be added quadratically, which is denoted by the symbol* $\oplus$*. Energy and momentum values are in units of* GeV*.*

large pseudorapidity values, cathode strip chambers (CSC) with higher granularity are used because of higher radiation rates. Furthermore, a muon trigger system is installed in the pseudorapidity range $|\eta| < 2.4$ to trigger for events with high-p_T-muons. In order to achieve response times of a few nanoseconds, resistive plate chambers (RPC) were selected in the barrel region $|\eta| < 1.05$ while in the end-cap ($1.05 < |\eta| < 2.4$) thin gap chambers (TGC) were chosen.

The main resolution goals in the design of the different detector parts are summarized in table 3.1. The actual detector performance was tested in first collision events [53] and using cosmic muon rays [52] and found to mainly fulfil the design values. The transverse momentum resolution σ_{p_T}/p_T (constant term) was found to be $1.6(1)\%$ for the inner detector [52], the calorimeter energy resolution (constant term) for photons and electrons was found to be $(1.2 \pm 0.6(syst))\%$ for $|\eta| < 1.37$ and $(1.8 \pm 0.4(syst))\%$ for $1.52 < |\eta| < 2.47$ [54]. The resolution of missing transverse energy measurements can be parametrised by $\sigma(E_x^{\mathrm{miss}}, E_y^{\mathrm{miss}}) = 0.37 \times (\Sigma E_T)^{1/2}$ [53].

3.2.5. Trigger System

The ATLAS detector is designed to study processes with much lower cross sections than the total cross section which means that only a small fraction of the total number of collision events are of interest. At the LHC luminosities during the operation period in 2012, the bunch crossing rate was around $20\,\mathrm{MHz}$, but the offline recording rate of the ATLAS detector was limited to an average of $400\,\mathrm{Hz}$, which corresponds to a data acquisition (DAQ) of around $600\,\mathrm{MB/s}$ [55]. Consequently, effective triggering for interesting events is required to keep data rates reasonable.

The ATLAS trigger system is hierarchically structured in three levels: level 1 (L1), level 2 (L2) and event filter (EF). The level 1 trigger is required to reduce the data rate to approximately $75\,\mathrm{kHz}$ within a few microseconds. Therefore, only a subset of the total detector information is used. This subset contains information from the muon trigger system and the calorimeters with reduced granularity. Events considered for further processing may contain high transverse-momentum muons, electrons, photons, jets or τ-leptons decaying into hadrons, but also events with high missing or total transverse energy are passed on to the L2 trigger.

Additionally, information on the detector region(s) in which possible interesting features were identified in the L1 triggering (so-called regions-of-interest, RoI) are collected for further triggering steps. The software based L2 trigger uses the full granularity and precision of available detector information within these regions of interest. By applying stricter selection criteria based on this enhanced information, the data rate is further reduced to about $3.5\,\mathrm{kHz}$. The final data rate of (in average) $400\,\mathrm{Hz}$ is achieved by the event filter selection which is implemented using offline analysis algorithms. The processing time of the three trigger levels, which was observed in 2012 data taking, increases from $2.5\,\mu\mathrm{s}$ (L1) to $60\,\mathrm{ms}$ for the level 2 trigger and to around $1\,\mathrm{s}$ for the event filter [55].

3.2.6. Collision Data

Proton-proton collisions were performed at the ATLAS detector in 2010 and 2011 at $\sqrt{s} = 7$ TeV and in 2012 at $\sqrt{s} = 8\,\mathrm{TeV}$. Collected data must satisfy predefined quality requirements in order to be considered for analysis. The corresponding integrated luminosity is $4.8\,\mathrm{fb}^{-1}$ for 2011 data and $20.7\,\mathrm{fb}^{-1}$ for 2012 data. The uncertainty on the total integrated luminosity for $8\,\mathrm{TeV}$ data is $\pm 3.6\%$ [56].

The analyses presented in this thesis are based on the whole data set collected in 2012 at $\sqrt{s} = 8\,\mathrm{TeV}$. For this 2012 data, more than 35 interactions per crossing were observed with the ATLAS detector. Figure 3.6 shows the distribution of the mean number of pile-up events for 2011 and 2012 data.

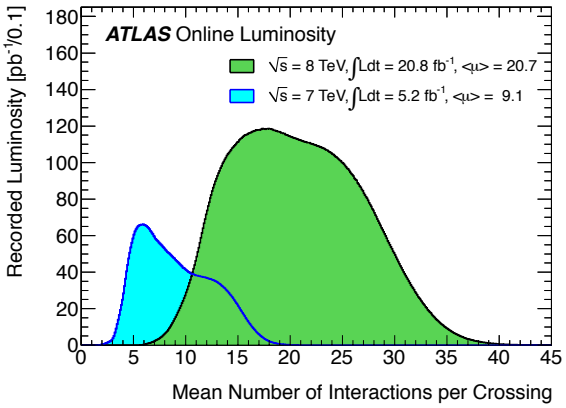

Figure 3.6.: *Luminosity-weighted distribution of the mean number of interactions per crossing for the 2011 and 2012 data. The mean number of interactions per crossing corresponds to the mean of the poisson distribution of the number of interactions per crossing ($\langle\mu\rangle$) calculated for each bunch [57].*

4. Signal and Background Processes

In order to analyse particular properties of the Higgs boson, the signal processes that are considered for the analysis must be defined, including production and decay mode of the Higgs boson. Since the Higgs boson production cross sections are much lower compared to the total production cross section at the LHC, relevant background processes must be well-known and estimated.

In the first two sections of this chapter, the signal processes and the most important background processes of this analysis are discussed. Afterwards, the prediction of relevant kinematics of the signal processes with simulated events is explained.

4.1. Signal Processes

In this analysis, the tensor structure of the Higgs-gluon coupling is studied. In the Standard Model, the Higgs-gluon coupling is mediated by a heavy quark loop. In section 2.4, an effective theory for the Higgs-gluon coupling vertex, which is described in reference [5], is introduced. In this effective theory approach, the Higgs-gluon vertex is parametrised by five coupling operators describing point-like vertices. The operator O_1 has mass dimension 5, while the operators $O_2 \dots O_5$ are of mass dimension 7.

In figure 2.11, which was also originally published in ref. [5], the individual contribution of these coupling operators to the Higgs boson production cross section is shown in comparison to the SM predicted cross sections. These distributions only consider events in which exactly one jet is radiated in the Higgs boson production process. It can be seen that the distributions differ in particular for high transverse momenta of the Higgs boson. In this analysis, the transverse momentum spectrum of the Higgs boson, which is observed in data taken with the ATLAS detector, is tested for a contribution of point-like coupling vertices described by the coupling operators O_i. The contribution of each coupling operator O_i is determined by the Wilson coefficient C_i. Each coefficient is investigated individually while the other coefficients are set to zero. For this investigation, only events with one jet radiated in the Higgs boson production process are considered as signal processes, treating all other jet multiplicities at matrix level (also called particle level) as background events. The transverse momentum of the Higgs boson is reconstructed in the $H \to \gamma\gamma$ decay channel.

The Feynman graph shown in figure 4.1 illustrates a typical signal process with two gluons in the initial state. The Higgs boson is produced in a Higgs-gluon vertex and decays into two photons. Standard Model Feynman graphs representing Higgs boson production processes with a Higgs-gluon vertex and one or two (anti)quarks in the initial state are shown in figure 2.5. If the Higgs boson decays into two photons, these processes represent further signal

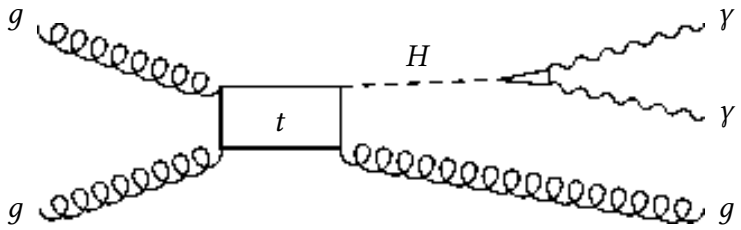

Figure 4.1.: *Feynman graph representing a typical signal process of this analysis in the Standard Model. The Higgs boson is produced via gluon fusion with one additional jet and then decays into two photons.*

processes predicted in the Standard Model. For each collision event, the total transverse momentum of the final state must be zero. Considering one-jet Higgs boson production events at matrix level, the transverse momenta of the Higgs boson and the radiated jet must have the same value. However, this cannot be expected for the measured values of transverse momenta due to various detector effects. These detector effects and their consideration in the event selection are described in the following chapter.

In this analysis, the loop-induced coupling of photons to the Higgs boson is considered to be described by the Standard Model. The branching ratio of a SM Higgs boson with $m_H = 125\,\mathrm{GeV}$ decaying into two photons is calculated to a value of $2.28(11) \times 10^{-3}$ [28].

4.2. Background Processes

In proton-proton collisions, two photons in the final state can be produced by many different processes of gluons and/or quarks interacting with much larger production cross sections compared to the signal processes. In analyses searching for $H \to \gamma\gamma$ events, the Higgs boson hence appears as an excess in events with two photons produced at the same vertex and an invariant mass of the diphoton system around the Higgs boson mass. Processes with the same particles in the final state as the signal process are considered as irreducible background. In addition, events with other final state particles contribute to the total background rate as reducible background due to particle misidentification. In this section, only background processes that contribute considerably in the diphoton mass range $105 \leq m_{\gamma\gamma}/\mathrm{GeV} \leq 160$ are discussed, so that e.g. $Z \to ee$ events are not relevant.

The leading order process of two photons produced by an interacting quark-anti-quark-pair is illustrated by the Feynman graph in figure 4.2a. There are plenty of possible NLO processes in which an additional jet is produced. One of them is shown in figure 4.2b. Two photons can also be produced by two gluons interacting as illustrated in figure 4.2c showing the corresponding leading order process. Considering the diphoton invariant mass spectrum, the irreducible diphoton background is continuous and can be parametrised as described in chapter 6. Shape and normalisation of the background mass spectrum are therefore obtained from data and do not have to be predicted by simulated events.

Irreducible background is mainly caused by the misidentification of jets as photons. Most of those misidentified jets contain neutral mesons, predominantly π^0-mesons, that decay into

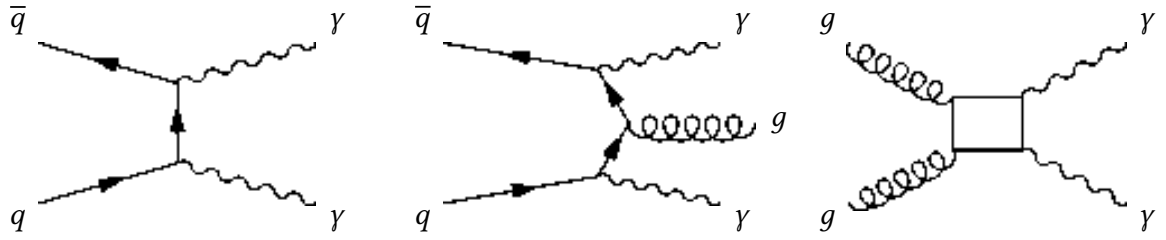

(a) $q\overline{q} \to \gamma\gamma$ *LO* (b) $q\overline{q} \to \gamma\gamma + 1$ *jet* (c) $gg \to \gamma\gamma$ *LO*

Figure 4.2.: *Examplary Feynman graphs of prompt diphoton production at hadron colliders representing irreducible background sources.*

photon pairs. Consequently, γ/*jet* or even *jet/jet* final states might be identified as two photon final states. The high hadronic background rates at the LHC require the fractional misidentification rate of jets identified as photons to be in the order of 1×10^{-4} (or smaller) to reduce this reducible background at least to the order of the irreducible background contribution. The jet rejection of the $H \to \gamma\gamma$ event selection is found to be very efficient and reduces the contribution of γ/*jet*- and *jet/jet*-events to the total background rate to a level of 15% and 1% [39], respectively.

In addition to events in which no Higgs boson is produced (non-resonant background), not all $H \to \gamma\gamma$ events are signal events according to the definition for this analysis, which is given in the previous section. Only events with a Higgs boson produced in a Higgs-gluon vertex with one jet radiated at matrix level are signal events. Events with Higgs bosons produced in other processes hence represent other irreducible background sources (resonant background). Table 4.1 gives the cross sections of different production modes for a Higgs boson with mass $m_H = 125\,\mathrm{GeV}$. Gluon fusion is the dominant production mode, but events with a Higgs boson produced via VBF might cause a considerable effect on kinematic distributions. Moreover, the VBF production comes with two additional jets (see figure 2.4b) that prefer a forward-backward configuration. In section 5.5.2, an event selection strategy that aims to reduce the VBF background based on this expected particular event topology is presented. The other production processes only have small contributions that will be considered for the results of the analysis with the exception of bbH, but no particular event selection to reduce this background is developed.

4.3. Simulated $H \to \gamma\gamma$ Events

The Higgs production in proton-proton collisions at $\sqrt{s} = 8\,\mathrm{TeV}$ and the detector response are simulated in order to make predictions of kinematic distributions. In addition to the prediction of the signal processes in gluon fusion Higgs production, as described in section 4.1, simulated events of the other Higgs production modes are used to estimate the resonant background contribution. For each production process, a Higgs boson mass of $m_H = 125\,\mathrm{GeV}$ is assumed. No simulated events of other background processes are used for this analysis since the estimation of non-resonant background events is performed completely based on data.

In this section, the event generators used for the simulation of $H \to \gamma\gamma$ events according

Production mode	Cross section σ [pb]	Relative Uncertainties [%] QCD Scale +	QCD Scale -	(PDF + α_s) +	(PDF + α_s) -
ggF	19.27	7.2	7.8	7.5	6.9
VBF	1.578	0.2	0.2	2.6	2.8
WH	0.7046	1.0	1.0	2.3	2.3
ZH	0.4153	3.1	3.1	2.5	2.5
ttH	0.1293	3.8	9.3	8.1	8.1
bbH	0.2035	10.3	14.8	6.2	6.2

Table 4.1.: *Higgs production cross sections and the corresponding relative theoretical uncertainties for proton-proton collisions at* $\sqrt{s} = 8\,\mathrm{TeV}$ *and a Higgs boson mass of* $m_H = 125\,\mathrm{GeV}$ *[28].*

to the Standard Model prediction are listed. The different steps of the full event simulation and the reweighting procedure for gluon fusion signal events, which is used to to generate kinematic distributions according to alternative theoretical predictions, are then discussed.

4.3.1. Monte Carlo Generators

For the prediction of signal events in gluon fusion Higgs boson production, events generated with Powheg [58–60] interfaced with Pythia8 [61] for underlying event, showering and hadronisation are used and represent the nominal signal Monte Carlo sample for this analysis. This sample consists of 3×10^6 simulated gluon fusion events with two photons in the final state. Powheg matches matrix element and parton shower calculations at NLO accuracy. Additional fudge factors are implemented in Powheg, so that it is tuned to match calculations with finite mass effects and soft-gluon resummations up to next-to-next-to-leading logarithmic order (NNLL) [62, 63]. Powheg uses the CT10 proton PDF [64] while normalisation and factorisation scales are set to the Higgs boson mass.

The VBF Higgs boson production process is also simulated using Powheg and Pythia8 while VH and ttH production are simulated at LO with Pythia8 using CTEQ6L1 [65] as the proton PDF. No bbH simulation sample was available but the contribution of this background is negligible. Stable particles are passed through a full detector simulation based on Geant4 [66, 67] and pileup is modelled.

All simulated events are weighted to obtain the overall normalisation according to the expected event yield in the detector. The normalisation is determined by the integrated data luminosity, the production cross sections, as given in table 4.1, and the $H \to \gamma\gamma$ branching ratio. The Higgs decay simulated by Pythia8 also contains Dalitz decay $H \to \gamma\gamma^*$ events. These events are not included in the calculation of the $H \to \gamma\gamma$ branching ratio. Since this branching ratio enters the overall normalisation that is applied on events simulated with Pythia8, the normalisation factors are increased by 6% to account for the presence of the additional Dalitz decay events. Studies have shown that they pass the event selection only at very low rate [68].

Several corrections are applied to Monte Carlo (MC) predictions. This includes a reweighting to match the pileup conditions and the primary vertex positions observed in data. The photon energy is smeared to account for differences between data and MC that were observed in $Z \to ee$ events [69]. Since the mass of the Z-boson is measured very precisely, measurements of the invariant mass of the electron-positron final state allow to determine the energy resolution of the detector. The shape of the Z-peak observed in data and MC is compared and simulated events are corrected to achieve agreement. The energy smearing depends on the calorimeter region and is around 1% to 2.5% [69]. The uncertainty on this smearing is considered as a systematic uncertainty in chapter 7. Moreover, the destructive interference of the gluon fusion process with the $gg \to \gamma\gamma$ background process [70] is considered by an additional event weight. These corrections range between −2% and −5%, depending on the diphoton invariant mass [56].

4.3.2. Event Simulation and Reweighting

Fully simulated events including the detector simulation are available for the SM gluon fusion $H \to \gamma\gamma$ process, as described in the previous section. In this analysis, the Higgs transverse momentum at reconstructed level is compared to theoretical predictions according to various values for the Wilson coefficients. Therefore, fully simulated events are required for various different values of the Wilson coefficients. These events are obtained by reweighting the existent POWHEG sample.

Gluon fusion events are generated using POWHEG at particle level based on calculations of the parton interaction probabilities and the transition matrix elements. In each event, a Higgs boson is produced in association with one additional jet that has an arbitrary low transverse momentum. Functions to calculate cross sections in $H + 1jet$ events for the effective theory and for the Standard Model are included in a package provided by the authors of reference [5] in which the effective theory is originally formulated.

The cross sections of these $H + 1jet$ events at matrix level are calculated at LO accuracy, corresponding to NLO accuracy in simulated $gg \to H$ events. The functions provided to calculate the cross sections allow to give the strong coupling constant α_s as an input value. For this analysis, the α_s value as calculated in the CT10 proton PDF, which is used for the event generation in POWHEG, is evaluated at the scale $\mu = (m_H^2 + p_T^2)^{1/2}$. Here and further in this section, p_T denotes the transverse momentum of the Higgs boson at matrix level.

The cross section predictions for the Standard Model which are calculated in the provided framework are used in the reweighting procedure. Therefore, they are first compared to the predictions obtained in POWHEG. As stated before, POWHEG uses a fixed scale for its calculations, which are corrected to match NNLL calculations. Figure 4.3 shows the comparison for the predictions on $\mathrm{d}\sigma/\,\mathrm{d}p_T$. The calculated SM predictions are obtained using CT10 as the proton PDF while both fixed and dynamic mass scales were tested affecting the evaluation of α_s. For the Standard Model top loop calculations, a top mass of $173.2\,\mathrm{GeV}$ is inserted, while lighter quarks are not considered. Differences between the predictions can be observed for both calculations at dynamic and at fixed scale, which can presumably be attributed to the differing calculation accuracy. However, the differences are smaller when using a dynamic scale in the calculations which is adopted in the analysis.

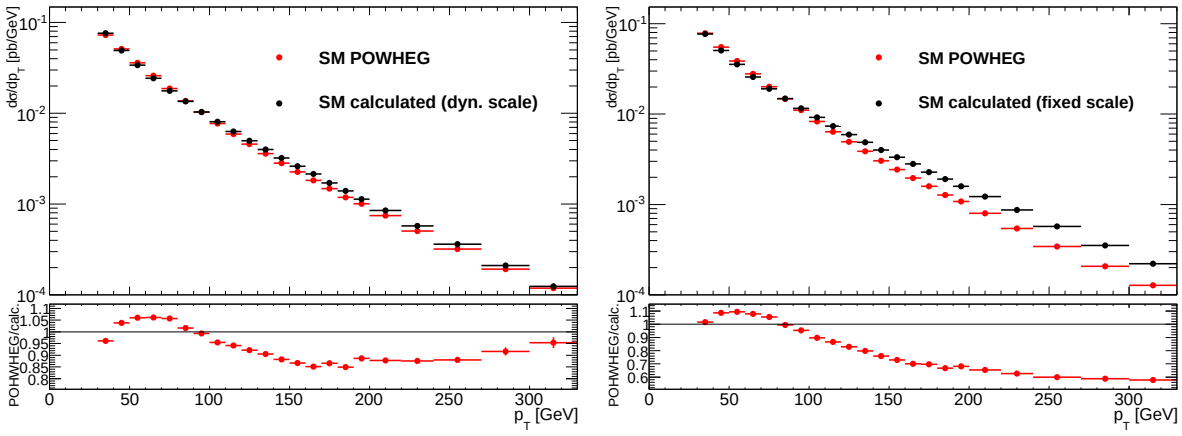

(a) *Dynamic scale* (b) *Fixed scale*

Figure 4.3.: *Comparison between* POWHEG *prediction of inclusive Higgs p_T distribution in 1jet events at parton level and leading order calculations with fixed and dynamic scale. The distribution obtained in* POWHEG *is normalised to the calculated one.*

For a given center of mass energy $\sqrt{s} = 8\,\mathrm{TeV}$, the kinematics of NLO gluon fusion events, as shown in figure 2.5, are mainly determined by the transverse momentum of the Higgs boson, p_T. The transverse momenta of the Higgs boson and the radiated jet are equal at particle level. The event kinematics can be described by the Mandelstam variables s, t and u. Defining Q_i^μ with $i \in \{1, 2\}$ as the four momentum vectors of the incoming interacting partons and P_i^μ as those of the outgoing particles (Higgs boson and jet), the Mandelstam variables can be expressed as

$$\begin{aligned} s &= x_1\, x_2\, (8\,\mathrm{TeV})^2 \\ t &\approx -2\, Q_1^\mu\, P_{\mu,1} \\ u &\approx -2\, Q_2^\mu\, P_{\mu,1} \end{aligned} \tag{4.1}$$

with x_i being the proton momentum fraction of parton i. The masses of involved particles can be neglected since they are small compared to the momentum transfer.

In this analysis, the possible presence of the coupling operators O_i as defined in (2.53) in addition to the Standard Model transition matrix element is considered. An event reweighting is performed in order to generate events according to the calculations following this effective theory approach. The event weights for this procedure are defined as the ratio of the squared matrix elements in the alternative theory to the squared matrix element in the Standard Model. The reweighting is performed for different hypotheses on the Wilson coefficients C_i representing free parameters in the effective theory. Considering contributions to the Standard Model cross section separately for each of the coupling operators O_1, O_2, O_3 and O_5, the cross sections depend on $\frac{C_1}{\Lambda}$ for O_1 and on $\frac{C_i}{\Lambda^3}$ for $i \geq 2$, respectively, so that this fraction can be considered as one single parameter (see equation (2.57)).

As mentioned before, some coupling operators only contribute for particular initial particle states adressing the particle types of the interacting partons. The coupling operator O_4 is not considered since it does not contribute to $H + 1jet$ cross sections. The coupling operator

O_5 does not contribute to Higgs boson production with two gluons in the initial state while O_3 does not contribute if a quark is involved in the interaction. Concerning the reweighting to coupling operators that do not contribute for particular initial particle states, the event weights for events with these initial states are 1. Otherwise, they depend on the particle type of the interacting partons a and b and the event kinematics. They are calculated for each of the Wilson coefficients C_i individually and take the form

$$w_i^{ab} = w_i^{ab}\left(\alpha_s(\mu), m_t, s, t, u, \frac{C_i}{\Lambda^n}\right) = \frac{|O_{\mathrm{SM}}|^2 + \left(\frac{C_i}{\Lambda^n}\right) O_{\mathrm{SM}} O_i^{\dagger} + \left(\frac{C_i}{\Lambda^n}\right)^2 |O_i|^2}{|O_{\mathrm{SM}}|^2}, i \in \{1, 2, 3, 5\} \tag{4.2}$$

with $n = 3$ for $i \geq 2$ and $n = 1$ otherwise. The validity of the cross section calculations is assumed to hold for $p_T > 30\,\mathrm{GeV}$. However, no cut is applied on this matrix level quantity, so that the event weights are calculated for every event in the gluon fusion POWHEG sample. The number of simulated events with $p_T < 30\,\mathrm{GeV}$ at matrix level passing the event selection is discussed in the following chapter.

The reweighting was tested using the Standard Model matching coefficients explained in section 2.4. These SM matching coefficients C_i^{SM} have a dependence on α_s and are therefore not constant for a dynamical scale. However, since only the consistency of the reweighted distributions is checked, the coefficients were set to constant values for this comparison. The choice of coefficients for this test is arbitrary, any other set of coefficients could have been used. Events are for this particular test reweighted according to the Lagrangian in (2.52). The reweighted p_T distributions were compared at particle level to direct calculations of the cross section contributions in the effective theory using again CT10 as the proton PDF.

The reweighted distributions in figure 4.4 were corrected for the differences observed in the SM prediction in figure 4.3a so that only the consistency of the reweighting procedure is investigated. This correction is only applied for this particular test of the reweighting procedure and not in the further analysis. Figure 4.4 shows this comparison for the inclusive (including all possible initial states) p_T distributions for the contributions of $O_1 O_i$ to the cross section. The distributions for the gg, gq/qg and $q\overline{q}$ initial states are separately shown in the appendix B.1. The differences are observed to be larger for the $q\overline{q}$ initial state for which the cross section is suppressed by about two orders relative to the gg initial state. These differences are again mainly attributed to differences in the SM prediction for this particular initial state that are not resolved by the correction applied according to the differences in the inclusive distributions.

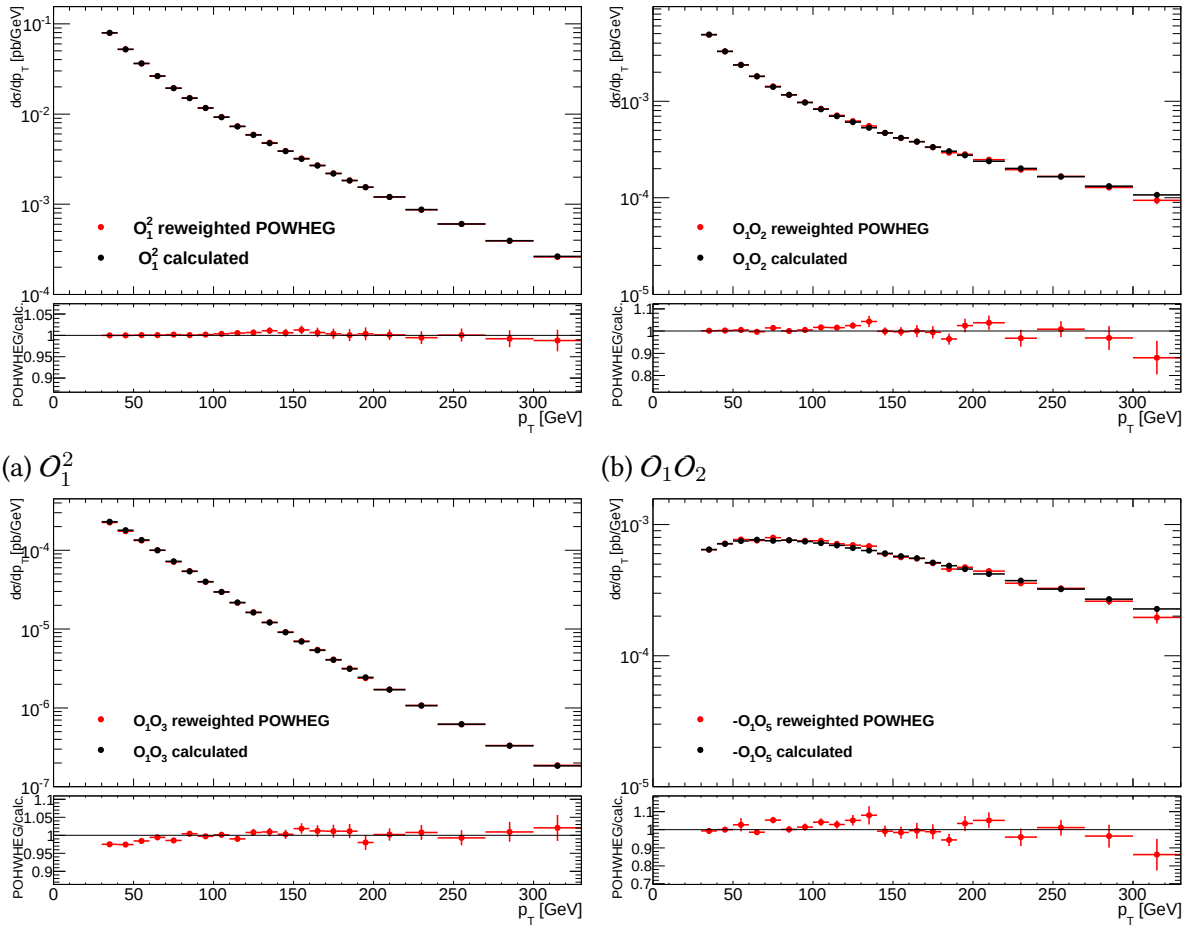

(a) O_1^2

(b) $O_1 O_2$

(c) $O_1 O_3$

(d) $-O_1 O_5$

Figure 4.4.: *Comparison between reweighted* POWHEG *prediction of contribution of different operator terms to the differential Higgs production cross section dependent on p_T in 1jet events at parton level and the corresponding leading order calculations. The reweighted* POWHEG *distributions are normalised according to the normalisation factor obtained for the SM distributions in figure 4.3a.*

5. Particle Reconstruction and Event Selection Strategies

Particles traversing the ATLAS detector cause characteristic signatures in the different detector parts described in section 3.2. In order to analyse the processes in which those particles were produced, reconstruction and selection strategies must be developed. Since this analysis studies events with Higgs boson decays into two photons, the identification and reconstruction of photons is of particular importance. In this chapter, the reconstruction of photons and jets is summarised. Other physical objects such as muons or electrons also need to be reconstructed and identified in order to distinguish particles and to remove overlapping particle tracks. The corresponding reconstruction strategies are described e.g. in references [71] and [72], respectively. The event selection uses the information on the reconstructed and categorised objects to further limit the number of events which are considered to presumably represent $H \to \gamma\gamma$ decays. The object definition and event selection of this analysis is mainly identical to those used for the ATLAS analysis of Higgs boson production differential cross sections, which is presented in ref. [68].

5.1. Reconstruction and Identification of Photons

Photons are reconstructed as isolated objects from clusters of energy deposits in the electromagnetic calorimeters. As photons can convert in the detector material, they might be detected as electron-positron pairs. In order to distinguish between electrons, converted photons and unconverted photons, the energy clusters are matched to tracking information of the inner detector. The presence of a fully reconstructed track matching an electromagnetic cluster is a clear signature of an electron or positron. At least one track originating from a conversion vertex candidate reconstructed in the inner tracking volume, that can be associated to an energy cluster in the electromagnetic calorimeter, is required for the reconstruction of a converted photon [73]. No tracking information is found in the case of unconverted photons. Since photons lose energy on their way through the detector outside the observed energy clusters, an energy calibration is performed separately for converted and unconverted photons. A photon cleaning procedure is applied to remove photons that are reconstructed with information of clusters labelled as "bad" (not fulfilling quality criteria on the detector operation). Figure 5.1 shows event displays for $H \to \gamma\gamma$ candidates with unconverted reconstructed photons.

Mainly two different object definitions for the identification of photons are used within the ATLAS collaboration: so-called loose and tight photons [75]. Loose photons are defined mainly for triggering purposes by identification criteria based on the shapes of the showers

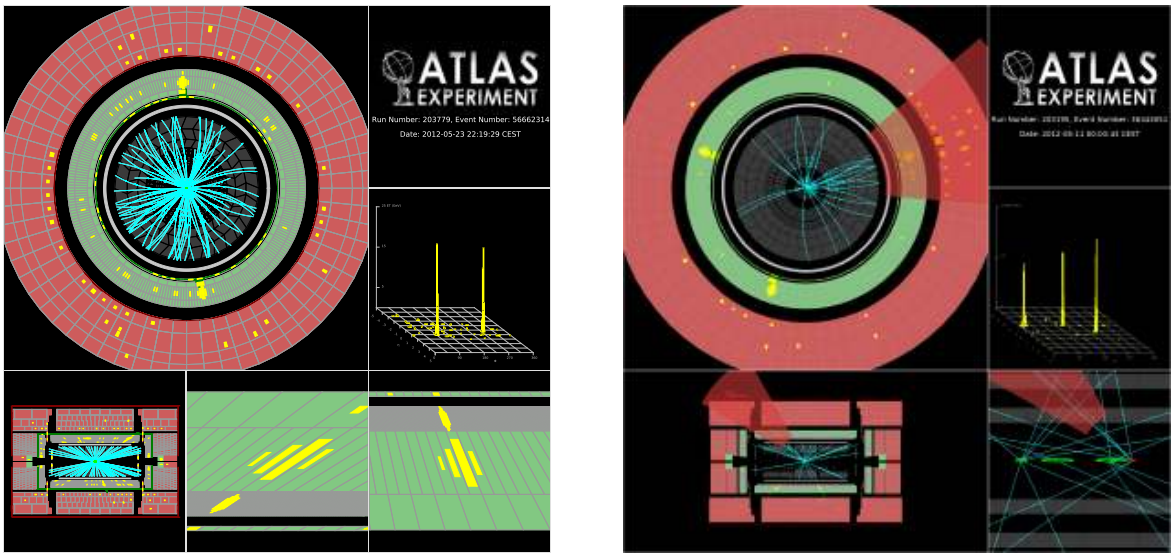

(a) *Diphoton event candidate.* (b) *Diphoton with a jet event candidate.*

Figure 5.1.: *Event displays of diphoton candidates where both photons are unconverted. Both events were recorded at* $\sqrt{s} = 8\,\mathrm{GeV}$. *Only reconstructed tracks with* $p_T > 1\,\mathrm{GeV}$, *hits in the pixel and SCT layers and TRT hits with a high threshold are shown [74]. The photons appear as energy deposits (yellow clusters) in the electromagnetic calorimeter while for the reconstructed jet additional inner tracks and energy deposits in the HCAL can be seen.*

in the middle layer of the liquid argon calorimeter. Cuts were optimized to reject fake signatures from QCD jets by comparing possible energy deposits in the hadronic calorimeter with the energy clusters in the electromagnetic calorimeter [73]. The loose photon definition is harmonized with the corresponding definition for electrons. The tight photon definition is based on additional information from the strip layer of the electromagnetic calorimeter that provides high granularity. The tight selection is separately optimized for unconverted and converted photons to provide a photon identification efficiency of about 85% for photon candidates with transverse energy $E_T > 40\,\mathrm{GeV}$ and a corresponding background rejection factor of about 5000 [73, 75]. One of the backgrounds that is intended to be rejected is the decay of neutral mesons, e.g. $\pi^0 \to \gamma\gamma$ background. Figure 5.2 shows the efficiency ϵ_{ID} of reconstructed unconverted photons satisfying defined isolation criteria (see section 5.2) to pass the tight photon identification criteria in a given $|\eta|$ region depending on the transverse energy E_T.

5.2. Inclusive Diphoton Event Selection

The analysis described in this thesis is based on the inclusive selection of two photons which is described in the following.

Events are pre-selected using a diphoton trigger that requires at least two photon candidates with $E_T > 35(25)\mathrm{GeV}$ for the leading (subleading) photon candidate. Both photon candidates must further pass the loose photon identification criteria. Events must belong to

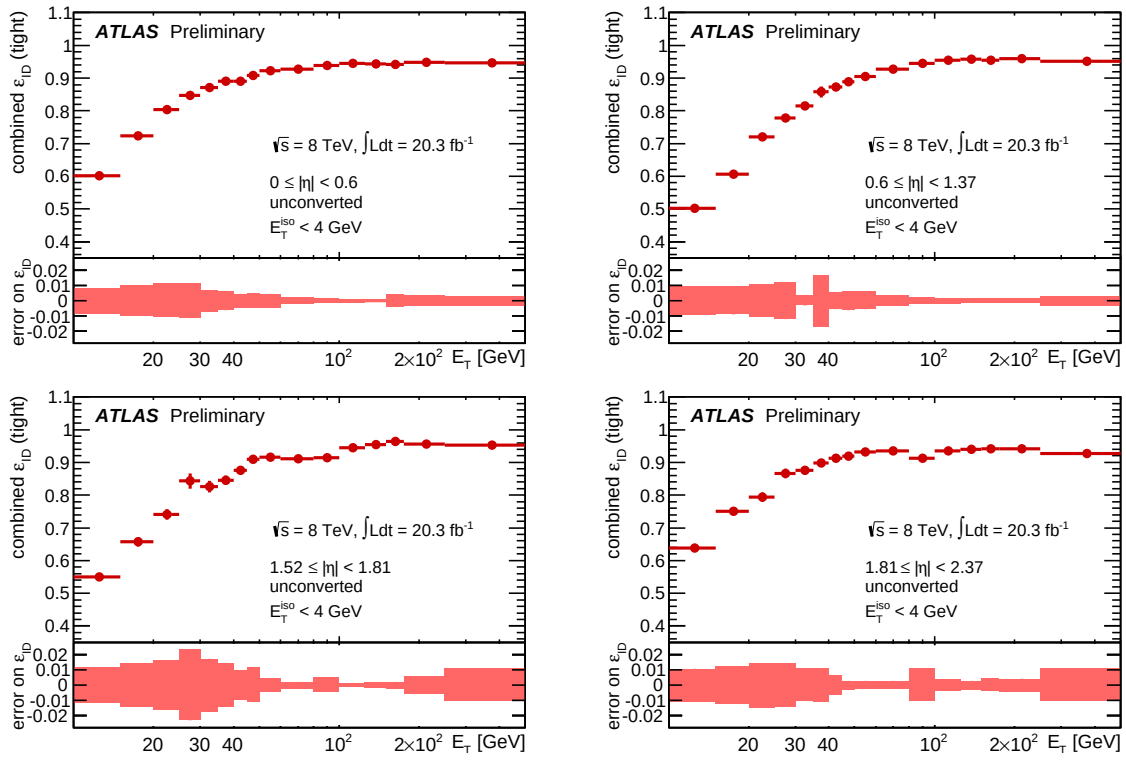

Figure 5.2.: *Combination of the data-driven measurements of ϵ_{ID} for unconverted tight photons in the transverse energy range $10\,\mathrm{GeV} < E_T < 500\,\mathrm{GeV}$ with respect to reconstructed photons satisfying the isolation requirement $E_T^{iso} < 4\,\mathrm{GeV}$. The ϵ_{ID} curves are shown in four different η regions. The error bars show the statistical and systematic uncertainties from the combination of the measurements in the overlapping E_T regions [76].*

blocks specified in a so-called Good run list (GRL) guaranteeing that all relevant subdetectors were operating well while the corresponding data was taken. Additionally, standard event cleaning is applied that rejects events with incomplete calorimeter information. At least one primary vertex must be reconstructed in every event that is considered for selection.

The loose photons in the pre-selected events must be in the pseudorapidity range $|\eta| < 2.37$ while the region $1.37 \leq |\eta| < 1.56$ is excluded. They are further required to have $E_T > 25\,\mathrm{GeV}$. The two leading (with highest p_T) photons define the "Higgs candidate" and are used to identify the primary vertex. This primary vertex selection uses "pointing" information of the photons in the calorimeters and combines it in a neural network using $\sum p_T$ and $\sum p_T^2$ of tracks associated to reconstructed vertices, the azimuthal angle difference $\Delta\phi$ between the diphoton system and the vector sum of the track momenta. The z-position of the selected vertex is then used to correct the η and hence the transverse energy E_T and momentum p_T of the two photons.

Figure 5.3 shows the efficiency ϵ_{PV} to reconstruct the diphoton vertex within $0.3\,\mathrm{mm}$ to the production vertex, measured in $Z \to ee$ data and predicted with simulated events. For the study with $Z \to ee$ data, the vertex is identified using the neural network with removed electron tracks and then compared to the true vertex position, which is identified using the electron tracks in the inner detector. The number of high p_T tracks and therefore the vertex

reconstruction efficiency ϵ_{PV} increase with the transverse momentum of the two-particle-system. Since the p_T-distribution is harder for $H \to \gamma\gamma$ events than in $Z \to ee$ events, the vertex reconstruction efficiency is higher and can be predicted from $Z \to ee$ data using a p_T-reweighting [39].

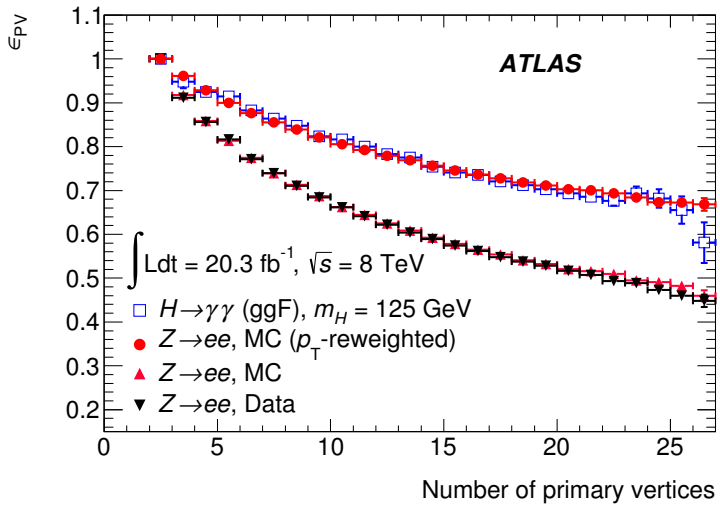

Figure 5.3.: *Efficiency ϵ_{PV} to select a diphoton vertex within $0.3\,\mathrm{mm}$ of the production vertex as a function of the number of primary vertices in the event. The plot shows ϵ_{PV} for simulated ggF events ($m_H = 125\,\mathrm{GeV}$) with two unconverted photons (hollow blue squares), for $Z \to ee$ events with the electron tracks removed for the neural network-based identification of the vertex, both in data (black triangles) and simulation (red triangles), and the same simulated $Z \to ee$ events re-weighted to reproduce the p_T spectrum of simulated ggF events (red circles) [39].*

After this pre-selection, kinematic cuts are applied on the two leading photons. For this analysis, relative p_T cuts are used requiring $p_T > 0.35(0.25)\, m_{\gamma\gamma}$ for the leading (subleading) photon. The four vector of the diphoton system is calculated as the vector sum of the two four vectors for the leading photons. The mass $m_{\gamma\gamma}$ is defined as the invariant mass of this diphoton four vector representing the Higgs boson candidate. Cuts on the photon-p_T relative to the diphoton mass $m_{\gamma\gamma}$ are used instead of absolute photon-p_T cut values to prevent distortions of the diphoton mass spectrum in events with low p_T of the Higgs boson candidate (see chapter 6). The diphoton invariant mass is required to fulfil $m_{\gamma\gamma} \in [105\,, 160]\mathrm{GeV}$. Furthermore, the two leading photons are then tested to pass the tight identification criteria and are rejected if they do not.

In the last step of the inclusive diphoton selection, the two photons must satisfy isolation requirements. These isolation criteria are defined using information from the inner detector and the calorimeter. For both photons, the energy deposit in the calorimeter in a cone of $\Delta R = 0.4$ around it must be less than $6\,\mathrm{GeV}$. In addition, the scalar sum of tracks with $p_T > 1\,\mathrm{GeV}$ detected in the inner detector, that originate from the reconstructed diphoton primary vertex and are within $\Delta R = 0.2$ to the photon, must be less than $2.6\,\mathrm{GeV}$ for both of the reconstructed photons.

Table 5.1 gives the number of simulated events selected in the successive selection steps described in this section. The number of events passing all selection criteria was checked to

be in accordance to ref. [68] (numbers given in the supporting documentation). The total selection efficiency is found to be around 37%.

Step	Requirement	Number of Events ($\times 10^3$)	Selection efficiency of this step [%]	Selection efficiency up to this step [%]
0	-	2995.0	-	100.0
1	Diphoton Trigger	1997.5	66.7	66.7
2	Primary Vertex	1997.4	>99.9	66.7
3	Two Loose Photons	1524.4	76.3	50.9
4	Kinematic Cuts	1390.7	91.2	46.4
5	Tight Photons	1220.0	87.7	40.7
6	Photon Isolation	1117.8	91.6	37.3

Table 5.1.: *Selection efficiencies for inclusive diphoton selection evaluated with unweighted simulated events. The Monte Carlo sample used is decribed in section 4.3.*

5.3. Jet Definition

Jets are defined using the anti-k_t algorithm [77] with a distance parameter $\Delta R = 0.4$. This algorithm clusters particles that are produced by the hadronisation[1] of a quark or a gluon and that are detected inside a particularly defined area to one physical object called jet. This jet clustering algorithm uses information of three-dimensional topological calorimeter clusters [78] taken at the electromagnetic scale. Figure 5.1b shows the event display of a $H \to \gamma\gamma$ candidate with one additional reconstructed jet. Further jet identification requirements are $p_T > 30\,\mathrm{GeV}$ and $|\eta| < 4.5$. In order to suppress the pile-up dependence of the reconstructed jets, an event-by-event evaluated calibration is applied for each jet [79]. Jets from additional pile-up interactions are further suppressed by requiring a jet vertex fraction (JVF) >0.25 for jets within $|\eta| < 2.4$ and with $p_T < 50\,\mathrm{GeV}$. The JVF is defined as the ratio of the (scalar) p_T sum of tracks within the jet coming from the reconstructed primary diphoton vertex, over the (scalar) p_T sum over all tracks associated to that jet [79].

5.4. Overlap Removal

By applying separate identification criteria for the reconstruction of different particle types, the detector signatures of one single particle might be reconstructed and selected as multiple particles. Overlapping particles are removed in a particularly defined hierarchy by applying isolation criteria based on the distance ΔR in the $(\eta - \phi)$-plane. The two leading photons are never removed in this procedure.

First, electrons within a cone of $\Delta R < 0.4$ around one of the two leading photons are removed. Afterwards, jets with distance $\Delta R < 0.2$ to an electron or $\Delta R < 0.4$ to one of the two photons

[1] Due to color confinement, free quarks or gluons produced in hadron colliders cannot exist individually and combine with quarks or gluons that are created.

are rejected. Finally, muons are removed if they are within $\Delta R < 0.4$ to a jet or one of the leading two photons. However, for this analysis, only the removal of jets has an influence.

5.5. Signal Selection

All events considered in this analysis at detector level must pass the inclusive diphoton event selection described previously. Further signal selection criteria are applied in most parts of the analysis and are described in the following subsections.

5.5.1. Jet Multiplicity

In the signal process for this analysis, exactly one jet is produced in association with the Higgs boson (see section 4.1) at matrix level (also called particle level). However, several effects such as final state radiation, jet identification inefficiencies, underlying events and misidentified pileup jets can cause a difference between the jet multiplicity observed at reconstruction level and the actual number of jets produced with the Higgs boson at matrix level. Moreover, it cannot be distinguished whether a reconstructed jet was radiated in the Higgs production process at matrix level or not. As a consequence, events considered as signal candidates are required to include at least one jet while higher jet multiplicities are allowed at reconstructed level. This selection strategy is used because it is assumed that the number of events with more than one jet radiated at matrix level is small compared to the number of events in which additional jets are reconstructed because of the mentioned detector effects. The reconstructed jet multiplicities for different simulated Higgs boson production processes are summarized in table 5.2[2] and illustrated in figure 5.4. The Jet reconstruction is explained in section 5.3 and includes the requirement $p_T > 30\,\mathrm{GeV}$ for each jet.

Jet multiplicity	ggF	VBF	VH+ttH	inclusive
0	222	3	4	229
1	100	11	6	117
2	28	14	6	48
≥ 3	10	3	4	17
inclusive	360	30	20	411

Table 5.2.: *Numbers of simulated $H \to \gamma\gamma$ events at $\sqrt{s} = 8\,\mathrm{TeV}$ passing inclusive diphoton event selection depending on production mode and reconstructed jet multiplicity. Jets are reconstructed according to the definition in section 5.3. Expected event yields are given for an integrated luminosity of $\int \mathcal{L}\,\mathrm{d}t = 20.7\,\mathrm{fb}^{-1}$.*

As mentioned beforehand, uncertainties on cross section calculations for events with one jet produced at matrix level rapidly increase for jet momenta smaller than about $30\,\mathrm{GeV}$. However, in the reweighting procedure, which was described in the previous chapter, event

[2] The numbers given in table 5.2 are rounded to integers, so that deviations can occur for inclusive event yields

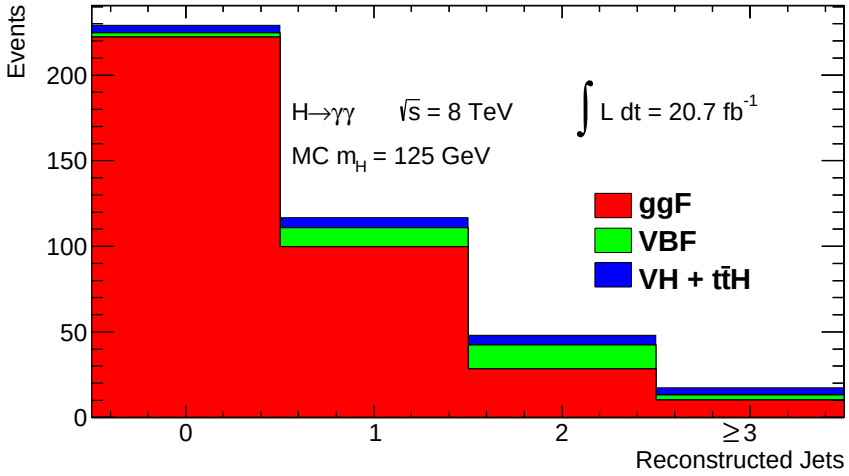

Figure 5.4.: *Jet multiplicities at reconstruction level for simulated $H \to \gamma\gamma$ events in different Higgs production modes passing the inclusive diphoton selection criteria. Jets are reconstructed according to the definition in section 5.3.*

weights were calculated for all simulated events regardless of the jet p_T at matrix level. With the selection requirement of one reconstructed jet with $p_T \geq 30\,\mathrm{GeV}$ in each event, the transverse momentum of the jet produced at matrix level in the same event should also mostly exceed the $30\,\mathrm{GeV}$ threshold or at least not be much smaller.

Indeed, this association is only appropriate if one of the reconstructed jets was actually radiated in the Higgs production process at matrix level, so that not all of them are attributed to other effects. Consequently, an additional selection requirement is introduced to suppress events with jet multiplicity zero at matrix level, but with jets reconstructed at detector level. In events with this particular characteristic, a low reconstructed Higgs boson transverse momentum is expected since the Higgs boson is then the only final state particle at matrix element before it decays to two photons. Using simulated gluon fusion $H \to \gamma\gamma$ events, it was found that an additional requirement of $p_T > 30\,\mathrm{GeV}$ of the reconstructed Higgs boson leads to a 71.5% reduction in the number of events passing the event selection in which the radiated jet at particle level has a transverse momentum below $30\,\mathrm{GeV}$. This additional requirement reduces the total number of events, however, only by 14.2%, and thus is introduced in the signal selection. The corresponding event numbers passing these selection criteria are given in table 5.3. From this table, it can be seen that only very few events with a jet transverse momentum below $30\,\mathrm{GeV}$ at particle level are expected to pass the event selection. Regarding the jet p_T distribution of those events at particle level, it is found that these momenta are mostly near to the requested threshold.

In section 4.1, it was discussed that for one-jet-events, the transverse momenta of Higgs boson and radiated jet are equal at matrix level. In addition to the discussed uncertainties on the jet multiplicity, including misidentified pileup jets and underlying events, uncertainties on the energy measurements of photons and jets cause inequalities on the aforementioned transverse momenta at detector level. Since photons are reconstructed more reliably compared to jets, the reconstructed Higgs boson transverse momentum is used in the further analysis to test for the presence of the coupling operators O_i.

Event category	no cut	Higgs $p_T^{\text{reco}} \geq 30\,\text{GeV}$	rejection rate
Selected events	138	118	14.2%
Jet $p_T \leq 30\,\text{GeV}$ at particle level	16	5	71.5%

Table 5.3.: *Efficiency of cut on Higgs $p_T > 30\,\text{GeV}$ at reconstructed level to reject events with $p_T < 30\,\text{GeV}$ of the radiated jet at particle level. Considered are simulated gluon fusion $H \to \gamma\gamma$ events at $\sqrt{s} = 8\,\text{TeV}$ passing the diphoton event selection in which at least one jet is reconstructed. Event yield is predicted according to an integrated data luminosity of $\int \mathcal{L}\,\text{d}t = 20.7\,\text{fb}^{-1}$.*

In figure 5.5, the invariant diphoton mass spectrum and the reconstructed diphoton transverse momentum spectrum are shown for selected events. As mentioned before, the reconstructed diphoton system represents the Higgs candidate. They still include most of the events originating from the background processes discussed in section 4.2.

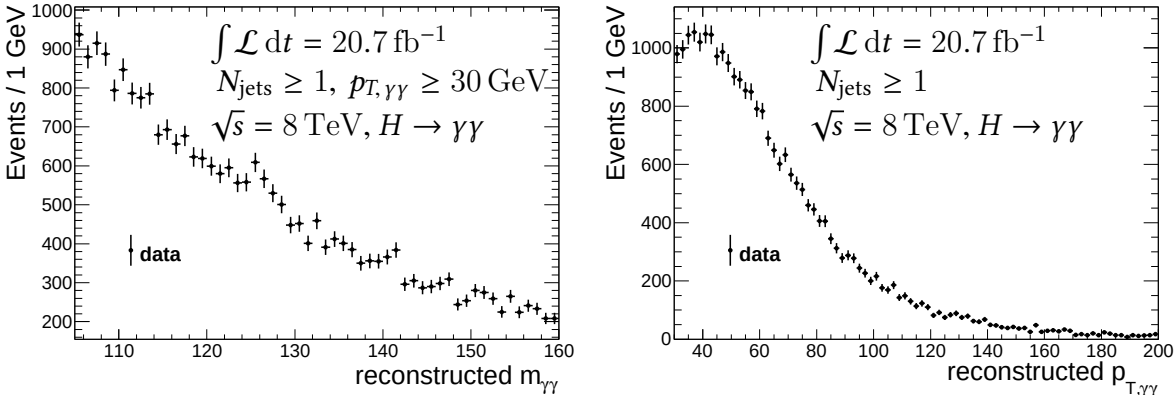

(a) *Invariant diphoton mass spectrum* (b) *Diphoton transverse momentum spectrum*

Figure 5.5.: *Reconstructed spectra of diphoton mass and diphoton transverse momentum for events passing the selection criteria discussed in the text. Data was taken with the ATLAS detector in 2012.*

5.5.2. Suppression of VBF Higgs Boson Production

Vector boson fusion is the Higgs boson production mode with the second largest production cross section after gluon fusion. As it can be seen in figure 5.4 and table 5.2, the contribution of this background is especially considerable in events with two reconstructed jets. Therefore, it was investigated with simulated events if additional requirements on the event selection are capable of increasing the simplified signal significance, defined as

$$\xi = \frac{s}{\sqrt{s+b}}\,. \tag{5.1}$$

Here, s is the number of expected signal events from gluon fusion Higgs boson production (in $20.7\,\text{fb}^{-1}$), while b is the the expected number of background events from other Higgs boson

production processes, namely VH and ttH. The non-Higgs background is not considered in this optimisation study since the continuum background contribution is estimated following the procedure outlined in chapter 6.

Since VBF events have a distinctive signature, characterised by the two forward jets, kinematic criteria to suppress the contribution of VBF events are investigated. Although other production processes are considered in the definition of b, the ability to maximise ξ will therefore depend on the ability to reduce the background contribution of VBF events.

This study is performed separately for events with one reconstructed jet and events with ≥ 2 reconstructed jets. No optimisation is done for events with no additional jets since these events are not considered in the analysis. For events with one jet, the following kinematic variables were considered for this optimisation study: The difference in pseudorapidity $\Delta\phi_{\gamma\gamma j}$ and the azimuthal angle difference $\Delta|\eta_{\gamma\gamma j}|$ between the jet and the combined diphoton system, the minimum difference $\Delta R_{\gamma j}$ (according to the definition of R in (3.5)) between the jet and either leading or subleading photon, and the invariant mass $m_{\gamma\gamma j}$ of the combined particle system consisting of the two leading photons and the reconstructed jet. However, no set of additional selection requirements on these variables led to any improvement in ξ, and thus the inclusive selection was deemed to be the most optimal for events with exactly one reconstructed jet.

For events with ≥ 2 reconstructed jets, the same kinematic variables were considered which are used in other studies for the definition of event categories enriched with VBF events [56]. In the first step, cuts on these variables were varied separately in order to test for an increase of the significance ξ. On the one hand, no enhanced significance ξ was found for cuts on the minimal difference $\Delta R_{\gamma j}$ between either leading/subleading jet and leading/subleading photon, on the azimuthal angle difference $\Delta\phi_{\gamma\gamma jj}$ between the combined diphoton system and the combined dijet system (defined of the two leading jets) or on the diphoton system pseudorapidity in the frame of the tagging jet pseudorapidity, defined as $\left|\eta_{\gamma\gamma} - \frac{1}{2}\left(\eta_{j1} + \eta_{j2}\right)\right|$. On the other hand, ξ could be increased through applying cuts on the rapidity separation $|\Delta\eta_{jj}|$ between the two leading jets and also for cuts on the invariant mass m_{jj} of the two leading jets. Normalised distributions of these two kinematic variables are shown in figure 5.6 for VBF and ggF events separately.

For these two kinematic variables, cuts are varied simultaneously in order to maximise ξ. Since gluon fusion dominates even for higher jet multiplicities, events are rejected only when they possess kinematic properties that are extremely consistent with the VBF topology. Thus, events are removed only if they have values of $\Delta\eta_{jj}$ and m_{jj} both simultaneously exceeding the specified cuts. For $|\Delta\eta_{jj}|$, cuts were varied in the range $2 \leq |\Delta\eta_{jj}| \leq 8$ in steps of 0.1 while for m_{jj}, cuts were varied within $200 \leq m_{jj}/\mathrm{GeV} \leq 1000$ in steps of $10\,\mathrm{GeV}$. It was found that ξ is maximised when events with $m_{jj} > 670\,\mathrm{GeV}$ and $|\Delta\eta_{jj}| > 3.5$ and $N_{\text{jet}} \geq 2$ are rejected. The rejection efficiencies of these cuts and the expected yields for events passing the cuts are given in table 5.4 for events produced in ggF, VBF or in VH and ttH .

The selection criteria derived in this section in order to reduce VBF background are not applied in the nominal analysis presented in this thesis. Instead, the expected background contribution from Higgs boson production in VBF, VH and ttH is derived from simulated events. It is subtracted from data after the estimation of the non-resonant background contribution.

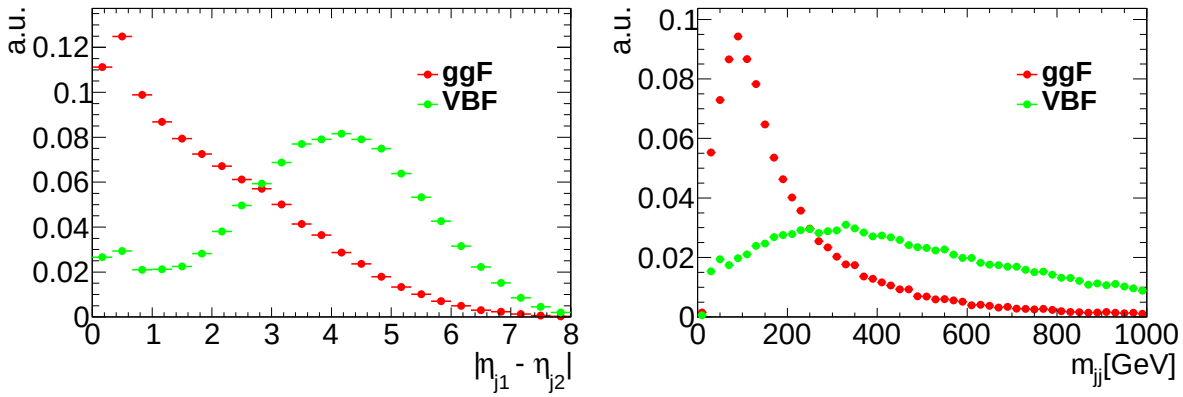

(a) *Normalized* $|\Delta\eta_{jj}|$ *distribution*

(b) *Normalized* m_{jj} *distribution*

Figure 5.6.: *Kinematic distributions of variables used to discriminate VBF background. Considered are simulated ggF and VBF* $H \to \gamma\gamma$ *events at* $\sqrt{s} = 8\,\mathrm{TeV}$ *with two reconstructed jets.*

production process	$N_{\mathrm{jet}} = 2$			$N_{\mathrm{jet}} \geq 3$		
	no cuts	after cuts	rejection rate	no cuts	after cuts	rejection rate
ggF	28.3	27.1	4.2%	10.2	9.7	4.9%
VBF	14.0	8.9	36.4%	2.9	2.2	24.1%
VH + ttH	5.6	5.6	-	4.1	4.1	-

Table 5.4.: *Simulated* $H \to \gamma\gamma$ *events at* $\sqrt{s} = 8\,\mathrm{TeV}$ *passing the inclusive diphoton selection with at least two reconstructed jets before and after applying cuts to reduce the VBF background contribution. Event yield is predicted according to an integrated data luminosity of* $\int \mathcal{L}\,\mathrm{d}t = 20.7\,\mathrm{fb}^{-1}$.

The derived selection strategy suppresses events produced in VBF, but still a non-negligible amount of events produced in VBF, VH and ttH processes passes these cuts. Consequently, the event yields would still need to be corrected for these events, but the additional cuts would increase the influence of systematic uncertainties on jet observables. Results including this approach of VBF reduction are given together with the nominal results in chapter 9.

6. Background Estimation

In order to compare the data taken with the ATLAS detector to the (reweighted) simulated gluon fusion $H \to \gamma\gamma$ events, the number of background events in data, that pass the event selection, need to be estimated. Those background events include two types of background: The resonant background of Higgs bosons that were produced in other processes than gluon fusion and the non-resonant background of events with two reconstructed photons that were not produced by a decaying Higgs particle. The background events belonging to this non-resonant background are predominantly attributed to prompt diphoton production or misidentified jets, as described in section 4.2. The estimation of all relevant background sources serves the purpose of extracting the signal Higgs boson p_T distribution (see section 4.1) from all data events passing the applied event selection.

The non-resonant background contribution is estimated using simulated $H \to \gamma\gamma$ events and data. The strategy pursued for this non-resonant background estimation is the focus of this chapter. Selected events are categorized due to the transverse momentum of the diphoton system that represents the Higgs candidate. As previously described, selected events are required to have at least one reconstructed jet. The same event selection and categorisation is applied to events from simulation and data. The following binning is adopted from reference [68] with the only modification that events with $p_T^{\gamma\gamma} < 30\,\mathrm{GeV}$ are already rejected in the event selection:

$$\{30, 40, 50, 60, 80, 100, 200\}\,\mathrm{GeV}\,. \tag{6.1}$$

Events with $p_T > 200\,\mathrm{GeV}$ are considered in an additional bin. The adopted binning was evaluated in [68] by estimating the non-resonant background in each $p_T^{\gamma\gamma}$-bin from sidebands in the $m_{\gamma\gamma}$ spectrum. The binning is assumed to be reasonable likewise for the modified event selection used in this analysis.

The diphoton mass spectrum observed in data is fitted by a particularly defined signal plus background function. The number of signal and background events in each p_T-bin can then be read off as the normalisation factors of the corresponding fit functions. Before this final fit including signal and background parametrisations is performed, signal and background parameters are evaluated in preceding fits including exclusively the parametrisation of the signal or the background shape, respectively. In the following sections, the choice of the signal and background models and the corresponding pre-fits for the evaluation of their parameters are discussed. The fits described in this chapter use the method of a binned maximum likelihood fit[1] and were performed using RooFit [81, 82].

[1] The method is described in more details in the appendix A and e.g. in reference [80]

6.1. Signal Modelling

The signal shape of the Higgs boson mass peak is modelled by the sum of a Crystal Ball function [83, 84] and a Gaussian component. For $m_H = 125\,\mathrm{GeV}$, the width of the observed Higgs mass peak is dominated by the detector resolution. The Crystal Ball function parametrises the core part of the mass peak resolution and a non-Gaussian tail towards lower mass values. The Gaussian component additionally accounts for wider outliers in the distribution. The parametrisation used for the Crystal Ball function is defined as [74]

$$C\left(m_{\gamma\gamma};\mu_{\mathrm{CB}},\sigma_{\mathrm{CB}},\alpha,n\right) = N\cdot\begin{cases}\exp(-t^2/2) & \text{if } t > -\alpha\\ \left(\frac{n}{\alpha}\right)^n\cdot\exp\left(-\alpha^2/2\right)\cdot\left(\frac{n}{\alpha}-\alpha-t\right)^{-n} & \text{otherwise}\end{cases},\ \alpha>0 \tag{6.2}$$

with $t = (m_{\gamma\gamma}-\mu_{\mathrm{CB}})/\sigma_{\mathrm{CB}}$. N is a normalisation parameter, μ_{CB} is the peak position representing the hypothesized Higgs boson mass, σ_{CB} represents the part of the diphoton invariant mass resolution that is modelled by the Crystal Ball component of the signal parametrisation, while n and α parametrise the exponential tail. The parameter n is, as applied in other ATLAS analyses, fixed to the arbitrary chosen value $n = 10$ in order to help the fit converging.

The peak position μ_{G} of the Gaussian component $\mathcal{G}$ is required to be at the same position as the Crystal Ball peak position $\mu_{\mathrm{CB}} = \mu_{\mathrm{G}} \equiv \mu$, while the Gaussian width σ_{G} is an additional free parameter. The complete normalised signal modelling function $\mathcal{S}$ is hence given by

$$\begin{aligned}\mathcal{S}\left(m_{\gamma\gamma};\mu,\sigma_{\mathrm{CB}},\alpha,\sigma_{\mathrm{G}},f_{\mathrm{CB}}\right) = {} & f_{\mathrm{CB}}\cdot C\left(m_{\gamma\gamma};\mu,\sigma_{\mathrm{CB}},\alpha\right)\\ & +(1-f_{\mathrm{CB}})\cdot\mathcal{G}\left(m_{\gamma\gamma};\mu,\sigma_{\mathrm{G}}\right)\end{aligned} \tag{6.3}$$

with f_{CB} being the fraction of the signal function parametrised by the Crystal Ball component.

The diphoton mass spectra of simulated $H\to\gamma\gamma$ events in all p_T-bins are simultaneously fitted while the peak position μ is required to be the same for all the bins. The other signal parameters are allowed to acquire different values for each bin in this maximum likelihood fit. The fit of the signal shape predicted with simulated $H\to\gamma\gamma$ events is performed in order to fix all signal parameters except the peak position and the signal yield for the later realised signal plus background fit to the data distributions. Any dependencies of the signal shape parameters on the Higgs boson mass are therefore neglected. They should be small since the actually measured Higgs boson mass is near to the simulated value of $125\,\mathrm{GeV}$. Moreover, the shape of the Higgs boson mass peak in data is assumed to be well modelled by the predictions of simulated events.

The fit results for the signal parameters are summarized in table 6.1. The corresponding parameters in the later discussed signal plus background fit are fixed to these values. Figure 6.1 shows the normalised Higgs boson mass peak for events with $40 \le p_T/\mathrm{GeV} < 50$ with the modelled signal function and its parameters. The other simultaneously modelled distributions are shown in the appendix B.2 for all the remaining p_T-bins. The fitted Higgs boson mass of $\mu = 124.625(3)\,\mathrm{GeV}$ differs from the nominal value $m_H = 125\,\mathrm{GeV}$ for which the

p_T/GeV	α	f_{CB}	σ_{CB}/GeV	σ_{G}/GeV
$[30, 40)$	1.37 ± 0.02	0.94 ± 0.02	1.77 ± 0.01	3.53 ± 0.16
$[40, 50)$	1.39 ± 0.02	0.89 ± 0.02	1.73 ± 0.01	3.05 ± 0.10
$[50, 60)$	1.43 ± 0.01	0.94 ± 0.02	1.76 ± 0.01	3.53 ± 0.15
$[60, 80)$	1.45 ± 0.02	0.93 ± 0.01	1.73 ± 0.01	3.48 ± 0.10
$[80, 100)$	1.59 ± 0.04	0.96 ± 0.01	1.76 ± 0.01	4.02 ± 0.20
$[100, 200)$	1.90 ± 0.03	0.95 ± 0.01	1.69 ± 0.01	3.97 ± 0.11
≥ 200	2.30 ± 0.10	0.95 ± 0.01	1.53 ± 0.01	3.81 ± 0.22

Table 6.1.: *Results on signal fit parameters obtained in simultaneous mass fit in p_T bins using simulated $H \to \gamma\gamma$ events with $\sqrt{s} = 8\,\mathrm{TeV}$ and a hypothesized Higgs mass $m_H = 125\,\mathrm{GeV}$.*

$H \to \gamma\gamma$ events were simulated. However, for this analysis, the fit result for the Higgs boson mass does not have any impact and therefore this shift is not further investigated.

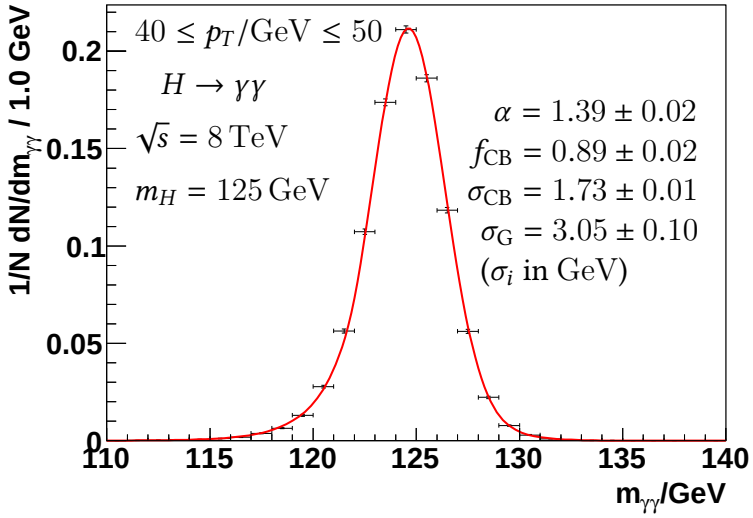

Figure 6.1.: *Normalized signal peak of simulated $H \to \gamma\gamma$ events for a hypothesized Higgs mass of $m_H = 125\,\mathrm{GeV}$ and the modelled signal function. Considered are events passing the event selection with $40 \leq p_T/\mathrm{GeV} < 50$. The common fitted peak position for all p_T-bins is $\mu = 124.625(3)\,\mathrm{GeV}$.*

6.2. Background Modelling

Several studies on the background parametrisation in the $H \to \gamma\gamma$ decay channel have been performed within the ATLAS collaboration. It was investigated that the mass spectra of non-resonant background events categorized in p_T bins are best described by an exponential of a polynomial of second order [68]. This parametrisation is assumed to hold for the modified event selection used in this analysis. This event selection differs to that applied in reference [68] concerning the requirements of one additional reconstructed jet and a minimum p_T for the Higgs boson candidate of 30 GeV, but the same relative p_T cuts on the two leading

photons were applied in both analyses. With absolute cuts of $p_T \geq 40(30)\text{GeV}$ applied on the (sub)leading photon, as used in former ATLAS analyses instead of the relative cuts, the background dominated mass spectrum becomes distorted for lower mass values in the low-p_T-bins.

The background parametrisation with the exponential of a polynomial of second order is adopted in all p_T-bins. The background parametrisation function is therefore defined as

$$\mathcal{B}(m_{\gamma\gamma};\, \beta, \gamma) = N \cdot \exp\left(-\left(\beta\, m_{\gamma\gamma} + \gamma\, m_{\gamma\gamma}^2\right)\right) \tag{6.4}$$

where N is a normalisation parameter while β and γ are free fit parameters.

This background parametrisation function is fitted to the diphoton mass spectra observed in data. In contrast to the signal fit parameters, the background fit parameters are not fixed in the fits using signal and background parametrisations (see section 6.3), but they are considered as initial values for the combined fit. The whole mass range of $105 \leq m_{\gamma\gamma}/\text{GeV} \leq 160$ is used for this background fit and no signal region is excluded. It was investigated that the exclusion of a signal region around $m_{\gamma\gamma} = 125\,\text{GeV}$ affects the results of the background only fit. However, no difference was found in the results of the combined fit, which uses these results only as initial values. For the results in this analysis, only the results of the combined fit are relevant and hence no signal region needs to be excluded.

Figure 6.2 shows the mass spectrum and the fitted background function for the bin with events of $40 \leq p_T/\text{GeV} < 50$. The plots of the remaining bins are shown in the appendix B.3.

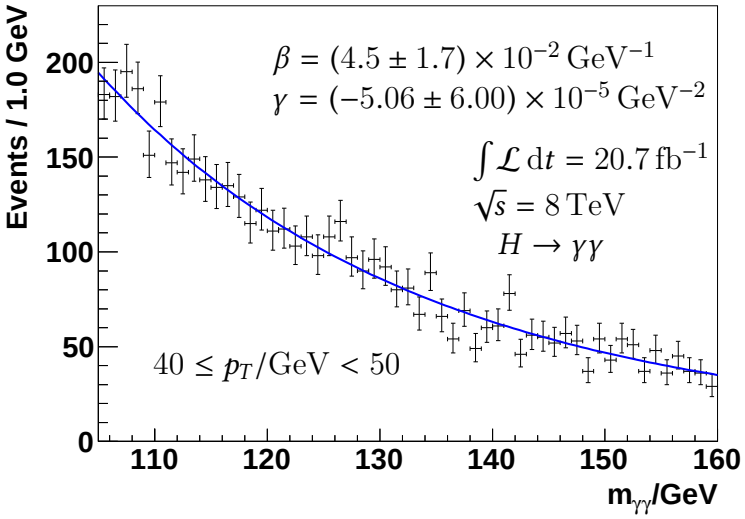

Figure 6.2.: *Mass spectrum observed in data at* $\sqrt{s} = 8\,\text{TeV}$ *with an integrated luminosity of* $\int \mathcal{L}\,\mathrm{d}t = 20.7\,\text{fb}^{-1}$ *and the modelled background function. Considered are events passing the event selection with* $40 \leq p_T/\text{GeV} < 50$.

6.3. Results

The results of the previously described separate signal and background fits are used to perform a binned extended maximum likelihood fit of a signal plus background parametrisation function to the diphoton mass spectra in each bin of p_T. The signal plus background parametrising function $\mathcal{F}$ is composed of the signal and background functions defined in (6.3) and (6.4) with the respective normalisation factors N_{sig} and N_{back} expressing the number of observed signal and background events:

$$\begin{aligned}\mathcal{F}(m_{\gamma\gamma}; N_{\text{sig}}, N_{\text{back}}, \mu,\ \beta,\ \gamma, f_{\text{CB}}, \alpha,\ \sigma_{\text{CB}},\ \sigma_{\text{G}}) = \\ N_{\text{sig}} \cdot \mathcal{S}(m_{\gamma\gamma}; \mu, \sigma_{\text{CB}}, \alpha, \sigma_{\text{G}}, f_{\text{CB}}) + N_{\text{back}} \cdot \mathcal{B}(m_{\gamma\gamma};\ \beta, \gamma)\end{aligned} \tag{6.5}$$

The signal parameters f_{CB}, α, σ_{CB} and σ_{G} are fixed to their values obtained in the signal fit while the background parametrisation parameters β and γ are again free fit parameters using the results of the background fit as start parameters. The binned extended maximum likelihood fit is performed simultaneously in all p_T-bins with the peak position μ being the only parameter that is constrained to adopt the same fitted value for all bins. The $m_{\gamma\gamma}$ bin width is $1\,\text{GeV}$ for the whole mass range.

The extended likelihood allows for a Poisson fluctuation of the overall normalisation in every bin by adding an additional term to the likelihood function (see the descriptions in the appendix A) and enables the calculation of separate fit errors on the number of signal events N_{sig} and the background contribution N_{back}. In table 6.2, the results for the free fit parameters obtained in the likelihood fit are given. Figure 6.3 shows the modelled mass spectrum for events with $40 \leq p_T/\text{GeV} < 50$. The mass spectra and fitted signal plus background functions of all remaining p_T-bins are shown in the appendix B.4.

p_T/GeV	N_{sig}	N_{back}	$\beta \cdot 10^2\,\text{GeV}$	$\gamma \cdot 10^4\,\text{GeV}^2$
$[30, 40)$	38 ± 31	5053 ± 77	7.3 ± 1.3	-1.47 ± 0.50
$[40, 50)$	59 ± 31	4939 ± 76	5.9 ± 1.3	-1.08 ± 0.51
$[50, 60)$	67 ± 29	4219 ± 71	3.0 ± 1.4	0.09 ± 0.55
$[60, 80)$	48 ± 33	5830 ± 83	4.8 ± 1.3	-0.78 ± 0.49
$[80, 100)$	51 ± 24	2933 ± 59	1.6 ± 1.7	0.22 ± 0.66
$[100, 200)$	46 ± 23	3005 ± 59	1.3 ± 1.8	0.08 ± 0.68
≥ 200	8 ± 6	213 ± 16	5.6 ± 5.4	-1.82 ± 2.00

Table 6.2.: *Results of simultaneous signal+background fit on the mass spectra in p_T-bins observed in data. Results are given for the free fit parameters. The best fit value for the Higgs boson mass is $m_H = (125.9 \pm 0.5)\,\text{GeV}$.*

The fit parameter N_{sig} in each bin represents an estimate on the number of Higgs bosons produced in events within the corresponding transverse momentum range that passed the event selection. It is hence not restricted to gluon fusion Higgs production, but includes Higgs bosons produced in all possible production processes. The definition of the bins in which the signal yield N_{sig} was extracted is based on the transverse momentum of the combined diphoton system of the two leading photons.

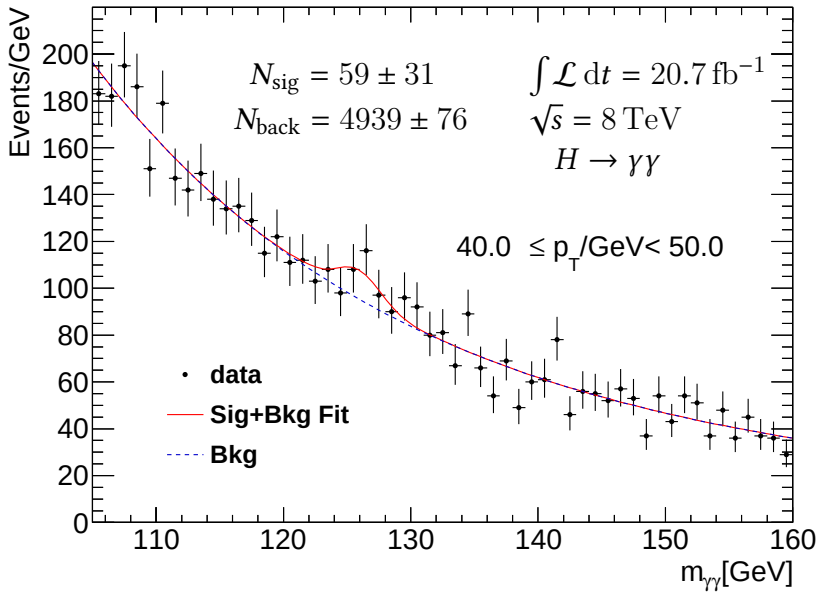

Figure 6.3.: *Mass spectrum observed in data at* $\sqrt{s} = 8\,\mathrm{TeV}$ *with an integrated luminosity of* $\int \mathcal{L}\,\mathrm{d}t = 20.7\,\mathrm{fb}^{-1}$ *and the fitted signal plus background function. The best fit value for the Higgs boson mass is* $m_H = (125.9 \pm 0.5)\,\mathrm{GeV}$*. Considered are events passing the event selection with* $40 \leq p_T/\mathrm{GeV} < 50$*.*

In figure 6.4a, the p_T spectrum of the Higgs boson candidates after subtracting the non-resonant background contribution is shown. Since the signal yield observed in a particular bin depends on the bin width, figure 6.4b shows the differential p_T distribution in which the event yield is divided by the corresponding bin width. For the analysis presented in this thesis, the yield in each bin is the relevant observable that is compared to predictions obtained with simulated events, but the differential distribution gives a representation of the actual shape of the Higgs boson p_T-distribution.

The errors on the background fit parameters are approximately of the order $\Delta N_{\mathrm{back}} = \sqrt{N_{\mathrm{back}}}$. The uncertainty on the signal yield in each bin, ΔN_{sig}, is also determined in the signal + background fit. Since it is influenced by the uncertainty on the background yield, the observed statistical uncertainty on the signal yield is for all bins much larger than $\sqrt{N_{\mathrm{sig}}}$, which is further discussed in section 8.1.

The p_T spectra shown in figure 6.4 are influenced by detector effects including particle identification inefficiencies and limited energy resolutions. Those detector effects can depend on the reconstructed diphoton transverse momentum so that the impact on the signal yield may vary between the bins. More over, differences between reconstructed observables and the 'true' kinematics at particle level can cause migration of events from one bin to another. Concerning the reconstructed diphoton transverse momentum, uncertainties on the measured energy scales and resolutions are particularly expected to have an influence. The detector effects can be corrected by applying an unfolding procedure in order to make the observed distribution directly comparable to theory predictions at particle level. However, in this analysis, comparisons are done at the reconstruction level, so that no unfolding procedure is necessary. The simulated events which were reweighted at particle level to different theoretical predictions (see section 4.3.2) are therefore also passed through a full detector

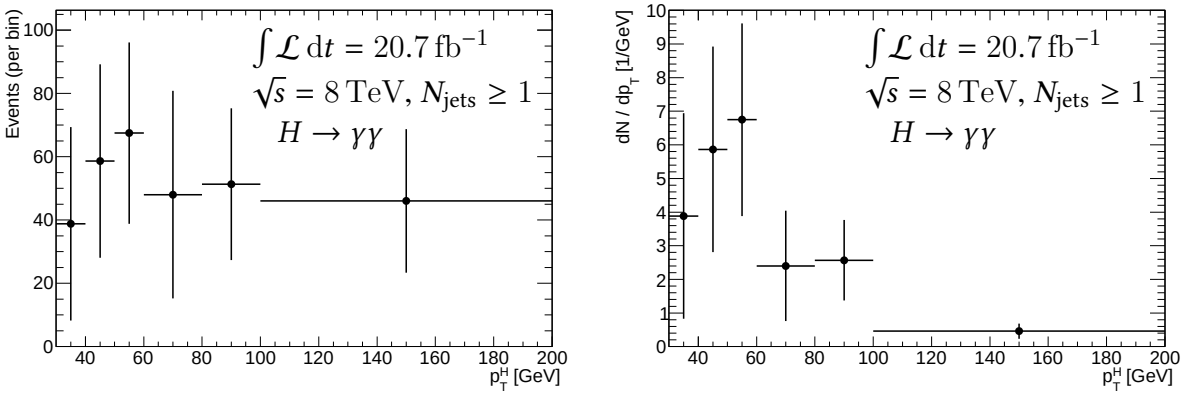

(a) *Event yield per bin* (b) *Event yield per bin divided by bin width*

Figure 6.4.: *Higgs boson transverse momentum distribution extracted from data after non-resonant background estimation. Data was taken with the ATLAS detector at* $\sqrt{s} = 8\,\mathrm{TeV}$ *reaching an integrated luminosity of* $\int \mathcal{L}\,dt = 20.7\,\mathrm{fb}^{-1}$*. The rest bin for events with* $\geq 200\,\mathrm{GeV}$ *is not shown.*

simulation. The influence of experimental systematic uncertainties including photon energy resolution and scale uncertainties and also jet energy resolution and scale uncertainties on the results of the analysis are discussed in chapter 7.

For this analysis, events with Higgs bosons produced in other processes than gluon fusion are considered as background (resonant background). The background estimation described in the previous sections covered the estimation of background events without Higgs production. However, the Higgs boson transverse momentum distribution at reconstruction level obtained by this procedure must be corrected for the presence of Higgs bosons produced in VBF, VH or ttH processes.

6.4. Resonant Background

In the previous sections, the inclusive Higgs boson p_T distribution was retrieved from data. The contribution of resonant background events attributed to VBF, VH and ttH Higgs boson production processes, is estimated using the predictions of simulated events. The corresponding production cross sections which are used for normalisation are given in table 4.1.

Table 6.3 gives the expected (using simulated events) and observed event yields in the Higgs boson p_T-bins. It can be seen that gluon fusion, which is the signal process for this analysis, is the dominant production mode in all bins. Moreover, the total number of observed events exceeds the expected inclusive (including all considered Higgs production processes) event yield. For events passing the selection criteria applied in this analysis, an inclusive signal strength of

$$\mu_{\mathrm{fid}} = 2.0 \pm 0.6 \tag{6.6}$$

p_T/GeV	ggF	VBF	VH + ttH	inclusive	$N_{\text{sig}}^{\text{obs}}$
$[30, 40)$	16.4	2.0	1.1	19.5	38 ± 31
$[40, 50)$	18.4	2.3	1.3	22.0	59 ± 31
$[50, 60)$	16.9	2.5	1.3	20.7	67 ± 29
$[60, 80)$	25.0	4.7	2.4	32.1	48 ± 33
$[80, 100)$	15.1	3.8	2.0	20.9	51 ± 24
$[100, 200)$	21.9	8.0	4.5	34.4	46 ± 23
≥ 200	4.5	1.7	1.4	7.6	8 ± 6
≥ 30	118.2	25.0	14.0	157.2	317 ± 71

Table 6.3.: *Predicted event yields from the considered Higgs boson production processes in the Higgs boson p_T-bins for $N_{jets} \geq 1$. Event yield is normalised to SM cross sections given in table 4.1 for an integrated luminosity $\int \mathcal{L}\,\mathrm{d}t = 20.7\,\mathrm{fb}^{-1}$. The observed event yields N_{sig}^{obs} are given for comparison.*

is observed. Since this analysis tests the SM prediction of the gluon fusion tensor structure, one must consider the possibility that the observed signal surplus is completely attributed to gluon fusion Higgs production. Consequently, in the nominal analysis, the event yield of other production processes is subtracted from the observed Higgs boson p_T spectrum according to their SM cross sections, which means that $\mu_{VBF} = \mu_{ZH} = \mu_{WH} = \mu_{t\bar{t}H} = 1$ are assumed. The subtracted event yields hence correspond to the numbers given in table 6.3. Figure 6.5 shows the Higgs p_T distribution obtained from data after the correction for Higgs events of production processes considered as background in this analysis. This distribution is in the further analysis used to test for the presence of the coupling operators O_i defined in the effective theory. The uncertainties on the corrected signal yield shown in this figure are still dominated by the fit uncertainty, but account for the expected statistical uncertainties on the Higgs background events in data. They do not consider theoretical uncertainties on the cross sections for the background Higgs production processes.

As an alternative ansatz, the observed signal strength is taken into account for the resonant background contribution. Therefore, the predicted event yields for the Higgs boson background processes are scaled by the observed signal strength and subtracted from the inclusive Higgs boson p_T spectrum that was extracted from data. However, for this ansatz, the signal strength observed in the inclusive diphoton selection is used instead of the signal strength observed in the defined signal region. This procedure was chosen since no assumption on the kinematic distributions in background Higgs boson production processes should enter the results. The number of produced Higgs bosons for the inclusive diphoton production including all production processes is determined in a fit to the inclusive diphoton mass spectrum. Here, all events passing the inclusive diphoton selection are considered without any further requirements. The fit follows the procedure described in the previous sections and is shown in figure 6.6. The fitted number of Higgs bosons is $N_{\text{sig}} = 659 \pm 126$ while the predicted event yield that was evaluated with simulated events can be taken from table 5.2 and is $N = 411$. The inclusive signal strength observed in data and the corresponding statistical uncertainty hence are

$$\mu_{\text{obs}} = 1.60 \pm 0.31\,(\text{stat})\ . \tag{6.7}$$

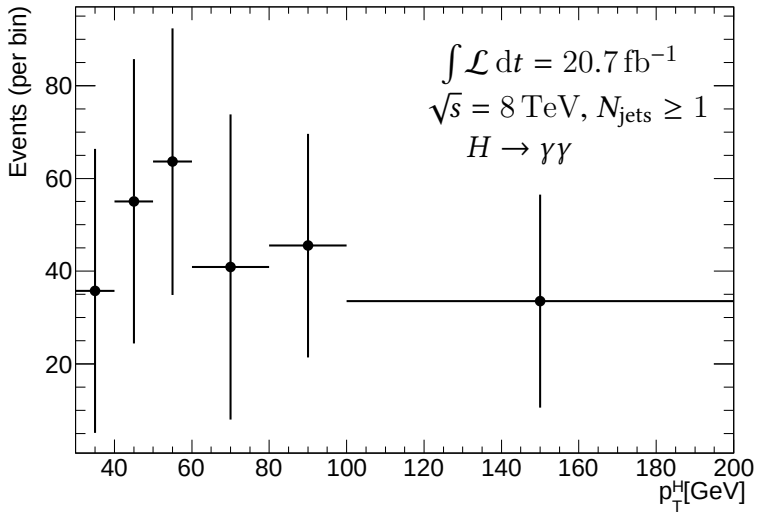

Figure 6.5.: *Higgs boson transverse momentum distribution extracted from data at reconstructed level corrected for Higgs background. Data was taken with the ATLAS detector at* $\sqrt{s} = 8\,\mathrm{TeV}$ *reaching an integrated luminosity of* $\int \mathcal{L}\,dt = 20.7\,\mathrm{fb}^{-1}$*. Considered are events with at least one reconstructed jet. The rest bin for events with* $\geq 200\,\mathrm{GeV}$ *is not shown.*

This value is in agreement to $\mu = 1.65 \pm 0.24(\mathrm{stat})^{+0.25}_{-0.18}(\mathrm{syst.})$ which was determined in an ATLAS analysis using the same dataset [56]. Results obtained with this alternative approach are given together with the nominal results in chapter 9.

For the approach including the selection criteria which were derived in order to suppress the VBF Higgs boson production background, events in data are selected using these additional selection requirements and the estimation of the non-resonant background is repeated following the procedure explained in the previous sections. The observed signal yields in this

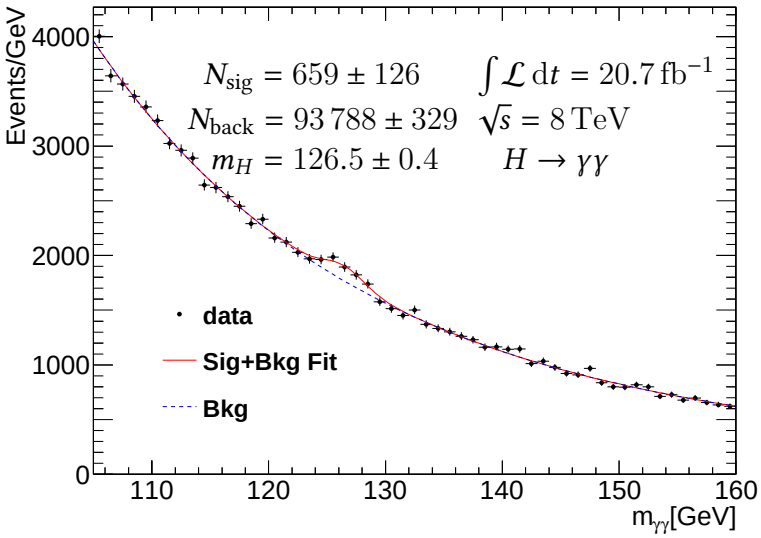

Figure 6.6.: *Inclusive diphoton mass spectrum observed in data at* $\sqrt{s} = 8\,\mathrm{TeV}$ *with an integrated luminosity of* $\int \mathcal{L}\,dt = 20.7\,\mathrm{fb}^{-1}$ *and the modelled signal plus background function.*

fit are slightly lower than without the additional selection criteria and are given in table 6.4. The resonant background contributions that remain with the tighter event selection are again subtracted according to their prediction evaluated with simulated events. This study is only performed for the assumption of $\mu = 1$ for the resonant background processes. As given in table 5.4, the additional selection criteria do not reduce the expected yields of events produced in VH or ttH production processes within the described accuracy. The expected event yields for each of the Higgs boson p_T-bins by applying the additional selection criteria to supress VBF Higgs boson production are given in table 6.4 for the ggF and VBF production processes. The results of this approach are also presented together with the nominal results.

p_T/GeV	ggF	VBF	$N_{\text{sig}}^{\text{obs}}$
$[30, 40)$	16.3	1.7	38 ± 30
$[40, 50)$	18.3	2.0	56 ± 31
$[50, 60)$	16.8	2.2	67 ± 29
$[60, 80)$	24.7	4.0	44 ± 33
$[80, 100)$	14.8	3.1	47 ± 24
$[100, 200)$	21.3	5.7	45 ± 22
≥ 200	4.3	1.0	8 ± 6
≥ 30	116.5	19.7	305 ± 70

Table 6.4.: *Predicted event yields from the ggF and VBF production processes in the Higgs boson p_T-bins for $N_{jets} \geq 1$ and the modified event selection in order to suppress VBF Higgs boson production. Event yield is normalised to SM cross sections given in table 4.1 for an integrated luminosity $\int \mathcal{L}\,\mathrm{d}t = 20.7\,\mathrm{fb}^{-1}$. The observed event yields N_{sig}^{obs} in the fit with modified event selection are also given.*

7. Systematic Uncertainties

The reconstructed Higgs boson transverse momentum depends on various experimental observables, in particular concerning the photon and jet reconstruction, that are possibly affected by various systematic uncertainties. Moreover, perturbatively performed calculations that were used to predict differential and total cross sections are subject to theoretical uncertainties. These experimental and theoretical systematic uncertainties can be further subdivided into shape uncertainties affecting the shape of the considered Higgs boson p_T distributions and yield uncertainties that only have an impact on the overall normalisation.

The impact of several systematic uncertainties on the results of this analysis is investigated using simulated gluon fusion $H \rightarrow \gamma\gamma$ events. Therefore, different observables are varied within their uncertainties and the effects of these systematic variations on the final results are detailed in chapter 9. In this chapter, the systematic uncertainties which are considered for these investigations are introduced. For the subset of experimental shape uncertainties, the influence on affected kinematic distributions, including the Higgs boson transverse momentum, is investigated.

7.1. Experimental Uncertainties

The transverse momentum spectrum of reconstructed Higgs bosons, which is used in this analysis as the discriminating observable to determine confidence intervals on Wilson coefficients, is reconstructed from the four vectors of the leading two reconstructed photons. The event selection further requires one additional jet with a transverse momentum above $30\,\mathrm{GeV}$. The results of this analysis are therefore primarily affected by uncertainties on photon and jet observables. Concerning jet uncertainties, only the impact on the number of events satisfying the requirement of one reconstructed jet with $p_T \geq 30\,\mathrm{GeV}$ is relevant for this analysis.

An additional experimental uncertainty, that is not attributed to photon or jet systematics, comes from the uncertainty on the luminosity measurement. The expected event yield for the 2012 ATLAS dataset is predicted with simulated events for an integrated luminosity of $\int \mathcal{L} = 20.7\,\mathrm{fb}^{-1}$. However, this measured quantity is accompanied by an uncertainty of ±3.6% [56] which must therefore be considered as an uncertainty on the expected event yield.

7.1.1. Photon Systematics

Photon uncertainties affecting the reconstructed transverse momentum of the diphoton system composed of the two leading photons are particularly attributed to the photon energy measurement in the electromagnetic calorimeters. These are subject to an uncertainty on the energy scale (PES) and an uncertainty on the resolution (PER). Another photon uncertainty is attributed to an uncertainty on the photon reconstruction efficiency.

Photon Energy Resolution

Simulated $H \to \gamma\gamma$ events are smeared to match observations on the measured energy resolution evaluated with $Z \to ee$ data [69]. The energy smearing depends on the calorimeter region and is around 1% to 2.5%. The uncertainty on this smearing correction is considered as a systematic uncertainty. For this investigation, the width of the applied smearing function is varied up and down by the 1σ uncertainty on the energy resolution. The uncertainty on the constant term of the energy resolution was investigated in the $Z \to ee$ studies to be about 50% [69]. The total relative uncertainty on the energy resolution is estimated to range between 5% and 20% for electrons with $E_T \sim 60\,\mathrm{GeV}$, depending on the region of the calorimeter . Newer calibrations based on the complete LHC Run 1 data reduce these uncertainties [85], but were not applied to the dataset used for this analysis. The event selection and definition of the Higgs boson candidate, following the procedure described in section 5.2, is then performed for the photons with varied simulated resolution of the energy measurement, so that this systematic uncertainty has an influence on the shape of the reconstructed Higgs boson p_T spectrum and on the overall event yield. For the event selection applied in this analysis, however, the effect on the yield is found to be $< 0.1\%$ and therefore negligible. Figure 7.1 shows the distribution of the difference between the energy

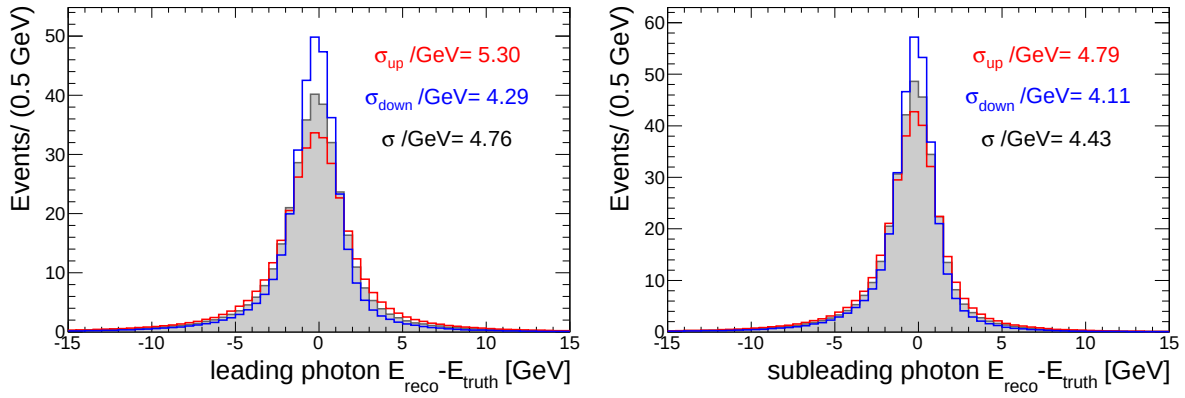

(a) *Leading photon* (b) *Subleading photon*

Figure 7.1.: *Resolution of the energy measurement for the leading and subleading photon. The best description on the energy resolution evaluated from data is shown in grey, up (down) variations by one standard deviation on the resolution are shown in red (blue). The event yield corresponds to an integrated luminosity of* $\int \mathcal{L} = 20.7\,\mathrm{fb}^{-1}$. *Considered are simulated gluon fusion* $H \to \gamma\gamma$ *events for* $\sqrt{s} = 8\,\mathrm{TeV}$ *passing the inclusive diphoton selection.*

of the (sub)leading photon at detector level with varied energy resolution and the photon

energy at truth level. Truth photons are defined for simulated events as the photon objects obtained after simulating radiation processes and before the detector simulation is applied. The average resolution is found to be approximately $(4.8 \pm 0.5)\,\mathrm{GeV}$ and $(4.4 \pm 0.4)\,\mathrm{GeV}$ for the leading and subleading photon, respectively. The absolute energy resolution is better for the subleading photon since $\sigma(E) \sim \sqrt{E}$ (see table 3.1). This explains the lower width observed in the distribution for the subleading photon in figure 7.1b compared to that of the leading photon in figure 7.1a. However, for the actual accuracy of the reconstructed photon vectors, the relative uncertainty $\sigma(E)/E \sim 1/\sqrt{E}$ is more important and lower for the leading photon.

Photon Energy Scale

The scale of the energy measurement is calibrated in order to restore agreement between energy scales in data and simulation. The overall systematic uncertainty on the energy scale evaluated with $Z \to ee$ data varies from 0.3% to 3%, depending on the elctron $|\eta|$ and E_T [69]. The average energy scale uncertainty for photons is reduced to 0.3% in datasets using new calibrations [85]. The nominal calibrations are applied on data, the impact of 1σ variations on this calibration is evaluated with simulated events. Figure 7.2 shows the distribution of the difference between the energy of the reconstructed (sub)leading photon with 1σ variation on the energy scale and the energy of the reconstructed (sub)leading photon for the nominal energy scale. Since this calibration is applied in the pre-selection, there are several other cor-

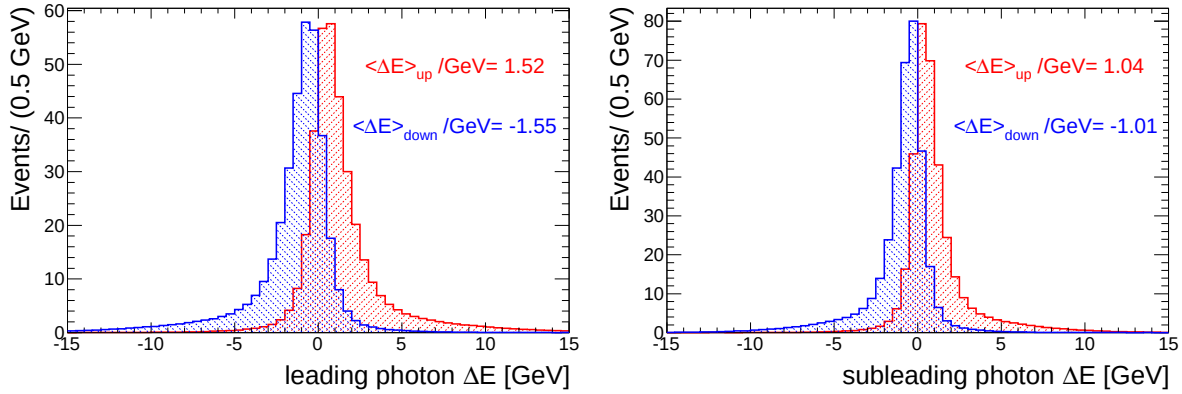

(a) *Leading photon* (b) *Subeading photon*

Figure 7.2.: *Impact of energy scale variation by* 1σ *on the reconstructed photon energy. The distribution of the energy difference between the reconstructed photon with varied energy scale and the reconstructed photon with nominal energy scale is shown for the leading and the subleading photon. Distribution for upwards scaling of the energy is shown in red, the one for downwards scaling of the energy in blue. The event yield corresponds to an integrated luminosity of* $\int \mathcal{L} = 20.7\,\mathrm{fb}^{-1}$. *Considered are simulated gluon fusion* $H \to \gamma\gamma$ *events passing the inclusive diphoton selection for* $\sqrt{s} = 8\,\mathrm{TeV}$.

rections applied in the photon reconstruction after this energy scale calibration. This includes corrections that account for the reconstructed primary vertex. These corrections may be different if applied on photons with varied energy scale. Moreover, it is possible that different photons are selected as (sub)leading photon for a varied photon energy scale. Consequently,

there are few events for which the energy of the reconstructed (sub)leading photon with upwards scaled energy is lower than the energy of the reconstructed (sub)leading photon with nominal energy scale and vice versa. The average impact of the scale variations on the reconstructed photon energies is found to be approximately $\pm 1.5\,\mathrm{GeV}$ and $\pm 1.0\,\mathrm{GeV}$ for the leading and subleading photon, respectively. The impact on the signal yield is found to be approximately $\pm 0.4\%$.

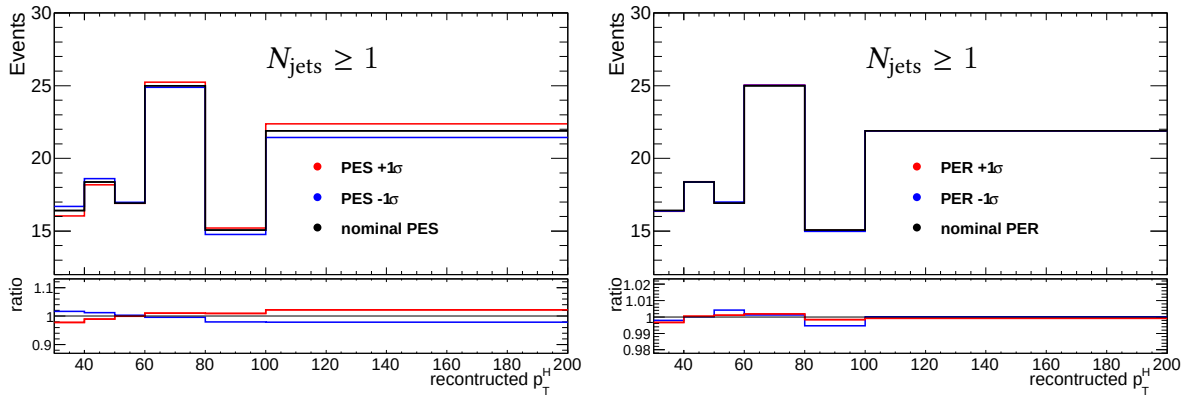

(a) *Photon energy scale variation* (b) *Photon energy resolution variation*

Figure 7.3.: *Higgs boson transverse momentum in simulated gluon fusion $H \to \gamma\gamma$ events that pass the full event selection at $\sqrt{s} = 8\,\mathrm{TeV}$ with photon energy systematics varied by $+1\sigma$ (blue) and -1σ (red) in comparison to nominal spectra. The event yield corresponds to an integrated luminosity of $\int \mathcal{L} = 20.7\,\mathrm{fb}^{-1}$.*

In figure 7.3, the Higgs boson p_T distribution is shown for varied PER and PES and each compared to the prediction for the nominal photon energies. It has to be considered that the event yield is plotted for p_T-bins with unequal width.

Photon Reconstruction Efficiency

Another experimental systematic concerning photon observables is attributed to an uncertainty on the photon reconstruction efficiency. The reconstruction efficiency ϵ_{ID} and its uncertainty depend on the photon pseudorapidity and transverse energy, as shown in figure 5.2 for unconverted photons. The corresponding distributions for converted photons can be found in ref. [76]. The uncertainty on the identification efficiency is smaller than 2.5%, regardless of photon kinematics. The effect on the shape of the Higgs boson p_T distribution from this uncertainty is assumed to be negligible. Therefore, the analysis presented here only considers the influence on the signal yield and assigns a conservative systematic uncertainty of 2.5% on the identification efficiency of all photons.

7.1.2. Jet Systematics

In this analysis, events are selected with a requirement on the reconstructed jet multiplicity. A requirement of $p_T \geq 30\,\mathrm{GeV}$ is applied on each jet and at least one jet must be reconstructed in every selected event. Consequently, systematic uncertainties on the jet transverse

momentum have an influence on the event selection and hence indirectly affect the reconstructed Higgs boson p_T spectrum. The uncertainty on the reconstructed jet p_T is mainly determined by the uncertainties on the jet energy measurement and is composed of a scale (JES) uncertainty and a resolution (JER) uncertainty.

Jet Energy Resolution

For the 2012 data set used in this analysis, the jet energy resolution in MC and observed in data are in agreement within uncertainty [86]. Therefore, no additional smearing is applied on jets in simulated events so that only the impact of an additional smearing can be investigated. Consequently, for investigations on this systematic uncertainty, an additional smearing of $+1\sigma$ on the jet resolution uncertainty is applied to jet energies and the effect of this uncertainty is assumed to be symmetric. The total uncertainties on the jet energy resolution measurements range from 20% to 10% for jets within $|y| < 2.8$ and with transverse momenta increasing from $30\,\mathrm{GeV}$ to $500\,\mathrm{GeV}$ [86]. The distribution of the reconstructed jet multiplicity, which is the only reconstructed jet observable relevant for the analysis results, is shown in figure 7.4 for nominal and varied jet energy resolution. Migrations from the zero jets bin to bins with higher jet multiplicities must be considered in particular since they influence the event selection of this analysis. For the jet energy resolution varied by $+1\sigma$, the expected yield for events with at least one reconstructed jet is increased due to migrated events by about 2%. The transverse momentum distribution of reconstructed Higgs bosons is also shown in figure 7.4. It can be seen that the event yield is increased mainly due to additionally selected events with a Higgs transverse momentum below $50\,\mathrm{GeV}$.

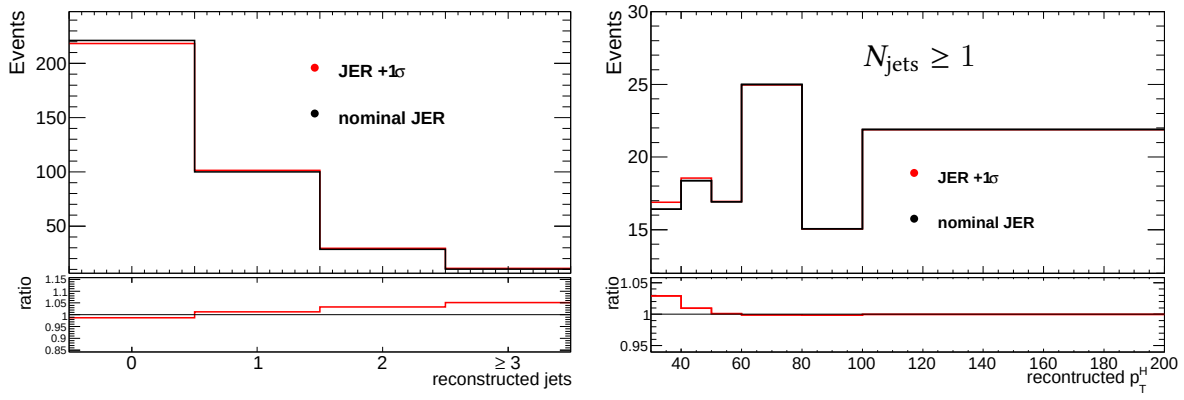

(a) *Jet multiplicity* (b) *Higgs boson transverse momentum*

Figure 7.4.: *Jet multiplicity and Higgs boson transverse momentum in simulated gluon fusion $H \to \gamma\gamma$ events at $\sqrt{s} = 8\,\mathrm{TeV}$ with jet energy resolution varied by $+1\sigma$ (red) in comparison to nominal JER. The event yield corresponds to an integrated luminosity of $\int \mathcal{L} = 20.7\,\mathrm{fb}^{-1}$. The jet multiplicity is shown for events passing the inclusive diphoton selection while for the Higgs boson p_T spectrum, the full event selection is applied.*

Jet Energy Scale

The uncertainty on the jet energy scale is evaluated by varying the scale corrections that are applied to simulated events within their respective $\pm 1\sigma$ uncertainties [87]. The maximum uncertainty for the jet calibration which is used in this analysis is found to be around 14% for low p_T jets with $3.2 \leq |\eta| < 4.5$. In the meanwhile, the jet energy calibration was improved by evaluating data with higher integrated luminosity [88], lowering the maximum uncertainty to about 6%. The jet uncertainty is composed of uncertainties on the various analysis methods performed for the calibration (see the given references), uncertainties attributed to pileup and additional uncertainties for particular event topologies. For this analysis, only the total uncertainty on the jet energy scale and its impact on the jet multiplicity is considered instead of analysing component uncertainties separately. On the one hand, the variation of the JES by $+1\sigma$ causes an increase of the expected signal yield for events with ≥ 1 reconstructed jets by approximately 6.5%. For a JES varied by -1σ, on the other hand, the expected event yield is lowered by around 6.2%. In figure 7.5, the jet multiplicity distribution is shown for the nominal and the varied jet energy scales. Considering the influence on the Higgs boson p_T, which is also shown in figure 7.5, it can be seen that an upwards (downwards) scaled jet energy particularly leads to an increase (decrease) of events with lower Higgs boson p_T. For the p_T-bin of $30 \leq p_T/\mathrm{GeV} \leq 40$, the effect is of the order ±10%.

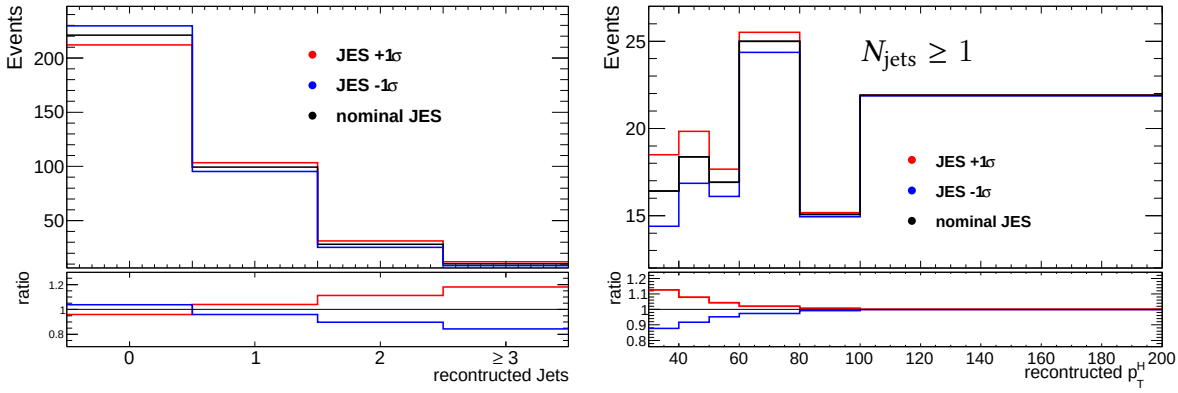

(a) *Jet multiplicity* (b) *Higgs boson transverse momentum*

Figure 7.5.: *Jet multiplicity and Higgs boson transverse momentum in simulated gluon fusion $H \to \gamma\gamma$ events at $\sqrt{s} = 8\,\mathrm{TeV}$ with jet energy scale varied by $\pm 1\sigma$ (red/blue) in comparison to nominal JES. Event yield corresponds to an integrated luminosity of $\int \mathcal{L} = 20.7\,\mathrm{fb}^{-1}$. The jet multiplicity is shown for events passing the inclusive diphoton selection while for the Higgs boson p_T spectrum, the full event selection is applied.*

Jet Vertex Fraction

A jet vertex fraction (JVF) was defined and applied in the jet reconstruction (see section 5.3). This JVF veto is introduced in order to suppress pileup jets, but is only applied on jets with $p_T < 50\,\mathrm{GeV}$ and $|\eta| < 2.4$. Jets in this kinematic range are rejected for a JVF ≤ 0.25, while a variation of this cut value can be considered as an additional systematic uncertainty.

The JVF up/down variation is calculated for each calibrated jet candidate individually using the transverse momentum and pseudorapidity of the jet candidate as input parameters. For example, for jets within $1.0 \leq |\eta| \leq 2.1$ and $p_T \geq 30\,\mathrm{GeV}$, the JVF threshold is varied upwards (downwards) to 0.27(0.23). The jet candidate is then tested to pass the JVF criteria according to the varied cut value. In figure 7.6, it can be seen that the impact of this JVF cut variation on the jet multiplicity and on the reconstructed Higgs boson transverse momentum is negligible. The influence on the expected event yield of selected events is $< 0.1\%$. This systematic uncertainty is therefore expected to have no considerable influence on analysis results and is not investigated further.

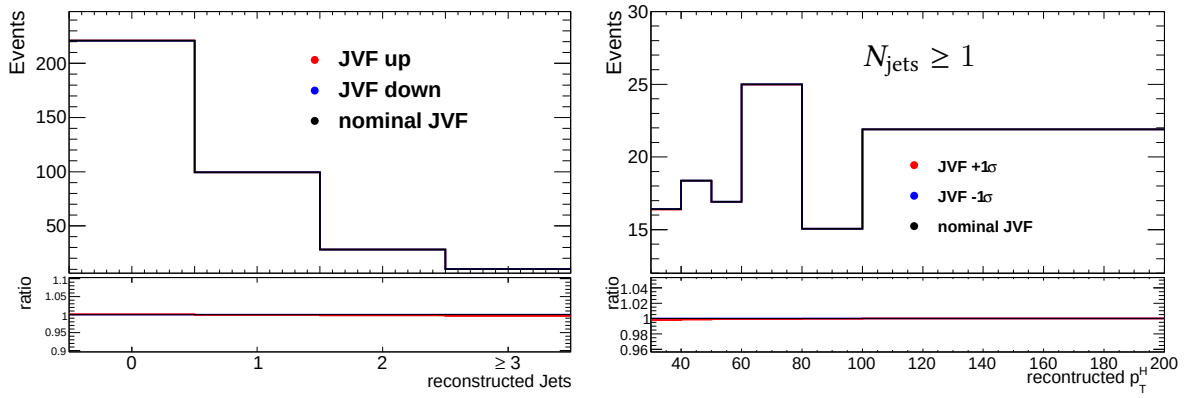

(a) *Jet multiplicity* (b) *Higgs boson transverse momentum*

Figure 7.6.: *Jet multiplicity and Higgs boson transverse momentum in simulated gluon fusion $H \to \gamma\gamma$ events at $\sqrt{s} = 8\,\mathrm{TeV}$ with varied JVF cuts. Event yield corresponds to an integrated luminosity of $\int \mathcal{L} = 20.7\,\mathrm{fb}^{-1}$. The jet multiplicity is shown for events passing the inclusive diphoton selection while for the Higgs boson p_T spectrum, the full event selection is applied.*

7.2. Theoretical Uncertainties

In this thesis, the event yield of simulated gluon fusion events is normalised according to the calculated gluon fusion cross section given in table 4.1. This cross section is calculated at NNLL QCD and NLO EW accuracies. As it can be seen in this table, this cross section prediction is influenced by two independent uncertainties: A QCD scale uncertainty attributed to factorisation and renormalisation scales and an uncertainty on the parton density function including the value of the strong coupling constant α_s which were used for the corresponding cross section calculation. In order to investigate the influence of those yield uncertainties, the predicted event yield is for each source of uncertainty varied within the given $\pm 1\sigma$ range (see table 4.1).

Since this analysis uses the p_T spectrum of Higgs bosons reconstructed in the $H \to \gamma\gamma$ decay channel, the predicted event yield also depends on the branching ratio $\mathrm{BR}(H \to \gamma\gamma)$. The uncertainty on this branching ratio is $^{+4.98}_{-4.89}\%$ and is considered as an additional yield uncertainty.

Uncertainties attributed to PDF and scale uncertainties influence not only the expected event yield, but also the shape of predicted kinematic distributions including the Higgs boson p_T spectrum. It was investigated if analysis results are affected by the scale at which the strong coupling constant α_s is evaluated for the calculation of cross sections in the effective theory. For the nominal results, α_s is evaluated at scale $\mu = (m_H^2 + p_{T,H}^2)^{1/2}$ in the reweighting procedure (see (4.2)). In order to investigate if the choice of μ has an impact on the results of this analysis, studies are made for different choices of μ. For this analysis, $\mu = m_H$, $\mu = ((1/2)m_H^2 + p_{T,H}^2)^{1/2}$ and $\mu = (2m_H^2 + p_{T,H}^2)^{1/2}$ are considered.

Powheg does itself not provide any information on theoretical uncertainties attributed to the proton PDF used for calculations. The impact on the predicted kinematic distributions and the analysis results can therefore not be investigated. The cross sections for $H + 1jet$ events are calculated in the effective theory at LO accuracy. However, uncertainties on these calculations are not considered in this analysis. Moreover, this investigation of theoretical uncertainties does not consider the differences that were observed comparing the SM prediction obtained with Powheg and the corresponding SM cross sections calculated in the reweighting procedure, either.

8. Confidence Intervals for Wilson Coefficients

The sensitivity to test for an additional contribution from the coupling operators O_i, which were introduced in section 2.4, in addition to the SM operator is predicted using simulated events. The contribution of each of the coupling operators O_i is adjusted by the corresponding Wilson coefficient C_i. The main goal of this analysis is to give confidence intervals for these Wilson coefficients C_i.

The strategy to derive frequentist confidence intervals for the Wilson coefficients uses the Neyman construction [89]. Therefore, confidence belts for the Wilson coefficients C_i depending on the likelihood estimators $\widehat{C_i}$ are derived in studies using simulated events. The estimators $\widehat{C_i}$ are evaluated using both a non-extended maximum likelihood fit and an extended maximum likelihood fit. This procedure requires to study the probability distributions of the likelihood estimators $f(\widehat{C_i};\, C_i)$ for all possible values of the Wilson coefficients C_i. Thus, these distributions are determined using pseudo-experiments emulating the transverse momentum spectrum of the Higgs boson observed in collision data.

The expected p_T distribution of the reconstructed Higgs boson at detector level is obtained from fully simulated events in Powheg for the SM prediction. The statistical uncertainty on this prediction is negligible due to the high number $N = 3 \times 10^6$ of simulated events. The theoretically predicted p_T distributions for different Wilson coefficients are obtained by reweighting the existent Powheg sample. This reweighting procedure was explained in section 4.3.2.

In this analysis, the additional presence of the coupling operators O_i is tested for each Wilson coefficient C_i separately while the other coefficients are set to zero. In this approach, the differential cross sections are composed of the operator terms given in (2.57). They depend on $\frac{C_1}{\Lambda}$ for O_1 and $\frac{C_i}{\Lambda^3}$ for $i \geq 2$. In the following, this fraction is considered as one single parameter and for simplicity in some cases also denoted by C_i. For each coupling operator O_i, the reweighting is performed for a set of discrete Wilson coefficients C_i, while $C_i = 0$ corresponds to the SM prediction. The number of values for each coefficient, for which the reweighting can be performed, is limited due to the high number of event weights that have to be calculated and stored. For each of the considered coupling operators O_i with $i \geq 2$, 180 Wilson coefficients are tested, corresponding to $180 \cdot 3 \times 10^6 = 5.4 \times 10^8$ event weights.

The choice of an appropriate parameter range was evaluated for each Wilson coefficient C_i in an iterative procedure: A particular parameter range was chosen, the SM Powheg sample was reweighted for this choice of parameters and the sensitivity given these parameters was investigated using the strategy described in the following sections. Based on the determined sensitivity, the parameter range was adjusted and the procedure was repeated until

the sensitivity was found to be such that parts of the parameter range could be excluded at 90% confidence level. It was found that this is not possible for the Wilson coefficient C_1. The problems dealing with the coupling operator O_1 are discussed later in this chapter.

This chapter is structured as follows: First, the general strategy for the generation of pseudo-experiments is explained. Afterwards, the distributions of the likelihood estimators $\widehat{C}_i$ are investigated using pseudo-experiment that were generated for the hypothesis that the SM is realised in data. Based on these results, the procedure to evaluate the estimator distributions using pseudo-experiments for different Wilson coefficients is developed and described in the subsequent section. These predictions are then taken to evaluate the Neyman confidence belts for the Wilson coefficients and are used in the following chapter to interpret the results obtained with the p_T distribution observed in 2012 collision data. Additionally, the influence of systematic uncertainties is studied. In the last section of this chapter, the procedure to derive also Bayesian confidence intervals is described.

8.1. Generation of Pseudo-experiments

The measurement of the Higgs boson p_T distribution is simulated using pseudo-experiments based on simulated events. Since the pseudo-experiments have to emulate the actual measurement, they have to reflect all relevant steps of the measurement. This includes the physical processes in the proton-proton collisions, the data taking with the ATLAS detector, the event selection and the background estimation. All steps concerning the physical processes, the ATLAS detector and the event selection are covered by the selection of signal events simulated with POWHEG. This also holds for the reweighted events. By using the binning given in (6.1), the predicted event yields in every Higgs boson p_T-bin i at detector level can therefore be predicted for several Wilson coefficients with negligible statistical uncertainty.

Indeed, the pseudo-experiments also have to reflect the statistical uncertainties that are related to the observed distributions. For the observed transverse momentrum spectrum of the Higgs boson, which had to be extracted from an overwhelming amount of events attributed to background processes, this particularly concerns the statistical uncertainty from the signal+background fit. These statistical uncertainties are represented by the uncertainties on the signal yield parameters N_{sig} given in table 6.2. It is found that they are much larger than it would be the case for a Poisson-distributed error, for which an uncertainty of approximately $\sqrt{N_{\text{sig}}}$ would be expected. Moreover, considering the estimated signal and background yields with their respective fit uncertainties in the given table, one can infer that the signal yield uncertainty ΔN_{sig} is affected by the number of background events N_{back} in the particular bin more than by the actual observed number of signal events N_{sig}. Consequently, the absolute uncertainty on the signal yield parameter is considered for the generation of the pseudo-experiments. The statistical uncertainty attributed to the resonant background events (dominated by VBF) which are subtracted from data is negligible compared to the fit uncertainty and therefore not considered.

In order to reflect the fit uncertainties ΔN_{sig} in the pseudo-experiments, a reasonable probability density function, by which the event yields in each of the seven p_T^H-bins are distributed,

has to be assumed. Each pseudo-experiment must be represented by a generated Higgs boson p_T distribution which is binned according to (6.1). The fluctuation of the signal yield in each bin must be distributed according to the probability density function that is supposed to describe the fit uncertainty. From the fit results concerning the background estimation in collision data, given in table 6.2, it can be seen that the extracted signal yields are for some bins compatible with the no signal hypothesis within 2σ. Consequently, if one would assume the bin contents to be Gaussian distributed, even negative signal events would have to be considered. However, negative signal yield parameters are not permitted in the signal+background fit which was discussed in section 6.3 and would therefore not represent a consistent treatment of the fit uncertainties. As a consequence, the extracted signal yields are assumed to be distributed following a log-normal distribution which ensures positive signal yield parameters. The log-normal distribution is parametrised by two parameters, $\tilde{\phi}$ and κ, and is defined by [90]

$$f(\phi; \tilde{\phi}, \kappa) = \frac{1}{\sqrt{2\pi}\log\kappa} \exp\left(-\frac{(\log(\phi/\tilde{\phi}))^2}{2(\log\kappa)^2}\right)\frac{1}{\phi} . \tag{8.1}$$

The parameter $\tilde{\phi}$ characterises the position of the distribution while κ represents its width. However, both parameters are not identical to the expectation value μ nor to the variance σ^2 of the distribution, which can be shown to satisfy

$$\mu = \tilde{\phi} \cdot \exp\left[\frac{1}{2}(\log\kappa)^2\right] , \tag{8.2}$$

$$\sigma^2 = \exp\left[2\log\tilde{\phi} + (\log\kappa)^2\right] \cdot \left(\exp\left[(\log\kappa)^2\right] - 1\right) . \tag{8.3}$$

Solving these two equations with respect to the parameters $\tilde{\phi}$ and κ then gives

$$\tilde{\phi} = \mu \cdot \left[\frac{\sigma^2}{\mu^2} + 1\right]^{-1/2} , \tag{8.4}$$

$$\kappa = \exp\left[\log\left(\frac{\sigma^2}{\mu^2} + 1\right)\right]^{1/2} . \tag{8.5}$$

In each bin, μ corresponds to the expectation value predicted by the simulated events. For σ, the uncertainty ΔN_{sig} on the signal yield extracted from the fit to the diphoton mass spectra in data is inserted. In this way, a large number of pseudo-experiments can be generated imitating the actual experiment. The generation of pseudo-experiments assumes that a particular theoretical hypothesis for the gluon fusion vertex is realised in data. Concerning this analysis, pseudo-experiments can be generated for each Wilson coefficient C_i that was considered in the reweighting procedure. In the following section, the generation of pseudo-experiments for the assumption that the SM is realised in data is discussed.

8.2. Studies with Standard Model Pseudo-experiments

The sensitivity of the analysis is tested with 5.0×10^4 pseudo-experiments that are generated under the hypothesis that the SM is realised in data. Figure 8.1 shows the p_T distribution of an example pseudo-experiment in comparison to the SM prediction from POWHEG with negligible statistical uncertainty.

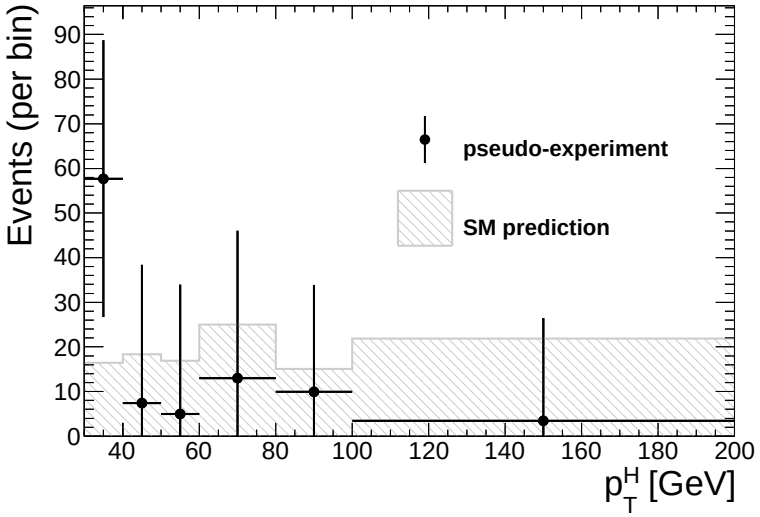

Figure 8.1.: *Higgs boson p_T spectrum at detector level observed in one exemplary SM pseudo-experiment and the high precision prediction for the SM hypothesis. Considered are events that pass all selection criteria applied in this analysis. The uncertainties indicated for the pseudo-experiment distribution are the values for ΔN_{sig} observed for the fit in data and entered the parameters of the log-normal distribution applied for the generation of the SM pseudo-experiments. The pseudo-experiment shown contains a total number of 97 events.*

The generated SM pseudo-experiments are compared in a binned maximum likelihood (ML) fit and in a binned extended maximum likelihood (EML) fit to the Higgs boson p_T distributions predicted using the (reweighted) simulated $H \to \gamma\gamma$ events. The (extended) maximum likelihood fits yield estimators $\widehat{C_i}$ for the Wilson coefficients C_i. Using the pseudo-experiments generated under the hypothesis that the SM is realised in data, corresponding to $C_i = 0$, it is tested whether the likelihood estimators yield average values equal to zero, meaning $\langle \widehat{C_i} \rangle = 0$.

The method of maximum likelihood is explained in more detail in the appendix A. Using the notation chosen in the appendix, the parameter set $\boldsymbol{\theta}$ here is represented by the set of Wilson coefficients C_i, while the Higgs transverse momentum p_T^H is the considered observable x. For each p_T^H-bin, the predicted fractional bin content $p_i(C_j)$ is obtained using the prediction of the (reweighted) simulated gluon fusion signal events.

According to (A.4), for the non-extended likelihood, the theoretical prediction ν_i for the event yield in bin i, is normalised to the number of events observed in the considered pseudo-experiment n_{tot},

$$\nu_i(C_j) = n_{\text{tot}} \cdot p_i(C_j) \ . \tag{8.6}$$

In the extended binned maximum likelihood fit, the theory prediction is normalised to the theoretically predicted total number of events $\nu_{\text{tot}}(C_j)$ (see equation (A.5))

$$\nu_i(C_j,\, \nu_{\text{tot}}) = \nu_{\text{tot}}(C_j) \cdot p_i(C_j)\ . \tag{8.7}$$

The probability density function for the distribution of the event yield n_i in every bin i of a particular pseudo-experiment is given by the log-normal distribution, which was assumed for the generation of the pseudo-experiments (see (8.1)). Using the aforementioned parametrisation by the mean μ and the variance σ^2, only the expectation μ depends on the values for the Wilson coefficients C_j since the variance σ^2 is taken from the uncertainties observed in data, so that

$$\begin{aligned} f_i(n_i) &= f_i(n_i; \mu_i = \nu_i(C_j), \sigma_i^2) && \text{non-extended ML} \\ f_i(n_i) &= f_i(n_i; \mu_i = \nu_i(C_j,\, \nu_{\text{tot}}), \sigma_i^2) && \text{extended ML} \end{aligned} \tag{8.8}$$

with the log-normal function f as defined in (8.1). The likelihood function $\mathcal{L}(C_j)$ for a particular pseudo-experiment with bin contents $\boldsymbol{n} = (n_1, n_2, \ldots, n_N)$ is then given as the product of the individual probability density functions f_i for each bin, so that the log-likelihood functions read

$$\log \mathcal{L}(\boldsymbol{n};\, C_j) = \sum_{i=1}^{N} \log f_i(n_i; \mu_i = \nu_i(C_j)) \tag{8.9}$$

$$\log \mathcal{L}^{\text{ext}}(\boldsymbol{n};\, C_j) = \sum_{i=1}^{N} \log f_i(n_i; \mu_i = \nu_i(C_j, \nu_{\text{tot}})) \tag{8.10}$$

which is also derived for the general case in (A.7) and (A.8).

In figures 8.2 and 8.3, the distributions of the non-extended and the extended maximum likelihood estimators $\widehat{C_i}$ for the Wilson coefficients from the many pseudo-experiments are shown. Only a reduced number of Wilson coefficients and pseudo-experiments was used in the fit of the operator O_1 since no sensitivity to determine the estimator $\widehat{C_1}$ in a local maximum of the log-likelihood function was found in the non-extended likelihood fit. This can be seen by the fact that most of the pseudo-experiments give fit values at the low and high limit of the considered C_1 parameter range. The parameter range would therefore have to be increased to find the likelihood estimators in a local maximum of the likelihood function and not in a boundary maximum.

For the Wilson coefficient C_1, the sensitivity of the extended likelihood is completely attributed to the predicted and observed total event yield. This circumstance was confirmed in a fit using only one p_T-bin for all events which did not lead to a considerable difference in the distribution of the extended maximum likelihood estimators for this Wilson coefficient.

Thus, it was not considered as reasonable to further increase the C_1 coefficient range in the non-extended likelihood fit, although most of the estimators were placed at the edges of the considered parameter range. An increased parameter range would include values that can be excluded based on the predicted event yield using the extended likelihood fit. Furthermore, for large values of C_1/Λ, the operator term $O_1 O_1^\dagger$ becomes dominant compared to the $O_{\text{SM}} O_1^\dagger$

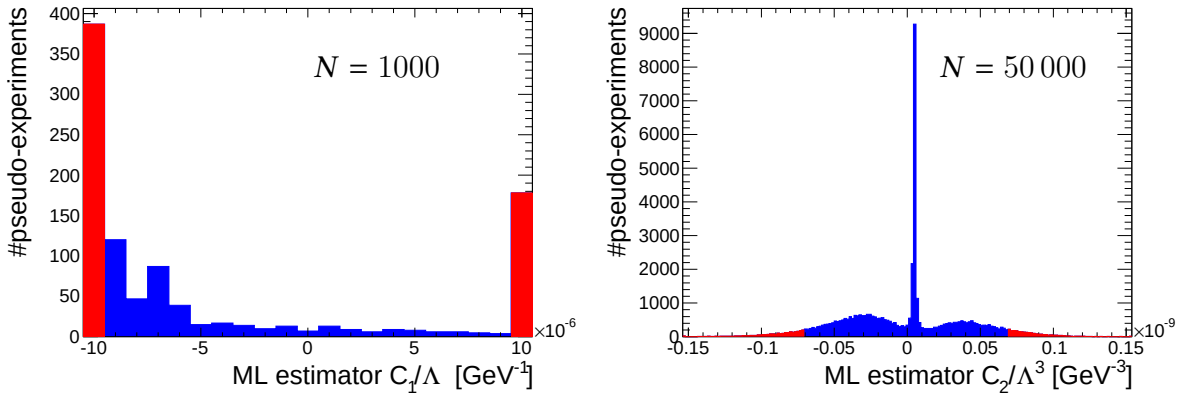

(a) $|O_{SM}|^2 + (C_1/\Lambda)\, O_{SM}O_1^\dagger + (C_1/\Lambda)^2|O_1|^2$ (b) $|O_{SM}|^2 + (C_2/\Lambda^3)\, O_{SM}O_2^\dagger + (C_2/\Lambda^3)^2|O_2|^2$

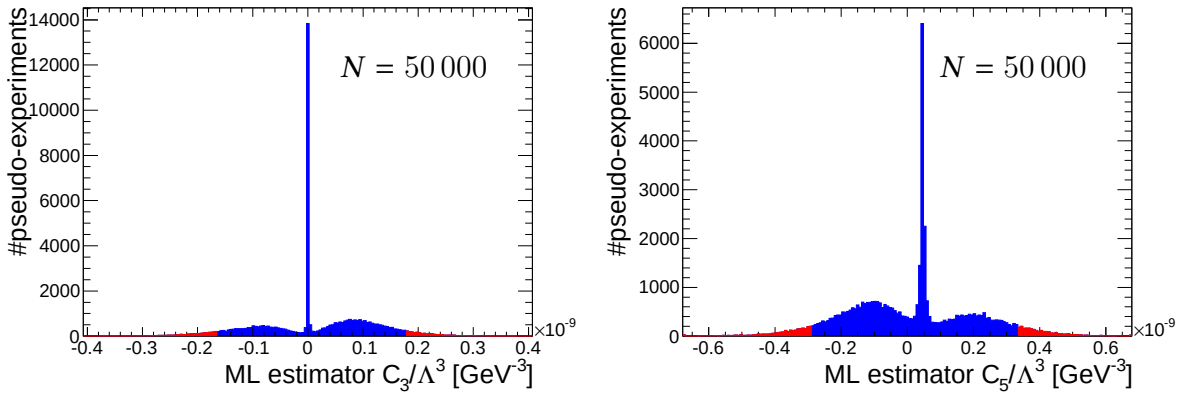

(c) $|O_{SM}|^2 + (C_3/\Lambda^3)\, O_{SM}O_3^\dagger + (C_3/\Lambda^3)^2|O_3|^2$ (d) $|O_{SM}|^2 + (C_5/\Lambda^3)\, O_{SM}O_5^\dagger + (C_5/\Lambda^3)^2|O_5|^2$

Figure 8.2.: *Maximum likelihood estimators for Wilson coefficients C_i for the admixture of the coupling operators O_i to the SM predicted cross sections fitted to SM pseudo-experiments. N gives the number of pseudo-experiments. The bins left (right) from the 5% (95%) quantiles are illustrated in red. The quantiles are illustrated approximatively since they can be placed between the bin edges while each bin is filled with one single colour. Fit results represented in the first and last bin in (a) indicate that the maximum likelihood estimator for the respective pseudo-experiment was found at boundaries of the considered parameter range, indicating that the true maximum likelihood estimator lies outside this range.*

and even the $O_{\mathrm{SM}}O_{\mathrm{SM}}^\dagger$ operator term.

The $O_1O_1^\dagger$ operator term is the dominant term when approximating the top quark loop induced Higgs-gluon coupling in an effective theory. Consequently, it is plausible that no exclusion limit on the Wilson coefficient C_1 can be determined by testing the shape of the Higgs boson p_T distribution for the presence of the O_1 operator in addition to the SM. The operator O_1 is also not further studied using the extended likelihood since this would not give any deeper insight to the gluon fusion coupling structure than any signal strength measurement.

Tables 8.1 and 8.2 give the mean values of the remaining distributions for $\widehat{C}_i$ shown in figures 8.2 and 8.3 together with the root mean square (RMS) and the statistical error on the mean value, given by RMS/$\sqrt{N}$. Additionally, the average of the 1σ uncertainty of all (extended)

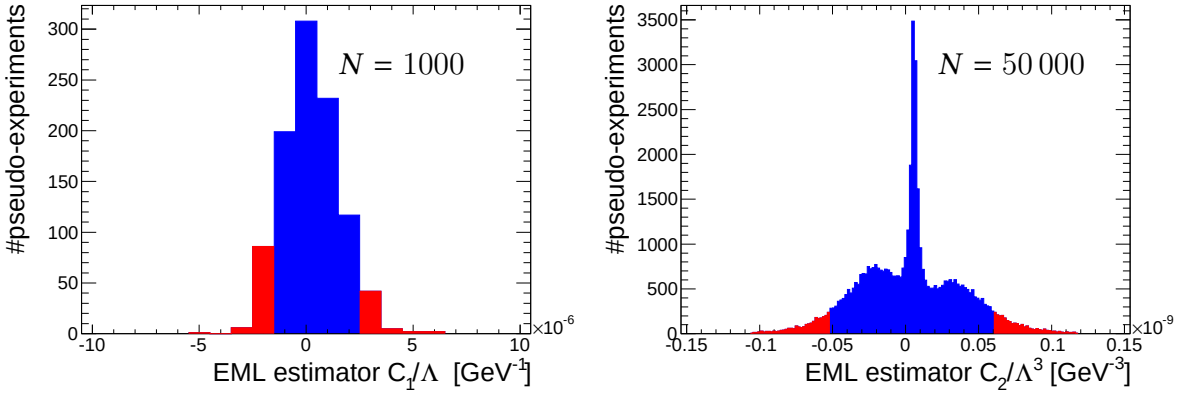

(a) $|O_{SM}|^2 + (C_1/\Lambda)\, O_{SM}O_1^\dagger + (C_1/\Lambda)^2|O_1|^2$ (b) $|O_{SM}|^2 + (C_2/\Lambda^3)\, O_{SM}O_2^\dagger + (C_2/\Lambda^3)^2|O_2|^2$

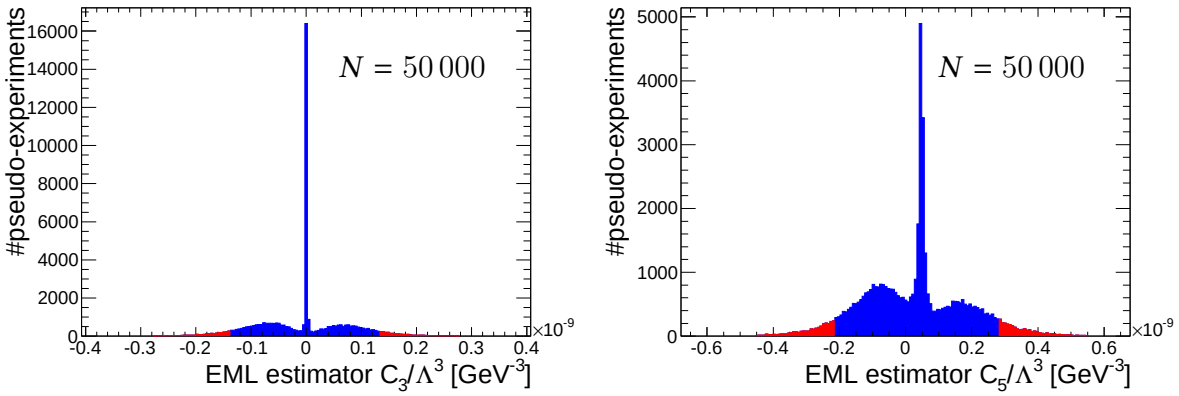

(c) $|O_{SM}|^2 + (C_3/\Lambda^3)\, O_{SM}O_3^\dagger + (C_3/\Lambda^3)^2|O_3|^2$ (d) $|O_{SM}|^2 + (C_5/\Lambda^3)\, O_{SM}O_5^\dagger + (C_5/\Lambda^3)^2|O_5|^2$

Figure 8.3.: *Extended maximum likelihood estimators on Wilson coefficients for the admixture of the coupling operators O_i to the SM predicted cross sections fitted to SM pseudo-experiments. N gives the number of pseudo-experiments. The bins left (right) from the 5% (95%) quantiles are illustrated in red. The quantiles are illustrated approximatively since they can be placed between the bin edges while each bin is filled with one single colour.*

maximum likelihood fits is given. This value is for each fit evaluated by reading off the Wilson coefficients $C_i^{1\sigma}$ for which counts $\log \mathcal{L}(C_i^{1\sigma}) = \log \mathcal{L}(\widehat{C}_i) - 1/2$. Details on this method (called graphical method) can be found e.g. in [80]. Two values $C_i^{1\sigma}$ are obtained in this way, for each likelihood curve the average difference of those two values to the (extended) maximum likelihood estimator $\widehat{C}_i$ is calculated representing a symmetrised uncertainty. The procedure is illustrated in figure 8.4. The tables 8.1 and 8.2 give the mean $\langle(\Delta \log \mathcal{L})_{1/2}\rangle$ of the obtained distribution.

From tables 8.1 and 8.2, it can be seen that the means of the observed (extended) maximum likelihood estimator distributions (see figures 8.2 and 8.3) are not compatible to $\langle\widehat{C}_i\rangle = 0$ within their statistical uncertainties. For an unbiased estimator, $\langle\widehat{C}_i\rangle = 0$ should hold when investigating SM pseudo-experiments. Moreover, for the limit of an infinite number of events in the experiment, the estimator distributions should follow a Gaussian probability density function. This is obviously not the case for the predicted event yield corresponding to an integrated luminosity of $\int \mathcal{L} = 20.7\,\mathrm{fb}^{-1}$. In the following, the reasons for the shape and the bias of the estimator distributions obtained with SM pseudo-experiments are investigated.

	Mean	RMS	RMS/$\sqrt{N}$	$\langle(\Delta \log \mathcal{L})_{1/2}\rangle$
C_2/Λ^3	-2.0×10^{-12}	4.3×10^{-11}	1.92×10^{-13}	3.1×10^{-11}
C_3/Λ^3	-1.05×10^{-11}	1.04×10^{-10}	4.65×10^{-13}	7.7×10^{-11}
C_3/Λ^3	1.16×10^{-11}	1.92×10^{-10}	8.58×10^{-13}	1.32×10^{-10}

Table 8.1.: *Mean value, RMS and uncertainty on the mean for the distribution of maximum likelihood estimators for C_i/Λ^3 in the fit to $N = 50000$ SM pseudo-experiments. Additionally, the average uncertainty $\langle(\Delta \log \mathcal{L})_{1/2}\rangle$ evaluated in every likelihood fit, as described in the text, is given. All values are in units of* GeV^{-3}.

	Mean	RMS	RMS/$\sqrt{N}$	$\langle(\Delta \log \mathcal{L})_{1/2}\rangle$
C_2/Λ^3	3.4×10^{-12}	3.4×10^{-11}	1.53×10^{-13}	2.4×10^{-11}
C_3/Λ^3	-4.9×10^{-12}	8.1×10^{-11}	3.63×10^{-13}	6.5×10^{-11}
C_5/Λ^3	2.67×10^{-11}	1.53×10^{-10}	6.86×10^{-13}	1.11×10^{-10}

Table 8.2.: *Mean value, RMS and uncertainty on the mean for the distribution of extended maximum likelihood estimators for C_i/Λ^3 in the fit to $N = 50000$ SM pseudo-experiments. Additionally, the average uncertainty $\langle(\Delta \log \mathcal{L})_{1/2}\rangle$ evaluated in every likelihood fit, as described in the text, is given. All values are in units of* GeV^{-3}.

For Gaussian distributed likelihood estimators, the values for the root mean square and $\langle(\Delta \log \mathcal{L})_{1/2}\rangle$ should give comparable values. However, as it can be seen in the given tables, the root mean square of the estimator distributions is for all fitted operators larger than the evaluated averaged uncertainty in each fit. This observation can be explained by the form of the example likelihood function shown in figure 8.4b. In some (extended) likelihood fits, two local maxima are observed. Since the fit uncertainty is read off around the largest of all local maxima (corresponding to minima in the $-\log \mathcal{L}$ function), as illustrated in figure 8.4b, the fit uncertainty is underestimated using this method. Consequently, the actually observed root mean square in the distribution of the (extended) maximum likelihood estimators gives larger values accounting for those double-maxima.

Likelihood curves with two local maxima are observed in many pseudo-experiments and for all considered Wilson coefficients C_i with $i \geq 2$. These likelihood curves with the characteristic of two local maxima are supposed to cause the sub-peaks left and right from the main peak in the likelihood estimator distributions shown in figures 8.2 and 8.3. The reason for this double-maxima structure of the likelihood function $\mathcal{L}(C_i)$ is therefore further investigated.

For this purpose, the predicted mean of the Higgs boson p_T distribution in the theoretical predictions is regarded within the considered parameter ranges for C_i. The dependence of the predicted mean transverse momentum of the Higgs boson on the Wilson coefficients is shown in figure 8.5. Note that the mean p_T was evaluated from the bin contents and positions of the binned theoretically predicted p_T distributions and is therefore most likely biased. However, this bias should not have a considerable influence on the shape of the curves which is interpreted here. It can be seen that a minimum of the mean transverse momentum of the Higgs boson is predicted for Wilson coefficient values near to the SM value of $C_i = 0$. Moreover, it is found that the positions of these local minima approximately match the posi-

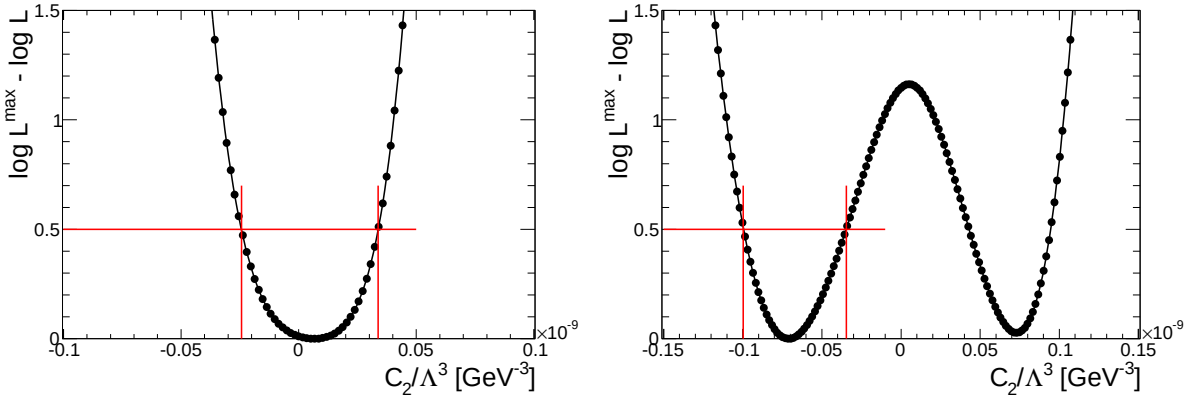

(a) *One local minimum* (b) *Two local minima*

Figure 8.4.: *Two exemplary* $(-\log\text{likelihood})$ *curves fitting the Wilson coefficient* C_2 *to SM pseudo-experiments. A* $(-\log\mathcal{L}(C_2))$*-curve with one local minima and a curve with two local minima are shown to illustrate the procedure evaluating the fit uncertainty.*

tions of the most likely (extended) likelihood estimators evaluated in figures 8.2 and 8.3. For pseudo-experiments with an average transverse momentum $\langle p_T^H \rangle$ smaller than the minimum mean transverse momentum which is found regarding the curves in figure 8.5, the (extended) likelihood estimators for all Wilson coefficients are supposed to most likely get assigned to the correspondingly observed position of the local minima in these curves. Furthermore, the parabolic form of the mean p_T dependencies in figure 8.5 has the characteristic that two different Wilson coefficients C_i are predicted to lead to the same average transverse momentum of the Higgs boson. This is a possible explanation for the observation of likelihood curves with two local maxima.

In the extended likelihood, the observed signal yield is considered in the likelihood function in addition to the shape of the distributions. Figure 8.6 therefore shows the predicted event yield depending on the Wilson coefficients C_i. However, these curves show the same parabolic form that was observed for the dependencies of the mean Higgs boson p_T on the Wilson coefficients. Consequently, the same conclusions concerning the impact on the shape of the likelihood curves and the distributions of the extended likelihood estimators can be drawn.

The parabolic form of the signal yield depending on the Wilson coefficients C_i indicates that the squared operator terms $O_i O_i^\dagger$ contribute significantly in the considered parameter range. Without taking into account these operator terms, the cross section contributions of the operator terms $|O_{\text{SM}}|^2 + C_i/\Lambda^3\, O_{\text{SM}} O_i^\dagger$ depend linearly on the Wilson coefficients C_i. Therefore, the cross section contribution of those two terms becomes negative for a particular Wilson coefficient $C_i \in \mathbb{R}$. The squared operator terms force the total cross sections to give positive values and cause the parabolic dependence of the event yields.

The observed dependencies for the predicted mean p_T^H and the predicted event yield on the Wilson coefficients can cause the double-maxima observed in the likelihood curves and therefore possibly explain the shape of the distributions for the maximum likelihood estimators. Additionally, it is investigated if the estimators are consistent meaning that they are asymptotically unbiased. The bias found for the predicted event yield corresponding to

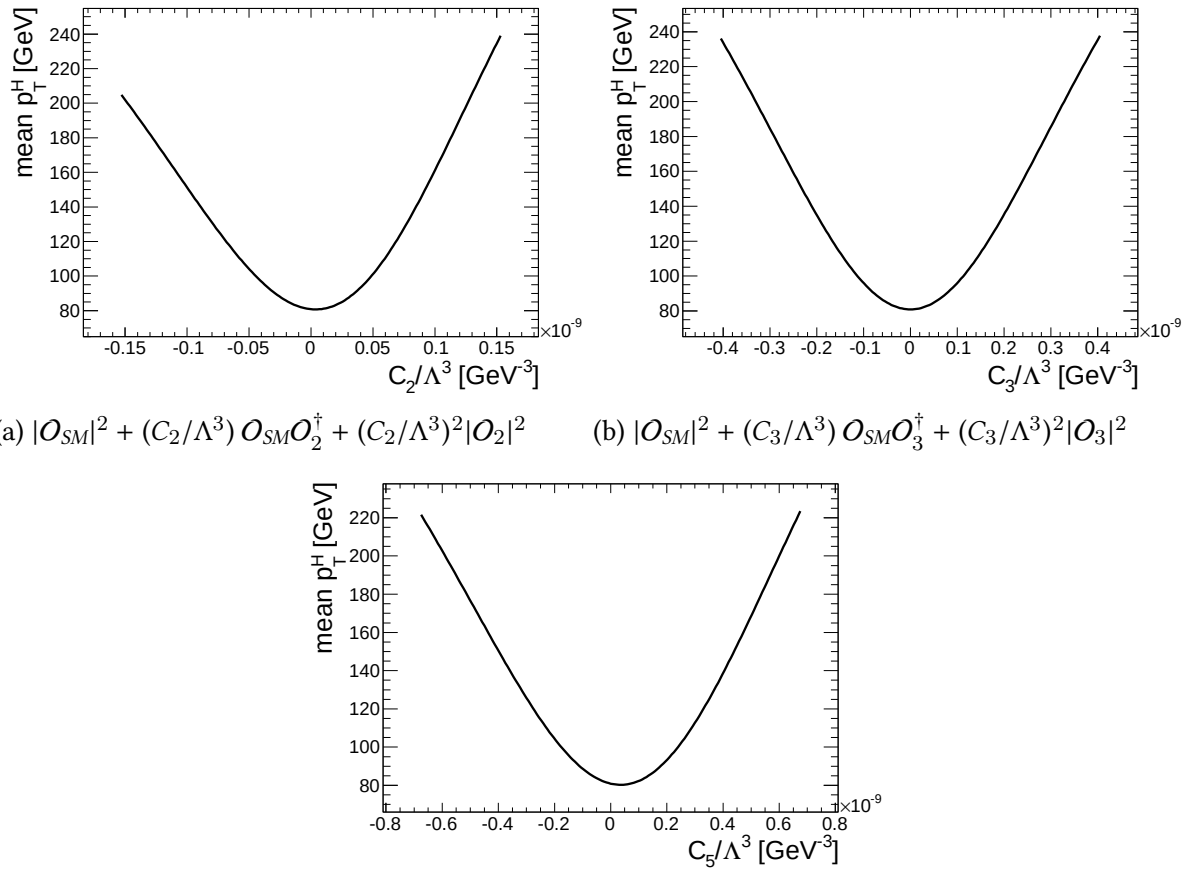

(a) $|O_{SM}|^2 + (C_2/\Lambda^3)\, O_{SM}O_2^\dagger + (C_2/\Lambda^3)^2|O_2|^2$ (b) $|O_{SM}|^2 + (C_3/\Lambda^3)\, O_{SM}O_3^\dagger + (C_3/\Lambda^3)^2|O_3|^2$

(c) $|O_{SM}|^2 + (C_5/\Lambda^3)\, O_{SM}O_5^\dagger + (C_5/\Lambda^3)^2|O_5|^2$

Figure 8.5.: *Mean Higgs transverse momentum in binned theoretical prediction depending on the Wilson coefficients C_i. The absolute p_T^H values are most likely biased due to the binning.*

the integrated luminosity of currently available collision data could then be attributed to the limited statistics of signal events in data.

For this investigation, the expectation value for the number of events in each pseudo-experiment is increased from the SM predicted value of ~ 118 events to $100\,000$. Tables 8.3 and 8.4 give the observed mean values of the estimator distributions for increased event yield in every pseudo-experiment. It can be seen that the observed mean values tend to zero by increasing the predicted event yield, though at different rates for the various coupling operators O_i. For the studies with $100\,000$ events per pseudo-experiment (see tables 8.3 and 8.4), a finer binning and adjusted parameter range for the Wilson coefficients was used. For a further increased number of events in each experiment, the estimators for the Wilson coefficients always yield $\widehat{C_i} = 0$ so that a further refined binning in the Wilson coefficients would be necessary for such a study, which was therefore not done here. The estimator distributions for the event yield increased to $100\,000$ events are shown in the appendix B.5.

As a result, the (extended) maximum likelihood estimators are biased but supposed to be consistent. Consequently, a strategy was developed to take into account the observed fit bias and to evaluate confidence intervals for the Wilson coefficients. This procedure is described in the following section.

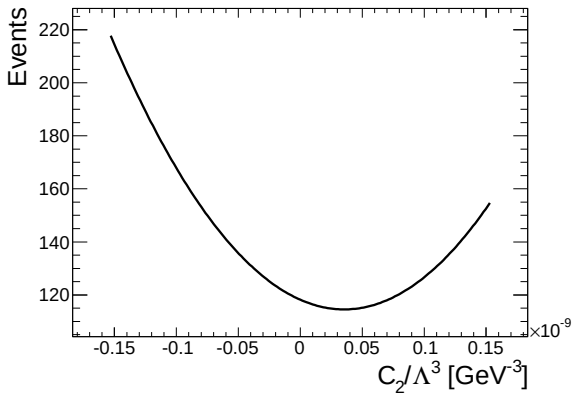

(a) $|O_{SM}|^2 + (C_2/\Lambda^3)\, O_{SM} O_2^\dagger + (C_2/\Lambda^3)^2 |O_2|^2$

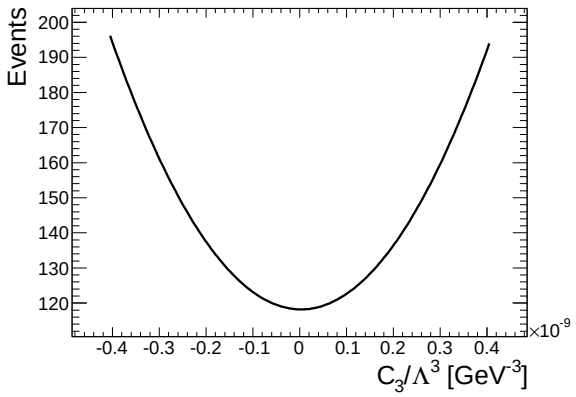

(b) $|O_{SM}|^2 + (C_3/\Lambda^3)\, O_{SM} O_3^\dagger + (C_3/\Lambda^3)^2 |O_3|^2$

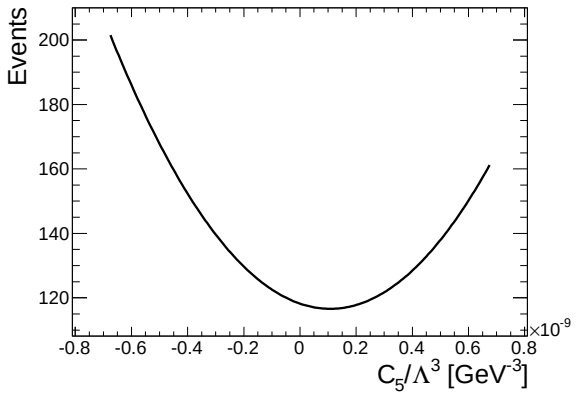

(c) $|O_{SM}|^2 + (C_5/\Lambda^3)\, O_{SM} O_5^\dagger + (C_5/\Lambda^3)^2 |O_5|^2$

Figure 8.6.: *Event yield in theoretical prediction depending on the Wilson coefficients C_i. The case $C_i = 0$ corresponds to the SM prediction of ~ 118 events.*

8.3. Frequentist Confidence Intervals for Wilson Coefficients

The strategy to derive confidence intervals for the Wilson coefficients uses the Neyman construction [89]. Further details on this method can be found e.g. in [80]. The goal of this analysis with pseudo-experiments using simulated events is therefore the construction of Neyman confidence belts. The Neyman confidence belts give confidence intervals for the Wilson coefficients C_i for each possible outcome of the measurement, which is here represented by the (extended) maximum likelihood estimator $\widehat{C}_i$. For this procedure, the coverage probability $1 - \alpha = 90\%$ is specified. From the confidence belts, which are evaluated in this section, two values $C_i^{5\%}(\widehat{C}_i)$ and $C_i^{95\%}(\widehat{C}_i)$ can be determined for each possible estimator $\widehat{C}_i$ that satisfy

$$P(C_i^{5\%} \leq C_i \leq C_i^{95\%}) = 1 - \alpha = \int_{C_i^{5\%}}^{C_i^{95\%}} f(\widehat{C}_i;\, C_i)\, \mathrm{d}\widehat{C}_i \tag{8.11}$$

with the probability distribution of the (extended) maximum likelihood estimators $f(\widehat{C}_i;\, C_i)$.

	Average number of events per pseudo-experiment	
	118	100000
C_2/Λ^3	-2.00×10^{-12}	1.25×10^{-13}
C_3/Λ^3	-1.05×10^{-11}	4.52×10^{-13}
C_5/Λ^3	1.16×10^{-11}	8.16×10^{-15}

Table 8.3.: *Mean of maximum likelihood estimators for increased number of events per pseudo-experiment. For the SM prediction of 118 events, 50000 pseudo-events were generated whereas for the increased event yield, 5000 pseudo-experiments are used. All values are in units of* GeV^{-3}. *The corresponding estimator distributions are shown in the appendix B.5.*

	Average number of events per pseudo-experiment	
	118	100000
C_2/Λ^3	3.40×10^{-12}	3.96×10^{-15}
C_3/Λ^3	-4.93×10^{-12}	4.16×10^{-13}
C_5/Λ^3	2.67×10^{-11}	5.12×10^{-15}

Table 8.4.: *Mean of extended maximum likelihood estimators for increased number of events per pseudo-experiment. For the SM prediction of 118 events, 50000 pseudo-events were generated whereas for the increased event yield, 5000 pseudo-experiments are used. All values are in units of* GeV^{-3}. *The corresponding estimator distributions are shown in the appendix B.5.*

In the previous section, the distributions of the (extended) maximum likelihood estimators were investigated using SM pseudo-experiments. In figures 8.2 and 8.3, the 5% quantile $\widehat{C}_i^{\,5\%}$ and the 95% quantile $\widehat{C}_i^{\,95\%}$ of the distributions of the (extended) maximum likelihood estimators evaluated with SM pseudo-experiments were illustrated approximately. These values are defined by

$$\begin{aligned} 1 - \alpha/2 &= \int_{-\infty}^{\widehat{C}_i^{\,5\%}} f(\widehat{C}_i;\, C_i)\, \mathrm{d}\widehat{C}_i \\ 1 - \alpha/2 &= \int_{\widehat{C}_i^{\,95\%}}^{\infty} f(\widehat{C}_i;\, C_i)\, \mathrm{d}\widehat{C}_i \,. \end{aligned} \tag{8.12}$$

In order to derive the aforementioned confidence belts using the Neyman construction [89], the likelihood fits using SM pseudo-experiments, as described in the previous section, must be repeated for pseudo-experiments that assume a particular Wilson coefficient $C_i \neq 0$ to be realised in data.

For each Wilson coefficient C_i, pseudo-experiments are generated in a defined step width for the coefficient values. Table 8.5 gives the step widths of Wilson coefficient values for which pseudo-experiments were generated. In addition, the parameter range for each Wilson coefficient C_i and the finer binning of the Wilson coefficients for the theoretically predicted p_T^H distributions, that are used for the maximum likelihood fit, are given in this table. For each coupling operator, 50000 pseudo-experiments are generated for 47 Wilson coefficients $C_i \in \mathbb{Q}$ (including $C_i = 0$) while 180 Wilson coefficients are considered in the likelihood fit.

	Range for $\pm C_i$ $[1 \times 10^{-10}\,\mathrm{GeV}^{-3}]$	step width in (E)ML fit $[1 \times 10^{-12}\,\mathrm{GeV}^{-3}]$	interval for confidence belts $[1 \times 10^{-11}\,\mathrm{GeV}^{-3}]$
C_2/Λ^3	1.5385	1.70	0.51
C_3/Λ^3	4.0725	4.50	1.35
C_5/Λ^3	6.7875	7.50	2.25

Table 8.5.: *Parameter ranges and binning for Wilson coefficients in the likelihood fit and for the generation of pseudo-experiments.*

For each set of generated pseudo-experiments, that assume a particular true coefficient C_i, the maximum likelihood and the extended maximum likelihood fit are performed. From the obtained distribution of the (extended) maximum likelihood estimators $\widehat{C}_i$, the 5% and 95% quantiles are determined as defined in (8.12). A linear interpolation between the discrete values of Wilson coefficients, that were tested in the likelihood fits, is used for the calculation of these quantiles. Using this procedure, intervals including 90% of the (extended) maximum likelihood estimators $\widehat{C}_i$ are evaluated for various realisations of Wilson coefficients in data here represented by the pseudo-experiments. The union of these intervals for all values C_i is known as the Neyman confidence belt [80].

Figure 8.7 shows example probability distributions $f(\widehat{C}_i;\, C_i)$ of EML estimators for two hypothesised values of the Wilson coefficient C_2. For both distributions, the 5% and 95% quan-

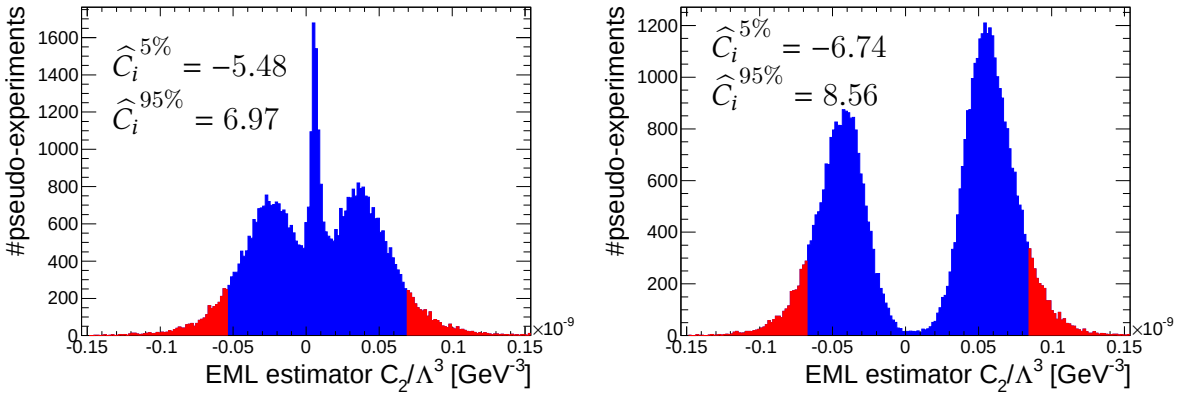

(a) $C_2^{\mathrm{true}} = 2.55 \times 10^{-11}\,\mathrm{GeV}^{-3}$ (b) $C_2^{\mathrm{true}} = 5.10 \times 10^{-11}\,\mathrm{GeV}^{-3}$

Figure 8.7.: *EML estimator distribution for two different values of the Wilson coefficient C_2 realised in the $N = 50000$ pseudo-experiments. The 5% and 95% quantiles are shown approximatively since all bins are filled in one colour. The more precise numerical values for the quantiles denoted in the plots are given in units of $1 \times 10^{-11}\,\mathrm{GeV}^{-3}$.*

tiles are again illustrated approximatively (without the linear interpolation). The distribution in figure 8.7b illustrates a problem occurring while applying the aforementioned procedure: For a hypothesized Wilson coefficient of $C_2 = 5.1 \times 10^{-11}\,\mathrm{GeV}^{-3}$, the extended maximum likelihood estimators additionally peak around $C_2 = -5 \times 10^{-11}\,\mathrm{GeV}^{-3}$. The same behaviour can be observed in the non-extended likelihood fit and for all considered Wilson coefficients. The the second peak at negative values is also supposed to be explained by the dependencies of the predicted mean p_T^H and the event yield on the Wilson coefficients C_i. These dependen-

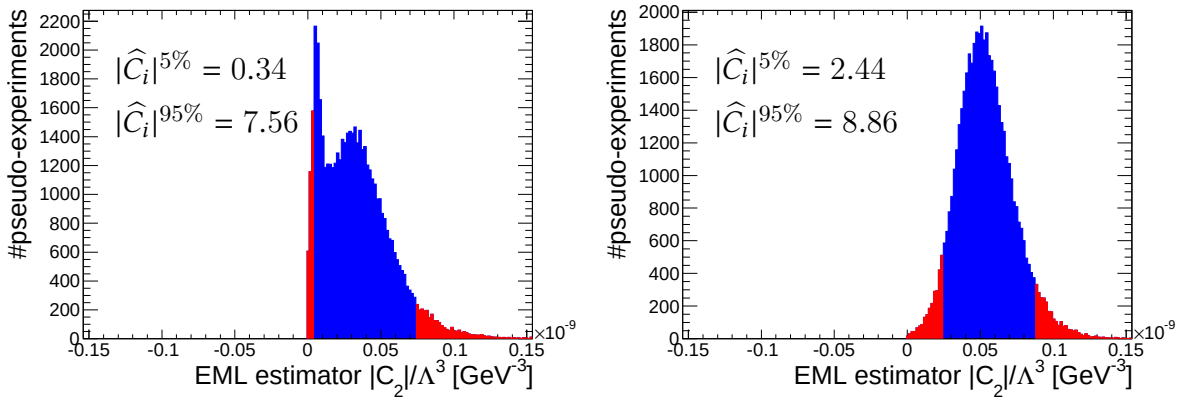

(a) $C_2^{\text{true}} = 2.55 \times 10^{-11}\ \text{GeV}^{-3}$ (b) $C_2^{\text{true}} = 5.10 \times 10^{-11}\ \text{GeV}^{-3}$

Figure 8.8.: *Distribution of absolute values of EML estimators for two different values of the Wilson coefficient C_2 realised in the $N = 50000$ pseudo-experiments. The 5% and 95% quantiles are shown approximatively since all bins are filled in one colour. The more precise numerical values for the quantiles denoted in the plots are given in units of $1 \times 10^{-11}\ \text{GeV}^{-3}$.*

cies were shown in figures 8.5 and 8.6, respectively. Considering these curves, it can be seen that they are not injective and therefore there is an ambiguity of Wilson coefficients for a given value of the mean transverse momentum of the Higgs boson or a given value of the event yield. This ambiguity is supposed to lead to the second peak seen in the probability density functions of the likelihood estimators. This leads to the situation that for $C_i \neq 0$, the range between the 5% quantile and the 95% quantile of the estimator distributions $f(\widehat{C}_i;\, C_i)$ gets quite large. Moreover, $\widehat{C}_i = 0$ is included in this range although there is a clear minimum of the estimator distributions at this value, which can be seen in the example in figure 8.7b.

For the further analysis, it was therefore decided to only consider absolute values $|\widehat{C}_i|$. Technically, the (extended) maximum likelihood fits are still permitted to yield negative estimators, but the quantiles are evaluated using the probability distributions $f(|\widehat{C}_i|;\, C_i)$. Figure 8.8 shows the distributions for $|\widehat{C}_i|$ using the same Wilson coefficients as in figure 8.7. Considering the distribution $f(|\widehat{C}_i|;\, C_i)$ shown in figure 8.8b, it can be seen that it is now possible to determine a reasonable low exclusion limit on the absolute value of the extended likelihood estimator $\widehat{C}_2$ with 90% probability. Though, the SM expectation value $|\widehat{C}_i| = 0$ is the left parameter limit in this procedure.

Due to the discrete binning of possible estimators that can be obtained in the (extended) maximum likelihood fits, a likelihood estimator $|\widehat{C}_i|$ has the intrinsic accuracy of $\pm(1/2)\Delta|\widehat{C}_i|$ with $\Delta|\widehat{C}_i|$ denoting the step width of coefficient values used in the reweighting procedure, given in the second column of table 8.5. As stated before, a linear interpolation between the discrete values of the (extended) likelihood estimators $\widehat{C}_i$, more precisely in the range $[|\widehat{C}_i| - (1/2)\Delta|\widehat{C}_i|\,,\ |\widehat{C}_i| + (1/2)\Delta|\widehat{C}_i|]$, was used to determine the quantiles of the estimator distributions. Therefore, if more than 10% of the estimators give $|\widehat{C}_i| = 0$, the linear interpolation starting at $-(1/2)\Delta|\widehat{C}_i|$ gives a negative value for the 5% quantile although the distribution for $|\widehat{C}_i|$ was considered. The binning in the Wilson coefficients is therefore not fine enough to give a statistical appropriate value for the 5% quantile or the 95% quantile if more than 5% of the events are in the first or respectively in the last bin of the consid-

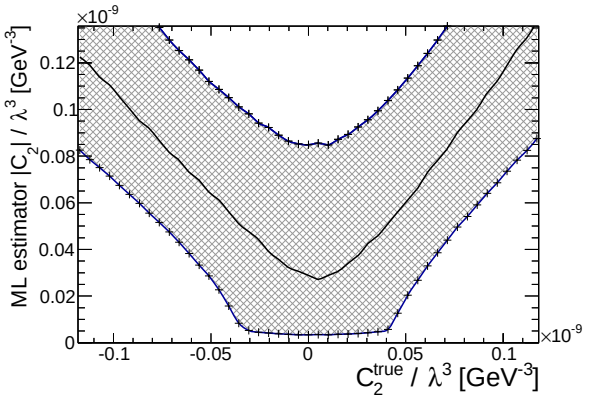

(a) $|O_{SM}|^2 + (C_2/\Lambda^3)\, O_{SM}O_2^\dagger + (C_2/\Lambda^3)^2|O_2|^2$

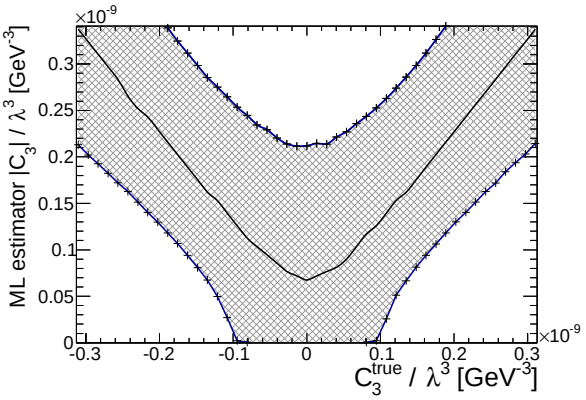

(b) $|O_{SM}|^2 + (C_3/\Lambda^3)\, O_{SM}O_3^\dagger + (C_3/\Lambda^3)^2|O_3|^2$

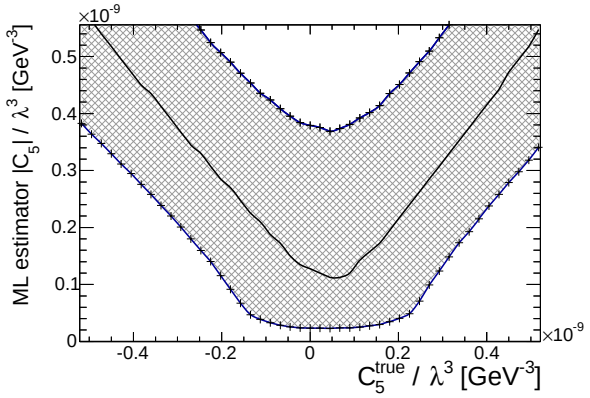

(c) $|O_{SM}|^2 + (C_5/\Lambda^3)\, O_{SM}O_5^\dagger + (C_5/\Lambda^3)^2|O_5|^2$

Figure 8.9.: *Neyman confidence belts at 90% C.L. for Wilson coefficients evaluated in non-extended likelihood fit. The lower curve is determined by the 5% quantiles of the likelihood estimator distributions, the upper curve by the 95% quantiles (both dark blue). The black curve between the quantile curves represents the median of the estimator distributions.*

ered parameter range for $\widehat{C}_i$. If this is the case, the quantiles are nevertheless calculated, but the obtained curves representing the 5% and 95% quantiles are only considered in parameter ranges excluding this binning problem.

Figures 8.9 and 8.10 show the Neyman confidence belts (in the following referred to as gauge curves) for the estimators $|\widehat{C}_i|$ which are evaluated using the non-extended and the extended maximum likelihood fit, respectively. The points on the upper curve are determined by the 95% quantiles of the (extended) likelihood estimator distributions, the points on the lower curve by the 5% quantiles. The line between these curves represents the median of the estimator distributions. It can be seen that for some $|\widehat{C}_i| \approx 0$, empty intervals of zero length are obtained since these estimator values are for all estimator distributions $f(|\widehat{C}_i|;\, C_i)$ lower than the determined 5% quantile. These empty intervals are possible for the Wilson coefficients C_2 and C_5, while for the coefficient C_3, the 5% quantile curve intersects the horizontal line at $\widehat{C}_i = 0$ (here corresponding to the x-axis). Empty confidence intervals are avoided by interpreting fit values using the Bayesian method, which is described in section 8.4.

The gauge curves are interpreted as follows: The Wilson coefficients C_i are fitted to the Higgs boson p_T spectrum observed in the data taken with the ALTAS detector. For each

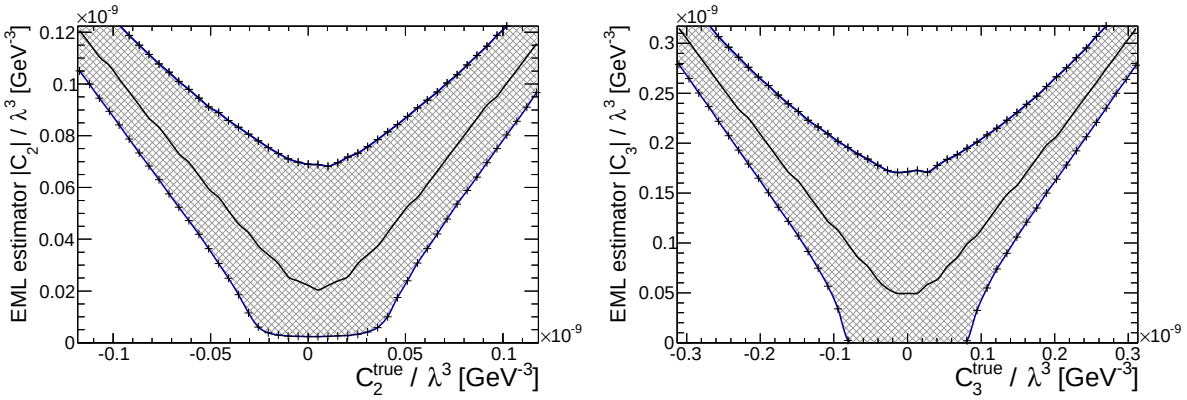

(a) $|O_{SM}|^2 + (C_2/\Lambda^3)\, O_{SM}O_2^\dagger + (C_2/\Lambda^3)^2|O_2|^2$ (b) $|O_{SM}|^2 + (C_3/\Lambda^3)\, O_{SM}O_3^\dagger + (C_3/\Lambda^3)^2|O_3|^2$

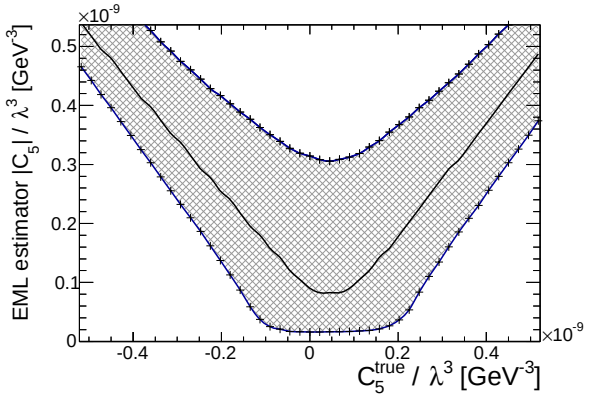

(c) $|O_{SM}|^2 + (C_5/\Lambda^3)\, O_{SM}O_5^\dagger + (C_5/\Lambda^3)^2|O_5|^2$

Figure 8.10.: *Neyman confidence belts at 90% C.L. for Wilson coefficients evaluated in the extended likelihood fit. The lower curve is determined by the 5% quantiles of the extended likelihood estimator distributions, the upper curve by the 95% quantiles (both dark blue). The black curve between the quantile curves represents the median of the estimator distributions.*

of the Wilson coefficients C_2, C_3 and C_5, a value for the (extended) maximum likelihood estimator $|\widehat{C}_i|$ is obtained. This value for $|\widehat{C}_i|$ is then evaluated at the y-axis of the gauge curve. The limits of the confidence interval for each of the Wilson coefficients C_i are then given by the Wilson coefficients for which the gauge curve boundaries intersect $y = |\widehat{C}_i|$. Consequently, the y-value of the upper gauge curve for $C_i^{\text{true}} = 0$ corresponds to the highest estimator value that can be obtained in the (extended) likelihood fit to data so that the SM predicted value $C_i = 0$ is still contained in the evaluated confidence interval. The coverage probability of 90% states that 90% of the confidence intervals obtained for (hypothetically) repeated measurements cover the true parameter value C_i.

Additionally, it is possible to give expected confidence intervals for the Wilson coefficients C_i assuming that the SM is realised in data. These intervals can be evaluated in the following way: The median of the estimator distributions (in figures 8.9 and 8.10 illustrated by the middle curve) is evaluated at $C_i^{\text{true}} = 0$ representing the expected (extended) maximum likelihood estimator $\widehat{C}_i^{\text{SM}}$. The expected confidence interval limits for the SM realisation are then determined by evaluating the gauge curve at this estimator $\widehat{C}_i^{\text{SM}}$. The expected confidence limits obtained in this way are given in table 8.6.

	low ML limit $[1 \times 10^{-11}\,\mathrm{GeV}^{-3}]$	high ML limit $[1 \times 10^{-11}\,\mathrm{GeV}^{-3}]$	low EML limit $[1 \times 10^{-11}\,\mathrm{GeV}^{-3}]$	high EML limit $[1 \times 10^{-11}\,\mathrm{GeV}^{-3}]$
C_2/Λ^3	-5.13	5.79	-3.86	4.95
C_3/Λ^3	-13.51	13.57	-10.37	10.48
C_5/Λ^3	-21.34	29.62	-16.01	25.29

Table 8.6.: *Expected frequentist confidence intervals assuming the SM to be realised in data. The intervals are evaluated from the Neyman confidence belts in the procedure given in the text. Results are shown for the non-extended ML fit and the extended ML fit.*

The evaluation of frequentist confidence intervals for the Wilson coefficients described in this section concerned the nominal analysis without considering any uncertainties. In section 6.4, two alternative approaches were described concerning the treatment of resonant background. For the approach using a tightened event selection in order to suppress VBF Higgs boson production, separate gauge curves are produced considering the modified selection criteria. The gauge curves for this approach are given in section 9.2.2. For the ansatz to subtract the predicted Higgs boson background events according to the observed inclusive signal strength, the gauge curves derived in this section can be used to interpret the likelihood fit to the modified Higgs boson p_T distribution extracted from data. The gauge curves do not change since the statistical uncertainties attributed to the resonant background events were neglected in the studies using pseudo-experiments.

The treatment of systematic uncertainties to be considered by the confidence intervals is described in the following subsection.

8.3.1. Systematic Uncertainties

The systematic uncertainties which are considered in this analysis and their impact on the Higgs boson transverse momentum are described in chapter 7. In this section, the procedure to investigate the influence of these systematic uncertainties on the results presented in this thesis is explained. The goal of these studies is to give confidence intervals for the Wilson coefficients that consider all investigated systematic variations. In addition, the relative impact of each individual systematic uncertainty is addressed.

In this procedure, the Neyman confidence belts described in section 8.3 are produced for each systematic variation separately. Therefore, the theoretical predictions of the Higgs transverse momentum considered in the (extended) likelihood fit are evaluated for each systematic variation and Wilson coefficient C_i. The pseudo-experiments, however, are not affected by the variations within the systematic uncertainties because of two reasons. First, they emulate the measurement of the Higgs transverse momentum with the ATLAS detector and the actual data is not varied, either. Secondly, the change in the theoretical prediction for the systematic variation is assessed, for the same observed p_T spectrum in data. Note that changing the theoretical predictions and the pseudo-experiments at the same time would leave the estimator distributions roughly unchanged, apart from the slightly different statistical uncertainties.

In order to assess the influence of systematic uncertainties concerning the prediction of confidence intervals, the differences seen in the gauge curves produced for each systematic uncertainty separately are added in quadrature (as described below) in order to obtain one single gauge curve that incorporates all systematic uncertainties. Moreover, the statistical uncertainties represented in the nominal gauge curves have to be considered.

Thus, $\Delta R_{0j}^{5\%}$ is defined as the distance at curve point[1] j between the curve representing the 5% quantiles and the curve representing the medians, both evaluated using the nominal gauge curve. $\Delta R_{0j}^{95\%}$ is defined accordingly. These distances to the median represent the statistical spread attributed to the probability density functions of the likelihood estimators.

In addition, $\Delta R_{kj}^{5\%}$ is defined as the distance at point j between the 5% quantile curve for systematic k and the nominal 5% quantile curve. $\Delta R_{kj}^{95\%}$ is defined accordingly. These distances represent the impact of the systematic uncertainty k at each point j of the gauge curve. For some uncertainties, observables were varied upwards and downwards, as for example done for the photon energy scale, while other uncertainties such as the jet energy resolution could only be varied in one direction. In order to consider both sources of uncertainty with the same weight, the absolute differences to the nominal gauge curve boundaries are averaged for the case of upwards and downwards variations:

$$\Delta R_{kj}^{5\%} = \frac{\left|\Delta R_{kj,\,\mathrm{up}}^{5\%}\right| + \left|\Delta R_{kj,\,\mathrm{down}}^{5\%}\right|}{2} \qquad \Delta R_{kj}^{95\%} = \frac{\left|\Delta R_{kj,\,\mathrm{up}}^{95\%}\right| + \left|\Delta R_{kj,\,\mathrm{down}}^{95\%}\right|}{2} \tag{8.13}$$

Here, $\Delta R_{kj,\,\mathrm{up}}^{5\%}$ denotes the distance at point j between the 5% quantile curve for upwards scaled systematic k and the nominal 5% quantile curve. The other quantities are labelled in the same way, respectively.

A gauge curve incorporating both the statistical spread of the estimators, as well as systematic uncertainties, can then be constructed. The distances $\Delta R_{j,\,\mathrm{tot}}$ of the systematic quantile curves to the median of the nominal gauge curve are at each point j are given by

$$\Delta R_{j,\,\mathrm{tot}}^{5\%} = \sqrt{\sum_{k=0}^{N}\left(\Delta R_{kj}^{5\%}\right)^2} \qquad \Delta R_{j,\,\mathrm{tot}}^{95\%} = \sqrt{\sum_{k=0}^{N}\left(\Delta R_{kj}^{95\%}\right)^2}\,. \tag{8.14}$$

Here, N denotes the number of considered sources of systematic uncertainties. The individual gauge curves are therefore combined such that every systematic uncertainty causes widened confidence intervals.

In this analysis, 11 uncertainties are considered and described in chapter 7. Uncertainties attributed to the photon energy scale (PES), the photon energy resolution (PER), the photon reconstruction efficiency (PEff), the jet energy scale (JES), the jet energy resolution (JER) and the luminosity measurement are considered as experimental uncertainties. Additionally, the branching ratio (BR) calculation and the effect on the gluon fusion cross section (XS) due to

[1] Each gauge curve was evaluated using pseudo-experiments that were generated for 47 different values for each of the Wilson coefficients C_i. The corresponding 47 parameter values for each curve with calculated quantiles are here numbered by the index j

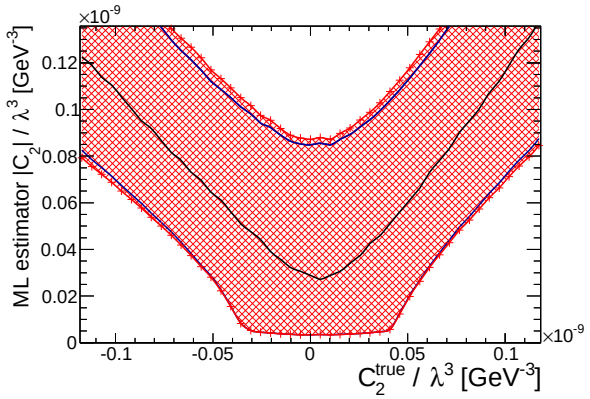

(a) $|O_{SM}|^2 + (C_2/\Lambda^3)\, O_{SM}O_2^\dagger + (C_2/\Lambda^3)^2|O_2|^2$

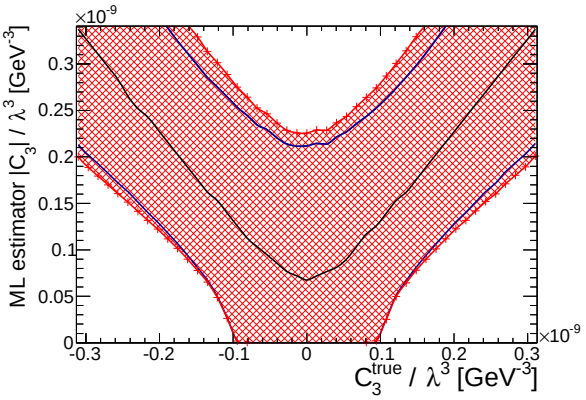

(b) $|O_{SM}|^2 + (C_3/\Lambda^3)\, O_{SM}O_3^\dagger + (C_3/\Lambda^3)^2|O_3|^2$

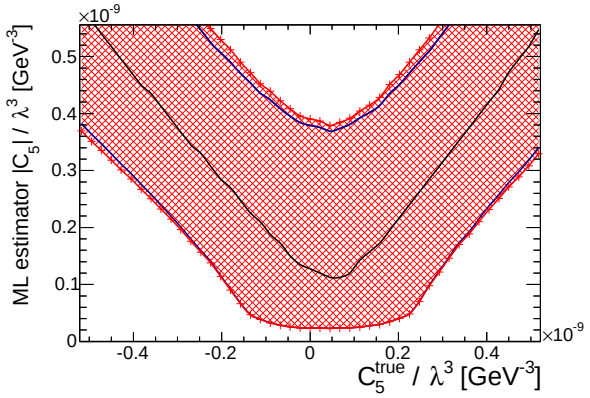

(c) $|O_{SM}|^2 + (C_5/\Lambda^3)\, O_{SM}O_5^\dagger + (C_5/\Lambda^3)^2|O_5|^2$

Figure 8.11.: *Neyman confidence belts at 90% C.L. for Wilson coefficients including systematic uncertainties evaluated in non-extended likelihood fit. The curves including systematic uncertainties are shown in red, the nominal curves are shown in dark blue (quantiles) and black (median) for comparison.*

the QCD scale uncertainty and the α_s uncertainty are considered as theoretical uncertainties as well as varied and fixed scales in the reweighting procedure.

Figures 8.11 and 8.12 show the gauge curves representing all considered systematic uncertainties in comparison to the nominal gauge curves. Both the results obtained with the non-extended maximum likelihood fit and the extended maximum likelihood fit are shown. Considering the varied gauge curves, it can be seen that the effect of systematic uncertainties is small compared to the statistical uncertainty for small Wilson coefficients C_i, but increases for larger values. In general, the extended maximum likelihood estimators are more prone to systematic uncertainties than the non-extended maximum likelihood estimators. This is particularly the case for the Wilson coefficient C_3.

The expected quantitative impact of the systematic uncertainties on the confidence intervals can be evaluated considering the expected confidence levels including systematic uncertainties for the assumption that the SM is realised in data. The procedure to evaluate these confidence intervals is the same as described in the previous section for the derivation of expected frequentist confidence intervals without including systematic uncertainties. The gauge curves including systematic uncertainties are therefore evaluated using the median of

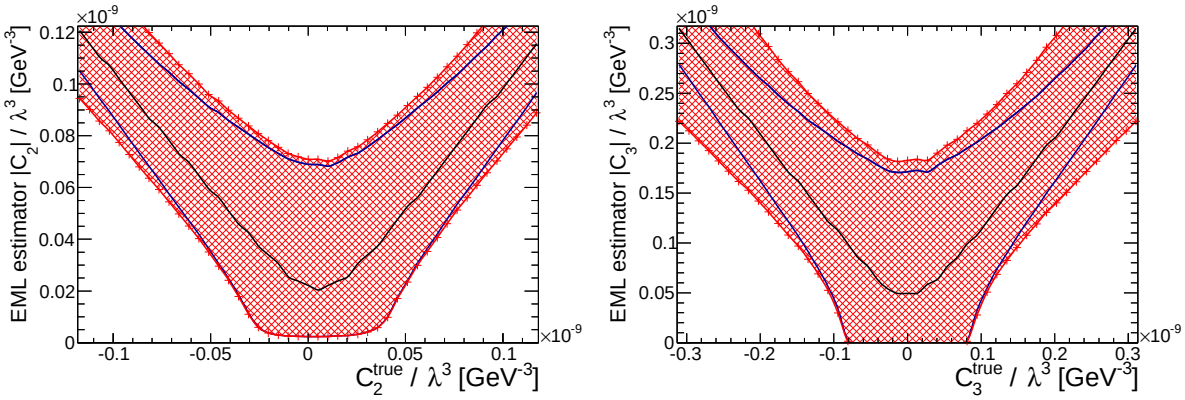

(a) $|O_{SM}|^2 + (C_2/\Lambda^3)\, O_{SM}O_2^\dagger + (C_2/\Lambda^3)^2|O_2|^2$ (b) $|O_{SM}|^2 + (C_3/\Lambda^3)\, O_{SM}O_3^\dagger + (C_3/\Lambda^3)^2|O_3|^2$

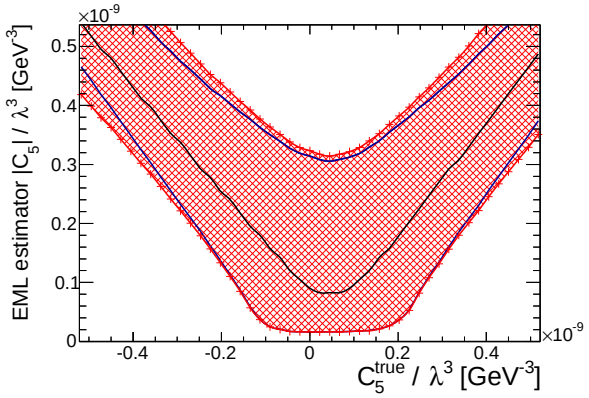

(c) $|O_{SM}|^2 + (C_5/\Lambda^3)\, O_{SM}O_5^\dagger + (C_5/\Lambda^3)^2|O_5|^2$

Figure 8.12.: *Neyman confidence belts at 90% C.L. for Wilson coefficients including systematic uncertainties evaluated in extended likelihood fit. The curves including systematic uncertainties are shown in red, the nominal curves are shown in dark blue (quantiles) and black (median) for comparison.*

	low ML limit $[1 \times 10^{-11}\,\mathrm{GeV}^{-3}]$	high ML limit $[1 \times 10^{-11}\,\mathrm{GeV}^{-3}]$	low EML limit $[1 \times 10^{-11}\,\mathrm{GeV}^{-3}]$	high EML limit $[1 \times 10^{-11}\,\mathrm{GeV}^{-3}]$
C_2/Λ^3	−5.19	5.83	−3.91	5.00
C_3/Λ^3	−13.75	13.79	−10.62	10.73
C_5/Λ^3	−21.53	29.79	−16.21	25.45

Table 8.7.: *Expected frequentist confidence intervals including systematic uncertainties for the assumption that the SM is realised in data. Results are shown for the non-extended ML fit and the extended ML fit.*

the estimator distributions that are obtained for SM pseudo-experiments. The corresponding confidence interval limits are given in table 8.7 and can be compared directly to the results without any uncertainties given in table 8.6. As expected, the intervals are slightly wider when including systematic uncertainties. The increase of approximately 7% for the interval width is largest for the Wilson coefficient C_5 using the non-extended likelihood, while it is only approximately 1% for the same Wilson coefficient when using the extended likelihood

fit. For the Wilson coefficients C_2 and C_3, the effect ranges from 1% to 2.5%.

Additionally to considering the overall uncertainty, the influence of the individual sources of uncertainties is investigated. In order to give one value as an averaged estimate for each uncertainty, the fraction α_k is defined for each systematic uncertainty k. For each point j on the curve representing the 5% quantiles, the value α_{kj}, defined as

$$\alpha_{kj} = \frac{|\Delta R_{kj}^{5\%}|}{\sqrt{\sum_{k=1}^{N} \left(\Delta R_{kj}^{5\%}\right)^2}}\,, \tag{8.15}$$

is calculated and then averaged over all points j. It represents the ratio of the systematic effect k on the gauge curve to the effect of all systematic uncertainties. Only the 5% quantile curve is evaluated for this study. The likelihood estimators $|\widehat{C_i}|$ for the fit to data are expected to adopt values for which the confidence levels are determined only by the 5% quantile curves in figures 8.11 and 8.12. Tables 8.8, 8.9 and 8.10 give the values of α_k for all considered uncertainties and for the non-extended likelihood fit as well as for the extended likelihood fit. In addition, the quantity $\beta_k = \alpha_k^2$ is also given since one finds $\Sigma_k \beta_k = 1$ which can be interpreted as the fractional contribution of the individual uncertainties.

The values given in tables 8.8, 8.9 and 8.10 for the three Wilson coefficients which are considered show that the theoretical uncertainty of using a fixed scale $\mu = m_H$ in the reweighting instead of the nominal choice $\mu = (m_H^2 + p_T^2)^{(1/2)}$ has by far the largest impact on the results for all operators and fit modes. Yield uncertainties have by construction no observable influence on the results obtained in the non-extended likelihood fit. The jet energy scale has the largest influence of all experimental uncertainties in the non-extended likelihood fit. The influence is smaller for the extended likelihood fit. This observation can be explained considering that the influence of this uncertainty on the shape and the signal yield can have cancelling effects on the extended likelihood estimators. In the appendix B.6, the gauge curves are shown as examples for the fixed mass scale uncertainty, the jet energy scale uncertainty and the uncertainty on the gluon fusion cross section attributed to the QCD scale, which is the largest yield uncertainty. Note that these gauge curves represent 1σ variations so that no error propagation is contained in these figures[2].

The results of likelihood fits to the data taken with the ATLAS detector are described in the following chapter. These likelihood fits are performed only with the nominal theoretical predictions. The obtained (extended) maximum likelihood estimators are then applied to derive confidence intervals using the nominal gauge curves and the gauge curves including all systematic uncertainties, respectively.

[2] This means that these curves represent the gauge curves initially obtained for the applied 1σ variation of the corresponding uncertainty. The curves shown in the appendix therefore need to be combined in the above described procedure with the gauge curves that do not include any systematic uncertainties in order to properly estimate the statistical uncertainties and the influence of the respective systematic uncertainty.

	non-extended likelihood		extended likelihood	
Systematic	α[%]	β[%]	α[%]	β[%]
PES	12.83	1.65	12.67	1.61
PER	1.14	0.01	0.47	0.00
PEff	0	0	19.56	3.82
JES	21.97	4.83	19.50	3.80
JER	2.97	0.09	2.34	0.05
luminosity	0	0	14.28	2.04
BR	0	0	19.31	3.73
ggF XS QCD scale	0	0	29.22	8.54
ggf XS α_s	0	0	27.87	7.77
varied mass scale	30.52	9.32	11.09	1.23
fixed mass scale	91.71	84.11	82.10	67.41

Table 8.8.: *Influence of individual systematics on confidence intervals for Wilson coefficient C_2. The quantities α and β are defined in the text.*

	non-extended likelihood		extended likelihood	
Systematic	α[%]	β[%]	α[%]	β[%]
PES	4.66	0.22	0.29	0.00
PER	5.58	0.31	0.26	0.00
PEff	0	0	22.86	5.22
JES	49.44	24.44	2.17	0.05
JER	5.76	0.33	0.30	0.00
luminosity	0	0	16.31	2.66
BR	0	0	22.57	5.09
ggF XS QCD scale	0	0	36.89	13.61
ggf XS α_s	0	0	34.00	11.56
varied mass scale	8.14	0.66	4.94	0.24
fixed mass scale	86.04	74.04	78.46	61.56

Table 8.9.: *Influence of individual systematics on confidence intervals for Wilson coefficient C_3. The quantities α and β are defined in the text.*

	non-extended likelihood		extended likelihood	
Systematic	α[%]	β[%]	α[%]	β[%]
PES	11.09	1.23	10.63	1.13
PER	0.75	0.01	0.60	0.00
PEff	0	0	20.38	4.15
JES	21.17	4.48	11.33	1.28
JER	3.41	0.12	0.78	0.01
luminosity	0	0	14.46	2.09
BR	0	0	20.08	4.03
ggF XS QCD scale	0	0	31.08	9.66
ggf XS α_s	0	0	29.94	8.96
varied mass scale	4.12	0.17	4.64	0.22
fixed mass scale	96.95	94.00	82.74	68.46

Table 8.10.: *Influence of individual systematics on confidence intervals for Wilson coefficient C_5. The quantities α and β are defined in the text.*

8.4. Bayesian Confidence Intervals for Wilson coefficients

The Neyman confidence belts described in the previous section are derived using a frequentist statistical approach. For each likelihood estimator $\widehat{C}_i$ that could be observed in a likelihood fit to the data taken with the ATLAS detector, a confidence interval is given stating that the true Wilson coefficient is covered by this interval to a given coverage probability, in this analysis 90%. These predictions were derived by simulating the actual measurement many times for different parameter hypotheses. However, in this approach it can happen that for particular observations in data an empty confidence interval is derived.

Using the Bayesian statistical method, this situation is avoided. The confidence interval is derived from the likelihood function obtained for the (extended) maximum likelihood fit to the Higgs transverse momentum distribution extracted from data. Consequently, no probability density function for the estimators has to be evaluated.

Using the Bayes' theorem [91], the probability for a particular Wilson coefficient C_i given the data $\boldsymbol{x}$ is calculated according to

$$P(C_i|\boldsymbol{x}) = \frac{\mathcal{L}(C_i;\boldsymbol{x})\pi(C_i)}{\int \mathcal{L}(C_i';\boldsymbol{x})\pi(C_i')\,\mathrm{d}C_i'} \,. \tag{8.16}$$

Here, $\mathcal{L}(C_i;\boldsymbol{x})$ denotes the likelihood function and the quantity $\pi(C_i)$ is the prior probability for the corresponding Wilson coefficient C_i. In this analysis, the same prior probability is assumed for all Wilson coefficients C_i, therefore

$$\pi(C_i) = \text{const.} \tag{8.17}$$

The probability $P(C_i|\boldsymbol{x})$ then equals the normalised likelihood function that is obtained in the fit to the data taken with the ATLAS detector:

$$P(C_i|\boldsymbol{x}) = \frac{\mathcal{L}(C_i;\boldsymbol{x})}{\int \mathcal{L}(C_i';\boldsymbol{x})\,\mathrm{d}C_i'} \,. \tag{8.18}$$

According to the coverage probability of 90% applied in the Neyman confidence belts, for each operator O_i, a parameter range I for the Wilson coefficients C_i with $P(C_i \in I\,|\boldsymbol{x}) = 90\%$ can be given by evaluating the 5% and 95% quantiles of the respective normalised binned likelihood distribution. The quantiles $C_i^{5\%}$ and $C_i^{95\%}$ are defined by

$$\begin{aligned} 5\% &= \int_{-\infty}^{C_i^{5\%}} P(C_i|\boldsymbol{x})\,\mathrm{d}C_i \\ 95\% &= \int_{C_i^{95\%}}^{\infty} P(C_i|\boldsymbol{x})\,\mathrm{d}C_i \end{aligned} \tag{8.19}$$

Again, a linear interpolation is applied between the discrete Wilson coefficient values to determine the quantiles.

The procedure to evaluate the Bayesian confidence intervals is illustrated in figure 8.13. It shows the normalised likelihood functions used to evaluate the Bayesian limits for the same example pseudo-experiments as in figure 8.4.

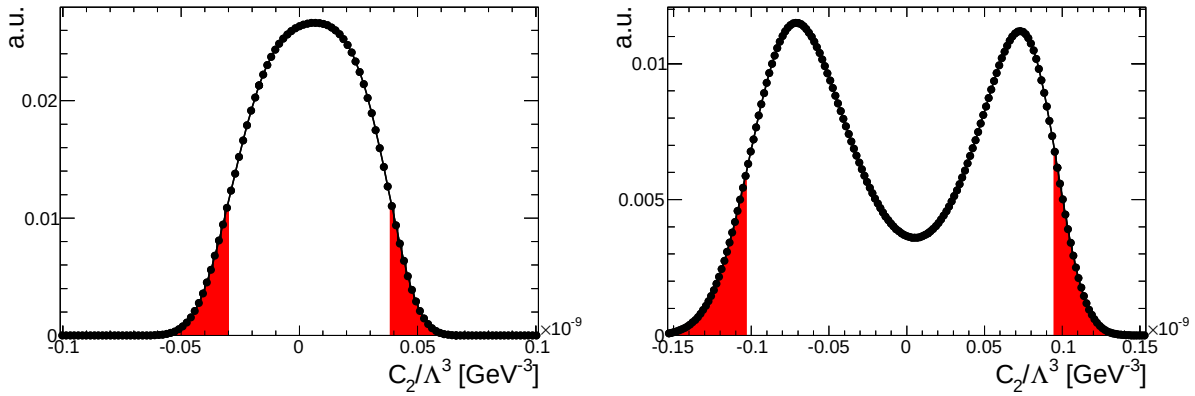

Figure 8.13.: *Normalised likelihood functions illustrating Bayesian limits. The same likelihood fits of the C_2 Wilson coefficient to SM pseudo-experiments as in figure 8.4 are shown. The Bayesian exclusion limits (coloured red) determined by the 5% and 95% quantiles are illustrated approximatively (without linear interpolation).*

Additionally, this parameter range can also be evaluated for each of the generated pseudo-experiments. Table 8.11 gives the average limits evaluated with the SM pseudo-experiments. These values can be interpreted as the expected Bayesian exclusion limits for the assumption

	low ML limit $[1 \times 10^{-11}\,\mathrm{GeV}^{-3}]$	high ML limit $[1 \times 10^{-11}\,\mathrm{GeV}^{-3}]$	low EML limit $[1 \times 10^{-11}\,\mathrm{GeV}^{-3}]$	high EML limit $[1 \times 10^{-11}\,\mathrm{GeV}^{-3}]$
C_2/Λ^3	-5.23	5.53	-3.59	4.86
C_3/Λ^3	-13.20	13.20	-10.39	10.47
C_5/Λ^3	-20.01	28.06	-14.32	24.24

Table 8.11.: *Expected Bayesian confidence intervals evaluated with SM pseudo-experiments. Results are shown for the non-extended ML fit and the extended ML fit. For each of the 5×10^4 SM pseudo-experiments, the Bayesian limits using the (extended) likelihood function were evaluated and then averaged.*

that the SM is realised in data.

Comparing these values to the respective results using frequentist confidence intervals, given in table 8.6, it can be seen that the differences are small. However, it has to be reminded that the Bayesian results given in the following chapter do not depend on any studies with pseudo-experiments, while the frequentist results use the results given in figures 8.9 and 8.10 to interpret the likelihood estimator obtained with data.

9. Results

The confidence belts evaluated in the previous section are evaluated in this chapter to give confidence intervals on the Wilson coefficients. In the analysis presented in this thesis, the Wilson coefficients C_i adjust the presence of the coupling operators O_i in addition to the SM operator. A non-extended maximum likelihood fit and an extended maximum likelihood fit are performed for each Wilson coefficient individually while the other coefficients are set to zero. In these likelihood fits, the reconstructed transverse momentum of the Higgs boson is analysed. The event selection used for this analysis is described in chapter 5. The main selection requirements are two reconstructed and isolated photons, at least one reconstructed jet with $p_T \geq 30\,\mathrm{GeV}$ and a minimum transverse momentum of the reconstructed Higgs boson candidate of $30\,\mathrm{GeV}$.

In the previous chapter, frequentist confidence belts for the Wilson coefficients C_i depending on the likelihood estimators $|\widehat{C_i}|$ were determined. In this chapter, the results of the (extended) likelihood fit to the distribution of the Higgs boson p_T observed in collision data are presented. This (extended) likelihood fit uses the same likelihood function as described in section 8.2. The results of this fits are then used to give confidence intervals for the Wilson coefficients using the derived Neyman confidence belts (see section 8.3).

Additionally, the likelihood fit results obtained with data are interpreted using the Bayes' theorem. In the interpretation using the Bayesian method, the effects of systematic uncertainties are omitted. These results are determined only by the shape of the likelihood functions obtained in the likelihood fits to data.

The Higgs boson p_T distribution in gluon fusion signal events was extracted from data by estimating and subtracting resonant and non-resonant background contributions, as described in chapter 6. The p_T^H distribution which is then observed in data is shown in figure 6.5. This distribution is fitted to obtain the (extended) maximum likelihood estimators for the Wilson coefficients C_i. The theoretically predicted p_T distributions depending on the Wilson coefficients C_i are obtained by reweighting the POWHEG sample with generated SM gluon fusion $H \to \gamma\gamma$ events, as described in section 4.3. The same event selection criteria as applied to data are used for the simulated events. The Higgs boson p_T distributions are predicted for discrete Wilson coefficients, the step widths used for the coefficients C_2, C_3 and C_5 are given in the second column of table 8.5. These predicted Higgs boson p_T distributions are used to evaluate the estimators for the Wilson coefficients in a binned maximum likelihood fit to the distribution observed in data.

This section concentrates on the results without the consideration of systematic uncertainties. Results are given both for the frequentist statistical method and for the Bayesian statistical method. The results for the frequentist confidence intervals including systematic

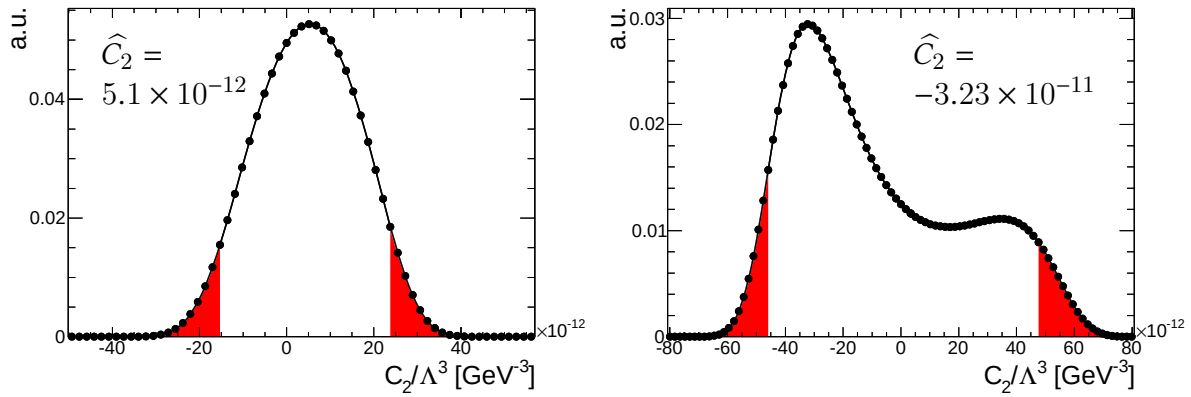

(a) *Non-extended likelihood* (b) *Extended likelihood*

Figure 9.1.: *Normalised likelihood functions observed in fit of the Wilson coefficient C_2 to data. The approximate 5% and 95% quantile boundaries of the distribution are illustrated in red. The estimators are given in units of* GeV^{-3}

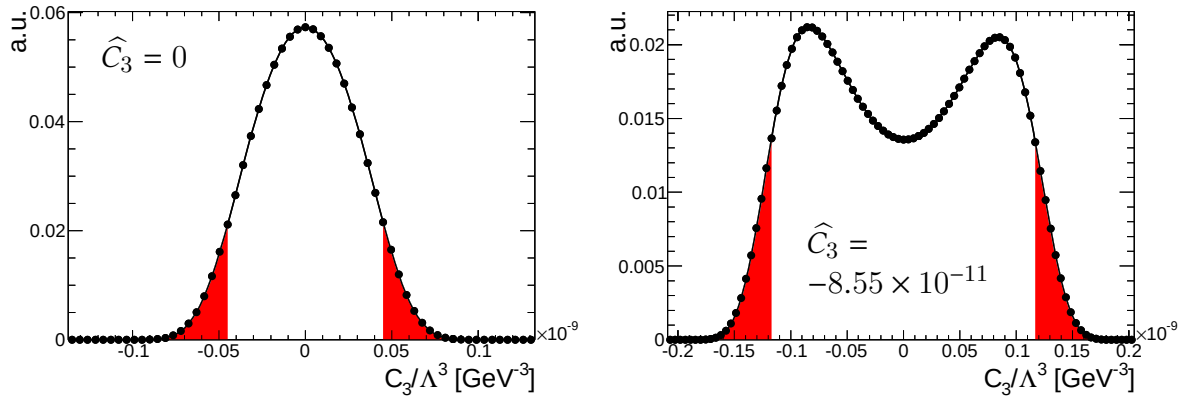

(a) *Non-extended likelihood* (b) *Extended likelihood*

Figure 9.2.: *Normalised likelihood functions observed in fit of the Wilson coefficient C_3 to data. The approximate 5% and 95% quantile boundaries of the distribution are illustrated in red. The estimators are given in units of* GeV^{-3}.

uncertainties and results for alternative analysis strategies are discussed in the following sections.

The normalised likelihood functions obtained when fitting the Wilson coefficients C_i to data are shown in figures 9.1, 9.2 and 9.3. In these three figures, the functions shown on the left-hand side are obtained in the non-extended likelihood fit. The functions on the right-hand side give the extended likelihood functions, respectively. Note that the scaling of the x-axis is different in each of these figures. The best fit values $\widehat{C}_i$ are represented by the maxima of each of these curves. More than one local maxima can be observed for the likelihood functions of the extended likelihood fits. The extended maximum likelihood estimators are therefore given by the positions of the highest maxima.

The best estimators $\widehat{C}_i$ for the Wilson coefficients obtained in the non-extended maximum likelihood fit and in the extended maximum likelihood fit to data are given in tables 9.1 and

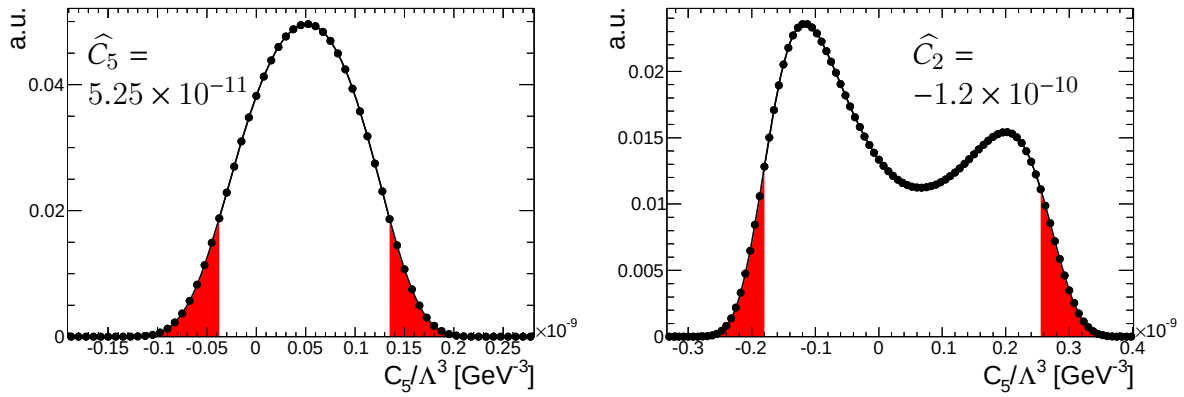

(a) *Non-extended likelihood* (b) *Extended likelihood*

Figure 9.3.: *Normalised likelihood functions observed in fit of the Wilson coefficient C_5 to data. The approximate 5% and 95% quantile boundaries of the distribution are illustrated in red. The estimators are given in units of* GeV^{-3}

	ML estimator $\widehat{C}_i$ $[1 \times 10^{-11}\,\mathrm{GeV}^{-3}]$	low limit $[1 \times 10^{-11}\,\mathrm{GeV}^{-3}]$	high limit $[1 \times 10^{-11}\,\mathrm{GeV}^{-3}]$
C_2/Λ^3	0.51	−2.96	3.77
C_3/Λ^3	0.00	−7.50	7.53
C_5/Λ^3	5.25	−14.12	22.90

Table 9.1.: *Non-extended maximum likelihood estimators and corresponding frequentist confidence interval limits at 90% C.L. for the observed data and without systematic uncertainties.*

9.2, respectively. The likelihood estimators have an intrinsic accuracy determined by the step width used in the fit (see table 8.5). The absolute values $|\widehat{C}_i|$ are used to determine the frequentist confidence intervals using the Neyman confidence belts discussed in section 8.3. They were constructed for each Wilson coefficient and fit mode (see figures 8.9 (non-extended likelihood) and 8.10 (extended likelihood)). The limits of the frequentist confidence intervals are determined by the points of intersection between a horizontal line with $y = |\widehat{C}_i|$ and the curve representing the 5% quantiles. For all observed estimators $|\widehat{C}_i|$, the applied horizontal line does not intersect the curve representing the 95% quantiles so that the SM value $C_i = 0$ is always covered by the confidence intervals. The determination of the confidence intervals based on the estimator $|\widehat{C}_i|$ and the Neyman confidence belts is illustrated in figures 9.4, 9.5 and 9.6. The intersection points are determined using a linear interpolation between the points for which the gauge curves were calculated. The confidence intervals which are obtained following this procedure for all Wilson coefficients C_i and for both likelihood fit modes are also given in tables 9.1 and 9.2. These confidence intervals consider only statistic uncertainties while confidence intervals additionally including systematic uncertainties are given in the following section.

Comparing the results for the non-extended likelihood and the extended likelihood, it can be seen that the estimators of the non-extended likelihood give values which are nearer to the SM predicted value $C_i = 0$. Moreover, the frequentist confidence intervals are smaller using

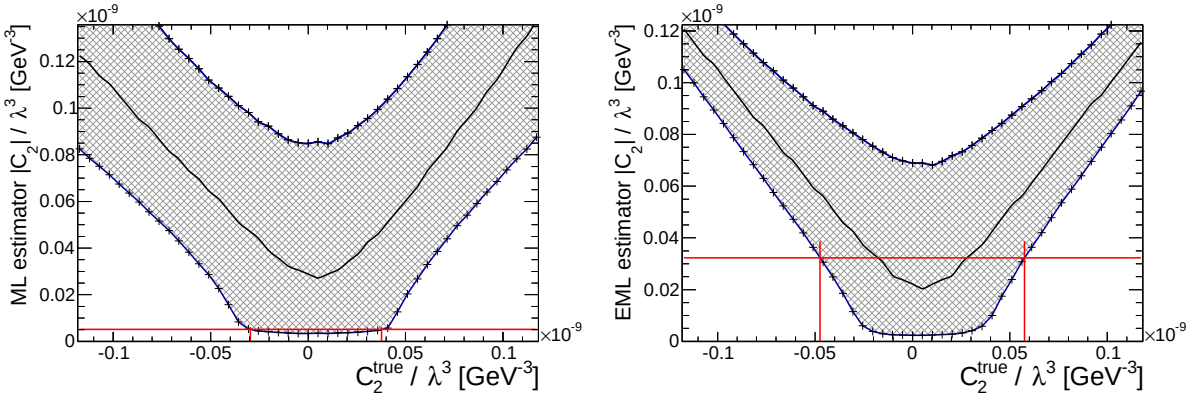

(a) *Confidence interval for non-extended likelihood. The marked estimator is* $|\widehat{C_2}| = 0.51 \times 10^{-11}\,\mathrm{GeV}^{-3}$*, the confidence interval is* $C_2 \in [-2.96, 3.77] \times 10^{-11}\mathrm{GeV}^{-3}$.

(b) *Confidence interval for ext. likelihood. The marked estimator is* $|\widehat{C_2}| = 3.23 \times 10^{-11}\,\mathrm{GeV}^{-3}$*, the confidence interval is* $C_2 \in [-4.74, 5.75] \times 10^{-11}\mathrm{GeV}^{-3}$.

Figure 9.4.: *Determination of confidence intervals using the Neyman confidence belts for the Wilson coefficient* C_2.

	EML estimator $\widehat{C_i}$ $[1 \times 10^{-11}\,\mathrm{GeV}^{-3}]$	low limit $[1 \times 10^{-11}\,\mathrm{GeV}^{-3}]$	high limit $[1 \times 10^{-11}\,\mathrm{GeV}^{-3}]$
C_2/Λ^3	-3.23	-4.74	5.75
C_3/Λ^3	-8.55	-13.03	13.14
C_5/Λ^3	-12.00	-18.64	27.90

Table 9.2.: *Extended maximum likelihood estimators and corresponding frequentist confidence interval limits at 90% C.L. for the observed data and without systematic uncertainties.*

the non-extended likelihood. The maxima for the extended likelihood functions are found at negative Wilson coefficients. This is consistent with the signal strength $\mu_{\mathrm{sig}} = 2.0 \pm 0.6$ that was observed in data for the event selection applied in this analysis (see equation (6.6)). The dependence of the predicted event yield on the Wilson coefficients, which is shown in figure 8.6, show that the negative Wilson coefficients obtained as estimators in the extended likelihood fit predict larger production cross sections.

Additionally, the observed confidence intervals given in tables 9.1 and 9.2 can be compared to the confidence intervals that are expected for the hypothesis that the SM is realised in data. These intervals are given in table 8.6. The confidence intervals observed in the non-extended likelihood are for all Wilson coefficients slightly smaller than expected for the SM realisation in data. For the extended maximum likelihood fit, the observed confidence intervals are larger than expected for the SM hypothesis. However, the differences between the observed confidence intervals and the expected intervals for the SM hypothesis are most likely attributed to statistical fluctuations and do not alter the fact that the observed confidence intervals are all consistent with the SM prediction.

The frequentist confidence intervals in tables 9.1 and 9.2 are given for the parameters C_i/Λ^3, which were for simplicity also denoted as C_i. They are therefore given in units of GeV^{-3}.

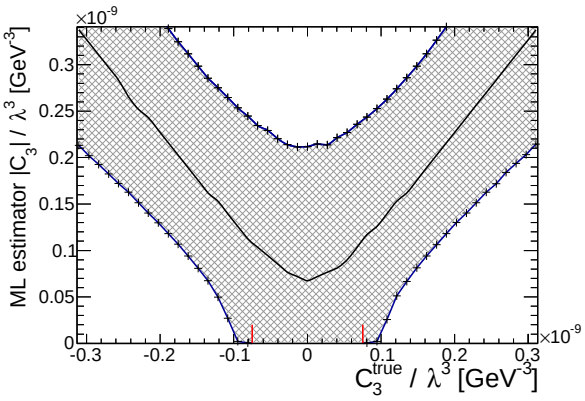

(a) *Confidence interval for non-extended likelihood. The marked estimator is* $|\widehat{C_3}| = 0.0 \times 10^{-11}\,\mathrm{GeV}^{-3}$*, the confidence interval is* $C_3 \in [-7.50, 7.53] \times 10^{-11}\mathrm{GeV}^{-3}$.

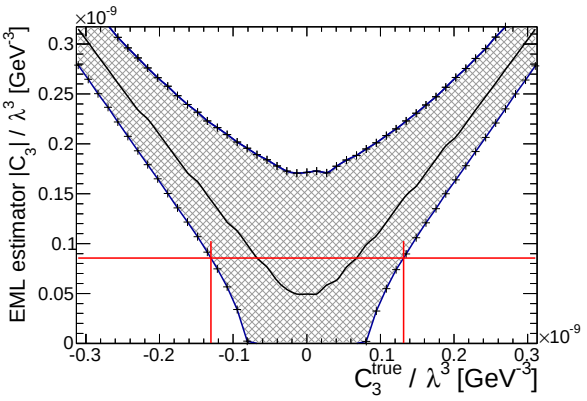

(b) *Confidence interval for ext. likelihood. The marked estimator is* $|\widehat{C_3}| = 8.55 \times 10^{-11}\,\mathrm{GeV}^{-3}$*, the confidence interval is* $C_2 \in [-13.03, 13.14] \times 10^{-11}\mathrm{GeV}^{-3}$.

Figure 9.5.: *Determination of confidence intervals using the Neyman confidence belts for the Wilson coefficient* C_3.

Wilson coefficient	$\Lambda = m_t$		$\Lambda = 1000\,\mathrm{GeV}$	
	low limit	high limit	low limit	high limit
C_2	-1.51×10^{-4}	1.92×10^{-4}	-2.96×10^{-2}	3.77×10^{-2}
C_3	-3.82×10^{-4}	3.83×10^{-4}	-7.50×10^{-2}	7.53×10^{-2}
C_5	-7.18×10^{-4}	1.17×10^{-3}	-1.41×10^{-1}	2.29×10^{-1}

Table 9.3.: *Numerical values for confidence levels of dimensionless Wilson coefficients for* $\Lambda = m_t$ *and* $\Lambda = 1\,\mathrm{TeV}$*. The results are calculated for the values of* C_i/Λ^3 *obtained in the non-extended likelihood fit.*

The paramter Λ represents the scale of possible new physics that might be observable by the point-like coupling operators O_i. Consequently, a numerical illustration of the dimensionless Wilson coefficients C_i can be given for any hypothesis of Λ. In order to give some values as examples, numerical representations of the confidence intervals for the Wilson coefficients are reported in table 9.3 for $\Lambda = m_t \sim 172\,\mathrm{GeV}$ and for $\Lambda = 1000\,\mathrm{GeV}$. The values in this table refer to the results for the non-extended maximum likelihood fit.

The values obtained for $\Lambda = m_t$ are of the same order of magnitude as the Wilson coefficients that match the effective theory to the SM. They were given in section 2.4 (see equation (2.56)). However, the exact numerical values are not comparable since in this analysis, an admixture of the point-like coupling operators to the SM operator is investigated, so that the SM expectation value is $C_i = 0$ for all Wilson coefficients. The interpretation of the numerical values for $\Lambda = 1\,\mathrm{TeV}$ would require a particular theoretical prediction on the magnitude of these coefficients in a specific model.

Confidence intervals are additionally evaluated using the Bayesian method without the incorporation of systematic uncertainties. The Bayesian confidence intervals at 90% C.L. are specified by the 5% quantiles and the 95% quantiles of the corresponding normalised like-

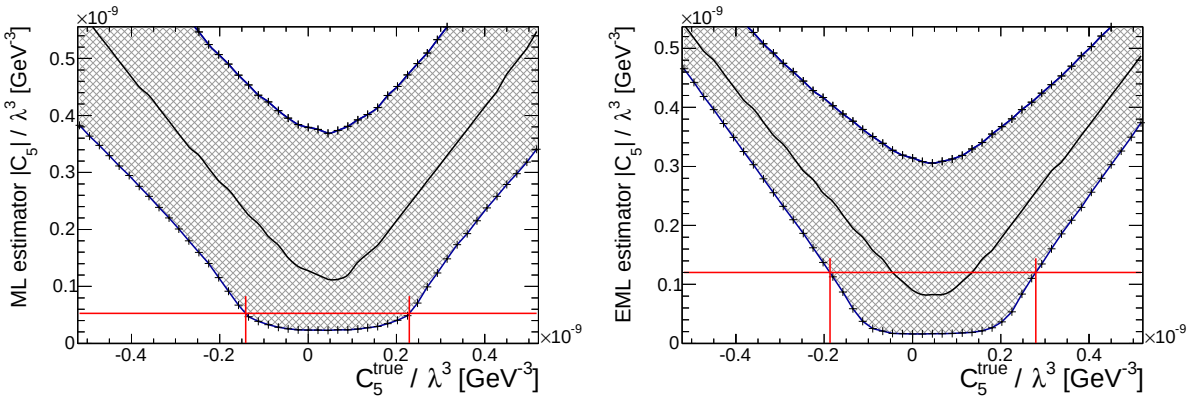

(a) *Confidence interval for non-extended likelihood. The marked estimator is* $|\widehat{C_5}| = 5.25 \times 10^{-11}\,\mathrm{GeV}^{-3}$*, the confidence interval is* $C_2 \in [-14.12, 22.90] \times 10^{-11}\mathrm{GeV}^{-3}$.

(b) *Confidence interval for ext. likelihood. The marked estimator is* $|\widehat{C_5}| = 12.0 \times 10^{-11}\,\mathrm{GeV}^{-3}$*, the confidence interval is* $C_5 \in [-18.64, 27.90] \times 10^{-11}\mathrm{GeV}^{-3}$.

Figure 9.6.: *Determination of confidence intervals using the Neyman confidence belts for the Wilson coefficient* C_5.

	low ML limit $[1 \times 10^{-11}\,\mathrm{GeV}^{-3}]$	high ML limit $[1 \times 10^{-11}\,\mathrm{GeV}^{-3}]$	low EML limit $[1 \times 10^{-11}\,\mathrm{GeV}^{-3}]$	high EML limit $[1 \times 10^{-11}\,\mathrm{GeV}^{-3}]$
C_2/Λ^3	-1.45	2.38	-4.62	4.78
C_3/Λ^3	-4.66	4.69	-11.78	11.77
C_5/Λ^3	-4.07	13.64	-17.72	25.65

Table 9.4.: *Bayesian confidence intervals extracted from data. Results are shown for the non-extended ML fit and the extended ML fit.*

lihood functions observed in the likelihood fits to data. They are illustrated in figures 9.1, 9.2 and 9.3. For the calculation of numerical values, again a linear interpolation is applied between the discrete Wilson coefficients considered in the likelihood fit. The Bayesian confidence intervals observed in the likelihood fits of the Wilson coefficients to data are given in table 9.4.

The Bayesian confidence limits are smaller when using the non-extended likelihood. This is clearly caused by the double-maxima seen in the likelihood functions when performing the extended likelihood fit to data.

Furthermore, the Bayesian confidence limits can be compared to the frequentist confidence intervals, both including only statistical uncertainties. The Bayesian limits using the non-extended likelihood are smaller then the corresponding frequentist intervals. The likelihood functions observed in the non-extended likelihood fits to data show for all Wilson coefficients only one local maxima. In the studies using pseudo-experiments, double-maxima were observed in some cases also in the non-extended likelihood fits and are therefore considered in the Neyman confidence belts. The Bayesian limits are therefore smaller because they only consider the one single likelihood fit to data.

	low ML limit $[1 \times 10^{-11}\,\mathrm{GeV}^{-3}]$	high ML limit $[1 \times 10^{-11}\,\mathrm{GeV}^{-3}]$	low EML limit $[1 \times 10^{-11}\,\mathrm{GeV}^{-3}]$	high EML limit $[1 \times 10^{-11}\,\mathrm{GeV}^{-3}]$
C_2/Λ^3	-2.97	3.78	-4.84	5.83
C_3/Λ^3	-7.50	7.53	-13.69	13.82
C_5/Λ^3	-14.17	22.94	-18.97	28.15

Table 9.5.: *Frequentist confidence intervals including an estimation of systematic uncertainties. The intervals are obtained by evaluating the gauge curves including systematic uncertainties using the nominal likelihood fit results in data. Results are shown for the non-extended ML fit and the extended ML fit.*

9.1. Results Including Systematic Uncertainties

Systematic uncertainties on experimental observables and uncertainties on theoretical predictions have an influence on the results given in this thesis. The influence of several experimental and theoretical uncertainties on the frequentist confidence intervals is therefore investigated. The systematic uncertainties considered in this analysis are explained in chapter 7. In section 8.3.1, Neyman confidence belts including systematic uncertainties were constructed. The procedure for the inclusion of systematic uncertainties in the confidence belts is also explained in the referred section. Figures 8.11 and 8.12 show the gauge curves including systematics for the non-extended likelihood fit and the extended likelihood fit, respectively. These gauge curves were constructed such that each considered systematic uncertainty causes wider confidence intervals.

The (extended) maximum likelihood fits to data are only performed using the nominal theoretical Higgs boson p_T distributions. The corresponding results for the (extended) likelihood estimators $|\widehat{C_i}|$ were given in the previous section. The systematic gauge curves are therefore evaluated using these estimators $|\widehat{C_i}|$. The likelihood fit is therefore not repeated for every systematic uncertainty and the corresponding varied theoretical predictions. The influence of systematic uncertainties is assessed in the construction of the corresponding gauge curve including systematic uncertainties. In these studies, the likelihood fits using varied theoretical predictions were already performed using simulated events. An additional separate fit for each source of uncertainty to the Higgs boson p_T distribution observed in collision data would yield various different estimators for the Wilson Coefficients and it is unclear how they would have to be combined.

The confidence intervals obtained by evaluating the gauge curves including systematic uncertainties shown in figures 8.11 and 8.12 are given in table 9.5. They can be compared to the nominal results given in tables 9.1 and 9.2. It is found that the influence of systematic uncertainties is negligible for the non-extended likelihood. The width of the confidence intervals for the non-extended likelihood increases only by less than 0.3% for all Wilson coefficients. Using the extended maximum likelihood fit, the influence of systematics is small but noticeable. This is in particular the case for the Wilson coefficient C_3, for which the width of the confidence interval increases by approximately 5.1% because of systematic uncertainties. For the coefficients C_2 and C_5, the effect is approximatively 1.8% and 1.2%, respectively. The

larger influence of systematic uncertainties using the extended maximum likelihood compared to the influence on the results using the non-extended likelihood is supposed to be explained by the additional consideration of signal yield uncertainties.

Consequently, the results presented in this thesis are mainly dominated by statistical uncertainties. Datasets with higher statistics therefore represent the most promising option to further reduce the range of the confidence intervals for the Wilson coefficients. They will (hopefully) become available in the upcoming run 2 of the LHC physics programme.

The statistical uncertainties in this analysis are mostly attributed to the non-resonant background contribution. The signal yield was extracted by fitting the diphoton mass spectra for events categorised in p_T^H-bins. This procedure requires to have a sufficient amount of signal events in each p_T^H-bin, so that the number of bins is very limited. In this analysis, the Higgs transverse momentum spectrum was extracted from data in a histogram of 7 bins. The relative statistical uncertainty on the event yield per bin is nevertheless of the order $40\% - 80\%$. This fit uncertainty is therefore for the 2012 data set much larger than the Poisson fluctuation of the signal yield.

9.2. Results for Alternative Analysis Strategies

Two alternative analysis strategies were introduced in sections 5.5.2 and 6.4 concerning the estimation of resonant background. In the nominal analysis, the resonant background is estimated using simulated events. The yield of resonant background events from VBF, VH and ttH Higgs boson production processes is subtracted from the $H \to \gamma\gamma$ events observed in data according to the SM predicted cross sections.

Since the inclusive (only applying the diphoton selection criteria) signal strength observed for $H \to \gamma\gamma$ events in data is $\mu = 1.6$, an alternative analysis approach is tested. In this approach, the resonant background yield predicted in the SM is scaled by the observed μ.

Furthermore, it was investigated if the resonant background contribution from VBF Higgs boson production can be reduced by exploiting the characteristic kinematics of VBF events. Therefore, a tightened event selection was developed. The remaining resonant background events are then subtracted according to the SM predictions of simulated events.

The following two subsections give the confidence intervals derived in the likelihood fits of the Wilson coefficients to data using these alternative analysis approaches. The results presented for the alternative analysis strategies do not include the influence of systematic uncertainties.

9.2.1. Equally Distributed Signal Strength

In this analysis approach, the resonant background is subtracted from the $H \to \gamma\gamma$ events observed in data according to the observed signal strength of $\mu = 1.6$. This approach therefore assumes that the observed increased signal strength is evenly distributed over the different Higgs boson production processes.

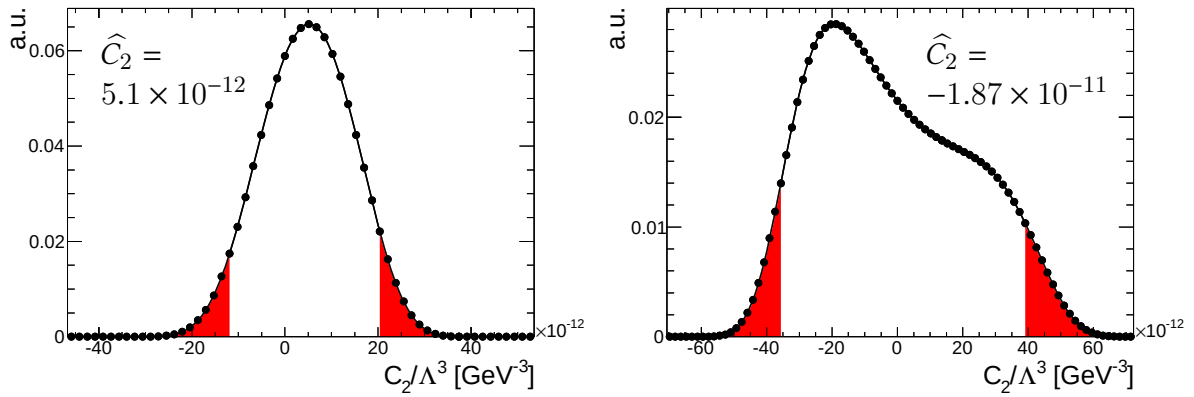

(a) *Non-extended likelihood* (b) *Extended likelihood*

Figure 9.7.: *Normalised likelihood functions observed in fit of the Wilson coefficient C_2 to data for the resonant background estimation normalised according to observed inclusive signal strength. The approximate 5% and 95% quantile boundaries of the distribution are illustrated in red. The estimators are given in units of* GeV^{-3}

Since the resonant background is subtracted from data, the Neyman confidence belts based on studies with simulated gluon fusion events, are not affected. The contribution to the statistical uncertainty from the subtraction of the non-resonant background is negligible compared to the uncertainty on the signal yield which was extracted from data using a signal+background fit of the $m_{\gamma\gamma}$ spectra in p_T^H-bins. This negligible contribution of the resonant background to the statistical uncertainty was therefore not considered in the studies using pseudo-experiments. Consequently, the Neyman confidence belts derived in section 8.3 are also valid for this analysis approach. However, the likelihood fits to data are repeated using the modified Higgs boson p_T distribution extracted from data.

The likelihood functions that are observed in the non-extended maximum likelihood fit and the extended maximum likelihood fit for the modified background estimation are shown in figures 9.7, 9.7 and 9.9. It is observed that the estimators obtained in the non-extended likelihood stay the same for all Wilson coefficients C_i with respect to the nominal analysis. This was a priori not expected since the p_T distribution of the Higgs boson depends on the production process. A different normalisation of the subtracted resonant background therefore has an influence on the Higgs boson p_T distribution extracted from data. However, since the estimators are observed to be unchanged, the confidence intervals for the non-extended likelihood (see table 9.1) do not change, either.

The extended maximum likelihood estimators and the corresponding confidence intervals are given in table 9.6. Compared to the results obtained using the nominal analysis strategy, the extended likelihood estimators $\widehat{C}_i$ yield values nearer to $\widehat{C}_i = 0$. The confidence intervals are therefore also smaller by about 22%. This difference is explained by the decreased number of events in the data distribution used in the extended likelihood fit. In this analysis approach, more events are considered as resonant background events and therefore subtracted. The smaller absolute values of the extended likelihood estimators are then attributed to the dependence of the predicted event yield on the Wilson coefficients (see figure 8.6).

The Bayesian limits obtained for this alternative analysis approach are given in table 9.7.

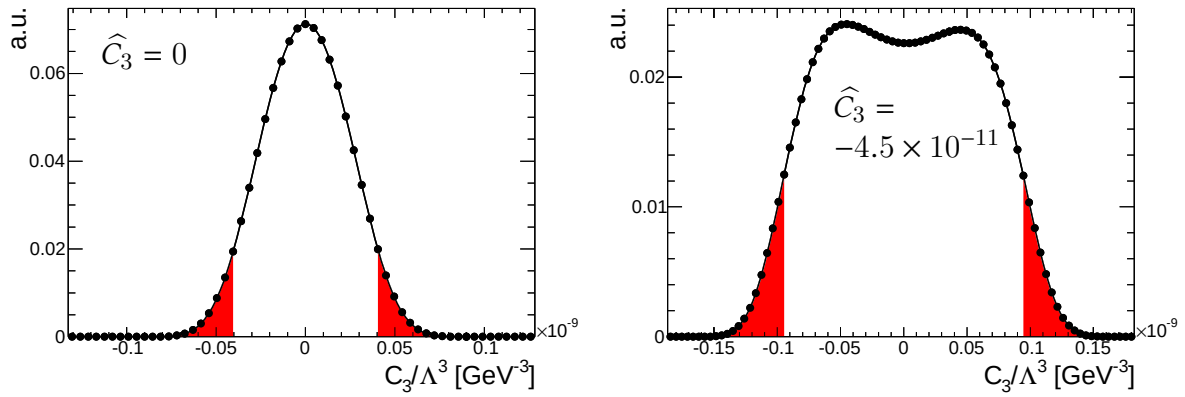

(a) *Non-extended likelihood* (b) *Extended likelihood*

Figure 9.8.: *Normalised likelihood functions observed in fit of the Wilson coefficient C_3 to data for the resonant background estimation normalised according to observed inclusive signal strength.The approximate 5% and 95% quantile boundaries of the distribution are illustrated in red. The estimators are given in units of* GeV^{-3}

	EML estimator $\widehat{C}_i$ $[1 \times 10^{-11}\,\mathrm{GeV}^{-3}]$	low limit $[1 \times 10^{-11}\,\mathrm{GeV}^{-3}]$	high limit $[1 \times 10^{-11}\,\mathrm{GeV}^{-3}]$
C_2/Λ^3	-1.87	-3.58	4.68
C_3/Λ^3	-4.50	-10.11	10.21
C_5/Λ^3	-6.00	-13.61	22.98

Table 9.6.: *Extended maximum likelihood estimators and corresponding frequentist confidence interval limits at 90% C.L. The reported results are obtained applying the resonant background estimation according to the observed inclusive signal strength*

Though the ML estimators stayed the same compared to the nominal analysis, the Bayesian confidence intervals determined by the shape of the likelihood function are slightly different (see table 9.4 for comparison). This shows that though the maximum of the likelihood curves for the non-extended likelihood did not change, the shape of the curves is different compared to the nominal analysis. The Bayesian limits using the extended maximum likelihood are smaller compared to the nominal analysis for the same reasons that were given concerning the frequentist confidence intervals.

9.2.2. Tightened Selection Criteria Suppressing VBF

In section 5.5.2, a tightened event selection was developed. The additional cuts are capable to suppress the resonant background contribution from VBF Higgs boson production. The optimised cuts reject events that satisfy $m_{jj} > 670\,\mathrm{GeV}$ and $|\Delta\eta_{jj}| > 3.5$ and $N_{\mathrm{jet}} \geq 2$. However, these additional selection criteria were not included in the nominal analysis since the predicted remaining resonant background is still considerable (see table 6.4) and has to be subtracted. Moreover, the additional cuts might increase the influence of jet uncertainties. This is not further studied since the results including the tightened selection criteria are

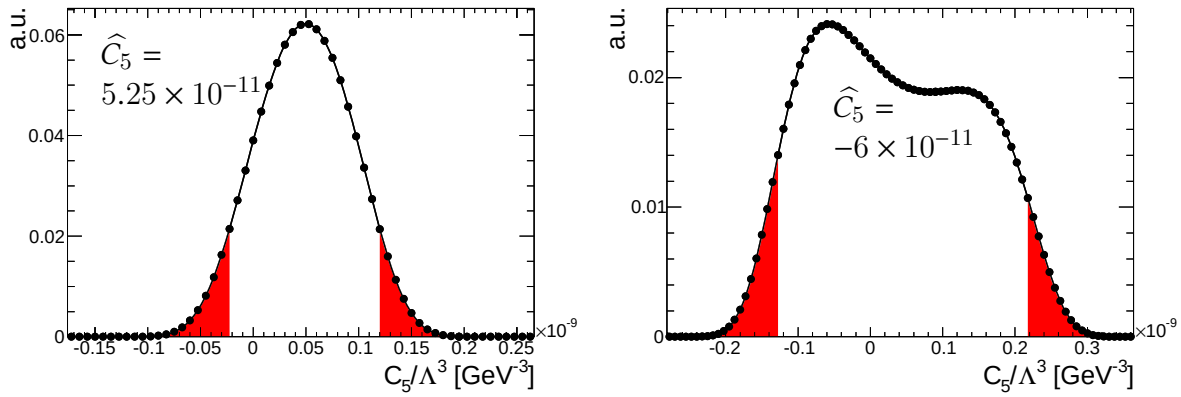

(a) *Non-extended likelihood* (b) *Extended likelihood*

Figure 9.9.: *Normalised likelihood functions observed in fit of the Wilson coefficient C_5 to data for the resonant background estimation normalised according to observed inclusive signal strength. The approximate 5% and 95% quantile boundaries of the distribution are illustrated in red. The estimators are given in units of* GeV^{-3}

	low ML limit $[1 \times 10^{-11}\,\mathrm{GeV}^{-3}]$	high ML limit $[1 \times 10^{-11}\,\mathrm{GeV}^{-3}]$	low EML limit $[1 \times 10^{-11}\,\mathrm{GeV}^{-3}]$	high EML limit $[1 \times 10^{-11}\,\mathrm{GeV}^{-3}]$
C_2/Λ^3	−1.12	2.08	−3.54	3.95
C_3/Λ^3	−3.89	3.93	−9.26	9.27
C_5/Λ^3	−2.57	12.20	−13.04	21.41

Table 9.7.: *Bayesian confidence intervals observed with data. Results are shown for the non-extended ML fit and the extended ML fit. The reported results are obtained applying the resonant background estimation according to the observed inclusive signal strength.*

only given in addition to the nominal results and without an investigation of systematic uncertainties.

The results obtained when including the VBF suppressing selection criteria are given in this section. In order to account for the tightened event selection, separate Neyman confidence belts had to be evaluated for this analysis approach. The Higgs boson p_T distribution extracted from data and the predicted p_T distributions for various Wilson coefficients are modified according to the additional selection criteria. The SM predicted event yields applying the modified event selection to simulated gluon fusion events are given in table 6.4.

The likelihood functions observed in the (extended) maximum likelihood fit to data using the modified event selection are shown in figures 9.10, 9.11 and 9.11. The non-extended likelihood estimators give the same values as obtained using the nominal event selection. The frequentist confidence levels for the non-extended likelihood fit can nevertheless change since the confidence intervals are determined using the modified gauge curves. The gauge curves for the tightened event selection are shown together with the illustration of the corresponding confidence intervals in figures 9.13, 9.14 and 9.15.

From the values given in table 9.8, it can be seen that the VBF suppressing event selection leads to slightly smaller confidence intervals when using the non-extended likelihood.

	ML estimator $\widehat{C}_i$ $[1 \times 10^{-11}\,\mathrm{GeV}^{-3}]$	low limit $[1 \times 10^{-11}\,\mathrm{GeV}^{-3}]$	high limit $[1 \times 10^{-11}\,\mathrm{GeV}^{-3}]$
C_2/Λ^3	0.51	−2.85	3.70
C_3/Λ^3	0.00	−7.15	7.20
C_5/Λ^3	5.25	−13.82	22.59

Table 9.8.: *Non-extended maximum likelihood estimators and corresponding frequentist confidence interval limits at 90% C.L. The reported results are obtained applying the tightened event selection criteria in order to suppress VBF Higgs boson production.*

	EML estimator $\widehat{C}_i$ $[1 \times 10^{-11}\,\mathrm{GeV}^{-3}]$	low limit $[1 \times 10^{-11}\,\mathrm{GeV}^{-3}]$	high limit $[1 \times 10^{-11}\,\mathrm{GeV}^{-3}]$
C_2/Λ^3	−3.91	−5.23	6.25
C_3/Λ^3	−9.90	−13.84	13.97
C_5/Λ^3	−14.25	−20.20	29.46

Table 9.9.: *Extended maximum likelihood estimators and corresponding frequentist confidence interval limits at 90% C.L. The reported results are obtained applying the tightened event selection criteria in order to suppress VBF Higgs boson production.*

The corresponding nominal results are reported in table 9.1. The differences concerning the lengths of the confidence intervals range between 2% to 5% for the three Wilson coefficients. The results for the extended maximum likelihood fit are given in table 9.9. Compared to the nominal analysis (see table 9.2), it can be seen that in this case the confidence intervals are slightly larger than without the additional cuts to suppress VBF Higgs boson production. The differences range between 6% to 9%. The same effect can be observed for the Bayesian confidence levels given in table 9.10 both for the non-extended and for the extended likelihood fit. The Bayesian limits for the nominal event selection are given in table 9.4.

The additional selection requirements in order to suppress VBF production processes are considered as an alternative analysis approach. Consequently, neither the nominal analysis nor this alternative approach are a priori expected to give improved confidence intervals compared to each other. The results show that the alternative event selection yields smaller confidence levels when using the non-extended likelihood fit, while in all other cases the

	low ML limit $[1 \times 10^{-11}\,\mathrm{GeV}^{-3}]$	high ML limit $[1 \times 10^{-11}\,\mathrm{GeV}^{-3}]$	low EML limit $[1 \times 10^{-11}\,\mathrm{GeV}^{-3}]$	high EML limit $[1 \times 10^{-11}\,\mathrm{GeV}^{-3}]$
C_2/Λ^3	−1.91	2.78	−5.25	5.25
C_3/Λ^3	−5.71	5.74	−13.24	13.23
C_5/Λ^3	−6.15	15.31	−20.40	27.87

Table 9.10.: *Bayesian confidence intervals observed with data. Results are shown for the non-extended ML fit and the extended ML fit. The reported results are obtained applying the tightened event selection criteria in order to suppress VBF Higgs boson production.*

nominal analysis gives smaller confidence intervals. It is therefore not possible to claim that one or the other analysis strategy yields better results. Moreover, the reasons for the observed differences in the results of both analysis strategies were not further investigated.

The comparison between the confidence intervals obtained for the tightened event selection suppressing VBF Higgs boson production and the nominal analysis was done without the inclusion of systematic uncertainties. Since the selection criteria applied for the VBF suppression depend on jet observables, the comparison could yield different results if systematic uncertainties are considered.

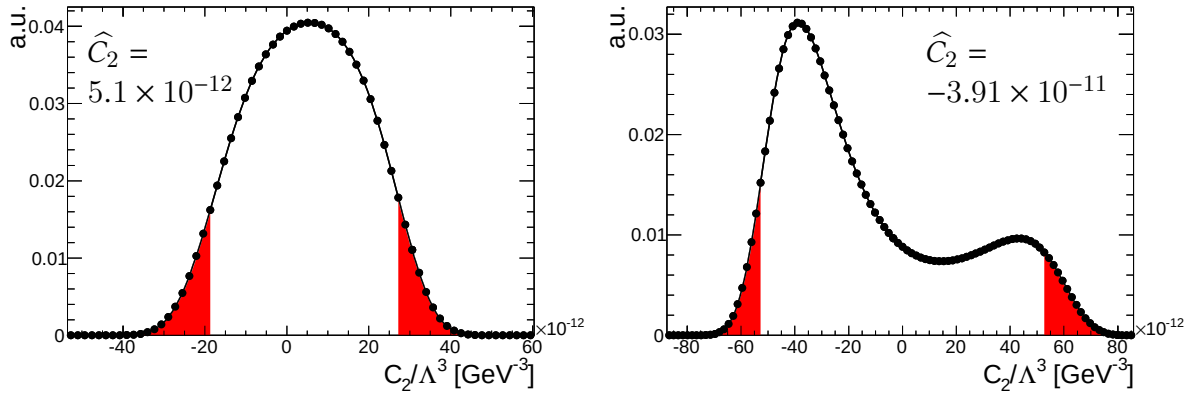

(a) *Non-extended likelihood* (b) *Extended likelihood*

Figure 9.10.: *Normalised likelihood functions observed in fit of the Wilson coefficient C_2 to data using VBF suppressing event selection. The approximate 5% and 95% quantile boundaries of the distribution are illustrated in red. The estimators are given in units of* GeV^{-3}

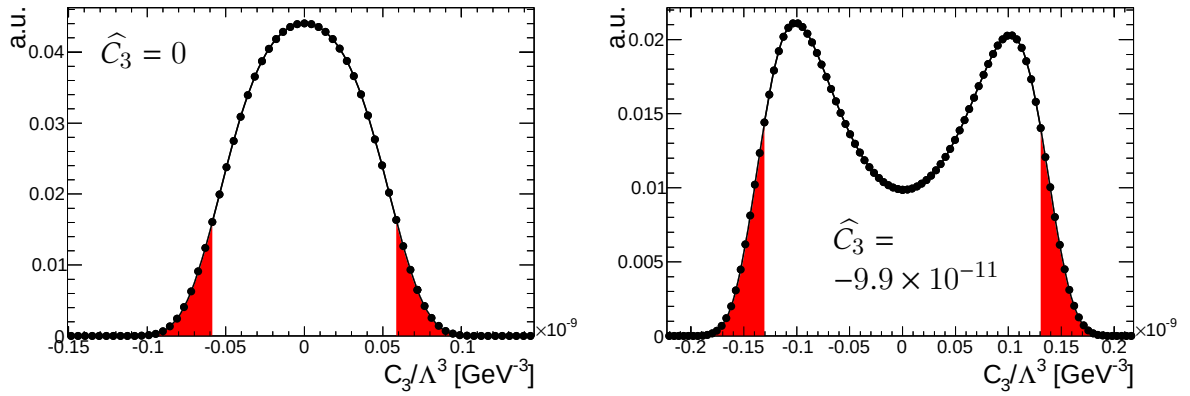

(a) *Non-extended likelihood* (b) *Extended likelihood*

Figure 9.11.: *Normalised likelihood functions observed in fit of the Wilson coefficient C_3 to data using VBF suppressing event selection. The approximate 5% and 95% quantile boundaries of the distribution are illustrated in red. The estimators are given in units of* GeV^{-3}

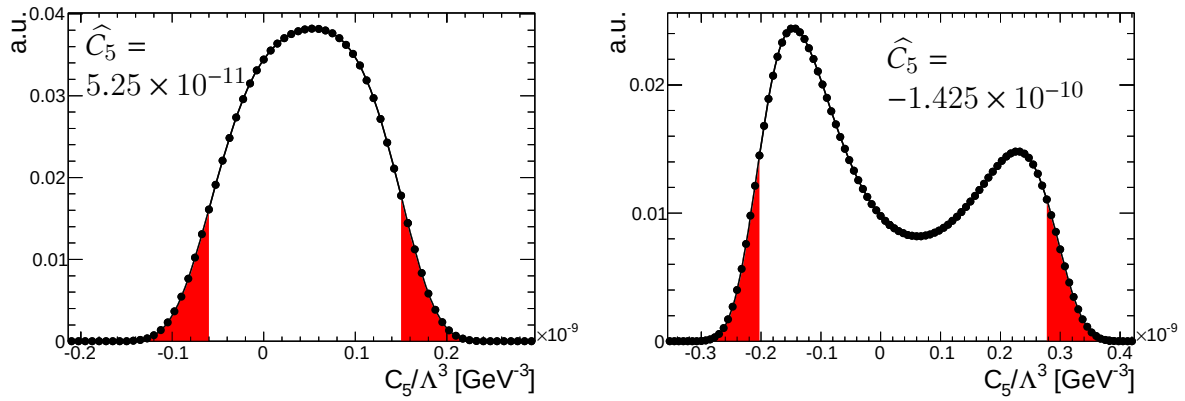

(a) *Non-extended likelihood*

(b) *Extended likelihood*

Figure 9.12.: *Normalised likelihood functions observed in fit of the Wilson coefficient C_5 to data using VBF suppressing selection strategy. The approximate 5% and 95% quantile boundaries of the distribution are illustrated in red. The estimators are given in units of* GeV^{-3}

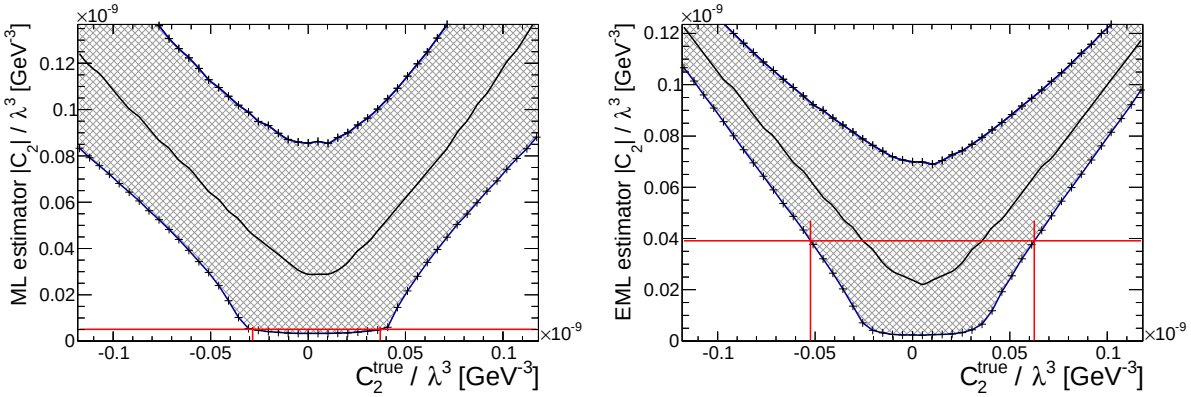

(a) *Confidence interval for non-extended likelihood. The marked estimator is* $|\widehat{C_2}| = 0.51 \times 10^{-11}\,\mathrm{GeV}^{-3}$*, the confidence interval is* $C_2 \in [-2.85, 3.70] \times 10^{-11}\mathrm{GeV}^{-3}$.

(b) *Confidence interval for ext. likelihood. The marked estimator is* $|\widehat{C_2}| = 3.91 \times 10^{-11}\,\mathrm{GeV}^{-3}$*, the confidence interval is* $C_2 \in [-5.23, 6.25] \times 10^{-11}\mathrm{GeV}^{-3}$.

Figure 9.13.: *Determination of confidence intervals using the Neyman confidence belts for the Wilson coefficient C_2 and applied VBF suppressing tightened event selection.*

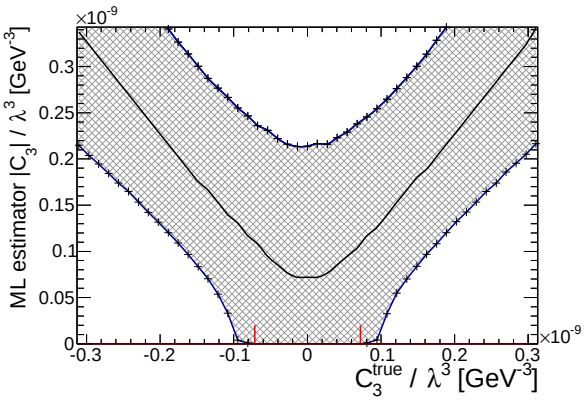

(a) *Confidence interval for non-extended likelihood. The marked estimator is* $|\widehat{C_3}| = 0.0 \times 10^{-11}\,\mathrm{GeV}^{-3}$*, the confidence interval is* $C_3 \in [-7.15, 7.20] \times 10^{-11}\mathrm{GeV}^{-3}$.

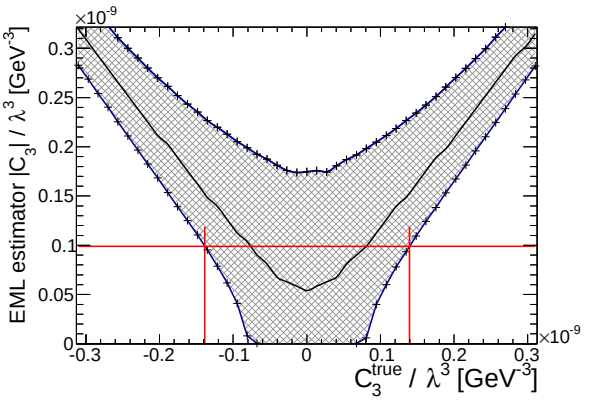

(b) *Confidence interval for ext. likelihood. The marked estimator is* $|\widehat{C_3}| = 9.90 \times 10^{-11}\,\mathrm{GeV}^{-3}$*, the confidence interval is* $C_2 \in [-13.84, 13.97] \times 10^{-11}\mathrm{GeV}^{-3}$.

Figure 9.14.: *Determination of confidence intervals using the Neyman confidence belts for the Wilson coefficient* C_3 *and applied VBF suppressing tightened event selection.*

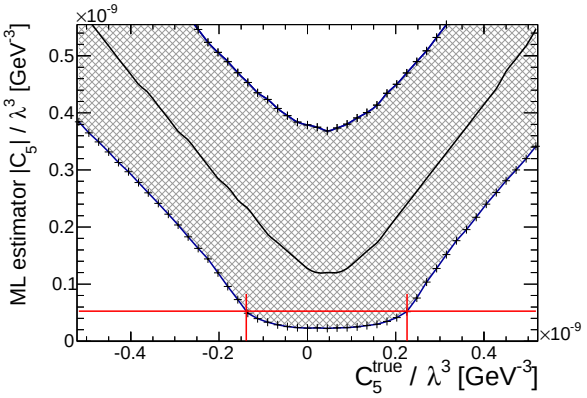

(a) *Confidence interval for non-extended likelihood. The marked estimator is* $|\widehat{C_5}| = 5.25 \times 10^{-11}\,\mathrm{GeV}^{-3}$*, the confidence interval is* $C_2 \in [-13.82, 22.59] \times 10^{-11}\mathrm{GeV}^{-3}$.

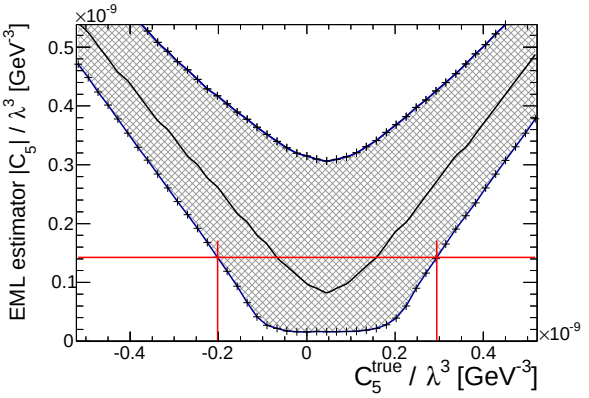

(b) *Confidence interval for ext. likelihood. The marked estimator is* $|\widehat{C_5}| = 14.25 \times 10^{-11}\,\mathrm{GeV}^{-3}$*, the confidence interval is* $C_5 \in [-20.20, 29.46] \times 10^{-11}\mathrm{GeV}^{-3}$.

Figure 9.15.: *Determination of confidence intervals using the Neyman confidence belts for the Wilson coefficient* C_5 *and applied VBF suppressing event selection.*

10. Conclusion

In this thesis, an analysis of the Higgs-gluon coupling tensor structure was presented. The analysis is based on data taken with the ATLAS detector in 2012 in proton-proton collisions at a center of mass energy $\sqrt{s} = 8\,\mathrm{TeV}$ and investigates events in the $H \to \gamma\gamma$ decay channel. The integrated luminosity of the data set is $\int \mathcal{L} = 20.7\,\mathrm{fb}^{-1}$.

The Higgs-gluon coupling can be described in an effective field theory [5] using point-like coupling operators O_i ($i = 1 \ldots 5$). The operator O_1 is of mass dimension five and describes a quark loop in the infinite mass limit while the other operators are of mass dimension seven. The operator O_4 does not contribute to processes considered in this analysis. This effective theory can be used to approximate the SM prediction of a top-loop induced Higgs-gluon coupling, but might also be capable to identify new physics at higher energy scales Λ emerging in an additional contribution of the point-like vertices to the coupling processes predicted in the Standard Model.

In this analysis, the Higgs boson transverse momentum distribution in events with at least one reconstructed jet is extracted from the ATLAS data and tested for an admixture of the point-like coupling operators O_i in addition to the SM operator. The contribution of each coupling operator is determined by the corresponding Wilson coefficient C_i. Confidence intervals are evaluated for each of the Wilson coefficients C_i separately while the other coefficients are set to zero. This approach is used to account for the limited statistics of signal events in the currently available data. Theoretical predictions at reconstruction level for the Higgs boson transverse momentum in $H + 1jet$ gluon fusion signal events for various Wilson coefficients are obtained by reweighting the corresponding SM Powheg sample.

The statistical uncertainties are dominated by uncertainties attributed to the estimation of the continuous diphoton background. This non-resonant background contribution is estimated in a signal+background fit to the diphoton mass spectra of events categorized due to the reconstructed transverse momentum of the Higgs boson candidate. The statistical uncertainty on the signal yield varies between approximately 50% and 80% in the seven p_T-bins. The signal strength observed in data for the applied event selection and after the continuum background subtraction is 2.0 ± 0.6. The resonant background, which is dominated by the VBF Higgs production process, is estimated using simulated events.

The frequentist confidence intervals for the Wilson coefficients are examined using the Neyman construction. Both the non-extended and the extended maximum likelihood method are applied. No confidence intervals could be constructed for the Wilson coefficient C_1. This is because the operator O_1 describes the Higgs-gluon coupling in the infinite quark mass limit and the shape of the Higgs boson p_T distribution for an additional presence of this operator is not distinguishable to that predicted in the SM with the currently available data set.

The influence of several systematic uncertainties was investigated and incorporated to the Neyman confidence belts for the Wilson coefficients C_2, C_3 and C_5.

A maximum likelihood fit and an extended maximum likelihood fit are applied to the Higgs p_T distribtion extracted from the ATLAS data in order to evaluate the likelihood estimators $\widehat{C}_i$ and to derive observed confidence intervals. The confidence intervals for the Wilson coefficients C_2, C_3 and C_5 using the data taken with the ATLAS detector are observed to be

	non-extended likelihood	extended likelihood
$C_2/\Lambda^3 \in$	$[-2.97\,,3.78] \times 10^{-11}\mathrm{GeV}^{-3}$	$[-4.84\,,5.83] \times 10^{-11}\mathrm{GeV}^{-3}$
$C_3/\Lambda^3 \in$	$[-7.50\,,7.53] \times 10^{-11}\mathrm{GeV}^{-3}$	$[-13.69\,,13.82] \times 10^{-11}\mathrm{GeV}^{-3}$
$C_5/\Lambda^3 \in$	$[-14.17\,,22.94] \times 10^{-11}\mathrm{GeV}^{-3}$	$[-18.97\,,28.15] \times 10^{-11}\mathrm{GeV}^{-3}$

These confidence intervals are determined for a coverage probability of 90%. They include both statistical and systematic uncertainties. The SM predicted value $C_i = 0$ is included in the confidence interval in all cases. Consequently, no deviation from the p_T distribution of the Higgs boson as predicted in the Standard Model is found. The larger intervals observed using the extended maximum likelihood are attributed to the increased signal strength observed in the ATLAS data set used in this analysis.

The confidence intervals are also evaluated using Bayesian statistics without considering systematic uncertainties, which yields smaller intervals particularly when using the non-extended likelihood. Moreover, results are additionally reported for two alternative analysis strategies concerning the estimation of resonant background. In all approaches, no deviation from the SM prediction was found while the interval limits are slightly different due to different assumptions made for their construction.

The influence of systematic uncertainties on the width of the confidence intervals for most Wilson coefficients is of the order 1% to 3% and is for all coefficients smaller than 5.2%. The impact of systematic uncertainties is dominated by theoretical uncertainties concerning the QCD scale used in the reweighting procedure. However, the overall uncertainty is dominated by the statistical uncertainties attributed to the non-resonant background estimation. The usage of data sets with higher statistics, which will become available in the run 2 of the LHC, therefore represents the most promising option to further reduce the range of the confidence intervals for the Wilson coefficients.

Bibliography

[1] M. Planck, *Vorträge Reden Erinnerungen*, ed. by H. Roos and A. Hermann, Springer Berlin Heidelberg, 2012, ISBN: 9783642625206, DOI: 10.1007/978-3-642-56594-6.

[2] ATLAS Collaboration, "Observation of a new particle in the search for the Standard Model Higgs boson with the ATLAS detector at the LHC", *Phys.Lett.* B716 (2012), 1–29, DOI: 10.1016/j.physletb.2012.08.020, arXiv: 1207.7214 [hep-ex].

[3] CMS Collaboration, "Observation of a new boson at a mass of 125 GeV with the CMS experiment at the LHC", *Phys.Lett.* B716 (2012), 30–61, DOI: 10.1016/j.physletb.2012.08.021, arXiv: 1207.7235 [hep-ex].

[4] Nobel Media AB 2014, ed., *The Nobel Prize in Physics 2013*, 2013, URL: www.nobelprize.org/nobel_prizes/physics/laureates/2013 (visited on 10/12/2014).

[5] R. V. Harlander and T. Neumann, "Probing the nature of the Higgs-gluon coupling", *Phys. Rev. D* 88 (7 Oct. 2013), 074015, DOI: 10.1103/PhysRevD.88.074015.

[6] D. Griffiths, *Introduction to Elementary Particles*, Physics Textbook, Wiley, 2008, ISBN: 9783527406012.

[7] S. Braibant, G. Giacomelli, and M. Spurio, *Particles and Fundamental Interactions: An Introduction to Particle Physics*, Undergraduate Lecture Notes in Physics, Springer, 2011, ISBN: 9789400724648.

[8] J. Beringer et al. (Particle Data Group), "Review of Particle Physics", *Physical Review D* 86.010001 (2012), 2013 partial update for the 2014 edition, URL: http://pdg.lbl.gov.

[9] M. Peskin and D. Schroeder, *An Introduction to Quantum Field Theory*, Advanced book classics, Addison-Wesley Publishing Company, 1995, ISBN: 9780201503975.

[10] P. Schmüser, *Feynman - Graphen und Eichtheorien Für Experimentalphysiker*, Lecture notes in physics, Springer Berlin Heidelberg, 1995, ISBN: 9783540584865.

[11] Y. Fukuda et al., "Evidence for oscillation of atmospheric neutrinos", *Phys.Rev.Lett.* 81 (1998), 1562–1567, DOI: 10.1103/PhysRevLett.81.1562, arXiv: hep-ex/9807003 [hep-ex].

[12] Q. Ahmad et al., "Measurement of the rate of $\nu_e + d \rightarrow p + p + e^-$ interactions produced by ^8B solar neutrinos at the Sudbury Neutrino Observatory", *Phys.Rev.Lett.* 87 (2001), 071301, DOI: 10.1103/PhysRevLett.87.071301, arXiv: nucl-ex/0106015 [nucl-ex].

[13] K. Eguchi et al., "First results from KamLAND: Evidence for reactor anti-neutrino disappearance", *Phys.Rev.Lett.* 90 (2003), 021802, DOI: 10.1103/PhysRevLett.90.021802, arXiv: hep-ex/0212021 [hep-ex].

[14] ATLAS Collaboration, "Measurement of the Higgs boson mass from the $H \rightarrow \gamma\gamma$ and $H \rightarrow ZZ^* \rightarrow 4l$ channels in pp collisions at center-of-mass energies of 7 and 8 TeV with the ATLAS detector", *Phys. Rev. D* 90 (5 Sept. 2014), 052004, DOI: 10.1103/PhysRevD.90.052004.

[15] CMS Collaboration, "Observation of the diphoton decay of the Higgs boson and measurement of its properties", *The European Physical Journal C* 74.10, 3076 (2014), ISSN: 1434-6044, DOI: 10.1140/epjc/s10052-014-3076-z, arXiv: 1407.0558 [hep-ex].

[16] S. Glashow, "Partial Symmetries of Weak Interactions", *Nucl.Phys.* 22 (1961), 579–588, DOI: 10.1016/0029-5582(61)90469-2.

[17] A. Salam, "Weak and Electromagnetic Interactions", *Conf.Proc.* C680519 (1968), 367–377.

[18] S. Weinberg, "A Model of Leptons", *Phys.Rev.Lett.* 19 (1967), 1264–1266, DOI: 10.1103/PhysRevLett.19.1264.

[19] V. Ezhela, S. Lugovsky, and O. Zenin, *Hadronic part of the muon g-2 estimated on the* $\sigma^{tot}_{2003}(e^+e^- \to \textit{hadrons})$ *evaluated data compilation*, IHEP-2003-35, 2003, arXiv: hep-ph/0312114 [hep-ph].

[20] G. 'tHooft, "Renormalization of massless Yang-Mills fields", *Nuclear Physics B* 33.1 (1971), 173–199, ISSN: 0550-3213, DOI: 10.1016/0550-3213(71)90395-6.

[21] P. W. Higgs, "Broken Symmetries and the Masses of Gauge Bosons", *Phys. Rev. Lett.* 13 (16 Oct. 1964), 508–509, DOI: 10.1103/PhysRevLett.13.508.

[22] P. W. Higgs, "Spontaneous Symmetry Breakdown without Massless Bosons", *Phys. Rev.* 145 (4 May 1966), 1156–1163, DOI: 10.1103/PhysRev.145.1156.

[23] F. Englert and R. Brout, "Broken Symmetry and the Mass of Gauge Vector Mesons", *Phys. Rev. Lett.* 13 (9 Aug. 1964), 321–323, DOI: 10.1103/PhysRevLett.13.321.

[24] P. W. Anderson, "Plasmons, Gauge Invariance, and Mass", *Phys. Rev.* 130 (1 Apr. 1963), 439–442, DOI: 10.1103/PhysRev.130.439.

[25] G. S. Guralnik, C. R. Hagen, and T. W. B. Kibble, "Global Conservation Laws and Massless Particles", *Phys. Rev. Lett.* 13 (20 Nov. 1964), 585–587, DOI: 10.1103/PhysRevLett.13.585.

[26] T. W. B. Kibble, "Symmetry Breaking in Non-Abelian Gauge Theories", *Phys. Rev.* 155 (5 Mar. 1967), 1554–1561, DOI: 10.1103/PhysRev.155.1554.

[27] H. v. Radziewski, "Search for the Neutral Higgs Bosons of the Minimal Supersymmetric Standard Model in the $\tau_e\tau_\mu$-Decay Mode at $\sqrt{s} = 7\,\mathrm{GeV}$ with the ATLAS Detector", PhD thesis, 2014, URN: urn:nbn:de:bsz:25-opus-94873.

[28] LHC Higgs Cross Section Working Group, *Handbook of LHC Higgs Cross Sections: 3. Higgs Properties*, CERN-2013-004, 2013, DOI: 10.5170/CERN-2013-004, arXiv: 1307.1347 [hep-ph].

[29] B. W. Lee, C. Quigg, and H. B. Thacker, "Weak interactions at very high energies: The role of the Higgs-boson mass", *Phys. Rev. D* 16 (5 Sept. 1977), 1519–1531, DOI: 10.1103/PhysRevD.16.1519.

[30] S. Dittmaier and M. Schumacher, "The Higgs Boson in the Standard Model - From LEP to LHC: Expectations, Searches, and Discovery of a Candidate", *Prog.Part.Nucl.Phys.* 70 (2013), 1–54, DOI: 10.1016/j.ppnp.2013.02.001, arXiv: 1211.4828 [hep-ph].

[31] J. Ellis et al., "The probable fate of the Standard Model", *Physics Letters B* 679.4 (2009), 369–375, ISSN: 0370-2693, DOI: 10.1016/j.physletb.2009.07.054.

[32] M. Baak et al., July 2014, URL: http://project-gfitter.web.cern.ch/project-gfitter/Standard_Model/index.html.

[33] M. Baak et al., *The global electroweak fit at NNLO and prospects for the LHC and ILC*, DESY-14-124, 2014, arXiv: 1407.3792 [hep-ph].

[34] S. D. Drell and T.-M. Yan, "Partons and their applications at high energies", *Annals of Physics* 66.2 (1971), 578–623, ISSN: 0003-4916, DOI: 10.1016/0003-4916(71)90071-6.

[35] J. M. Campbell, J. W. Huston, and W. J. Stirling, "Hard interactions of quarks and gluons: a primer for LHC physics", *Reports on Progress in Physics* 70.1 (2007), 89, DOI: 10.1088/0034-4885/70/1/R02.

[36] C. N. Yang, "Selection Rules for the Dematerialization of a Particle into Two Photons", *Phys. Rev.* 77 (2 Jan. 1950), 242–245, DOI: 10.1103/PhysRev.77.242.

[37] L. D. Landau, "The moment of a 2-photon system", *Doklady Akademii Nauk SSSR* 60 (1948), 207–209.

[38] ATLAS Collaboration, "Evidence for the spin-0 nature of the Higgs boson using ATLAS data", *Physics Letters B* 726.1–3 (2013), 120–144, ISSN: 0370-2693, DOI: 10.1016/j.physletb.2013.08.026.

[39] ATLAS Collaboration, *Measurement of Higgs boson production in the diphoton decay channel in pp collisions at center-of-mass energies of 7 and 8 TeV with the ATLAS detector*, CERN-PH-EP-2014-198, 2014, arXiv: 1408.7084 [hep-ex].

[40] ATLAS Collaboration, *Updated coupling measurements of the Higgs boson with the ATLAS detector using up to 25 fb^{-1} of proton-proton collision data*, ATLAS-CONF-2014-009, Mar. 2014.

[41] Z. Maki, M. Nakagawa, and S. Sakata, "Remarks on the unified model of elementary particles", *Progress of Theoretical Physics* 28.5 (1962), 870–880, DOI: 10.1143/PTP.28.870.

[42] G. Bertone, D. Hooper, and J. Silk, "Particle dark matter: evidence, candidates and constraints", *Physics Reports* 405.5–6 (2005), 279–390, ISSN: 0370-1573, DOI: 10.1016/j.physrep.2004.08.031.

[43] N. Berger, "The Mu3e Experiment", *Nuclear Physics B - Proceedings Supplements* 248–250 (2014), 35–40, ISSN: 0920-5632, DOI: 10.1016/j.nuclphysbps.2014.02.007.

[44] A. V. Manohar, "Effective field theories", *Perturbative and nonperturbative aspects of quantum field theory*, Springer, 1997, 311–362.

[45] E. Fermi, "Tentativo di una Teoria Dei Raggi β", Italian, *Il Nuovo Cimento* 11.1 (1934), 1–19, ISSN: 0029-6341, DOI: 10.1007/BF02959820.

[46] F. L. Wilson, "Fermi's Theory of Beta Decay", *American Journal of Physics* 36.12 (1968), 1150–1160, DOI: 10.1119/1.1974382.

[47] L. Evans and P. Bryant, "LHC Machine", *JINST* 3.08 (2008), S08001, DOI: 10.1088/1748-0221/3/08/S08001.

[48] ATLAS Collaboration, "The ATLAS Experiment at the CERN Large Hadron Collider", *JINST* 3.08 (2008), S08003, DOI: 10.1088/1748-0221/3/08/S08003.

[49] M. Hostettler and G. Papotti, *Luminosity Lifetime at the LHC in 2012 Proton Physics*, CERN-ACC-2013-0032, May 2013, 1403.

[50] G. Papotti et al., *Observations of beam-beam effects at the LHC*, CERN-2014-004, Sept. 2014, 1–5, DOI: 10.5170/CERN-2014-004, arXiv: 1409.5208 [physics.acc-ph].

[51] AC Team, "The four main LHC experiments", CERN-AC-9906026, June 1999, URL: http://cds.cern.ch/record/40525.

[52] ATLAS Collaboration, "Studies of the performance of the ATLAS detector using cosmic-ray muons", *The European Physical Journal C* 71.3, 1593 (2011), ISSN: 1434-6044, DOI: 10.1140/epjc/s10052-011-1593-6.

[53] ATLAS Collaboration, "Performance of the ATLAS detector using first collision data", *JHEP* 2010.9, 056 (2010), DOI: 10.1007/JHEP09(2010)056, arXiv: 1005.5254 [hep-ex].

[54] N. Nikiforou, *Performance of the ATLAS liquid argon calorimeter after three years of LHC operation and plans for a future upgrade*, June 2013, 1–12, DOI: 10.1109/ANIMMA.2013.6728060.

[55] B. A. Petersen, *The ATLAS Trigger Performance and Evolution*, ATL-DAQ-PROC-2012-071, Nov. 2012.

[56] ATLAS Collaboration, *Measurements of the properties of the Higgs-like boson in the two photon decay channel with the ATLAS detector using 25* fb^{-1} *of proton-proton collision data*, ATLAS-CONF-2013-012, Mar. 2013.

[57] ATLAS Collaboration, *Performance of pile-up subtraction for jet shapes*, ATLAS-CONF-2013-085, Aug. 2013.

[58] S. Frixione, P. Nason, and C. Oleari, "Matching NLO QCD computations with parton shower simulations: the POWHEG method", *JHEP* 2007.11, 070 (2007), DOI: 10.1088/1126-6708/2007/11/070.

[59] S. Alioli et al., "NLO Higgs boson production via gluon fusion matched with shower in POWHEG", *JHEP* 2009.04, 002 (2009), DOI: 10.1088/1126-6708/2009/04/002.

[60] P. Nason and C. Oleari, "NLO Higgs boson production via vector-boson fusion matched with shower in POWHEG", *JHEP* 2010.2, 37 (2010), DOI: 10.1007/JHEP02(2010)037.

[61] T. Sjöstrand, S. Mrenna, and P. Skands, "A brief introduction to PYTHIA 8.1", *Computer Physics Communications* 178.11 (2008), 852–867, ISSN: 0010-4655, DOI: 10.1016/j.cpc.2008.01.036.

[62] S. Catani et al., "Soft-gluon resummation for Higgs boson production at hadron colliders", *JHEP* 2003.07, 028 (2003), DOI: 10.1088/1126-6708/2003/07/028.

[63] D. de Florian et al., "Transverse-momentum resummation: Higgs boson production at the Tevatron and the LHC", *JHEP* 2011.11, 64 (2011), DOI: 10.1007/JHEP11(2011)064.

[64] H.-L. Lai et al., "New parton distributions for collider physics", *Phys. Rev. D* 82 (7 Oct. 2010), 074024, DOI: 10.1103/PhysRevD.82.074024.

[65] P. M. Nadolsky et al., "Implications of CTEQ global analysis for collider observables", *Phys. Rev. D* 78 (1 July 2008), 013004, DOI: 10.1103/PhysRevD.78.013004.

[66] ATLAS Collaboration, "The ATLAS Simulation Infrastructure", *The European Physical Journal C* 70.3 (2010), 823–874, ISSN: 1434-6044, DOI: 10.1140/epjc/s10052-010-1429-9.

[67] S. Agostinelli et al., "Geant4—a simulation toolkit", *Nuclear Instruments and Methods in Physics Research Section A: Accelerators, Spectrometers, Detectors and Associated Equipment* 506.3 (2003), 250–303, ISSN: 0168-9002, DOI: 10.1016/S0168-9002(03)01368-8.

[68] ATLAS Collaboration, *Differential cross sections of the Higgs boson measured in the diphoton decay channel using 8 TeV pp collisions*, ATLAS-CONF-2013-072, July 2013.

[69] ATLAS Collaboration, "Electron performance measurements with the ATLAS detector using the 2010 LHC proton-proton collision data", *The European Physical Journal C* 72.3, 1909 (2012), ISSN: 1434-6044, DOI: 10.1140/epjc/s10052-012-1909-1.

[70] L. Dixon and M. S. Siu, "Resonance-Continuum Interference in the Diphoton Higgs Signal at the LHC", *Phys. Rev. Lett.* 90 (25 June 2003), 252001, DOI: 10.1103/PhysRevLett.90.252001.

[71] ATLAS Collaboration, *Measurement of the muon reconstruction performance of the ATLAS detector using 2011 and 2012 LHC proton-proton collision data*, CERN-PH-EP-2014-151, 2014, arXiv: 1407.3935 [hep-ex].

[72] ATLAS Collaboration, *Electron efficiency measurements with the ATLAS detector using the 2012 LHC proton-proton collision data*, ATLAS-CONF-2014-032, June 2014.

[73] ATLAS Collaboration, *Expected photon performance in the ATLAS experiment*, ATL-PHYS-PUB-2011-007, Apr. 2011.

[74] ATLAS Collaboration, *Observation of an excess of events in the search for the Standard Model Higgs boson in the gamma-gamma channel with the ATLAS detector*, ATLAS-CONF-2012-091, July 2012.

[75] ATLAS Collaboration, *Measurements of the photon identification efficiency with the ATLAS detector using 4.9 fb−1 of pp collision data collected in 2011*, ATLAS-CONF-2012-123, Aug. 2012.

[76] ATLAS Collaboration, *Measurements of the photon identification efficiencies using* $20.3\ \mathrm{fb}^{-1}$ *of pp collisions collected by ATLAS at* $\sqrt{s} = 8\ \mathrm{TeV}$ *in 2012*, ATL-COM-PHYS-2014-542, 2014.

[77] M. Cacciari, G. P. Salam, and G. Soyez, "The Anti-k_t jet clustering algorithm", *JHEP* 0804, 063 (2008), DOI: 10.1088/1126-6708/2008/04/063, arXiv: 0802.1189 [hep-ph].

[78] W. Lampl et al., *Calorimeter Clustering Algorithms: Description and Performance*, ATL-LARG-PUB-2008-002. ATL-COM-LARG-2008-003, Apr. 2008.

[79] M. Cacciari and G. P. Salam, "Pileup subtraction using jet areas", *Physics Letters B* 659.1–2 (2008), 119–126, ISSN: 0370-2693, DOI: 10.1016/j.physletb.2007.09.077.

[80] G. Cowan, *Statistical Data Analysis*, Oxford science publications, Oxford University Press, 1998, ISBN: 9780198501558.

[81] W. Verkerke and D. Kirkby, *The RooFit toolkit for data modeling*, 2003, arXiv: physics/0306116 [physics.data-an].

[82] W. Verkerke and D. Kirkby, *RooFit Users Manual v2. 91*, 2008, URL: http://roofit.sourceforge.net.

[83] J. Gaiser, "Charmonium Spectroscopy from Radiative Decays of the J/ψ and ψ'", PhD thesis, 1982.

[84] M. J. Oreglia, "Study of the reactions $\psi' \to \gamma\gamma\psi$", PhD thesis, 1980.

[85] ATLAS Collaboration, "Electron and photon energy calibration with the ATLAS detector using LHC Run 1 data", *The European Physical Journal C* 74.10, 3071 (2014), ISSN: 1434-6044, DOI: 10.1140/epjc/s10052-014-3071-4.

[86] ATLAS Collaboration, "Jet energy resolution in proton-proton collisions at $\sqrt{s} = 7$ TeV recorded in 2010 with the ATLAS detector", *The European Physical Journal C* 73.3, 2306 (2013), ISSN: 1434-6044, DOI: 10.1140/epjc/s10052-013-2306-0.

[87] ATLAS Collaboration, "Jet energy measurement with the ATLAS detector in proton-proton collisions at $\sqrt{s} = 7\ \mathrm{TeV}$", *The European Physical Journal C* 73.3, 2304 (2013), ISSN: 1434-6044, DOI: 10.1140/epjc/s10052-013-2304-2.

[88] ATLAS Collaboration, *Jet energy measurement and its systematic uncertainty in proton-proton collisions at $\sqrt{s} = 7$ TeV with the ATLAS detector*, CERN-PH-EP-2013-222, 2014, arXiv: 1406.0076 [hep-ex].

[89] J. Neyman, "Outline of a Theory of Statistical Estimation Based on the Classical Theory of Probability", *Philosophical Transactions of the Royal Society of London. Series A, Mathematical and Physical Sciences* 236.767 (1937), 333–380, DOI: 10.1098/rsta.1937.0005.

[90] ATLAS Collaboration, CMS Collaboration, and LHC Higgs Combination Group, *Procedure for the LHC Higgs boson search combination in summer 2011*, ATL-PHYS-PUB-2011-011, CMS-NOTE-2011-005, 2011.

[91] T. Bayes, "An Essay towards Solving a Problem in the Doctrine of Chances.", *Philosophical Transactions* 53 (1763), 370–418, DOI: 10.1098/rstl.1763.0053.

[92] R. A. Fisher, "On the Mathematical Foundations of Theoretical Statistics", *Philosophical Transactions of the Royal Society of London. Series A, Mathematical and Physical Sciences* 222.594-604 (1922), 309–368, DOI: 10.1098/rsta.1922.0009.

A. The Method of Maximum Likelihood

The method of maximum likelihood [92] is used in various parts of the analysis described in this thesis. This section explains the basic theoretical principles of this method and is based on the descriptions in reference [80].

The method of maximum likelihood is a statistical method to estimate a parameter θ or a set of parameters $\boldsymbol{\theta}$ for which the realisation of an observed dataset with an observable x is considered as most likely. The method widely used in elementary particle physics and other fields of application for hypotheses tests. It is applicable if the probability density function of the observable depending on $\boldsymbol{\theta}$, $f(x;\, \boldsymbol{\theta})$, is analytically known. In this case, the joint probability density functions for n independent measurements $\boldsymbol{x} = \{x_1, \ldots, x_n\}$ of the observable x is obtained as the product of the individual probability density functions (pdf) for each realisation x_i:

$$f(\boldsymbol{x};\, \boldsymbol{\theta}) \;=\; \prod_{i=1}^{n} f(x_i;\, \boldsymbol{\theta}) \;. \tag{A.1}$$

This joint pdf is defined as the likelihood function $\mathcal{L}(\boldsymbol{\theta};\, \boldsymbol{x})$ for one particular set of measurements $\boldsymbol{x}$:

$$\mathcal{L}(\boldsymbol{\theta};\, \boldsymbol{x}) = \prod_{i=1}^{n} f(x_i;\, \boldsymbol{\theta}) \;. \tag{A.2}$$

The maximum likelihood estimator $\widehat{\boldsymbol{\theta}}$ is defined as the parameter set $\boldsymbol{\theta}$ that maximizes the likelihood function $\mathcal{L}(\boldsymbol{\theta};\, \boldsymbol{x})$ with respect to $\boldsymbol{\theta}$. For technical reasons, in many applications the natural logarithm $\log \mathcal{L}(\boldsymbol{\theta};\, \boldsymbol{x})$ is maximised:

$$\log\left(\mathcal{L}(\widehat{\boldsymbol{\theta}};\, \boldsymbol{x})\right) := \max \log\left(\mathcal{L}(\boldsymbol{\theta};\, \boldsymbol{x})\right) = \max \sum_{i=1}^{n} \log\left(f(x_i;\, \boldsymbol{\theta})\right) \;. \tag{A.3}$$

For the applications in this analysis, measured distributions of observables are recorded in histograms of N bins, hence a binned maximum likelihood fit is performed. More over, the actual measurement is in some parts of the analysis simulated by pseudo-experiments performed with Monte Carlo predictions. The histograms obtained in these pseudo-experiments are then treated in the same way as actual observations in data. The number of observations n_{tot}, which is for the applications in this thesis represented by the integral of the data histogram, can either be treated as fixed or be considered as another observable.

On the one hand, if n_{tot} is treated as fixed, only the shape of distributions is considered. In this case, the expectation value $\nu_i(\boldsymbol{\theta})$ for the content n_i of bin i with limits $x_i^{\min}$ and $x_i^{\max}$, that is determined by the corresponding pdf $f(x;\boldsymbol{\theta})$ of the binned observable x, is given by

$$\nu_i(\boldsymbol{\theta}) = n_{\text{tot}} \int_{x_i^{\min}}^{x_i^{\max}} f(x;\boldsymbol{\theta})\,\mathrm{d}x = n_{\text{tot}} \cdot p_i(\boldsymbol{\theta}) \ . \tag{A.4}$$

where $p_i(\boldsymbol{\theta})$ denotes the predicted probability for an observation of x in bin i and n_{tot} is the observed total number of events.

On the other hand, if n_{tot} is considered as an additional observable, an extended binned likelihood fit is performed. In this case, the expectation value ν_i additionally depends on the expected total number of observations, which is denoted by ν_{tot}, and is given by

$$\nu_i(\boldsymbol{\theta}, \nu_{\text{tot}}) = \nu_{\text{tot}} \int_{x_i^{\min}}^{x_i^{\max}} f(x;\boldsymbol{\theta})\,\mathrm{d}x = \nu_{\text{tot}} \cdot p_i(\boldsymbol{\theta}) \ . \tag{A.5}$$

The likelihood function for the observation of a particular histogram with bin contents $\boldsymbol{n} = (n_1, n_2, \ldots n_N)$ is given by the product of the probability functions $f_i(n_i)$ for each bin. The observations of the contents n_i in each bin are in all applications of this thesis treated as uncorrelated.

In most cases, the bin contents n_i are assumed to be Poisson-distributed, so that

$$f_i(n_i;\nu_i) = \frac{\nu_i^{n_i}\, e^{-\nu_i}}{n_i!} \tag{A.6}$$

with ν_i determined according to (A.5) or (A.4), respectively, depending on whether an extended likelihood is performed or not. Poisson-distributed bin contents are for example given for the fitted binned diphoton mass spectra in chapter 6. Indeed, for the pseudo-experiments generated based on MC predictions, which are described in section 8 and simulate the background subtracted Higgs transverse momentum spectrum observed in data, a log-normal distribution is chosen as probability density function for the bin contents to account for the fit uncertainties. The reasons for the choice of this function and its parametrisation are discussed in chapter 8.

Regardless of the actual form of the probability functions $f_i(n_i)$, the log-Likelihood function for the observation of a particular histogram with uncorrelated bin contents $\boldsymbol{n}$ is given analogous to (A.2) and (A.3) by

$$\log \mathcal{L}(\boldsymbol{\theta};\, \boldsymbol{n}) = \sum_{i=1}^{N} \log f_i(n_i;\nu_i(\boldsymbol{\theta})) \tag{A.7}$$

$$\log \mathcal{L}^{\text{ext}}(\boldsymbol{\theta};\, \boldsymbol{n}) = \sum_{i=1}^{N} \log f_i(n_i;\nu_i(\boldsymbol{\theta}, \nu_{\text{tot}})) \tag{A.8}$$

for the non-extended and the extended likelihood, respectively.

B. Additional Figures

B.1. Test of Reweighted Distributions

Including all initial states

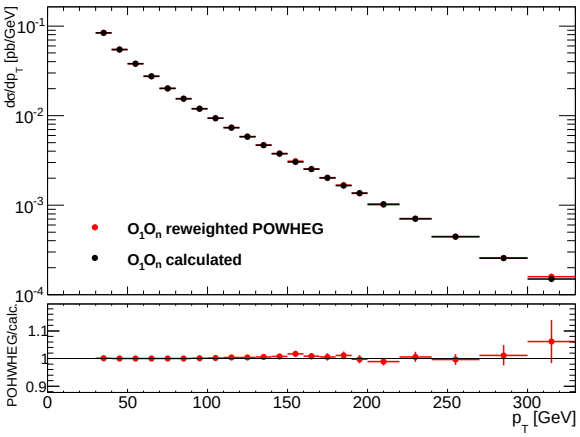

Figure B.1.: *Comparison between reweighted* POWHEG *prediction of* $\sum_{i=1}^{5} O_1 O_i$ *operator terms to the differential Higgs production cross section dependent on* p_T *in 1jet events at parton level and the corresponding leading order calculation. The reweighted* POWHEG *distribution is normalised according to the normalisation factor obtained for the SM distributions in figure 4.3a.*

gluon-gluon initial state

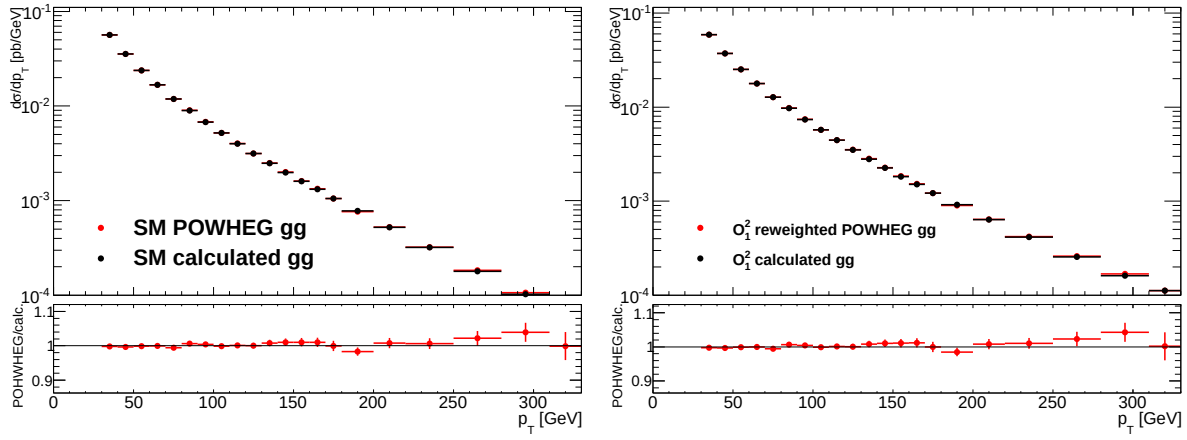

(a) *Standard Model*

(b) O_1^2

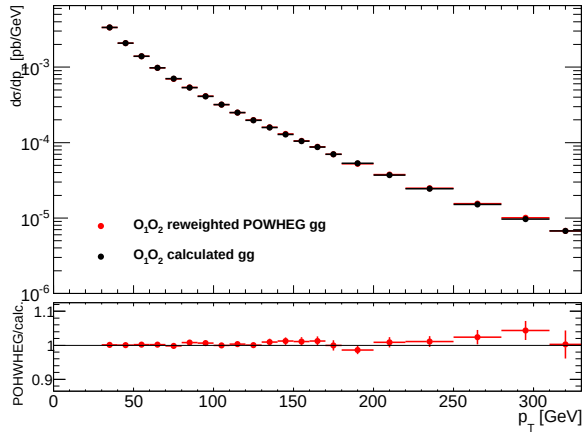

(c) O_1O_2

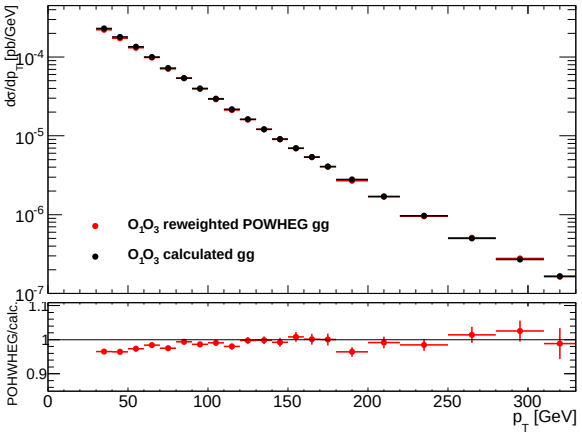

(d) O_1O_3

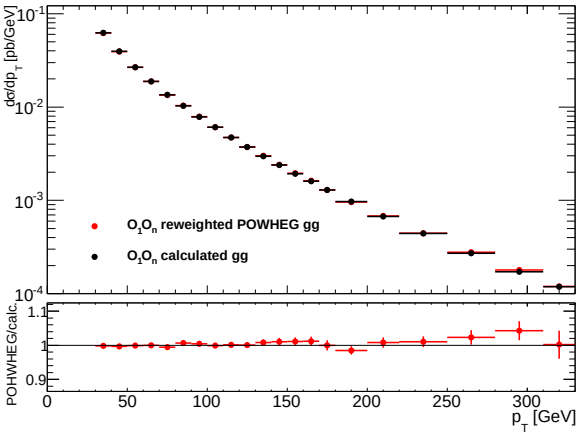

(e) $\Sigma O_1 O_i$

Figure B.2.: *Comparison between reweighted* POWHEG *prediction of contribution of different operator terms to the differential Higgs production cross section dependent on p_T in 1jet events at parton level and the corresponding leading order calculations in the gluon-gluon initial state channel. The reweighted* POWHEG *distributions are normalised according to the normalisation factor obtained for the SM distributions for which the* POWHEG *distribution is normalised to the calculated one.*

quark-gluon initial state

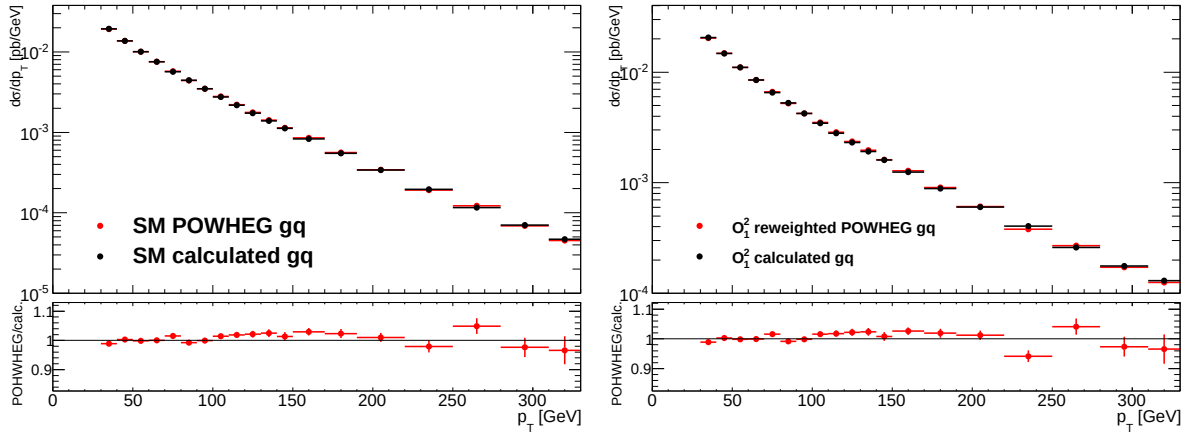

(a) *Standard Model*

(b) O_1^2

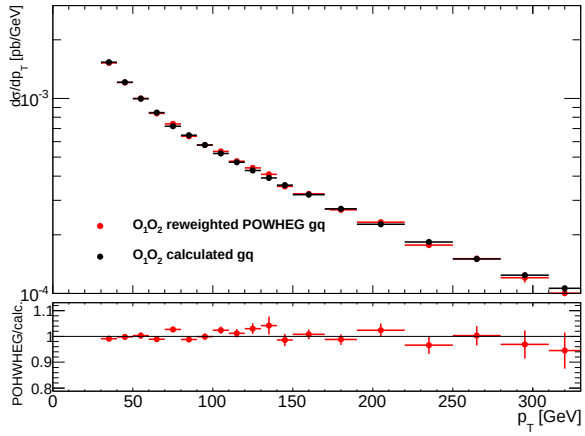

(c) $O_1 O_2$

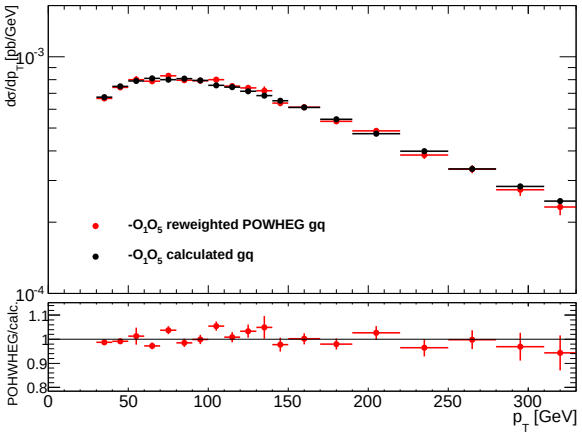

(d) $-O_1 O_5$

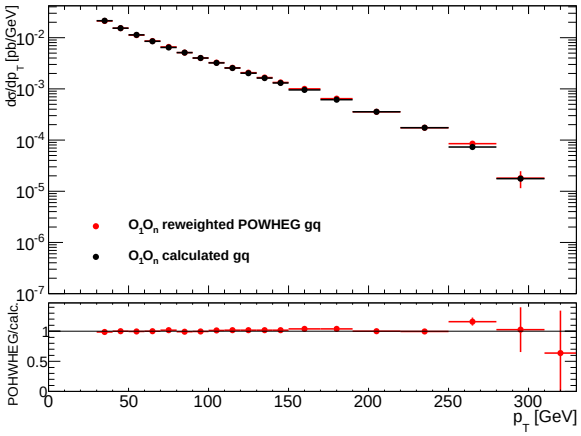

(e) $\Sigma O_1 O_i$

Figure B.3.: *Comparison between reweighted* POWHEG *prediction of contribution of different operator terms to the differential Higgs production cross section dependent on p_T in 1jet events at parton level and the corresponding leading order calculations in the gluon-(anti)quark initial state channel. The reweighted* POWHEG *distributions are normalised according to the normalisation factor obtained for the SM distributions for which the* POWHEG *distribution is normalised to the calculated one.*

quark-quark initial state

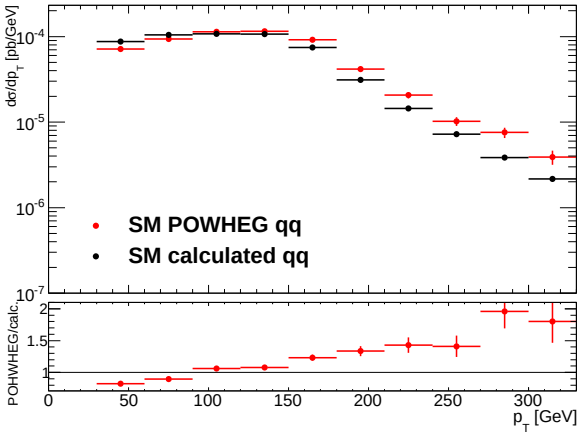

(a) *Standard Model*

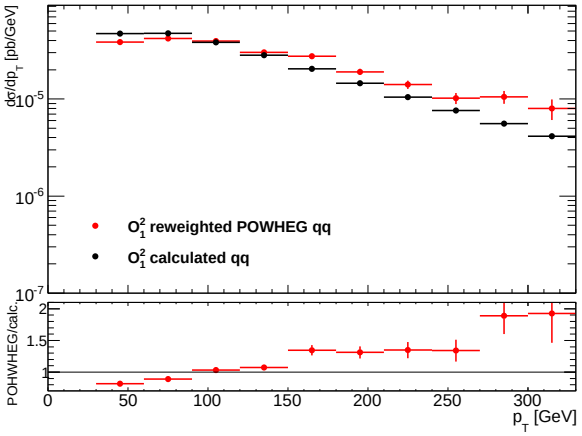

(b) O_1^2

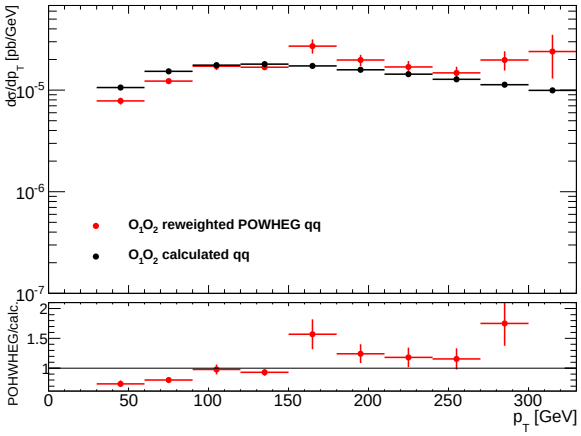

(c) $-O_1O_2$

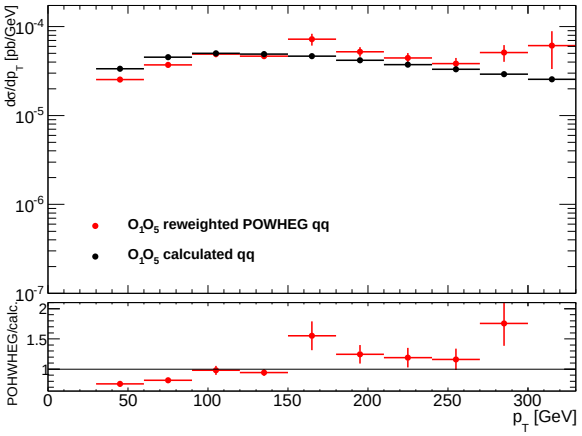

(d) O_1O_5

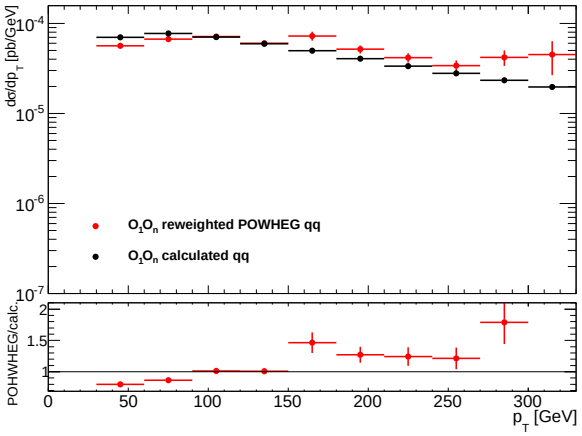

(e) $\Sigma O_1 O_i$

Figure B.4.: *Comparison between reweighted* POWHEG *prediction of contribution of different operator terms to the differential Higgs production cross section dependent on p_T in 1jet events at parton level and the corresponding leading order calculations in the quark-antiquark initial state channel. The reweighted* POWHEG *distributions are normalised according to the normalisation factor obtained for the SM distributions for which the* POWHEG *distribution is normalised to the calculated one.*

B.2. Signal Fit of Higgs Boson Mass Peak

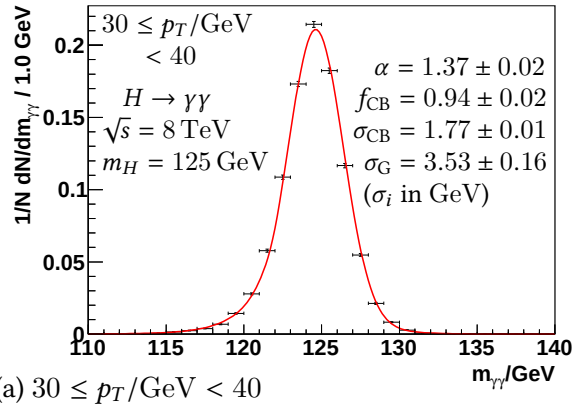

(a) $30 \leq p_T/\text{GeV} < 40$

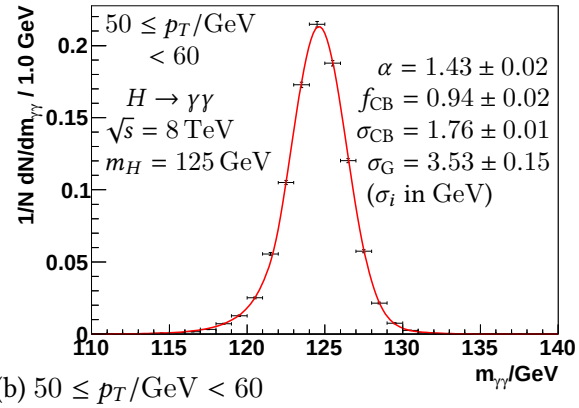

(b) $50 \leq p_T/\text{GeV} < 60$

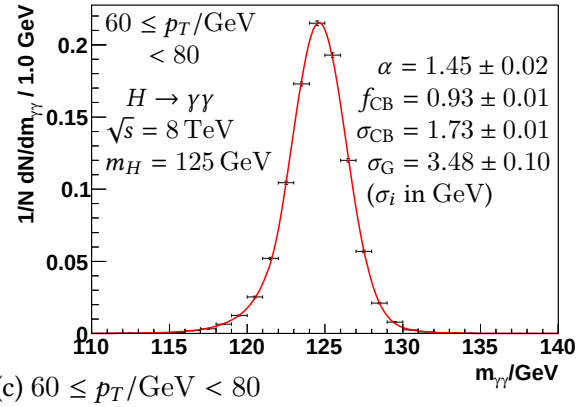

(c) $60 \leq p_T/\text{GeV} < 80$

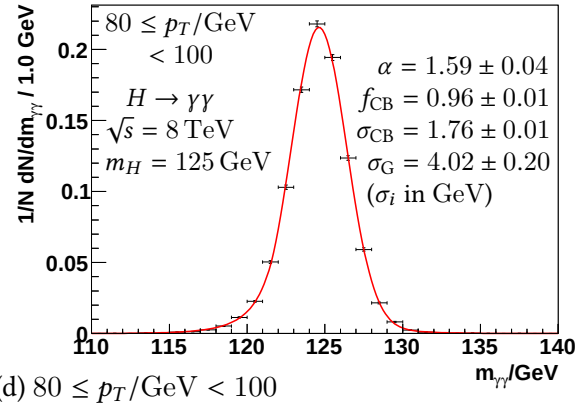

(d) $80 \leq p_T/\text{GeV} < 100$

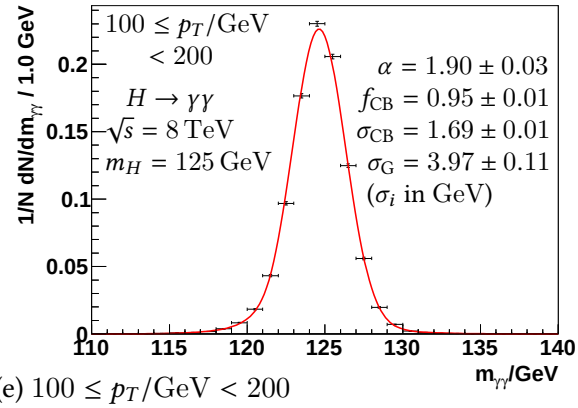

(e) $100 \leq p_T/\text{GeV} < 200$

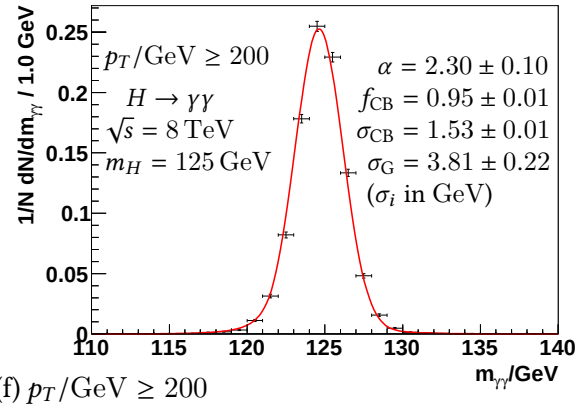

(f) $p_T/\text{GeV} \geq 200$

Figure B.5.: *Plots of simultaneous signal fit in p_T-bins using simulated $H \to \gamma\gamma$ events. The modelled peak position for all bins is* $\mu = 124.625(3)$ GeV.

B.3. Background Fit of Diphoton Mass Spectra

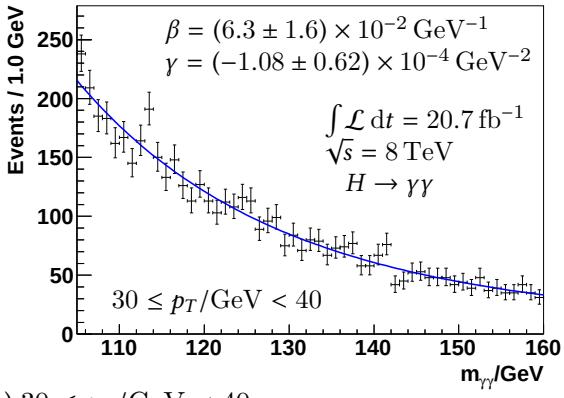

(a) $30 \le p_T/\mathrm{GeV} < 40$

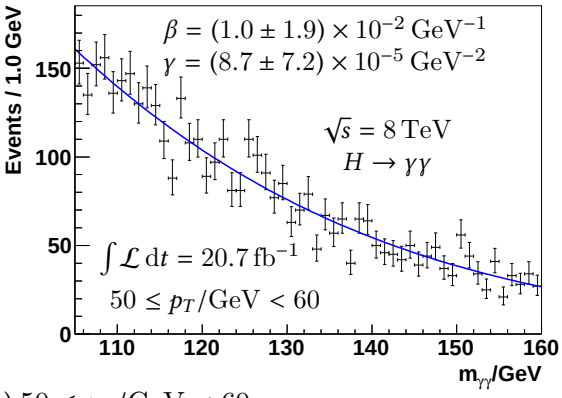

(b) $50 \le p_T/\mathrm{GeV} < 60$

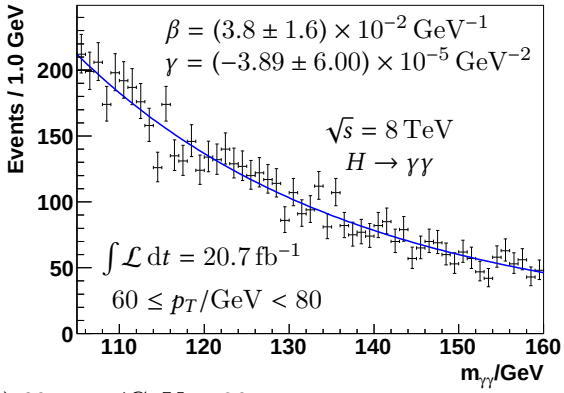

(c) $60 \le p_T/\mathrm{GeV} < 80$

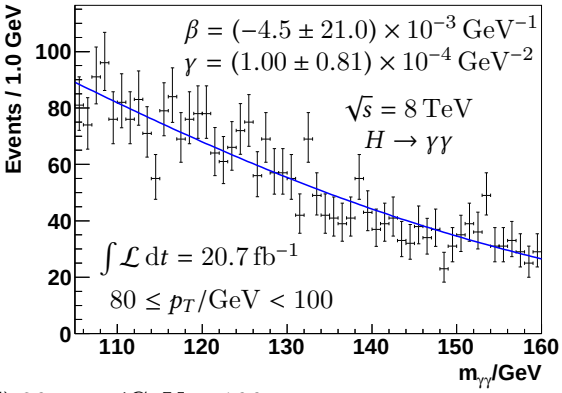

(d) $80 \le p_T/\mathrm{GeV} < 100$

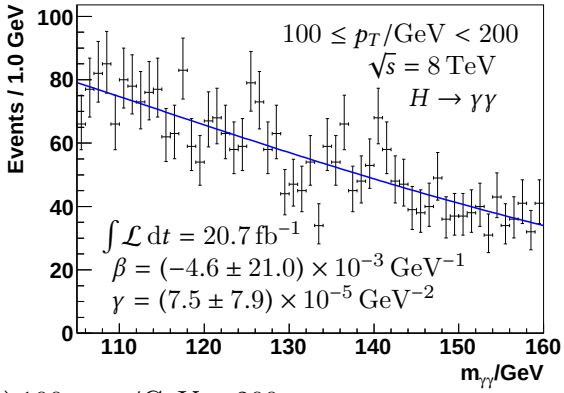

(e) $100 \le p_T/\mathrm{GeV} < 200$

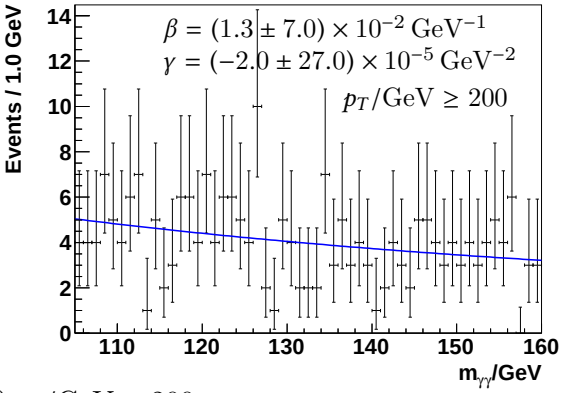

(f) $p_T/\mathrm{GeV} \ge 200$

Figure B.6.: *Plots of background fits on mass spectra in p_T-bins observed in $H \to \gamma\gamma$ data of proton-proton collisions at $\sqrt{s} = 8\,\mathrm{TeV}$ and an integrated luminosity of $\int \mathcal{L}\,\mathrm{d}t = 20.7\,\mathrm{fb}^{-1}$.*

B.4. Signal + Background Fit of Diphoton Mass Spectra

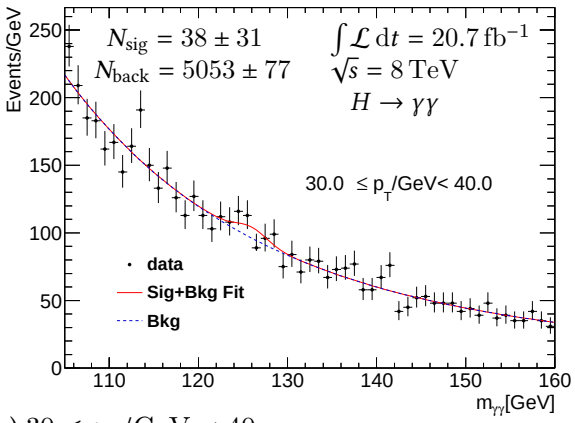

(a) $30 \leq p_T/\text{GeV} < 40$

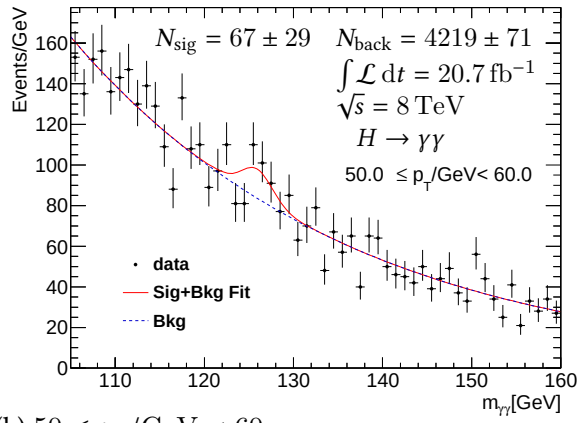

(b) $50 \leq p_T/\text{GeV} < 60$

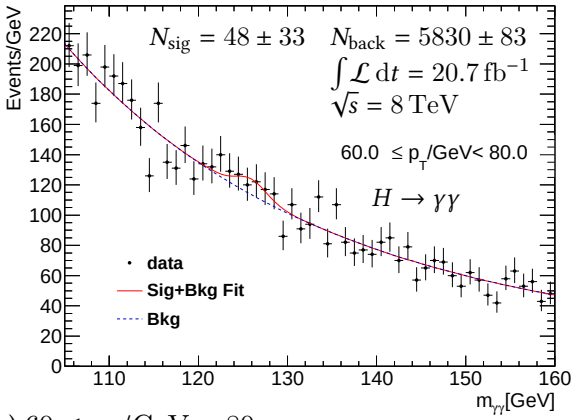

(c) $60 \leq p_T/\text{GeV} < 80$

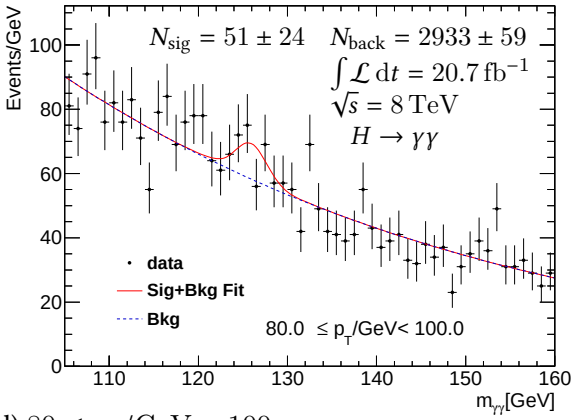

(d) $80 \leq p_T/\text{GeV} < 100$

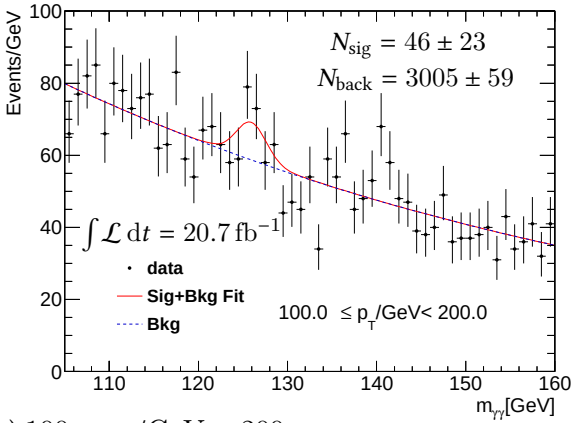

(e) $100 \leq p_T/\text{GeV} < 200$

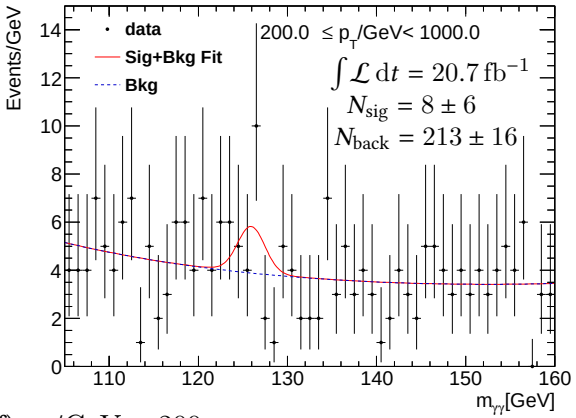

(f) $p_T/\text{GeV} \geq 200$

Figure B.7.: *Mass spectra in p_T-bins observed in data at $\sqrt{s} = 8\,\text{TeV}$ with an integrated luminosity of $\int \mathcal{L}\,dt = 20.7\,\text{fb}^{-1}$ and the modelled signal plus background functions. The fitted Higgs mass is $m_H = 125.9(5)\,\text{GeV}$.*

B.5. Likelihood Estimators for Increased Statistics

100000 Events

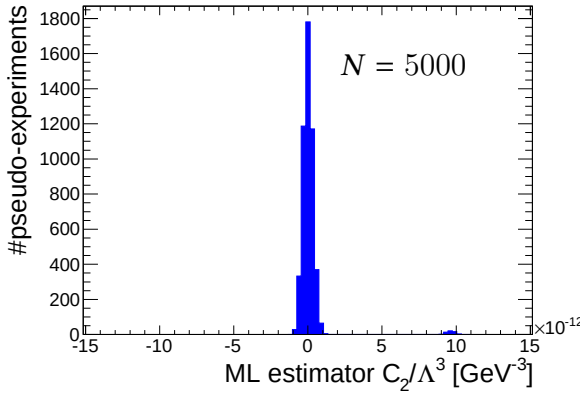

(a) $|O_{SM}|^2 + (C_2/\Lambda^3)\, O_{SM}O_2^\dagger + (C_2/\Lambda^3)^2|O_2|^2$

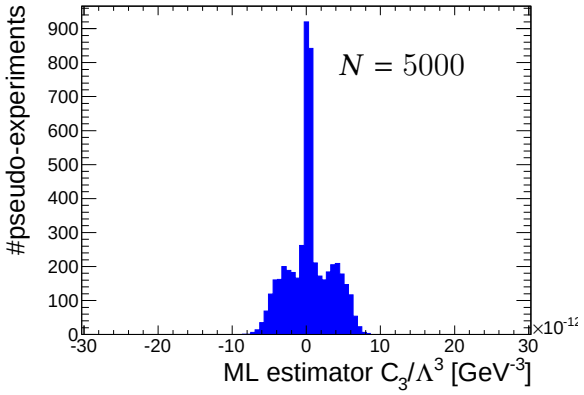

(b) $|O_{SM}|^2 + (C_3/\Lambda^3)\, O_{SM}O_3^\dagger + (C_3/\Lambda^3)^2|O_3|^2$

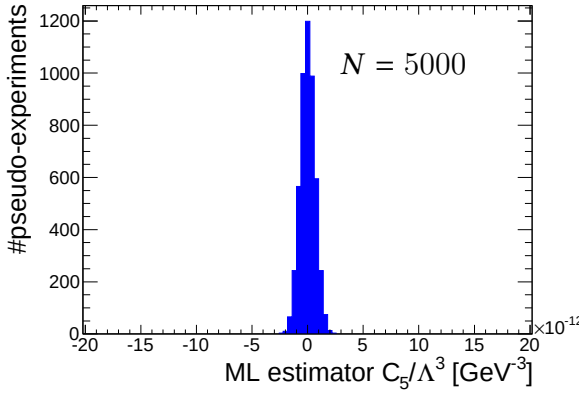

(c) $|O_{SM}|^2 + (C_5/\Lambda^3)\, O_{SM}O_5^\dagger + (C_5/\Lambda^3)^2|O_5|^2$

Figure B.8.: *Maximum likelihood estimators on Wilson coefficients for the admixture of the coupling operators O_i with $i \geq 2$ to the SM fitted to $N = 5000$ SM pseudo-experiments with event yield increased to 100000 events in each pseudo-experiment.*

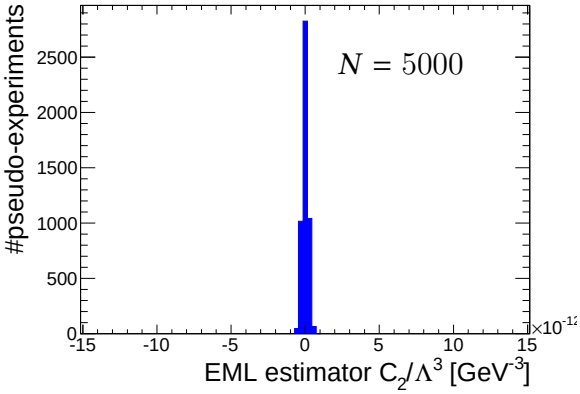

(a) $|O_{SM}|^2 + (C_2/\Lambda^3)\, O_{SM}O_2^\dagger + (C_2/\Lambda^3)^2|O_2|^2$

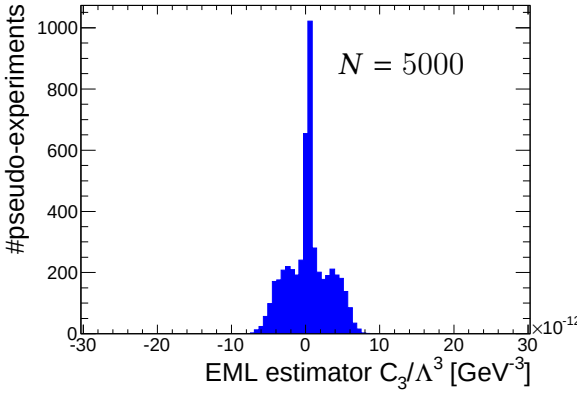

(b) $|O_{SM}|^2 + (C_3/\Lambda^3)\, O_{SM}O_3^\dagger + (C_3/\Lambda^3)^2|O_3|^2$

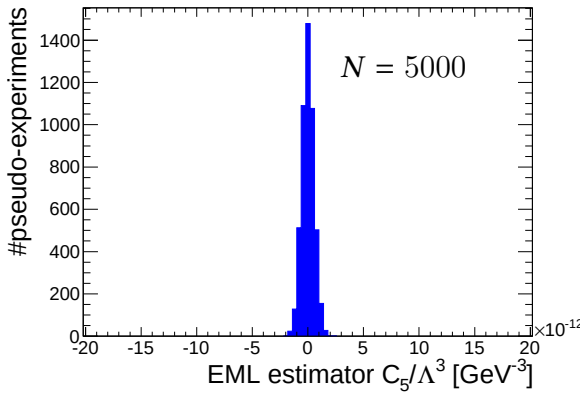

(c) $|O_{SM}|^2 + (C_5/\Lambda^3)\, O_{SM}O_5^\dagger + (C_5/\Lambda^3)^2|O_5|^2$

Figure B.9.: *Extended maximum likelihood estimators on Wilson coefficients for the admixture of the coupling operators O_i with $i \geq 2$ to the SM fitted to $N = 5000$ SM pseudo-experiments with event yield increased to 100000 events in each pseudo-experiment.*

B.6. Neyman Confidence Belts for Systematic Uncertainties

The gauge curves shown in this section represent 1σ variations so that no error propagation is contained in these figures. This means that these curves represent the gauge curves initially obtained for the applied 1σ variation of the corresponding uncertainty. The curves shown in the following therefore need to be combined in the above described procedure with the gauge curves that do not include any systematic uncertainties in order to properly estimate the statistical uncertainties and the influence of the respective systematic uncertainty.

Theoretical Uncertainty of fixed Mass Scale

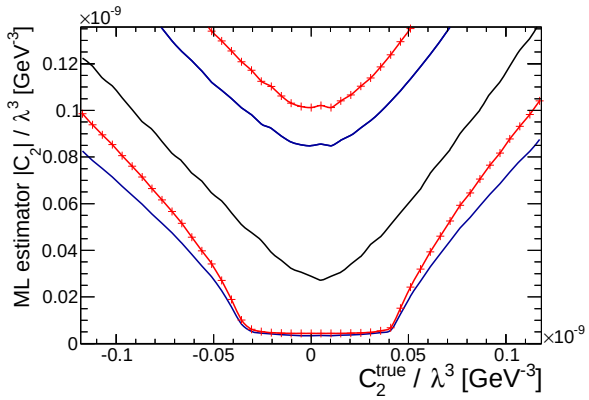

(a) $|O_{SM}|^2 + (C_2/\Lambda^3)\, O_{SM}O_2^\dagger + (C_2/\Lambda^3)^2|O_2|^2$

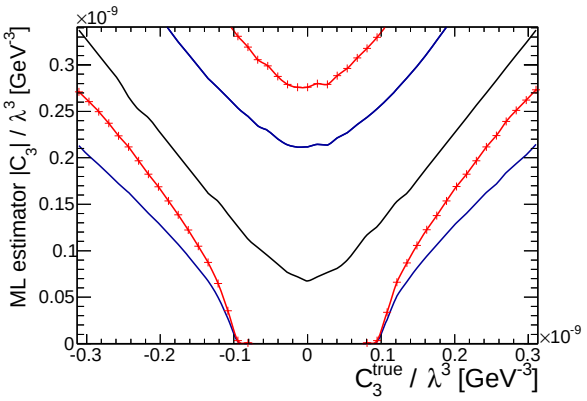

(b) $|O_{SM}|^2 + (C_3/\Lambda^3)\, O_{SM}O_3^\dagger + (C_3/\Lambda^3)^2|O_3|^2$

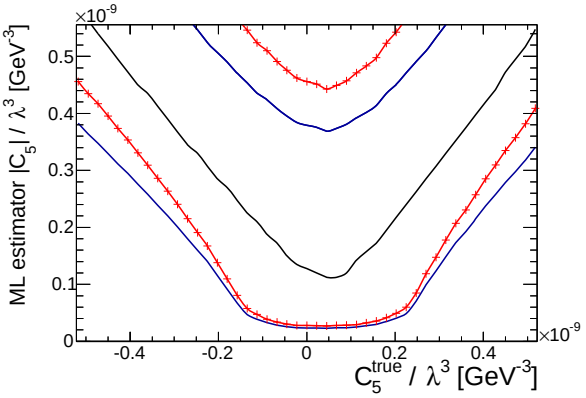

(c) $|O_{SM}|^2 + (C_5/\Lambda^3)\, O_{SM}O_5^\dagger + (C_5/\Lambda^3)^2|O_5|^2$

Figure B.10.: *Neyman confidence belts using non-extended likelihood for nominal analysis (black + dark blue) and for fixed mass scale (red) in the reweighting procedure.*

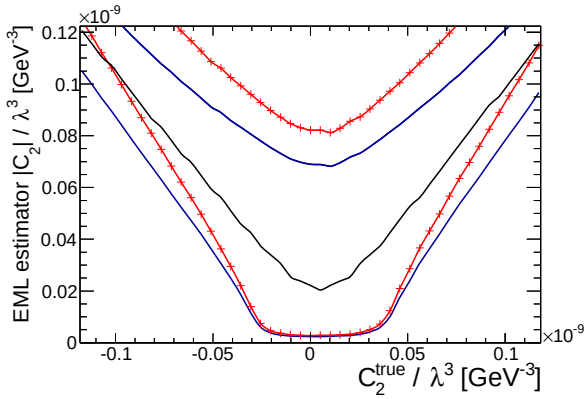

(a) $|O_{SM}|^2 + (C_2/\Lambda^3)\, O_{SM}O_2^\dagger + (C_2/\Lambda^3)^2|O_2|^2$

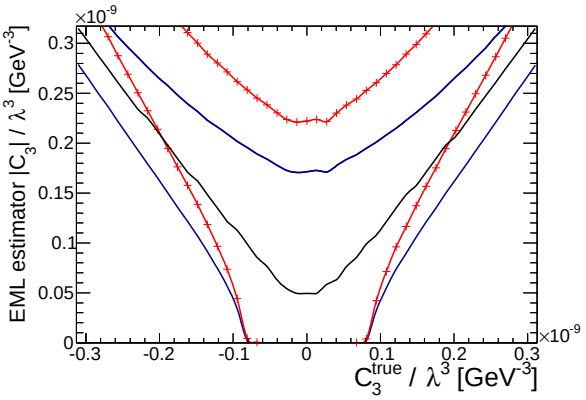

(b) $|O_{SM}|^2 + (C_3/\Lambda^3)\, O_{SM}O_3^\dagger + (C_3/\Lambda^3)^2|O_3|^2$

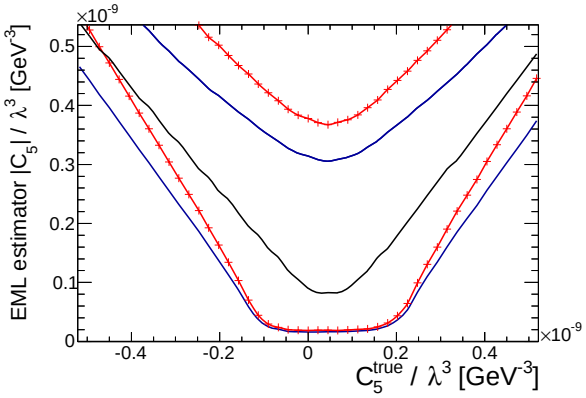

(c) $|O_{SM}|^2 + (C_5/\Lambda^3)\, O_{SM}O_5^\dagger + (C_5/\Lambda^3)^2|O_5|^2$

Figure B.11.: *Neyman confidence belts using extended likelihood for nominal analysis (black + dark blue) and for fixed mass scale (red) in the reweighting procedure.*

Jet Energy Scale Uncertainty

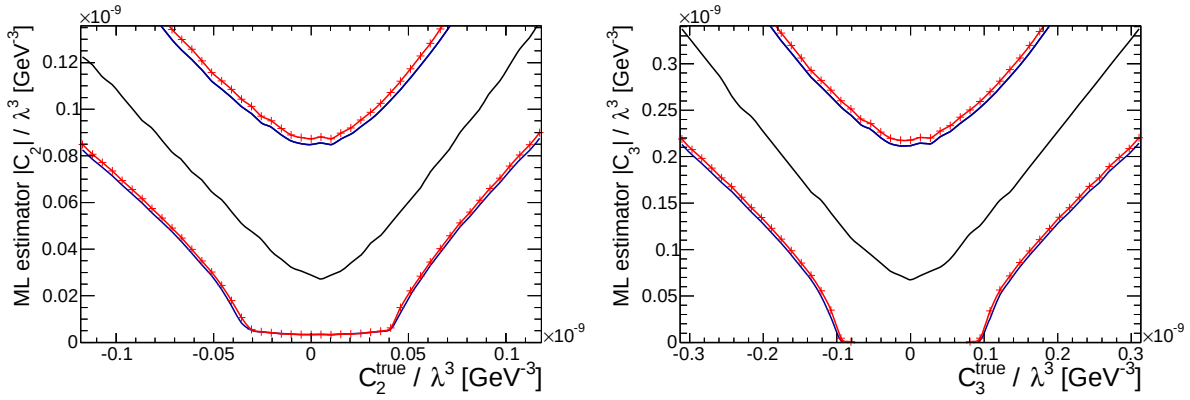

(a) $|O_{SM}|^2 + (C_2/\Lambda^3)\, O_{SM}O_2^\dagger + (C_2/\Lambda^3)^2|O_2|^2$ (b) $|O_{SM}|^2 + (C_3/\Lambda^3)\, O_{SM}O_3^\dagger + (C_3/\Lambda^3)^2|O_3|^2$

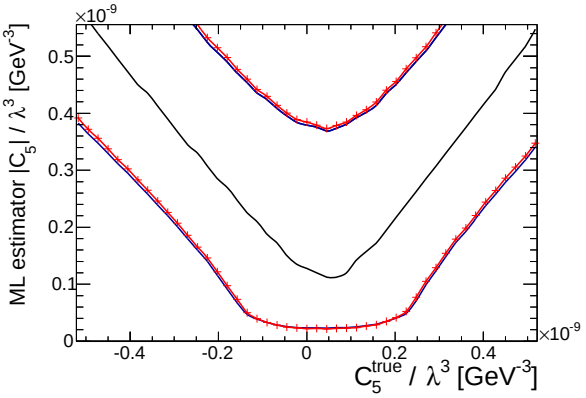

(c) $|O_{SM}|^2 + (C_5/\Lambda^3)\, O_{SM}O_5^\dagger + (C_5/\Lambda^3)^2|O_5|^2$

Figure B.12.: *Neyman confidence belts using non-extended likelihood for nominal analysis (black + dark blue) and for upwards scaled jet energy scale (red) in the reweighting procedure.*

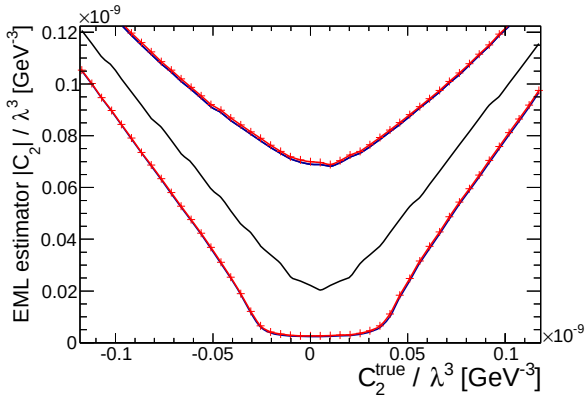

(a) $|O_{SM}|^2 + (C_2/\Lambda^3)\, O_{SM}O_2^\dagger + (C_2/\Lambda^3)^2|O_2|^2$

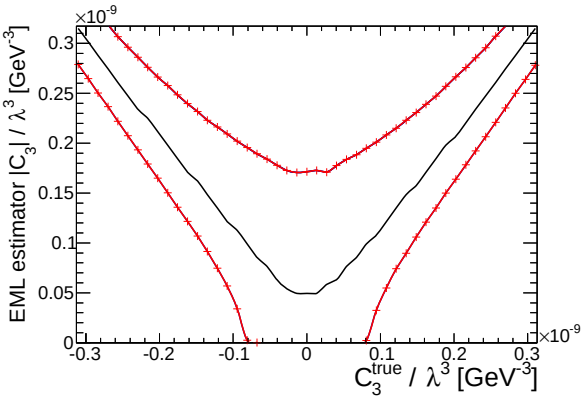

(b) $|O_{SM}|^2 + (C_3/\Lambda^3)\, O_{SM}O_3^\dagger + (C_3/\Lambda^3)^2|O_3|^2$

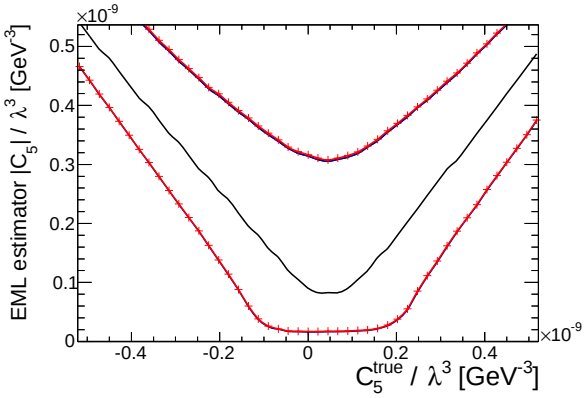

(c) $|O_{SM}|^2 + (C_5/\Lambda^3)\, O_{SM}O_5^\dagger + (C_5/\Lambda^3)^2|O_5|^2$

Figure B.13.: *Neyman confidence belts using extended likelihood for nominal analysis (black + dark blue) and for upwards scaled jet energy scale (red) in the reweighting procedure.*

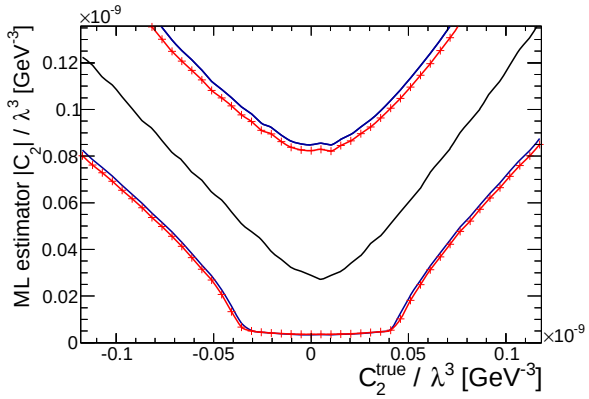

(a) $|O_{SM}|^2 + (C_2/\Lambda^3)\, O_{SM}O_2^\dagger + (C_2/\Lambda^3)^2|O_2|^2$

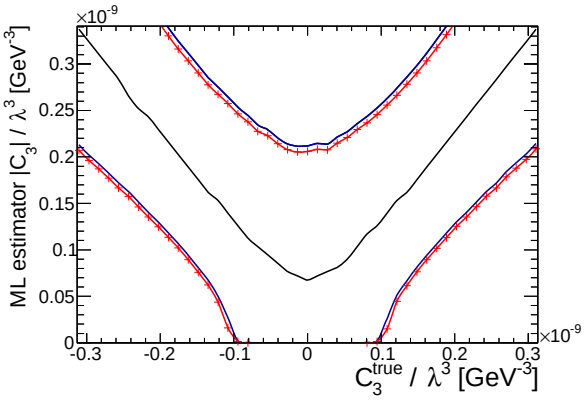

(b) $|O_{SM}|^2 + (C_3/\Lambda^3)\, O_{SM}O_3^\dagger + (C_3/\Lambda^3)^2|O_3|^2$

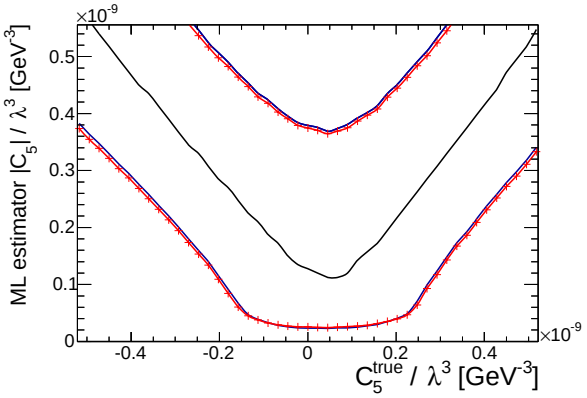

(c) $|O_{SM}|^2 + (C_5/\Lambda^3)\, O_{SM}O_5^\dagger + (C_5/\Lambda^3)^2|O_5|^2$

Figure B.14.: *Neyman confidence belts using non-extended likelihood for nominal analysis (black + dark blue) and for downwards scaled jet energy scale (red) in the reweighting procedure.*

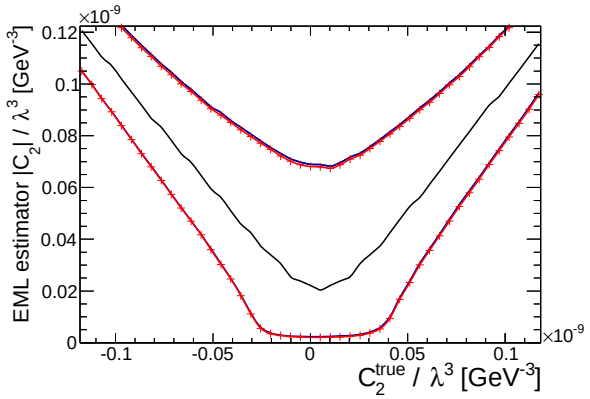

(a) $|O_{SM}|^2 + (C_2/\Lambda^3)\, O_{SM}O_2^\dagger + (C_2/\Lambda^3)^2|O_2|^2$

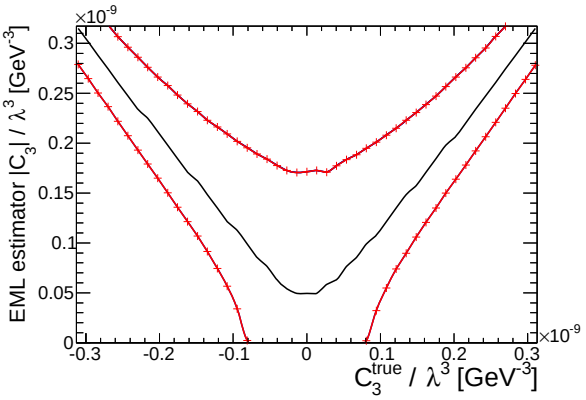

(b) $|O_{SM}|^2 + (C_3/\Lambda^3)\, O_{SM}O_3^\dagger + (C_3/\Lambda^3)^2|O_3|^2$

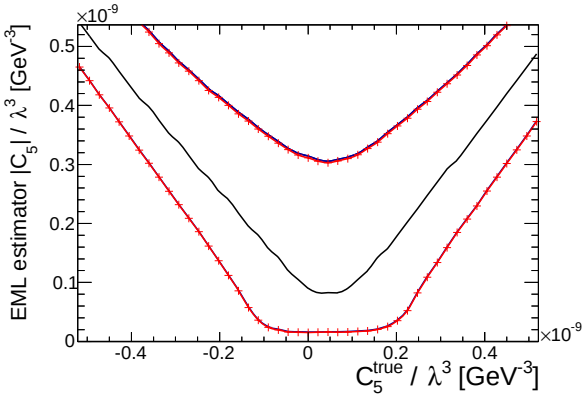

(c) $|O_{SM}|^2 + (C_5/\Lambda^3)\, O_{SM}O_5^\dagger + (C_5/\Lambda^3)^2|O_5|^2$

Figure B.15.: *Neyman confidence belts using extended likelihood for nominal analysis (black + dark blue) and for downwards scaled jet energy scale (red) in the reweighting procedure.*

Gluon Fusion Cross Section QCD Scale Uncertainty

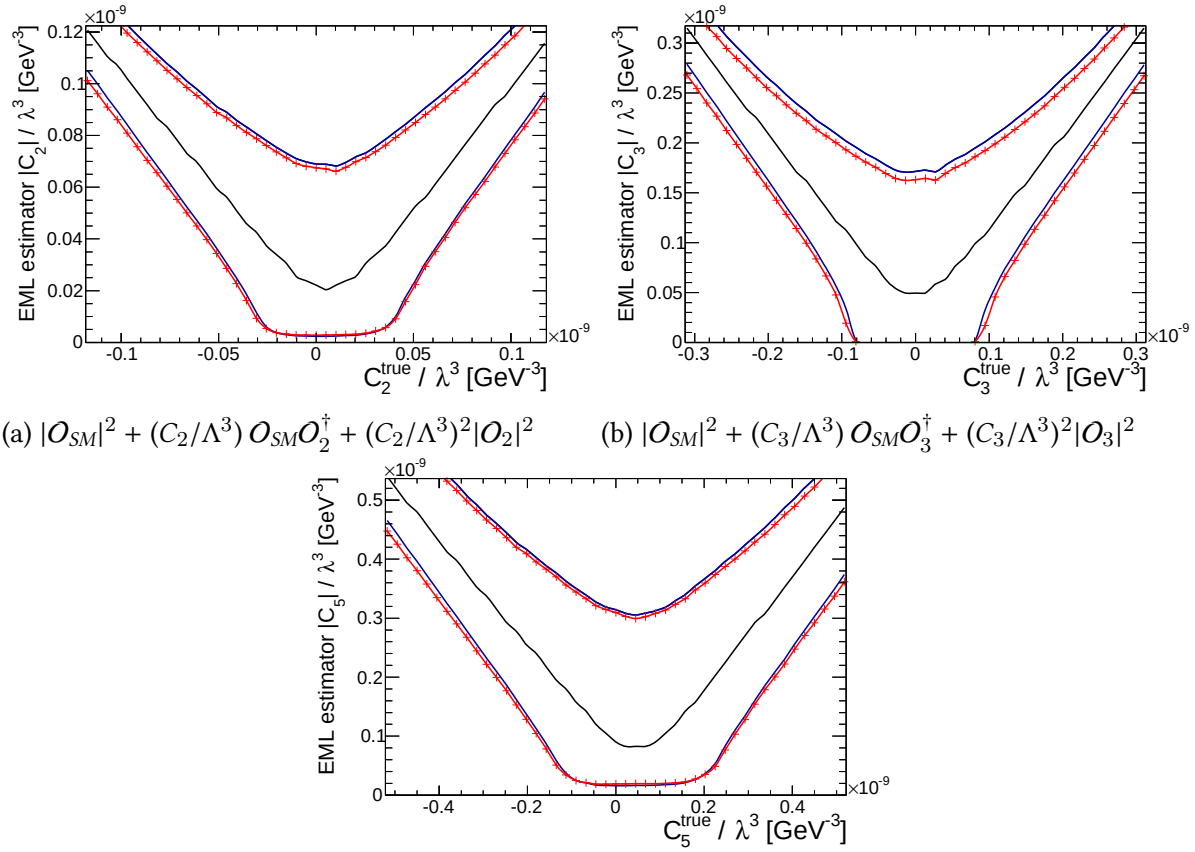

(a) $|O_{SM}|^2 + (C_2/\Lambda^3)\, O_{SM}O_2^\dagger + (C_2/\Lambda^3)^2|O_2|^2$ (b) $|O_{SM}|^2 + (C_3/\Lambda^3)\, O_{SM}O_3^\dagger + (C_3/\Lambda^3)^2|O_3|^2$

(c) $|O_{SM}|^2 + (C_5/\Lambda^3)\, O_{SM}O_5^\dagger + (C_5/\Lambda^3)^2|O_5|^2$

Figure B.16.: *Neyman confidence belts using extended likelihood for nominal analysis (black + dark blue) and for upwards scaled gluon fusion cross section due to QCD scale uncertainty (red) in the reweighting procedure.*

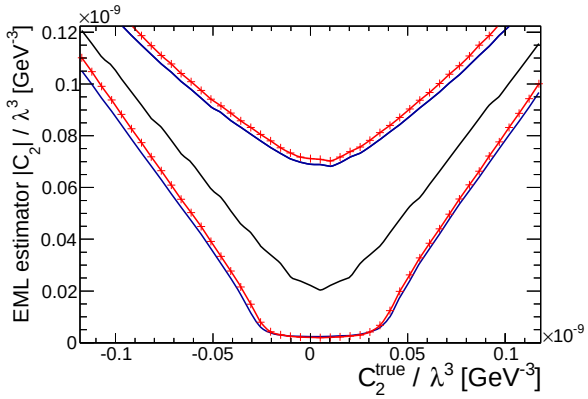

(a) $|O_{SM}|^2 + (C_2/\Lambda^3)\, O_{SM}O_2^\dagger + (C_2/\Lambda^3)^2|O_2|^2$

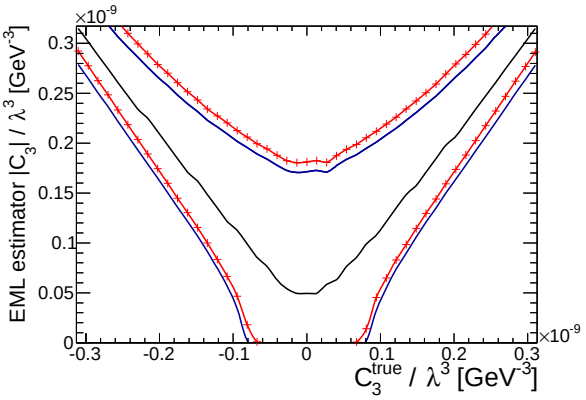

(b) $|O_{SM}|^2 + (C_3/\Lambda^3)\, O_{SM}O_3^\dagger + (C_3/\Lambda^3)^2|O_3|^2$

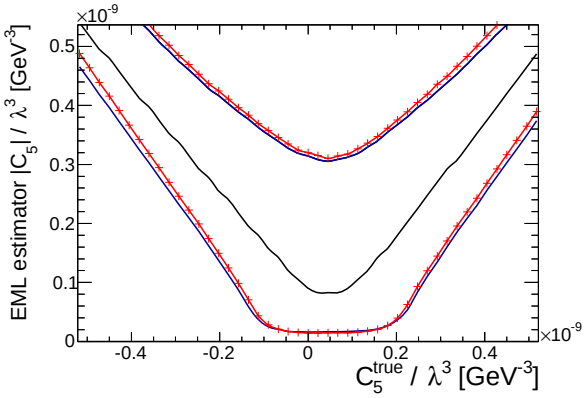

(c) $|O_{SM}|^2 + (C_5/\Lambda^3)\, O_{SM}O_5^\dagger + (C_5/\Lambda^3)^2|O_5|^2$

Figure B.17.: *Neyman confidence belts using extended likelihood for nominal analysis (black + dark blue) and for downwards scaled gluon fusion cross section due to QCD scale uncertainty (red) in the reweighting procedure.*

Acknowledgements

An dieser Stelle möchte ich mich bei allen Leuten bedanken, die mich in meinem Studium begleitet und unterstützt haben. Leider kann ich hier nicht alle namentlich erwähnen und beschränke mich auf diejenigen, die bei der Entstehung dieser Masterarbeit für mich von besonderer Bedeutung waren.

Zunächst möchte ich mich bei Markus Schumacher bedanken für die Möglichkeit, diese Masterarbeit in so einer netten Arbeitsgruppe anzufertigen. Danke auch dafür, dass ich im letzten Jahr viel über die Teilchenphysik lernen konnte und dich bei Problemen auch immer wieder direkt nach Rat fragen konnte. Ebenfalls bedanken möchte ich mich bei Stan. Dafür, dass du mich während meiner Arbeit im vergangenen Jahr immer hervorragend betreut und auch motiviert hast. Nicht nur zuletzt in der Schreibphase hast du mir immer wieder sehr weitergeholfen!

Bedanken möchte ich mich auch bei allen anderen (vorübergehenden) Mitgliedern der Arbeitsgruppe für die durchgehend gute Stimmung und eure Hilfsbereitschaft. Besonders erwähnen möchte ich dabei Flo, da ich dich immer wieder zu allen möglichen Fragen zu Photonen und anderem löchern konnte und du dir dann auch immer Zeit für mich genommen hast. Ein besonderer Dank geht auch an Christian und Michaela, die die längste Zeit meiner Masterarbeit ein Büro mit mir geteilt haben.

Zu guter Letzt möchte ich mich bei meinen Eltern bedanken, dafür, dass sie mich zu jeder Zeit meines Studiums unterstützt haben und diese Masterarbeit damit ermöglicht haben.

Erklärung

Hiermit versichere ich, die eingereichte Masterarbeit selbständig verfasst und keine anderen als die von mir angegebenen Quellen und Hilfsmittel benutzt zu haben. Wörtlich oder sinngemäß aus anderen Werken übernommene Inhalte wurden entsprechend den anerkannten Regeln wissenschaftlichen Arbeitens (lege artis) kenntlich gemacht. Ich erkläre weiterhin, dass die eingereichte Masterarbeit weder vollständig noch in wesentlichen Teilen Gegenstand eines anderen Prüfungsverfahrens war oder ist.

Ort, Datum ……..…… Unterschrift ……